If you have discovered material in AURA which is unlawful e.g. breaches copyright, (either yours or that of a third party) or any other law, including but not limited to those relating to patent, trademark, confidentiality, data protection, obscenity, defamation, libel, then please read our Takedown Policy and contact the service immediately

Computer simulation of radio-frequency methane/hydrogen plasmas and their interaction with GaAs surfaces

Russell Leyton Layberry

Doctor of Philosophy

The University of Aston in Birmingham.

June 1999.

This copy of the thesis has been supplied on condition that anyone who consults it is understood to recognise that its copyright rests with its author and that no quotation from the thesis and no information derived from it may be published without proper acknowledgement.

The University of Aston in Birmingham

Computer simulation of radio-frequency methane/hydrogen plasmas and their interaction with GaAs surfaces.

Russell Leyton Layberry

Doctor of Philosophy

1999

The following thesis describes the computer modelling of radio frequency capacitively coupled methane/hydrogen plasmas and the consequences for the reactive ion etching of (100) GaAs surfaces. In addition a range of etching experiments was undertaken over a matrix of pressure, power and methane concentration. The resulting surfaces were investigated using X-ray photoelectron spectroscopy and the results were discussed in terms of physical and chemical models of particle/surface interactions in addition to the predictions for energies, angles and relative fluxes to the substrate of the various plasma species.

The model consisted of a Monte Carlo code which followed electrons and ions through the plasma and sheath potentials whilst taking account of collisions with background neutral gas molecules. The ionisation profile output from the electron module was used as input for the ionic module. Momentum scattering interactions of ions with gas molecules were investigated via different models and compared against results given by quantum mechanical code. The interactions were treated as central potential scattering events and the resulting neutral cascades were followed. The resulting predictions for ion energies at the cathode compared well to experimental ion energy distributions and this verified the particular form of the electrical potentials used and their applicability in the particular geometry plasma cell used in the etching experiments.

The final code was used to investigate the effect of external plasma parameters on the mass distribution, energy and angles of all species impingent on the electrodes. Comparisons of electron energies in the plasma also agreed favourably with measurements made using a Langmuir electric probe.

The surface analysis showed the surfaces all to be depleted in arsenic due to its preferential removal and the resultant Ga:As ratio in the surface was found to be directly linked to the etch rate. The etch rate was determined by the methane flux which was predicted by the code.

KEYWORDS: PLASMA, RF, MODEL, GAAS, ETCH

To my parents and family.

Acknowledgements

I would like to thank Professor Sullivan for his help and guidance throughout the project. I would also like to thank Andrew Abbot and Dr. Saied for their assistance with experimental work.

I would also like to thank Keith Vanner and Caswell for supplying us with samples and their help with technical issues.

Special thanks go to George Pearce for both technical help and general advice, without which I would have been significantly disadvantaged.

I would also like to thank all of the Surface Science research group both past and present for creating a pleasant working atmosphere.

Finally, I would like to thank my family for their constant support.

Table of Contents

Page

1. Plasmas in reactive ion etching **16**
1.1 Etching of semiconductors 16
1.1.1 Device processing 16
1.1.2 Dry etching 17
1.2 Plasma discharges 20
1.2.1 The plasma state 20
1.2.1.1 DC plasmas 21
1.2.1.2 Sheath formation 22
1.2.1.3 Plasma chemistry 23
1.2.2 RF plasmas 24
1.2.2.1 DC bias and equilibrium discharges 25
1.2.2.2 The rf sheath 26
1.2.2.3 Electric field across sheath 27
1.2.2.4 The plasma potential 28
1.2.2.5 The Bohm criterion 30
1.2.2.6 Electron energies 31
1.2.2.7 Charged particle distributions 32
1.2.2.8 Ion trajectories 32
1.3 Review of modelling of ion energies 34
1.3.1 Circuit models 34
1.3.2 Fluid models 35
1.3.3 Particle in cell 36
1.3.4 Monte Carlo/sheath 37
1.3.4.1 Plasma potentials 37
1.3.4.2 Electric fields 38
1.3.4.3 Nature of interactions 39
1.4 Surface modification - theoretical 42
1.4.1 Review of ion surface interactions 42
1.4.2 Sputtering theory and sputter yield 43
1.4.3 Threshold sputter theory 45
1.4.4 Preferential sputtering 46
1.4.5 Surface binding energy 46
1.4.6 Gibbsian segregation 48
1.4.7 Codes 49
1.4.7.1 SUSPRE 49
1.4.7.2 TRIM 50
1.4.7.3 MARLOWE 50
1.4.7.4 Hyperchem 50
1.5 Review of etching of III-V's 50
1.5.1 GaAs devices 50
1.5.2 Etching chemistries 51
1.5.3 Hydrocarbon etching of GaAs 51
1.5.4 Stoichiometry change 53
1.5.4.1 Inert 53
1.5.4.2 Hydrocarbon 53
1.6 Research programme 54
1.6.1 Plasma 54
1.6.2 Surface interactions 55
1.6.3 XPS 55

2. Modelling of ion energies 56
2.1 The general collisionless model 56
2.1.1 Ion trajectories 56
2.1.2 Entering the sheath 56
2.1.3 The plasma and sheath potential 57
2.1.4 Equations of motion 58
2.1.5 Results 58
2.1.6 Comparison with published results 58
2.2 Argon collisions 61
2.2.1 Cross sections 61
2.2.2 Randomization of a collision event 61
2.2.3 Collisions 62
2.2.3.1 Charge transfer 62
2.2.3.2 Momentum scattering 63
2.2.4 Neutral cascades 65
2.2.5 Comparison with published data for argon 65
2.2.5.1 At the cathode 65
2.2.5.2 At the anode 66
2.3 Complex molecule scattering 67
2.3.1 The choice of interaction potentials 68
2.3.2 The model 69
2.3.3 Predictions for scattering angles 69
2.4 Extension of code to hydrogen 75
2.4.1 Cross sections 75
2.4.1.1 Collisions involving H^+ 76
2.4.1.2 Collisions involving H_2^+ 77
2.4.1.3 Collisions involving H_3^+ 77
2.4.2 Comparison with published data for hydrogen 78
2.5 Extension to methane fragments 79
2.5.1 Collisions involving H_2^+ 79
2.5.2 Collisions involving CH_3^+ 79
2.5.3 Collisions involving CH_4^+ 80
2.6 Extension to include ion creation processes 81
2.6.1 Electron motion and randomization 81
2.6.2 Scattering 81
2.6.3 Ionisation 83
2.6.4 Excitation 84
2.6.4.1 Electronic 84
2.6.4.2 Vibrational 85
2.6.4.3 Rotational 86
2.6.5 Electron recombinations 86
2.6.6 Electron induced secondary electrons 86
2.6.7 Ionisations used as source of ions 87
2.6.8 Ion induced secondary electrons 87
2.6.9 Electron cascades 87
2.6.10 Data output 88
2.6.10.1 Text file 88
2.6.10.2 Energy and angle distributions 90
2.6.10.3 EEDF 90
2.6.10.4 Ionisation and excitation profiles 90
2.6.10.5 Number density profile of electrons and ions 90

3. Plasma Surface Interaction 91
3.1 Hyperchem 91

3.1.1 The simulation 91
3.1.2 Result 93
3.2 Sputter yield 94
3.2.1 Etch rate 96
3.3 Damage 96
3.3.1 Penetration depth 96
3.3.2 Depth of damage 97
3.3.3 Depth of damage in equilibrium 98
3.4 The crystal structure of GaAs 100
3.4.1 The GaAs structure 100
3.4.2 Surface binding energy and preferential sputtering 100
3.4.3 The (100) surface and relaxation 101
3.3.4 Preferential sputtering 102
3.4.4.1 Direct knock-on 103
3.4.4.2 Increased surface release 106
3.5 Chemistry 108
3.6 Summary and predictions 109
3.6.1 Summary 109
3.6.2 Predictions 109
3.6.2.1 Physical 109
3.6.2.2 Chemical 110
3.7 Reconstruction of the subsurface 110
3.7.1 Computer code 110
3.7.2 The inelastic mean free path 112

4. Experimental set-up and analytical tools 114
4.1 The etching chamber 114
4.1.1 Chamber cleaning 115
4.1.2 Sample preparation 116
4.1.3 Experimental procedure 116
4.2 Plasma diagnostic tools 117
4.2.1 Langmuir probe 117
4.2.2 Mass/energy analyser 120
4.2.3 Measurement of sample potentials 124
4.2.4 Optical measurements 125
4.3 Surface techniques 125
4.3.1 X-ray photoelectron spectroscopy 125
4.3.2 Atomic force microscopy 125

5. Model results 127
5.1 Electron model 127
5.1.1 Effect of a change in V_f 128
5.1.2 Effect of a change in pressure 129
5.1.2.1 The floating potential 129
5.1.2.2 The ion and electron distribution functions 131
5.1.2.3 The ionisation profile 132
5.1.2.4 The electron temperature 133
5.1.3 Effect of addition of methane 138
5.1.3.1 The floating potential 138
5.1.3.2 The ion and electron distribution functions 139
5.1.4 Change in pressure of methane/hydrogen 139
5.1.5 Change in driving potential 139
5.1.6 Change in secondary electron emission coefficient - γ 141
5.2 Model for ions and neutrals 142

5.2.1 Effect of change in pressure (hydrogen) 143
5.2.1.1 Ion energy and angle distributions 143
5.2.1.2 Ion fluxes 146
5.2.1.3 Neutral energy and angle distributions 147
5.2.1.4 Neutral fluxes 150
5.2.2 Addition of methane 150
5.2.2.1 Ion energy and angle distributions 150
5.2.2.2 Ion fluxes 150
5.2.2.3 Neutral energy and angle distributions 151
5.2.2.4 Neutral fluxes 152
5.2.3 Change in pressure of methane/hydrogen 153
5.2.3.1 Ion energy and angle distributions 153
5.2.3.2 Ion fluxes 153
5.2.3.3 Neutral energy and angle distributions 154
5.2.3.4 Neutral fluxes 154
5.2.4 Change in driving potential (hydrogen) 155
5.2.4.1 Ion energy and angle distributions 155
5.2.4.2 Ion fluxes 155
5.2.4.3 Neutral energy and angle distributions 156
5.2.5 Change in driving potential (methane/hydrogen) 156
5.2.5.1 Ion energy and angle distributions 156
5.2.5.2 Ion fluxes 157
5.2.5.3 Neutral energy and angle distributions 158
5.2.6 Change in the cathode sheath width 158
5.2.7 Change in secondary electron emission coefficient - γ 159

6. Experimental Results **160**
6.1 Plasma diagnostics 160
6.1.1 Langmuir probe 160
6.1.1.1 Argon 160
6.1.1.2 Hydrogen 161
6.1.1.3 Methane/hydrogen 165
6.1.2 Mass probe 167
6.1.2.1 Results 167
6.1.2.2 Mass probe calibration 170
6.1.3 Voltages 173
6.1.3.1 The D.C. bias 173
6.1.3.2 Potential at the quartz plate 174
6.1.4 Sheath width 176
6.2 Etch rates 177
6.2.1 Fixed flow rate 178
6.2.2 Variable flow rate 180
6.2.3 Neon/hydrogen 181
6.3 AFM 182
6.3.1 Surface prior to etching 182
6.3.2 Surface after etching 182
6.4 XPS 185
6.4.1 Methane/hydrogen 185
6.4.1.1 10 mTorr 186
6.4.1.2 20 mTorr 192
6.4.1.3 As a function of pressure 194
6.4.1.4 As a function of power 198
6.4.1.5 Summary of methane/hydrogen etching 202
6.4.2 Neon/hydrogen 205

6.4.2.1 10 mTorr 205
6.4.2.2 20-80 mTorr 207
6.4.2.3 As a function of pressure 210
6.4.2.4 Summary of neon/hydrogen etching 214
6.5 Comparison of model and experimental results 215
6.5.1 Electron energies 215
6.5.2 Plasma potential and IEDs at the anode 216
6.5.2.1 Argon 216
6.5.2.2 Hydrogen 218
6.5.3 Ion fluxes 219
6.5.3.1 Hydrogen 219
6.5.3.2 Addition of methane 221
6.5.3.3 Increase in pressure of methane/hydrogen 223
6.5.3.4 Increase in power of methane/hydrogen 224
6.5.4 The predicted optical sheath width 225
6.5.5 Regimes of etching and deposition 227
6.6 Predictions for the etching experiments 228
6.6.1 Ion fluxes 228
6.6.2 Relevance of neutral fluxes 229
6.6.3 Neutral fluxes 231

7. Discussion 233
7.1 Modelling 233
7.1.1 Plasma modelling 233
7.1.2 Particle/surface interaction modelling 238
7.2 Plasma/surface interaction 239
7.2.1 Discussion of etch rates 239
7.2.2 Methane/hydrogen etching of GaAs 241
7.2.2.1 10 mTorr, 150 W 241
7.2.2.2 Changes in power 246
7.2.2.3 Changes in pressure, methane/hydrogen 247
7.2.2.4 Changes in pressure, pure hydrogen 247
7.2.3 Neon/hydrogen etching of GaAs 248
7.2.3.1 As a function of neon concentration, 10 mTorr 248
7.2.3.2 As a function of pressure 250

8. Conclusions and further work 251
8.1 Plasma modelling 251
8.2 Plasma/surface modification 251
8.3 Further work 252
8.3.1 Plasma modelling 252
8.3.2 Particle/surface interaction modelling 253
8.3.3 Etching experiments 253

References 254

Appendices
Appendix I Plasma program On Disc
Appendix II Scattering program On Disc
Appendix III ARXPS prediction code On Disc
Appendix IV Published papers 268

List of Figures

Figure **Page**

Figure 1.1 Five step diffusion process after Carroll [1]. 17
Figure 1.2 Isotropic and anisotropic etching. 18
Figure 1.3 'Barrel-type' plasma etching apparatus. 19
Figure 1.4 'Top-hat' type reactor. 19
Figure 1.5 Spatial distributions in a D.C. plasma. 22
Figure 1.6 The potential across and the physical extent of the rf sheath. 27
Figure 1.7 Different approximations to the electric field across the sheath. 28
Figure 1.8 Form of the plasma potential a) directly driven electrode b) capacitively coupled electrode where cathode area << anode area. 29
Figure 1.9 Plasma potential displaying predominantly capacitive or resistive nature. 30
Figure 1.10 Leaking of the electric field from the sheath into the plasma due to the Bohm criterion. 30
Figure 1.11 Spatial variation of ions and electrons in a helium-like gas. 32
Figure 1.12 Ion trajectories across and rf sheath. 33
Figure 1.13 Saddle-like structure exhibited by ions at the cathode of a plasma cell. 33
Figure 1.14 Schematic of an rf capacitively coupled plasma and the equivalent circuit. 35
Figure 1.15 Summary of surface processes. 43
Figure 2.1 Comparison of a) predicted and b) experimental results for the IEDs at the cathode of an rf oxygen plasma. 59
Figure 2.2 Comparison of a) predicted and b) experimental results for the IEDs at the cathode of an rf argon/hydrogen plasma. 60
Figure 2.3 Comparison of a) predicted and b) experimental results for the IEDs at the cathode of an rf carbon tetrafluoride plasma. 60
Figure 2.4 Cross section data for Ar^+ collisions with Ar. 61
Figure 2.5 Schematic of the interaction of a pair of particles via a central potential. 63
Figure 2.6 Schematic of the angle change of a scattered particle. 64
Figure 2.7 Comparison of a) predicted and b) experimental results for the IEDs at the cathode of argon rf plasma. 66
Figure 2.8 Comparison of a) predicted and b) experimental results for the IEDs at the anode of argon rf plasma. Pressure = 10 mTorr. 67
Figure 2.9 Comparison of a) predicted and b) experimental results for the IEDs at the anode of argon rf plasma. Pressure = 50 mTorr. 67
Figure 2.10 The four interaction potentials used to model polyatomic scattering. 69
Figure 2.11 Results of model 1. 70
Figure 2.12 Results of model 2. 70
Figure 2.13 Results of model 2. 71
Figure 2.14 Results of model 4. 71
Figure 2.15 Results for an energy of 10 eV. 72
Figure 2.16 Cross sections associated with scattering of θ_{min} (= 2°). 72
Figure 2.17 Dissociation of H_2 predicted by Hyperchem, model 3 and Phelps. 73
Figure 2.18 Scattering of CH_4 from H_2 - interaction energy 10 eV. 73
Figure 2.19 Scattering of CH_4 from H_2 - interaction energy 100 eV. 74
Figure 2.20 Cross sections for $H^+ + H_2$. 75
Figure 2.21 Cross sections for $H_2^+ + H_2$. 75
Figure 2.22 Cross sections for $H_3^+ + H_2$. 76
Figure 2.23 Comparison of a) Predicted and b) Experimental results for the IEDs at the anode of hydrogen rf plasma. Pressure = 9 mTorr. 78
Figure 2.24 Comparison of a) Predicted and b) Experimental results for the IEDs at the anode of argon rf plasma. Pressure = 27 mTorr. 78
Figure 2.25 Comparison of a) Predicted and b) Experimental results for the IEDs at the anode of argon rf plasma. Pressure = 65 mTorr. 78
Figure 2.26 Cross section for electron scattering from H_2 and CH_4. 82
Figure 2.27 The scattering of an electron by an angle θ. 82
Figure 3.1 9 Ga and 9 As atoms in a stable arrangement. 92

Figure 3.2 The arrangement in figure 3.1 from a different perspective. 92
Figure 3.3 Comparison of GaAs and methane molecule. 92
Figure 3.4 Average fraction of C-H bonds exceeding certain lengths at the simulation end as a function of interaction energy. 93
Figure 3.5 Comparison of sputter yields predicted for C into GaAs from the codes TRIM and SUSPRE. 94
Figure 3.6 Sputter yield as a function of the binding energy for 100 eV C onto Ga As. 95
Figure 3.7 Average penetration depth of hydrogen and carbon into GaAs. 97
Figure 3.8 Depth profile of target vacancies in GaAs due to 200 eV carbon atom. 98
Figure 3.9 Depth profile of target displacements in GaAs due to 200 eV carbon atom. 98
Figure 3.10 The vacancy creation function $f(x)$. 99
Figure 3.12 Relaxation of the (110) surface of GaAs. 102
Figure 3.13 Relaxation of the (100) surface of GaAs. 102
Figure 3.14 The energies of incident carbon atom and scattered arsenic atom as a function of angle for initial energy of 1000 eV. 104
Figure 3.15 The final angle of a gallium atom with initial energy 10 eV. leaving the surface as a function of its initial angle. 106
Figure 3.16 The relative sizes of the etch products arsine and tri-methyl gallium in comparison with a part of the GaAs lattice and a methane molecule. 108
Figure 3.17 Front end for program to predict ARXPS results from standard layered structure. 112
Figure 3.18 Problems of shadowing in ARXPS. 112
Figure 4.1 The etching chamber. 114
Figure 4.2 Schematic of the etching apparatus. 115
Figure 4.3 Schematic of the set-up of the diagnostic tools. 117
Figure 4.4 Typical Langmuir probe characteristic. 117
Figure 4.5 Method for finding the plasma potential. 119
Figure 4.6 The mass/energy analyser. 121
Figure 4.7 The mass probe orifice. 121
Figure 4.8 Energy change of ions traversing the mass/energy analyser. 122
Figure 4.9 Angle of acceptance for ions entering the probe orifice. 123
Figure 4.10 Ion trajectories between the orifice and lens 1. 124
Figure 5.1 Ionisation profile in position and phase space. 127
Figure 5.2 Ionisation profile in position and phase space with x and y axes transposed. 128
Figure 5.3 The multiplicity m_e as a function of the floating potential for a 40 mTorr hydrogen plasma. 129
Figure 5.4 The multiplicity m_e as a function of pressure for a hydrogen plasma with V_f = 17 V. 130
Figure 5.5 The number of electrons exceeding the simulation length as a function of the pressure, V_f = 17 V, hydrogen plasma. 130
Figure 5.6 The value of the floating potential necessary to give a value of the multiplicity of 0.9. 131
Figure 5.7 The spatial number density of ions and electrons, 10 mTorr. 132
Figure 5.8 The spatial number density of ions and electrons, 90 mTorr. 132
Figure 5.9 The ionisation profile, 10 mTorr. 133
Figure 5.10 The ionisation profile, 90 mTorr. 133
Figure 5.11 The EEDF, 10 mTorr. 134
Figure 5.12 The EEDF, 50 mTorr. 134
Figure 5.13 The EEDF, 90 mTorr. 134
Figure 5.14 A plot of $ln\left(f(\varepsilon)/\sqrt{\varepsilon}\right)$ against electron energy for a plasma at 10 mTorr. 135
Figure 5.15 A plot of $ln\left(f(\varepsilon)/\sqrt{\varepsilon}\right)$ against electron energy for a plasma at 40 mTorr. 136
Figure 5.16 A plot of $ln\left(f(\varepsilon)/\sqrt{\varepsilon}\right)$ against electron energy for a plasma at 80 mTorr. 136
Figure 5.17 Comparison between simulated EEDF at the plasma/sheath boundary and in the plasma bulk (midway between the electrodes) at 10 mTorr. 137
Figure 5.18 Comparison between simulated EEDF at the plasma/sheath boundary and in the plasma bulk (midway between the electrodes) at 90 mTorr. 137
Figure 5.19 Simulated EEDF with EEDFs neglecting rotational and vibrational excitations superimposed, pressure = 90 mTorr, measured in the plasma bulk. 138
Figure 5.20 Number of electrons exceeding the simulation time as a function of the methane concentration. 138

Figure 5.21 Floating potential as a function of the methane concentration. 139
Figure 5.22 The ionisation profile, pure hydrogen, 40 mTorr, for a range of cathode driving potentials, V_0. 140
Figure 5.23 Simulated EEDF for powers of 50 W, 100 W and 150 W at a pressure of 10 mTorr, measured in the plasma bulk (midway between the electrodes), 12 % methane. 141
Figure 5.24 The effect on simulated EEDFs of changes in the ion impact secondary electron emission function at a pressure of 50 mTorr in the plasma bulk, 12 % methane. 142
Figure 5.25 The effect on simulated EEDFs of changes in the ion impact secondary electron emission function at a pressure of 10 mTorr at the plasma/sheath boundary, 12 % methane. 142
Figure 5.26 Predicted H^+ IEDs at the cathode for a pressure of 10 mTorr. 143
Figure 5.27 Predicted H_2^+ IEDs at the cathode for a pressure of 10 mTorr. 143
Figure 5.28 Predicted H_3^+ IEDs at the cathode for a pressure of 10 mTorr. 143
Figure 5.29 Predicted H^+ IEDs at the cathode for a pressure of 90 mTorr. 144
Figure 5.30 Predicted H_2^+ IEDs at the cathode for a pressure of 90 mTorr. 144
Figure 5.31 Predicted H_3^+ IEDs at the cathode for a pressure of 90 mTorr. 145
Figure 5.32 Average energy of the three ion species as a function of pressure. 145
Figure 5.33 H_3^+ IAD at a) 10 mTorr and 90 mTorr b) 10 mTorr resolved into angle and energy and c) 90 mTorr resolved into angle and energy. 146
Figure 5.34 Relative fluxes to the cathode of the three ion species as a function of pressure. 147
Figure 5.35 H_2 NED at the cathode at a pressure of 10 mTorr. 148
Figure 5.36 H_2 NED at the cathode at a pressure of 90 mTorr. 148
Figure 5.37 H_2 NAD at a pressure of 10 mTorr. 149
Figure 5.38 H_2 NAD at a pressure of 90 mTorr. 149
Figure 5.39 Average energy of neutral H_2 molecules arriving at the cathode as a function of pressure. 150
Figure 5.40 Ratio of neutrals to ions arriving at the cathode as a function of pressure. 150
Figure 5.41 Relative fluxes to the cathode of the ion species as a function of methane concentration. 151
Figure 5.42 Average energies of H_2 and CH_4 neutrals at the cathode as a function of pressure. 152
Figure 5.43 Flux of H_2 neutrals and CH_4 neutrals at the cathode as a percentage of total ion flux as a function of methane concentration, 40 mTorr. 152
Figure 5.44 Average energy of the ion species at the cathode as a function of pressure. 153
Figure 5.45 Relative fluxes to the cathode of the ion species as a function of pressure. 153
Figure 5.46 Average energy of H_2 and CH_4 neutrals at the cathode as a function of pressure. 154
Figure 5.47 Relative flux of H_2 and CH_4 neutrals at the cathode as a function of pressure. 154
Figure 5.48 Average energy of the ion species at the cathode as a function of driving potential. 155
Figure 5.49 Relative flux of ions at the cathode as a function of driving potential. 156
Figure 5.50 Average energy of H_2 neutrals at the cathode as a function of driving potential. 156
Figure 5.51 Average energy of ions at the cathode as a function of driving potential. 157
Figure 5.52 Relative flux of ions at the cathode as a function of driving potential. 157
Figure 5.53 Relative flux of ions at the anode as a function of driving potential. 158
Figure 5.54 Average energy of neutrals at the cathode as a function of driving potential. 158
Figure 6.1 Plasma potential as a function of pressure for a 50 W and 150 W argon plasma. 160
Figure 6.2 The electron density as a function of pressure for a 50 W and 150 W argon plasma. 161
Figure 6.3 The ion density as a function of pressure for a 50 W and 150 W argon plasma. 161
Figure 6.4 Plasma potential as a function of pressure for a 50 W and 150 W hydrogen plasma. 162
Figure 6.5 The electron density as a function of pressure for a 50 W and 150 W hydrogen plasma. 162
Figure 6.6 The ion density as a function of pressure for a 50 W and 150 W hydrogen plasma. 163
Figure 6.7 The probe I-V characteristic for a 100 W 90 mT hydrogen plasma (sum of 10). 163
Figure 6.8 The logarithm of the pure electron current for a 100 W 90 mT hydrogen plasma. 164
Figure 6.9 The second differential of the pure electron current for a 100 W 90 mT hydrogen plasma. 164
Figure 6.10 The electron energy distribution function assuming Vp is 16 V. 165
Figure 6.11 The The electron energy distribution function assuming Vp is 10.5 V. 165
Figure 6.12 Five I-V characteristics superimposed for pure hydrogen. 166
Figure 6.13 Five I-V characteristics superimposed for methane/hydrogen = 1/7. 167
Figure 6.14 Five I-V characteristics superimposed for methane/hydrogen = 1/1. 167

Figure 6.15 Argon IEDs for a power of 50 W. 168
Figure 6.16 H_3^+ IED for a power of 50 W and pressure of 90 mTorr. 168
Figure 6.17 Peak values for the hydrogen species as a function of pressure at a power of 150 W. 169
Figure 6.18 Peak values for methane species as a function of pressure. 169
Figure 6.19 Peak values for methane species as a function of power. 170
Figure 6.20 Peak values for methane species as a function of methane/hydrogen ratio. 170
Figure 6.21 Flux of neutrals detected in the mass probe as a function of pressure for a) pure hydrogen and b) pure methane background gas. 171
Figure 6.22 Ratio of the counts of the different species to H_2^+ after correction for the ionisation cross section. 172
Figure 6.23 Flux of neutrals detected in the mass probe as a function of pressure for a 50 % methane and 50 % hydrogen background gas. 173
Figure 6.24 DC bias as a function of the applied power (pure hydrogen). 173
Figure 6.25 DC bias as a function of the pressure (pure hydrogen). 174
Figure 6.26 DC bias at the surface of the quartz as a function of the pressure (pure hydrogen). 175
Figure 6.27 DC bias at the surface of the quartz as a function of the pressure (pure hydrogen). - measured by A. S. Bunting. 175
Figure 6.28 Distance from the quartz surface to the cathode glow and plasma/sheath boundary (pure hydrogen). 176
Figure 6.29 Distance from the quartz surface to the plasma/sheath boundary (methane/ hydrogen 2/28) as a function of pressure. 177
Figure 6.30 Distance from the quartz surface to the plasma/sheath boundary (methane/ hydrogen 2/28) as a function of methane/hydrogen ratio. 177
Figure 6.31 The regimes of etching and deposition. 178
Figure 6.32 Etch depths after 30 minutes as a function of methane/hydrogen ratio at a pressure of 10 mTorr. 179
Figure 6.33 Etch depths after 30 minutes as a function of methane/hydrogen ratio at a pressure of 10 mTorr. 179
Figure 6.34 Etch depths after 30 minutes as a function of pressure. 180
Figure 6.35 Etch rate as a function of flow rate in CH_4/H_2 for methane percentages of 10 % and 20 %. 181
Figure 6.36 Polymethyl methacrylate (PMMA) mask. 181
Figure 6.37 AFM topographic image of unetched etched GaAs: 2.5 μm scale. 182
Figure 6.38 AFM topographic image of etched GaAs: 3:27, 100 W, 10 mTorr, 10 μm scale. 183
Figure 6.39 AFM topographic image of etched GaAs: 3:27, 100 W, 10 mTorr, 1000 nm scale. 183
Figure 6.40 AFM tip deflection image of etched GaAs: 3:27, 100 W, 10 mTorr, 100 nm scale. 184
Figure 6.41 AFM tip deflection image of etched GaAs: 3:27, 100 W, 10 mTorr, 200 Å scale. 184
Figure 6.42 $(Ga/As)_T$ as a function of methane concentration for 50 W and 10 mTorr 30 minutes. 186
Figure 6.43 $(Ga/As)_T$ as a function of methane concentration for 50 W and 10 mTorr 240 minutes. 187
Figure 6.44 $(Ga/As)_T$ as a function of methane concentration for 100 W and 10 mTorr 30 minutes. 187
Figure 6.45 $(Ga/As)_T$ as a function of methane concentration for 150 W and 10 mTorr 30 minutes. 188
Figure 6.46 $(Ga/As)_S$ as a function of methane concentration for 50 W and 10 mTorr 30 minutes. 188
Figure 6.47 $(Ga/As)_S$ as a function of methane concentration for 100 W and 10 mTorr 30 minutes. 189
Figure 6.48 $(Ga/As)_S$ as a function of methane concentration for 150 W and 10 mTorr 30 minutes. 189
Figure 6.49 $(Ga/As)_T$ as a function of power for pure hydrogen, 10 mTorr for 30 minutes. 190
Figure 6.50 (Ga/As)T as a function of power for a ratio of 1:29, 10 mTorr for 30 minutes. 190
Figure 6.51 $(Ga/As)_T$ as a function of power for a ratio of 2:28, 10 mTorr for 30 minutes. 191
Figure 6.52 $(Ga/As)_T$ as a function of power for a ratio of 3:27, 10 mTorr for 30 minutes. 191
Figure 6.53 $(Ga/As)_T$ as a function of power for a ratio of 4:26, 10 mTorr for 30 minutes. 191
Figure 6.54 $(Ga/As)_T$ as a function of power for a ratio of 5:25, 10 mTorr for 30 minutes. 192
Figure 6.55 $(Ga/As)_T$ as a function of power for a ratio of 6:24, 10 mTorr for 30 minutes. 192

Figure 6.56 $(Ga/As)_T$ as a function of methane concentration, power 50 W, 10 mTorr for 30 minutes. 193
Figure 6.57 $(Ga/As)_T$ as a function of methane concentration, power 100 W, 10 mTorr for 30 minutes. 193
Figure 6.58 $(Ga/As)_T$ as a function of methane concentration, power 150 W, 10 mTorr for 30 minutes. 194
Figure 6.59 $(Ga/As)_T$ as a function of pressure, power 50 W for 30 minutes. 194
Figure 6.60 $(Ga/As)_T$ as a function of pressure, power 100 W for 30 minutes. 195
Figure 6.61 $(Ga/As)_T$ as a function of pressure, power 150 W for 30 minutes. 195
Figure 6.62 $(Ga/As)_S$ as a function of pressure, power 50 W for 30 minutes. 196
Figure 6.63 $(Ga/As)_S$ as a function of pressure, power 100 W for 30 minutes. 196
Figure 6.64 $(Ga/As)_S$ as a function of pressure, power 150 W for 30 minutes. 197
Figure 6.65 $(Ga/As)_T$ as a function of pressure, ratio 1:29, power 100 W, 30 minutes. 197
Figure 6.66 $(Ga/As)_T$ as a function of pressure, ratio 1:29, power 150 W, 30 minutes. 198
Figure 6.67 $(Ga/As)_T$ as a function of power for pure hydrogen, 10 mTorr for 30 minutes. 198
Figure 6.68 $(Ga/As)_T$ as a function of power for pure hydrogen, 20 mTorr for 30 minutes. 199
Figure 6.69 $(Ga/As)_T$ as a function of power for pure hydrogen, 40 mTorr for 30 minutes. 199
Figure 6.70 $(Ga/As)_T$ as a function of power for pure hydrogen, 80 mTorr for 30 minutes. 200
Figure 6.71 $(Ga/As)_S$ as a function of power for pure hydrogen, 10 mTorr for 30 minutes. 200
Figure 6.72 $(Ga/As)_S$ as a function of power for pure hydrogen, 20 mTorr for 30 minutes. 201
Figure 6.73 $(Ga/As)_S$ as a function of power for pure hydrogen, 40 mTorr for 30 minutes. 201
Figure 6.74 $(Ga/As)_S$ as a function of power for pure hydrogen, 80 mTorr for 30 minutes. 202
Figure 6.75 $(Ga/As)_T$ as a function of etch depth at 10 mTorr displaying a) 0° ToA and b) 0°, 45° and 60° ToA. 203
Figure 6.76 $(Ga/As)_T$ as a function of etch depth at 20 mTorr. 204
Figure 6.77 $(Ga/As)_T$ as a function of etch depth at 40 mTorr. 204
Figure 6.78 $(Ga/As)_T$ as a function of etch depth at 80 mTorr. 204
Figure 6.79 $(Ga/As)_T$ as a function of neon concentration for 50 W and 10 mTorr 205 30 minutes.
Figure 6.80 $(Ga/As)_T$ as a function of neon concentration for 100 W and 10 mTorr 30 minutes. 205
Figure 6.81 $(Ga/As)_T$ as a function of neon concentration for 150 W and 10 mTorr 30 minutes. 206
Figure 6.82 $(Ga/As)_S$ as a function of neon concentration for 50 W and 10 mTorr 206 30 minutes.
Figure 6.83 $(Ga/As)_S$ as a function of neon concentration for 100 W and 10 mTorr 30 minutes. 207
Figure 6.84 $(Ga/As)_S$ as a function of neon concentration for 150 W and 10 mTorr 30 minutes. 207
Figure 6.85 $(Ga/As)_T$ as a function of neon concentration for 150 W and 20 mTorr 30 minutes. 208
Figure 6.86 $(Ga/As)_T$ as a function of neon concentration for 150 W and 40 mTorr 30 minutes. 208
Figure 6.87 $(Ga/As)_T$ as a function of neon concentration for 150 W and 80 mTorr 30 minutes. 209
Figure 6.88 $(Ga/As)_S$ as a function of neon concentration for 150 W and 20 mTorr 30 minutes. 209
Figure 6.89 $(Ga/As)_S$ as a function of neon concentration for 150 W and 40 mTorr 30 minutes. 210
Figure 6.90 $(Ga/As)_S$ as a function of neon concentration for 150 W and 80 mTorr 30 minutes. 210
Figure 6.91 $(Ga/As)_T$ as a function of pressure for 150 W and 18 % neon 30 minutes. 211
Figure 6.92 $(Ga/As)_T$ as a function of pressure for 150 W and 50 % neon 30 minutes. 211
Figure 6.93 $(Ga/As)_T$ as a function of pressure for 150 W and 72 % neon 30 minutes. 212
Figure 6.94 $(Ga/As)_T$ as a function of pressure for 150 W and 100 % neon 30 minutes. 212
Figure 6.95 $(Ga/As)_S$ as a function of pressure for 150 W and 18 % neon 30 minutes. 213
Figure 6.96 $(Ga/As)_S$ as a function of pressure for 150 W and 50 % neon 30 minutes. 213
Figure 6.97 $(Ga/As)_S$ as a function of pressure for 150 W and 72 % neon 30 minutes. 214
Figure 6.98 $(Ga/As)_S$ as a function of pressure for 150 W and 100 % neon 30 minutes. 214

Figure 6.99 Comparison of (a) predicted and (b) experimental results for the IEDs at the anode of an argon RF plasma. Pressure 40 mTorr. 216
Figure 6.100 Comparison of a) predicted and b) experimental results for the IEDs at the anode of an argon rf plasma. Pressure = 60 mTorr. 217
Figure 6.101 Comparison of a) predicted and b) experimental results for the IEDs at the anode of an argon rf plasma. Pressure = 80 mTorr. 217
Figure 6.102 Comparison of a) predicted and b) experimental results for the IEDs at the anode of an argon rf plasma. Pressure = 95 mTorr. 217
Figure 6.103 Comparison of a) predicted and b) experimental results for the IEDs at the anode of a hydrogen rf plasma. Pressure = 90 mTorr. 219
Figure 6.104 Experimental results of the fluxes of hydrogen ions to the anode as a function of pressure for a power of 150 W. 220
Figure 6.105 Predicted fluxes of hydrogen ions to the anode as a function of pressure for a power of 150 W. 220
Figure 6.106 Predicted fluxes of hydrogen ions to the cathode as a function of pressure for a power of 150 W. 221
Figure 6.107 Experimental results of the fluxes of ions to the anode as a function of methane concentration for a power of 150 W and pressure of 50 mTorr. 221
Figure 6.108 Predicted fluxes of ions to the anode as a function of methane concentration for a power of 150 W and pressure of 50 mTorr. 222
Figure 6.109 Predicted fluxes of ions to the cathode as a function of methane concentration for a power of 150 W and pressure of 50 mTorr. 223
Figure 6.110 Predicted corrected fluxes of ions to the anode as a function of methane concentration for a power of 150 W and pressure of 50 mTorr. 223
Figure 6.111 Experimental results of fluxes of ions to the anode as a function of pressure for a methane concentration of 7 % and a power of 150 W. 224
Figure 6.112 Predicted fluxes of ions to the anode as a function of pressure for a methane concentration of 7 % and a power of 150 W. 224
Figure 6.113 Experimental results of fluxes of ions to the anode as a function of power for a methane concentration of 7 % and a pressure of 50 mTorr. 225
Figure 6.114 Predicted fluxes of ions to the anode as a function of power for a methane concentration of 7 % and a pressure of 50 mTorr. 225
Figure 6.115 Spatial excitation profile for a range of conditions with the simulated electrical sheath width superimposed. 226
Figure 6.116 Ratio of (methane neutrals)/(hydrogen ions). 228
Figure 6.117 Ratio of (methane neutrals/total ion flux). 228
Figure 6.118 Predicted fluxes of methane and hydrogen ions to the cathode as a function of methane concentration at 10 mTorr and 150 W. 229
Figure 6.119 H_3^+ ions and H_2 neutrals superimposed for a pressure of 10 mTorr, 150 W, 3% methane concentration only neutrals above 12.5 eV are shown). 231
Figure 6.120 H_3^+ ions and H_2 neutrals superimposed for a pressure of 90 mTorr, 150 W, 3% methane concentration only neutrals above 12.5 eV are shown). 232
Figure 7.1 Predictions for the etch depths with the experimental results superimposed. 241
Figure 7.2 Predicted $(Ga/As)_T$ as a function of ToA. 242
Figure 7.3 Predicted Ga(GaAs)/Ga(total) as a function of ToA. 243
Figure 7.4 $(Ga/As)_T$ for 1:29 10 mTorr 150 W. 243
Figure 7.5 Ga(GaAs)/Ga(total) for 1:29 10 mTorr 150 W. 244
Figure 7.6 Predicted $(Ga/As)_T$ as a function of ToA. 245
Figure 7.7 Predicted Ga(GaAs)/Ga(total) as a function of ToA. 245
Figure 7.8 Predicted $(Ga/As)_S$ as a function of ToA. 245
Figure 7.9 Predicted $(Ga/As)_T$ a nd $(Ga/As)_S$ results for an oxide thickness of 23 Å containing a trace of arsenic. 249

Chapter 1. Plasmas in reactive ion etching

1.1 Etching of semiconductors

1.1.1 Device processing

The invention in 1948 of the transistor by Shockley, Bardeen and Brattain overcame some of the problems associated with the vacuum tube, namely reliability and heat transfer. The transistor was rugged and the reduction in size allowed many more components to be packed into a small space, which in turn allowed manufacturers to build in a level of redundancy and thereby increase overall circuit reliability [1]. This created the technology of microelectronics and integrated circuit technology where the whole electronic circuit is contained on one slice of semiconductor.

In integrated circuit technology, impurities are diffused into the semiconductor through masks in order to build up the desired pattern of p-n junctions which comprise the microcircuit. Figure 1.1 shows the basic fabrication process.

Firstly, a silicon substrate is covered with an oxide layer (silicon dioxide which is stable) formed by heating in an oxidizing atmosphere. The surface is then lithographically patterned by covering with a photoresist mask which is exposed and developed. The patterned mask is then selectively etched to open up windows in the insulator to the silicon substrate. After the removal of the mask impurities diffused into the substrate will create p or n type silicon, arrangements of which create the components such as resistors, capacitors *etc.*

The diffusion of p-type material is accomplished in an atmosphere of concentrated boric acid, a by-product of which is the formation of a borosilicate glass. The n-type silicon is formed in an atmosphere of phosphorous pentoxide, a by-product of which is a layer of silicon dioxide. The processes are alternated, each time through a specific mask which must be applied and subsequently removed in addition to the removal of the deposited glass films. Finally, the components are joined by masking and selectively etching through the silicon dioxide at the contact points of the junctions followed by deposition of a metallic conductor such as aluminium.

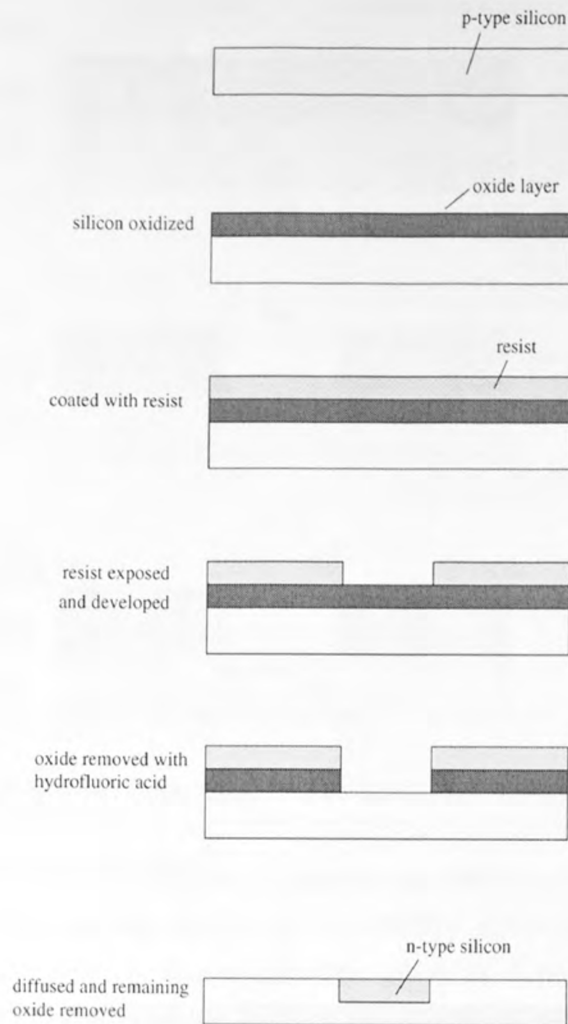

Figure 1.1 Five step diffusion process after Carroll [1]

An important aspect of the operation is the selectivity of the etching process. The oxide must be removed by a process which neither etches the photoresist nor the silicon substrate. In the above example this is achieved with hydrofluoric acid in a process known as wet etching. In modern devices, many operations are performed to produce the desired microchip and the etching process must be able to discriminate between a range of substrate chemistries.

1.1.2 Dry etching

The tendency in microelectronics is towards increased miniaturisation. Chemical or wet etching is an isotropic process where the etch occurs at the same rate regardless of the direction and this leads to mask undercut (figure 1.2) and consequently a limit to the extent of miniaturisation [2].

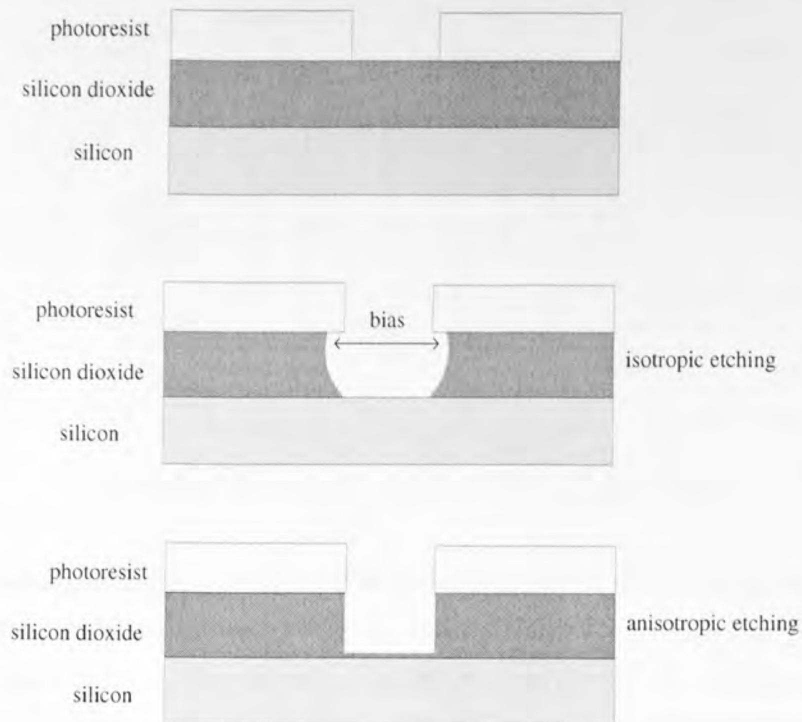

Figure 1.2 Isotropic and anisotropic etching.

This problem can be overcome by the use of plasmas in a technique known as dry etching in which a plasma is generated and the ions are electrically attracted toward the substrate which they strike at near perpendicular angles. The substrate material is removed both physically and in the case of reactive ion etching, chemically, with resulting vertical sidewall profiles. Other advantages of dry etching include a cleaner process since wet etching often uses noxious chemicals whereas dry etching is performed under partial vacuum in a sealed chamber. The anisotropy of the etch can also be varied by changing external plasma parameters such as the pressure which for certain devices is advantageous.

There are several different types of plasma etching apparatus which differ according to the arrangement of the electrodes, the method by which the power is applied and the specific etching task required. Ion milling uses high energy (500 - 800 eV) inert ion beams which give high anisotropy but due to the purely physical nature of the removal of the material, low selectivity between semiconductor and mask [3].

Figure 1.3 [4] is an example of a 'barrel-type' reactor where the electrodes are external to the reaction chamber. The sample sits at the floating potential of the plasma at a pressure >100 mTorr and is etched isotropically with the ions striking the substrate at relatively low energies.

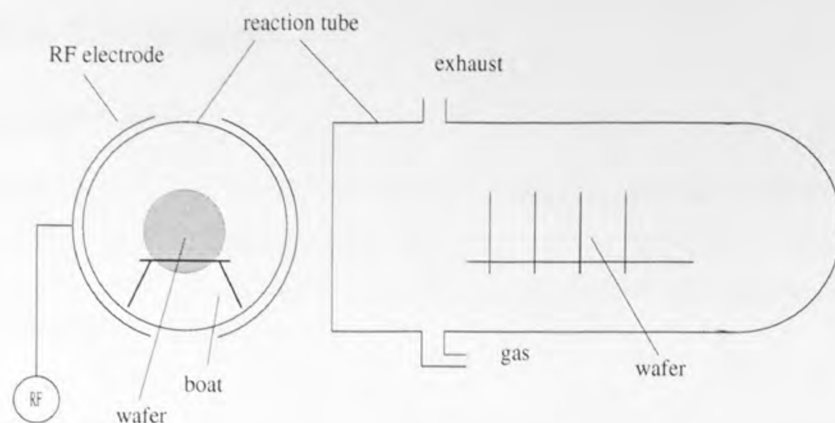

Figure 1.3 'Barrel-type' plasma etching apparatus.

Reactive ion etching is usually performed at lower pressures (10 - 100 mTorr) in a parallel plate reactor or a similar variation such as the 'top-hat' shown in figure 1.4. The etching is both physical and chemical, dependent on the plasma gas chemistry. Chemical etching allows greater selectivity between substrate materials than physical etching, whereas higher energy physical etching tends to be more anisotropic. These arrangements often have the cathode capacitively coupled to the rf source which allows the substrate to attain a D.C. bias. Careful control of the D.C. bias changes the energy of the incident ions and determines the physical/chemical nature of the etch in addition to the extent of damage to the substrate.

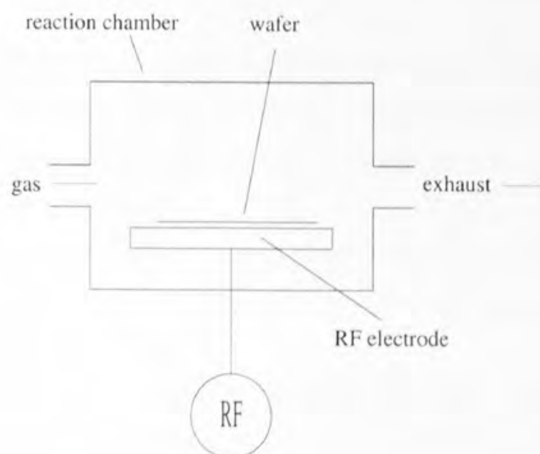

Figure 1.4 'Top-hat' type reactor.

Alternative techniques based on the capacitively coupled rf discharge in conjunction with microwave excitation of the plasma electrons are also used to increase the ionization of the plasma without an increase in the rf power applied. This allows the plasma to etch at a greater rate but with no increase in ion energy at the substrate.

1.2 Plasma discharges

1.2.1 The plasma state

The term plasma is used to describe electrically energized matter in the gaseous state [5]. It can be thought of as a gas consisting of ions, free radicals, stable molecules, photons and electrons, though to be termed a plasma rather than a collection of charged particles, it must also fulfil certain basic criteria [6].

1 - Within a given volume containing a large number of plasma particles, where the parameters defining the plasma (such as temperature *etc.*) are stationary, the net charge must be zero. Departures from charge neutrality can occur but only on a scale where a balance is struck between the thermal energy of the particles, which tends to lead to an imbalance in positive and negative charges (due to their mass differences), and the electrostatic forces which tend to redress the balance. This distance is known as the Debye length and is given by

$$\lambda_D = \left[\varepsilon_0 k T_e / \left(n_e e^2\right)\right]^{1/2} \qquad \text{eqn 1.1}$$

where T_e is the electron temperature and n_e is the electron number density. When a boundary is introduced to a plasma, the perturbation it produces extends up to λ_D from the surface. This perturbed layer is known as the plasma sheath. The first criterion is therefore that the size of the plasma is much greater than the Debye length.

2 - A Debye sphere is defined as a sphere within the plasma of radius λ_D. Due to the constraint of neutrality, any electric fields from outside the sphere are shielded by the particles within and make no contribution to the field at the centre of the sphere. It follows that any particles in the plasma feel effects only from those particles within the Debye sphere at which they are centre. Since the shielding is due to collective behaviour, the second criterion is that the number of electrons within each Debye sphere is large.

3 - When a plasma is disturbed, there is an electrostatic force which attempts to restore the equilibrium. This implies that there is a frequency of oscillation of electrons about their equilibrium positions and it is known as the plasma frequency. The third criterion is that the frequency of electron-neutral collisions is much less than this plasma frequency, otherwise the electrons will not be able to behave independently but will be in thermal equilibrium with the neutrals and the plasma is essentially a neutral gas.

Except for a small distance around perturbations in the plasma, the plasma is field free and at an equipotential. The value of this potential is known as the plasma potential, and is denoted V_p.

1.2.1.1 DC plasmas

The simplest plasma is the D.C. plasma formed between two parallel plates between which exists a uniform and constant electric field. Any stray charge between these plates (due to a cosmic ray or contamination) will be accelerated in the field and will cause secondary ionizations which in time leads to a cascade. This cascade would at high pressures cause a spark and at low pressures a glow discharge [7]. If the outer circuit allows a steady state current to flow then its power will determine the extent of ionization in the gas, which is said to be in the plasma state. The condition for breakdown is a function of the efficiency of ionization by ions and electrons and the field between the plates. Figure 1.5 (after Boenig [3]) shows the classic regions in a DC plasma.

Rather than as one might intuitively guess, the potential between the plates dropping linearly between anode and cathode, the existence of the plasma in the positive column expels most of the field and most of the potential in the system is dropped over the small sheath which is created over the cathode.

The cathode is constantly being bombarded by high energy ions and this in turn causes the ejection of secondary electrons which are accelerated into the plasma and help to sustain it. DC plasmas are well studied and many of their results can be applied to RF plasmas.

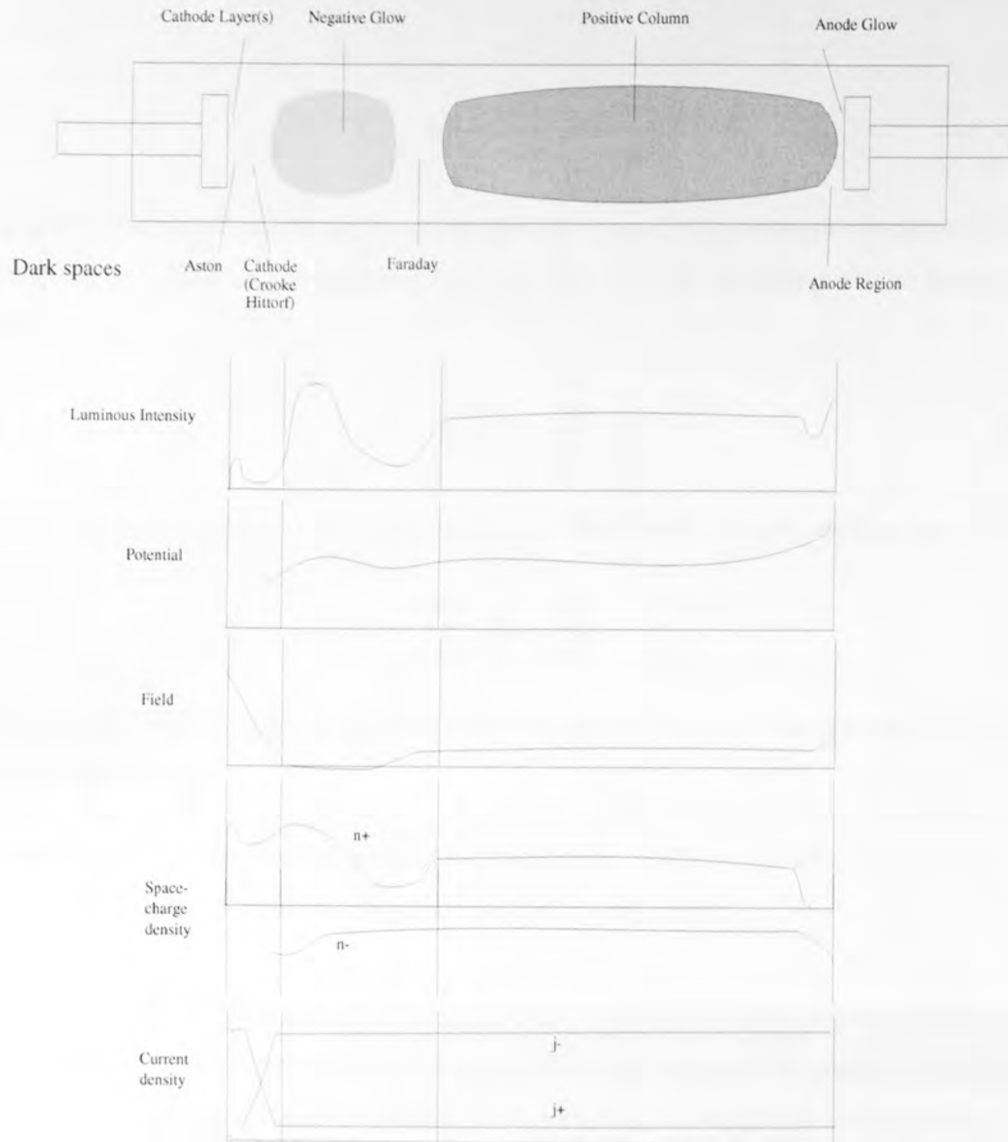

Figure 1.5 Spatial distributions in a D.C. plasma

1.2.1.2 Sheath formation

An electrically isolated substrate inserted into a plasma will initially be struck by fluxes of electrons and ions given by

$$j_e = \frac{en_e < v_e >}{4} \qquad j_i = \frac{en_i < v_i >}{4} \qquad \text{eqn 1.2}$$

where $<v_e>$ and $<v_i>$ are the average electron and ion velocities respectively and $n_{e,i}$ are the number densities [8]. Since the electron mass is small in comparison to the ion mass, j_e is large and the substrate immediately begins to charge up negatively, with the effect that electrons are repelled and ions attracted. This charging ceases when an equilibrium is established between the ion and electron fluxes. The value of the potential at the substrate when in equilibrium is known as the floating potential, V_f and it follows that $V_f < V_p$. Balancing the fluxes to the substrate and assuming the electrons have a Maxwell-Boltzmann distribution, the difference between the floating and plasma potential can be

derived as

$$V_p - V_f = \frac{kT_e}{2e} \ln\left(\frac{m_i T_e}{m_e T_i}\right) \qquad \text{eqn 1.3}$$

The negatively charged substrate is surrounded by a positively charged sheath known as the space charge. Poissons equation relates the space charge density ρ to the potential as follows

$$\frac{d^2V}{dx^2} = \frac{-\rho}{\varepsilon_0} \qquad \text{eqn 1.4}$$

where V is the potential and x is a distance across the sheath. It follows that because

$$E = \frac{-dV}{dx} \text{ then } \frac{dE}{dx} = \frac{\rho}{\varepsilon_0} \qquad \text{eqn 1.5}$$

and the electric field changes as we proceed from the substrate to the plasma bulk where the field is zero.

The sheath, being depleted of electrons and electronic excitation is dark in comparison to the plasma bulk and is sometimes referred to as the dark space.

1.2.1.3 Plasma chemistry

In all plasmas, the primary method of energy transfer to the gas is by electron impact. Elastic electron-molecule collisions result in an increase in energy of the gas while inelastic collisions lead to ionisation, excitation and fragmentation of the gas molecules [9]. Inelastic electron collisions are summarised below

Excitation $e + A \rightarrow A^* + e$

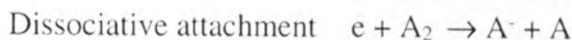

Dissociative attachment $e + A_2 \rightarrow A^- + A$

Dissociation $e + A_2 \rightarrow 2A + e$

Ionisation $e + A_2 \rightarrow A_2^+ + 2e$

Dissociative ionisation $e + A_2 \rightarrow A + A^+ + 2e$

Collisions between ions and neutrals in the gas cause the ion temperature to become thermalized and also cause a host of chemical reactions, dependent on the gas type. Collisions between ions and neutrals also occur as the ions traverse the sheath and this has a profound effect on the nature of the fluxes impingent on the electrode. The various inelastic collisions between heavy particles are outlined below

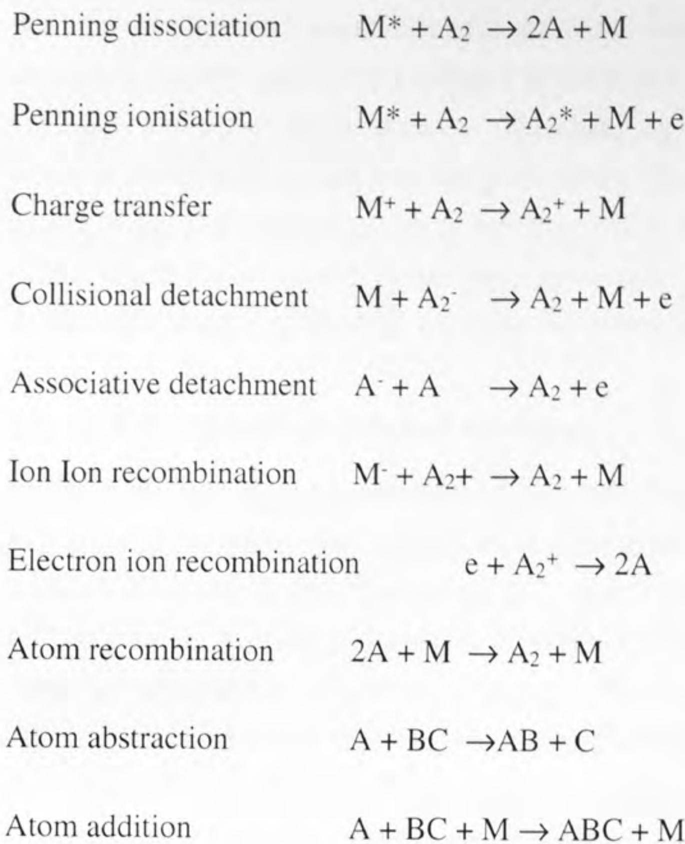

Penning dissociation	$M^* + A_2 \rightarrow 2A + M$
Penning ionisation	$M^* + A_2 \rightarrow A_2^* + M + e$
Charge transfer	$M^+ + A_2 \rightarrow A_2^+ + M$
Collisional detachment	$M + A_2^- \rightarrow A_2 + M + e$
Associative detachment	$A^- + A \rightarrow A_2 + e$
Ion Ion recombination	$M^- + A_2+ \rightarrow A_2 + M$
Electron ion recombination	$e + A_2^+ \rightarrow 2A$
Atom recombination	$2A + M \rightarrow A_2 + M$
Atom abstraction	$A + BC \rightarrow AB + C$
Atom addition	$A + BC + M \rightarrow ABC + M$

Where M is a third body.

In addition there is also the group of reactions which occur at the chamber wall

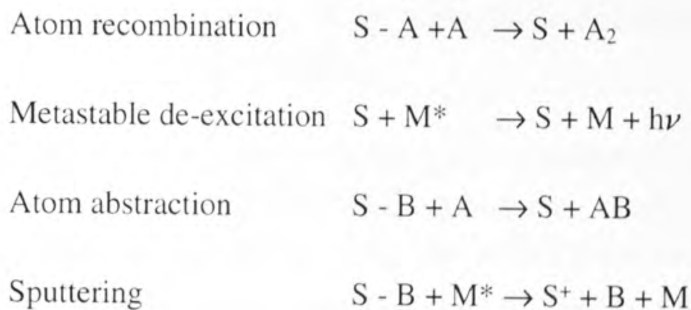

Atom recombination	$S - A + A \rightarrow S + A_2$
Metastable de-excitation	$S + M^* \rightarrow S + M + h\nu$
Atom abstraction	$S - B + A \rightarrow S + AB$
Sputtering	$S - B + M^* \rightarrow S^+ + B + M$

of which sputtering is the most important in materials processing and will be discussed at length later in the chapter.

1.2.2 Rf plasmas

Rf plasmas are now more commonly used than D.C. plasmas because they are far more efficient in converting the power from the supply into the plasma and more importantly they allow insulators to be etched. They are also capable of producing much lower energy ions at the cathode than in the D.C. case which reduces the damage caused to the sample. Many different frequencies of driving potential have been studied, the most popular being 13.56 MHz because this is in a window reserved for scientific study which does not interfere with communications. A common type of reactor used is the asymmetric type

with the chamber wall constituting the grounded anode and the cathode being driven. The cathode is usually capacitively coupled to the power supply in order to allow a negative D.C. bias to build up on the cathode. The changing rf field gives energy to the electrons, whereas the slower moving ions are given energy by the D.C. bias at the cathode. The extent of this D.C. bias is generally less than 800 V with values down to 100 V or so, below which the low power makes the plasma difficult to sustain. The driving potential is of the order of several hundred volts and the power is usually up to several hundred watts.

1.2.2.1 DC bias and equilibrium discharge

Initially, the potential at the cathode is sinusoidal with an average value of 0 V and peak to peak value up to several hundred volts. As the potential at the cathode begins to go positive, a cascade as described in the D.C. case is caused and the highly mobile electrons collide with the cathode, lowering its potential and therefore causing a potential across the capacitor between the cathode and rf supply. The ions are accelerated away from the cathode, but the distance they move is negligible before the field reverses direction. On the next half cycle, the cathode begins to go negative and electrons are accelerated away, thus increasing the value of the negative potential. The cathode becomes negative for most of the cycle and ions are accelerated towards it for most of the time. Due, therefore, to the higher mobilities of the electrons, over subsequent cycles the cathode acquires a D.C. bias consistent with the flux of electrons and ions to the cathode being equal in subsequent half cycles. The bulk of the plasma is at equipotential and therefore is field free, again with most of the potential lost over a small region known as the dark space or sheath above the cathode.

When equilibrium is reached, the rate of ionization is equal to the rate of recombination (mainly at the walls) and the power into the system is equal to the power dissipated (by heating the chamber, electrode and gas and in photo-emissions). There are two methods by which the supply powers the plasma. The first is by primary electrons which exist in the plasma and bounce between the relatively negatively charged walls and cathode. Although the electron temperature is only 2-5 eV or so, if an electron is reversing its direction at the same time that the field is reversing then it can gain considerable energy [10]. The second is by secondary electron emission. Electrons ejected from the walls by impacting ions can gain energy exceeding the gas ionization potential by being accelerated away from the negatively biased cathode, gaining energy similar to the sheath potential of several hundred eV.

The energy of the primary group of electrons is substantially above that of the ions (which are only a little above room temperature) and have temperatures which have been found to be in the range 0.5 - 2.5 eV [11].

1.2.2.2 The rf sheath

As with any plasma boundary, a sheath is created over the cathode, though in this case the cathode is not floating but at a DC biased sinusoidal potential. Figure 1.6 shows how the time variation of the plasma potential is driven by the sinusoidal variation of the cathode potential after equilibrium has been reached and a stable D.C. bias exists. In the positive part of the cycle, the electric field in the sheath breaks down and the cathode is bombarded by electrons which has the effect of increasing the plasma potential. When the potential of the cathode is negative, the potential of the plasma is given by the floating potential. The extent of the sheath is determined by the potential drop across itself and therefore the sheath oscillates. The sheath over the anode is much smaller and oscillates in anti-phase.

The ions that drift in the field free plasma bulk have energies which have been thermalized by the background gas atoms and are therefore of order .03 eV. This gives a velocity much lower than the velocity of the oscillation of the sheath. *ie.* for argon this energy corresponds to a velocity of 400 ms^{-1}, whereas at 13.6 MHz, the sheath is moving at approximately $1x10^4$ ms^{-1}, assuming the sheath moves 1 mm per cycle. The electrons, however, moving at 10^5 ms^{-1} essentially react to a static field.

It is the interaction between the electrons and the electric field which gives rise to the sheath. In order for electrons to reach the cathode, the sheath must collapse at some point every cycle, though the extent of the collapse will be determined by the distribution of higher energy electrons able to overcome the residual sheath potential.

The sheath region in an rf plasma appears dark due to the general repulsion of electrons from the wall for most of the rf cycle. Unlike a D.C. discharge, however, electrons penetrate deeply into the dark space for significant portions of the cycle. The dark space is therefore only some time-averaged version of the reduced electron density (as discussed by May *et al* [[12]]) and the observed dark space can only be taken as some approximation to the electrical sheath.

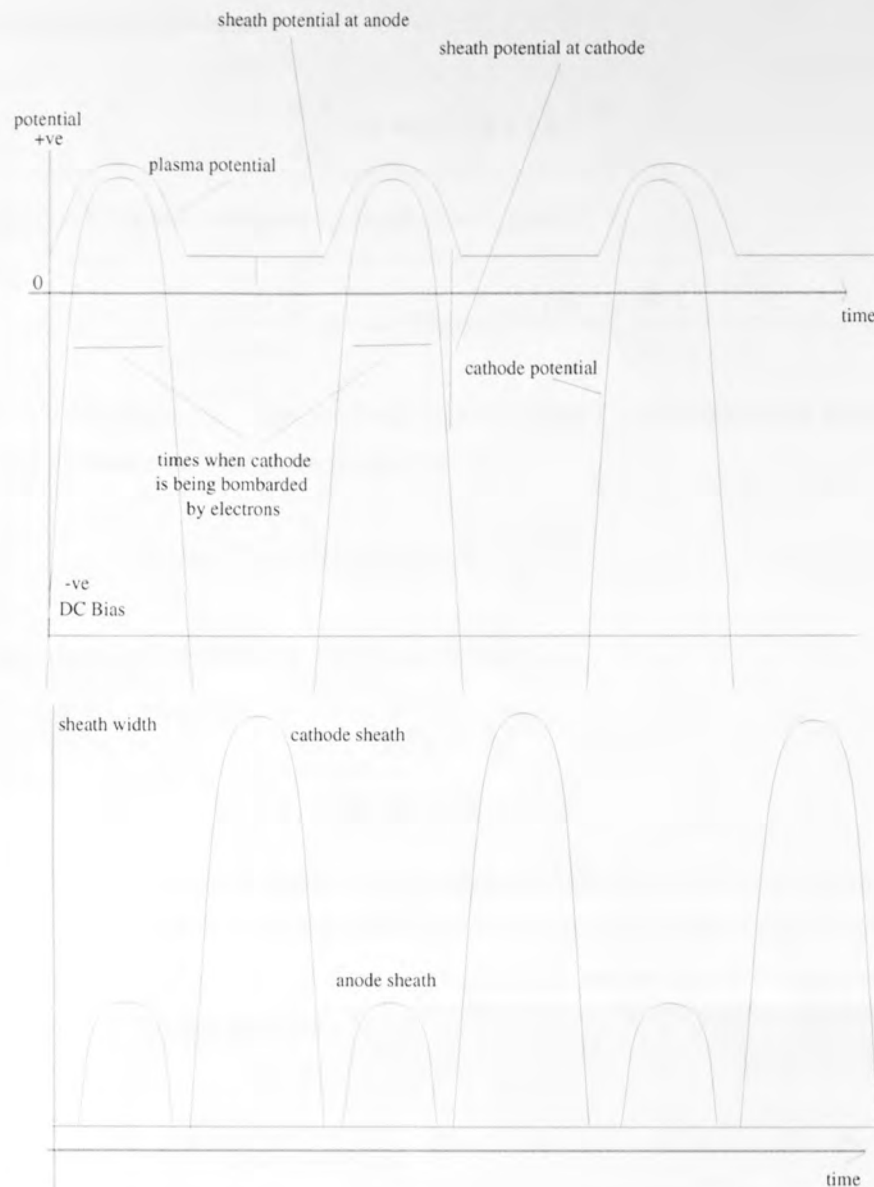

Figure 1.6 The potential across and the physical extent of the rf sheath

1.2.2.3 Electric field across the sheath

A common approximation to the electric field variation across the sheath is that it is a linear relationship, although this does not satisfy Poissons equation and so more often the Child-Langmuir relationship outlined below is used [13].

In an ideal situation of two parallel plates, A and B, one of which (A) emits particles and is at 0 V, the other (B) perfectly absorbs the particles and is at another potential, say V_B. If plate A emits particles of mass m and charge $-e$, then the velocity of the particle where the potential is V is

$$v = (2eV/m)^{1/2} \qquad \text{eqn 1.6}$$

and if the particle current density is j, the particle density at x ($x = 0$ at plate A) will be

$$n(x) = j[2eV(x)/m]^{1/2} \qquad \text{eqn 1.7}$$

Poissons equation then becomes

$$\frac{d^2V}{dx^2} = 4\pi ej\,(2eV/m)^{-1/2} \qquad \text{eqn 1.8}$$

Multiplying by dV/dx and integrating from $x = 0$, gives

$$\frac{1}{2}\left(\frac{dV}{dx}\right)^2 = 4\pi j\,(2me)^{1/2}\,V^{1/2} + \left(\frac{dV}{dx}\right)_0 \qquad \text{eqn 1.9}$$

In the limit that $(dV/dx)_0 = 0$ (space-charge-limited flow) and integrating between $x = 0$ and $x = d$ (the distance between the plates) we have

$$j = (2/me)^{1/2}\,\frac{V_B^{3/2}}{9\pi d^2} \qquad \text{eqn 1.10}$$

and as current density between the plates is constant,

$$V(x) \propto x^{4/3} \qquad \text{eqn 1.11}$$

$$ie.\, E(x) \propto x^{1/3} \qquad \text{eqn 1.12}$$

This is illustrated in figure 1.7 where is also displayed the electric field arising from a special version of the Child-Langmuir law where collisions are taken into account. This mobility limited version leads to an electric field which varies as $x^{1/2}$ (from the plasma/ sheath boundary toward the cathode).

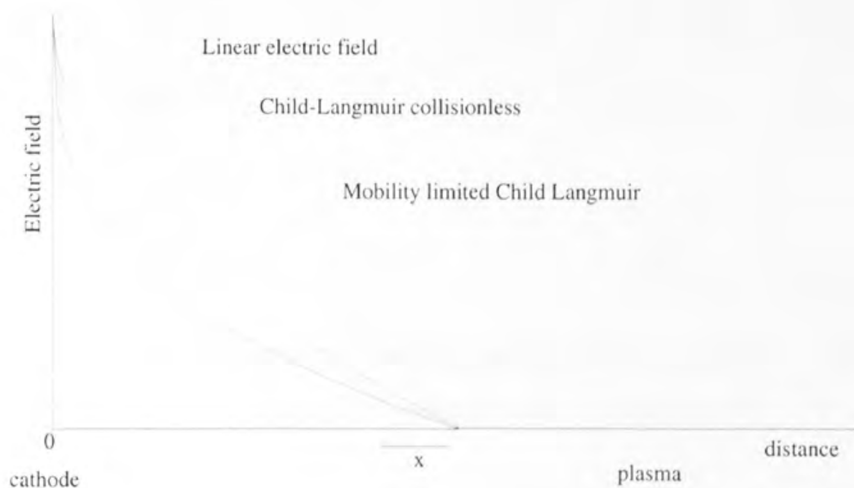

Figure 1.7 Different approximations to the electric field across the sheath.

1.2.2.4 The plasma potential

Figure 1.8 after Kohler *et al* [14] shows the form of the plasma potential with respect to the cathode potential and the grounded anode for a) a discharge where the electrode is directly powered from the supply and b) where the cathode is capacitively coupled allowing it to obtain a D.C. bias. In both cases, the plasma potential is at the highest potential of the

system. The high mobility of the electrons ensures this is the case. The exact form in which the plasma potential follows the cathode potential is in some debate. It is essentially determined by the mobility of the electrons and the properties of the sheath. Figure 1.9 shows the plasma potential variation for a sheath displaying either predominantly resistive or capacitive behaviour [15]. Recent analysis by Sobolewski [16] implies the plasma potential does not differ too much from a sinusoid, though the difference between the two models is not great for capacitively coupled discharges with a large D.C. bias.

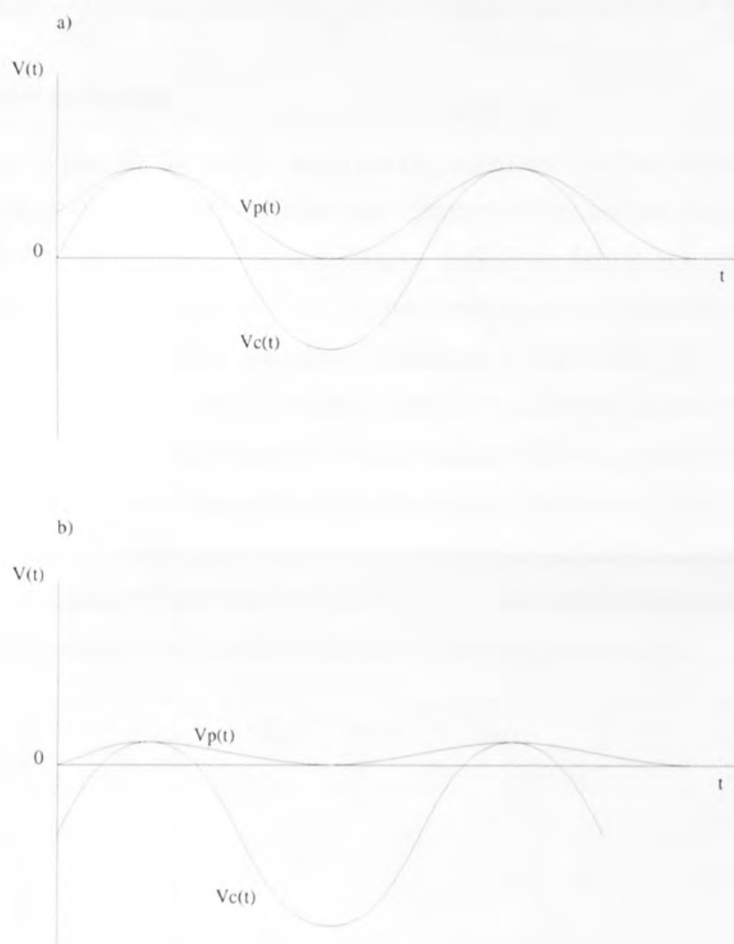

Figure 1.8 Form of the plasma potential a) directly driven electrode b) capacitively coupled electrode where cathode area << anode area.

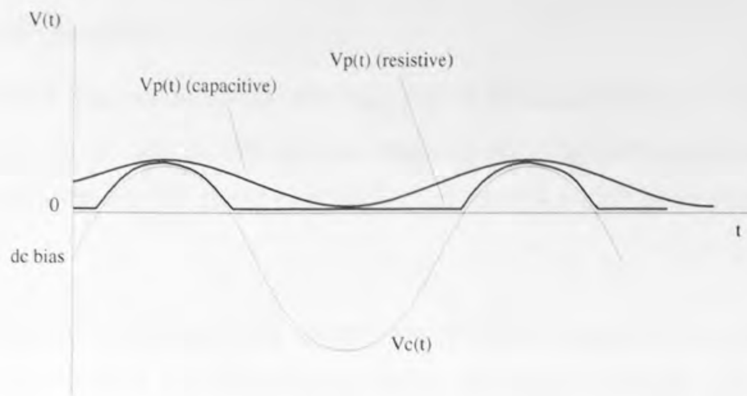

Figure 1.9 Plasma potential displaying predominantly capacitive or resistive nature.

1.2.2.5 The Bohm criterion

Standard analysis of sheath formation at a floating substrate can be characterized as follows [17]. The high mobility of the electrons charges the substrate negatively such that electrons are repelled and a positive space charge region or sheath is formed which shields the neutral plasma from the negative wall. A problem is encountered due to the distortion of the ion distribution due to wall losses and shielding is only possible if the 'Bohm Criterion' is fulfilled. This criterion demands that ions enter the sheath with velocities which are too high to be given by thermal motion alone. Consequently the ions must be accelerated by a field in some region between the sheath proper and the plasma known as the quasi neutral region or the pre-sheath. Effectively this is the field from the sheath 'leaking' into the plasma as illustrated in figure 1.10. The condition also reduces the ion flux entering the sheath by ~0.6 and modifies the floating potential to

$$(kT_e / 2) \ln (m_i / 2.3m_e) \qquad \text{eqn 1.13}$$

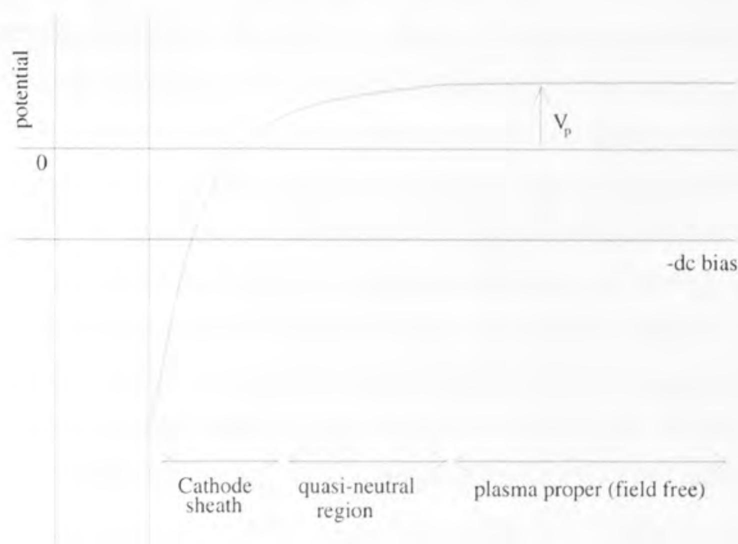

Figure 1.10 Leaking of the electric field from the sheath into the plasma due to the Bohm criterion.

1.2.2.6 Electron energies

The electrons in the plasma are generally thought of as made up of two components, the primary electrons which have a Maxwellian velocity distribution due to inelastic collisions with gas atoms and the higher energy secondary electrons which have been emitted from the walls.

The primary electrons gain energy by interaction with the sheath, the result of which is that they are reflected back into the plasma with a net gain of energy. This mechanism is known as 'wave riding' [18]. A Monte Carlo study by May *et al* [19] showed how the low energy electrons gain most energy (25 % or so) in interacting with the sheath and how they are swept back into the plasma as the sheath expands. The medium and high energy electrons can return energy to the cathode depending on the phase at which they arrive at the sheath and this provides an energy balance. The resulting primary electron energy distribution function will be a result of this sheath heating mechanism and the energy losses incurred by the electrons in collisions with gas molecules and the chamber walls. A model by Penning and Druvetsyn [20] predicts the primary electron energy distribution is essentially Maxwellian with a reduced high energy tail due to the high energy processes. Other models which solved for the electron transport similarly predict the distribution is Maxwellian except at the higher energies [21][22]. Complex Particle in Cell (PIC) models such as that of Surendra and Graves [23] have found electron energy distribution functions (EEDFs) which are in general complex and non-Maxwellian. Experimental measurements of EEDFs, however, show them to be essentially Maxwellian for the low pressure plasmas used in RIE [24][25].

On impact of an electron or ion with the electrode or walls of the reactor chamber, there is the probability of the emission of an electron. For the case of an incident ion, this probability is independent of the ion energy at the ion energies involved (<1 keV) because the time taken for the process to occur is much less than the time taken for the surface impact [26]. For incident electrons, however, the probability is a strong function of the incident electron energy [27]. The electrons from both processes are emitted with low kinetic energies and their energies in the plasma are therefore dominated by the sheath potential of several hundred volts. This is an important source of energy to the plasma and helps sustain the discharge [28][29]. The existence of these secondary electrons implies the secondary electron emission coefficient, γ, is an important parameter for the discharge and this has been confirmed by both Yao and Jiang [30] (who found the plasma density distribution to be significantly influenced by γ) and Xu and Sides [31] who found large changes in plasma density over the edge of a platen sitting on a cathode of a different γ value.

1.2.2.7 Charged particle distributions

The time averaged number density of electrons throughout the bulk plasma is approximately constant, with a rapid fall to zero through the sheath to the electrode. As previously mentioned, there are two methods of energy input to the plasma, the primary electrons which gain energy of tens of eV in the reversing field at the sheath edge and will cause ionisations at the sheath edge or in the plasma bulk and the secondary electrons, which gain energies of hundreds of eV in the sheath and will cause ionisations either in the sheath or in the plasma bulk depending on the cross section for ionisation. It is therefore to be expected that the rate of ionisations is highest at the sheath edge or in the plasma bulk (highly dependent on the pressure) and that the number density of ions throughout the plasma will be highest here and fall rapidly at the electrodes, any ions in the sheath being rapidly accelerated there.

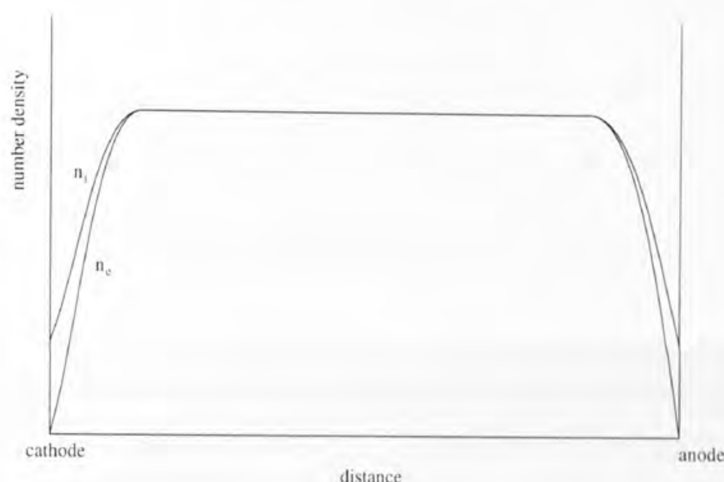

Figure 1.11 Spatial variation of ions and electrons in a helium-like gas.

Figure 1.11 shows the predicted spatial variation for ions and electrons for a helium-like gas at 1 Torr pressure using a self-consistent model devised by Date *et al* [32]. The numbers of ions and electrons in the plasma bulk are equal, resulting in the plasma bulk being roughly neutral, whilst in the sheaths, the number of ions exceeds the number of electrons, resulting in a positive space charge in the sheath. Particle models such as ES1 [33] give spatial ion production distributions which are similar to the above but peaked at the sheath edges where the maximum production occurs. This is confirmed by experimental observations which show distinct peaks in optical emission profiles at the sheath edge [34][35].

1.2.2.8 Ion trajectories

Ions created within the plasma drift randomly until they reach the plasma/sheath boundary (or are accelerated by the pre-sheath discussed in section 1.2.2.5) and are accelerated by the electric field in the sheath towards the cathode. Because ions react slowly with respect

to the plasma driving frequency, it takes several rf cycles for the ion to cross the sheath and during this time, the sheath has expanded and contracted, accelerating the ion in distinct 'bursts'. This is illustrated in figure 1.12 (after Field *et al* [36]) and shows how the light ions may cross the sheath in only one or two cycles whereas the heavier ions may take many cycles.

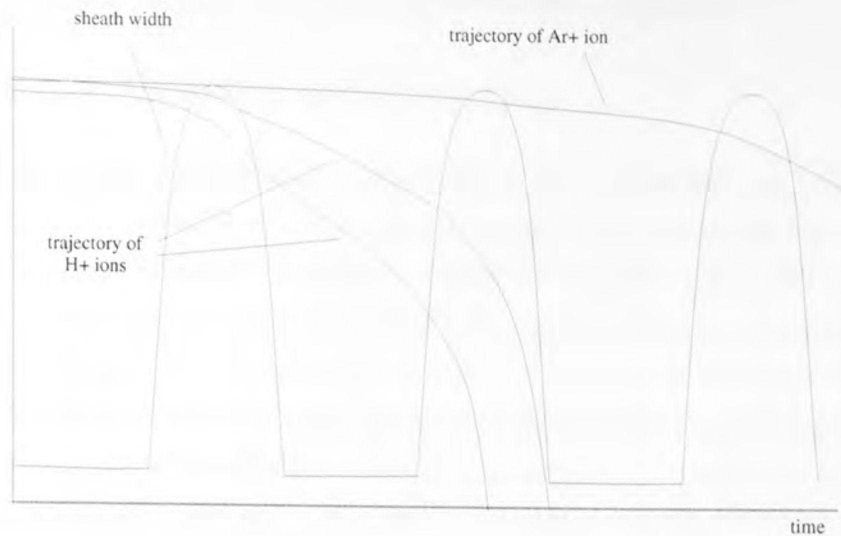

Figure 1.12 Ion trajectories across and rf sheath.

This leads to the result that the ions at the electrode acquire an energy dependent upon both their initial velocities on crossing the plasma/sheath boundary and the phase and therefore the extent of the sheath at the time. The resultant ion energy distributions have a 'saddle-like' structure as shown in figure 1.13 (after Kuypers [37]) with an average energy given by the average sheath potential and a peak width given by the ion mass, sheath width and rf frequency.

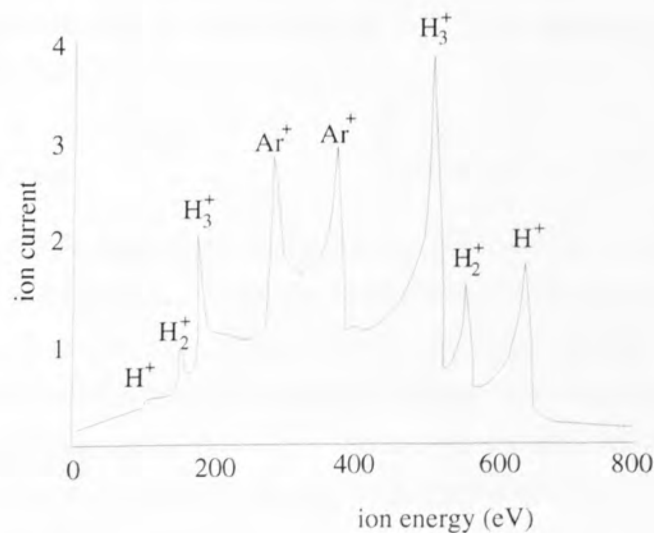

Figure 1.13 Saddle-like structure exhibited by ions at the cathode of a plasma cell.

Additionally, the most common reaction for ions in the sheath is the charge exchange reaction, which results in the creation of an ion in the sheath with zero velocity. This effect causes secondary peaks in the ion energy distribution [38] [39] which agree well with simulations [40][41].

The sheath can generally be regarded as collisionless at pressures below 10 mTorr but at pressures higher than this the effect of collisions becomes important.

1.3 Review of modelling of ion energies

In order to investigate the reactive ion etching of GaAs, it is necessary to build a model of the plasma in order to predict what is unknown and generally not measurable, the ion and neutral energies, angles and fluxes impingent upon the sample surface. In recent years there has been considerable activity in the field of plasma modelling, much of which has been summarised by Lister [42] in his review article. The range of pressures, frequencies and powers at which plasmas operate is great, depending on their use, and therefore different models exist which take advantage of approximations to different aspects of the plasma. It is necessary, therefore, to use the correct model with the correct assumptions for the range of plasma parameters of interest which gives the closest approximation to the desired results. In the case of the RIE of GaAs in CH_4/H_2, the plasma sheath is collisional, but not to the extent where a fully formed ion energy distribution results and the ion trajectories must therefore be followed. The potentials at the electrodes can be measured and certain plasma parameters such as the plasma potential and sheath width can be inferred with varying degrees of accuracy (though greater accuracy than a model would produce).

The form of the models used in the field of radio frequency capacitively couple discharges can be divided into analogue circuit models, fluid models, kinetic models and sheath models. Each model type has its own advantages and disadvantages, and a discussion of their relative merits follows.

1.3.1 Circuit models

Circuit models are simple models able to deduce some of the macroscopic properties of the discharge such as the current and voltage waveforms and the fluxes through the use of equivalent circuits which contain basic assumptions about the sheaths. Figure 1.14 shows the equivalent circuit for a capacitively coupled discharge where the sheaths are represented by capacitance and resistance C_s and R_s respectively and the plasma inductance and resistance are given by C_p and R_p respectively.

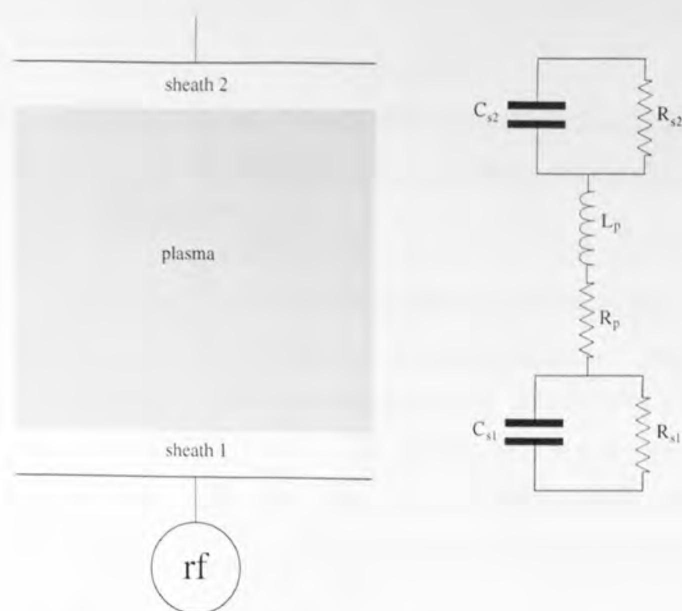

Figure 1.14 Schematic of an rf capacitively coupled plasma and the equivalent circuit.

When used with a matching circuit which minimises the reflected power to the generator, the impedance of the system is the complex conjugate of the output impedance and with assumptions about the sheath behaviour, it is possible to deduce some important parameters of the plasma [43].

Circuit models are unable, however, to deduce ion energies except by equating them to the time averaged sheath potential which is not applicable in the collisional sheath regime.

1.3.2 Fluid models

Rapid advances have been made in modelling of plasmas based on fluid theory. These fluid or continuum models work by coupling a mass, energy and momentum balance for ions and electrons with Poissons equation and solving the differential equations to find, after a large number of cycles, a steady state. High speed calculations are possible with fluid models. A limitation of fluid models, however, is that they have to make some approximations about the electron transport properties. Fluid models, therefore, are grouped according to their use of the local field approximation [44][45][46][47], the quasi thermal approximation [48][49][50][51][52] and the relaxation continuum model [53][54] and have been summarised by Makabe *et al* [55].

An example of a fluid model applicable for both electropositive and electronegative gases is described in detail by Gogolides and Sawin [56]. More recently Gogolides *et al* [57] have developed a methane discharge fluid model which when combined with a gas-phase kinetics model attempts to predict the spatial distribution of methane radicals.

There have also been attempts to develop 'hybrid' Monte Carlo/fluid models which whilst reducing computation time take proper account of the electron motion in the electric

field[58].

More recently, there has been progress in two dimensional fluid modelling which attempts to describe asymmetric reactors [59] and hybrid two dimensional models where the electrons are followed kinetically [60].

These models have been successful in computing external discharge parameters but their assumptions are generally only valid in the high pressure regime [61] and tend to be less accurate for pressure below 100 mTorr or at high powers. Most of the above models, are applied to plasmas at pressures greater than 500 mTorr. When a direct comparison is made between fluid models and more physically correct PIC models, the predictions tend to diverge at pressures below 100 mTorr as was shown by Nitschke and Graves [62].

1.3.3 Particle in cell

Particle in cell (PIC) models are more sophisticated models which follow groups of ions and electrons through a background gas. The particles interact with each other through the electric field created by their own charge distribution and with the neutral particles by random collisions as described for an argon model [63] and for a helium model [64]. The PIC method takes proper account of the electron motion which for many discharges is not in local thermal equilibrium, this being the problem with many fluid models. Because of the intrinsically higher dimensionality of PIC models over fluid models, they tend to be computationally very expensive and often have problems settling down into an equilibrium. The ES1 code [65] illustrates well many of these problems. PIC models tend to be used on model inert gases, such as Ar, He or He-like in order to reduce the physical number of interactions between particles which are needed for a realistic prediction. Uhomoibhi *et al* [66], are, however currently working on a code to model hydrogen discharges.

This therefore leaves the problem as to finding the ion energies at the electrode for a complicated gas mixture such as methane/hydrogen. It is possible to make certain assumptions about the plasma and sheath in order to drastically reduce computation time. If it can be assumed that the plasma is field free and the only electric field exists in the sheath, then it will only be necessary to know the species crossing the plasma/sheath boundary, the temporal and spatial variation of the electric field in the sheath and the nature of the interactions in the sheath to find the ion energy distributions in minimal computation time. This method is well suited to realistic situations where many of the potentials are known or can be derived from the experiment to compare with the model predictions. The approach of some of the authors involved is discussed below.

1.3.4 Monte Carlo/sheath

1.3.4.1 Plasma potentials

Kushner [67] used a parametric model for an rf sheath in conjunction with Monte Carlo [68] analysis to obtain the ion energy distribution and the ion angle distribution at the powered electrode of a capacitively coupled parallel plate discharge. The model used for the plasma potential and the sheath thickness was as follows

$$\phi_p(t) = \mathrm{MAX}\left(\phi_{dc} + \phi_{rf}\sin(\omega_{rf}t),\ \Delta\phi\right) \qquad \text{eqn 1.14}$$

and

$$l(t) = l_{dc} + l_{rf}\sin(\omega_{rf}t + \alpha) \qquad \text{eqn 1.15}$$

where $\phi_p(t)$ is the plasma potential at time t, $l(t)$ is the sheath width and $\Delta\phi$ approximates to the floating sheath potential. $MAX(a,b)$ is the maximum value of a and b. ϕ_{rf} indicates the applied cathode potential and ϕ_{dc} is the induced D.C. bias at the blocking capacitor. The frequency is given by ω_{rf} and α is the phase difference between the applied potential and the plasma potential. This gives a plasma potential which follows the positive cycle of the cathode potential, plus the small floating potential $\Delta\phi$ and is relevant for a sheath displaying resistive behaviour. The sheath potential is then given by the difference in the potential between the cathode and the plasma.

Song *et al* [69] used analysis of the fluxes of electrons and ions in an rf plasma to derive an expression for the D.C. bias at the capacitively coupled driven electrode in terms of the anode and cathode areas and the applied voltage. The derivations result in the following equations for the plasma potential

$$V_p(t) = (kT_e/e)\ln\left\{\left[1 + \left(\frac{A_c}{A_a}\right)\exp\left(\frac{eV_e(t)}{kT_e}\right)\right]\Big/\left[1 + \left(\frac{A_c}{A_a}\right)\right]\right\} + V_p^0 \qquad \text{eqn 1.16}$$

where T_e is the electron temperature, A_c/A_a is the geometrical cathode anode area ratio, $V_e(t)$ is the time-dependent electrode potential V_p^0 and is the floating potential, where

$$V_p^0 = (kT_e/2e)\ln(<v_e>/<v_i>) \qquad \text{eqn 1.17}$$

and $<v_e>$, $<v_i>$ are the average electron and ion velocities.

The electrode potential is given by

$$V_e(t) = V_0\sin(\omega t + \phi) - V_{dc} \qquad \text{eqn 1.18}$$

and the D.C. bias is given by

$$V_{dc} = V_0\sin[(\pi/2)(A_a - A_c)(A_c + A_a)] \qquad \text{eqn 1.19}$$

This results in a plasma potential which is more resistive than capacitive and also quite dependent on the electron temperature. It should also be noted that the value of A_c/A_a used is quite different from the value A_c/A_a found by measurement of the geometrical areas of the anode and the cathode. The value must be used as some effective area ratio which is necessary to fix the D.C. bias at a level consistent with experiment.

1.3.4.2 Electric fields

The spatial dependence of the electric field within the sheath was chosen by Kushner [70] to be

$$E(x, t) = E_0 [l(t) - x]^a \quad \text{eqn 1.20}$$

where a is a constant. With a = 1/3, this represents the Child-Langmuir law with space-charge mobility limited currents (low pressure) or with a = 1/2, this represents mobility limited ion currents (high pressure). The value of a was generally set to 1 indicating an electric field which increases linearly with distance towards the cathode. This was justified by spectroscopic measurements [71] which confirmed this linear dependence. He obtained IEDs with saddle-like structures which were relatively robust to changes in the value of a.

This was also the particular form of the electric field across the sheath used by Wild and Koidl [72], where it is additionally remarked that the ion density (given by the average of the sheath potential) is given by

$$E \sim x^{a-1} \quad \text{eqn 1.21}$$

By carefully comparing predicted IEDs to experimentally determined IEDs, good agreements were found for values of α in the range 0.4 - 0.5, where there was a tendency for the value to increase with increasing pressure as expected.

Other workers have used expressions for the electric field across the sheath derived from the assumption of linear fields [73], the Child-Langmuir potential and ion mobility limited approximations [74][75].

Thompson and Sawin [76] considered the effect of both time-invariant and time-dependent sheath fields. They concluded that while the rf field changes detailed components of the resulting IED, the average values are not significantly changed, though the resulting IEDs are generally fully developed and do not display the expected saddle structure which can result only from an rf component.

Field *et al* [77] predicted IEDs at the cathode in the collisionless regime for a number of gases and found a good comparison with the experimental results of Kuypers [78]. They

additionally investigated a linear field, a space-charge limited potential and a mobility limited potential. It was found that the linear approximation made no difference to the IED and should in any case be avoided because it violates ion flux conservation. They found the difference between collisionless and mobility limited approximations was small and they concluded that the precise form of the sheath potential is not important.

The authors also investigated the consequences of the Bohm sheath criterion on ion energy distributions and point out a number of problems associated with the Bohm formulae. Firstly it uses the assumption of a zero ion temperature and secondly it is valid only in the limit of a collisionless sheath. Furthermore, the preacceleration of ions required at the plasma sheath boundary will be complicated by the movement of the boundary itself and the ions may not have time to accelerate in this pre sheath region before being enveloped by the sheath proper. Nevertheless, they attempted to model the effect by the addition of the required energy to the initial ion energy in a direction toward the electrode on crossing the plasma/sheath boundary. The result was only slightly different and again could be negated by small changes in the sheath width or the driving potential

1.3.4.3 Nature of interactions

Davis and Vanderslice [79] followed trajectories of argon ions in a sheath where charge exchange collisions were important. The resultant ion flux, however, was perpendicular to the electrode surface by virtue of the direction of the electric field. This was improved upon by Kushner [80] who randomized the phase and the velocity of ions crossing the plasma/sheath boundary. This resulted in the classic saddle-like structure to the IEDs and also gave realistic ion angle distributions (IADs).

Charge exchange collisions were included in the analysis and the mean free path between collisions was defined as

$$\lambda_{mfp} = (\sigma N)^{-1} \qquad \text{eqn 1.22}$$

where σ is the collision cross section and N is the number density of the background gas. A collision occurs over a distance Δx if

$$\Delta x \leqslant \lambda_{mfp} \ln(r) \qquad \text{eqn 1.23}$$

where r is a random number between 0 and 1 [81]. Elastic scattering collisions were ignored as they have a cross-section much lower than that for charge exchange. A constant value of 50 Å^2 was used for the charge exchange reaction, with the newly formed ion having a randomized initial velocity and direction. The effect of the charge exchange reactions was to thermalize the distribution to an extent dependent on the pressure.

Wild and Koidl [82] obtained a good fit between simulated and experimental ion energies in an argon plasma by a similar model which also only included charge exchange reactions. Similarly, they used a constant cross section for charge exchange, though of 40 Å^2. The predictions described the appearance of a range of subsidiary peaks in the IED which were due to the convolution of the effect of charge exchange collisions on the initial saddle-like structure of the IED.

Thompson and Sawin [83] used a Monte Carlo method to model the transport of ions through an rf sheath where ion-molecule scattering was taken into account. They paid particular attention to the effect of different scattering functions to the resulting ion energy distributions. They also used the concept of a 'null' collision to take into account the energy dependence of the various collision cross sections.

A constant interaction cross section σ was used to generate the distance the ion travels between interactions with neutrals. This constant cross section gives an exponential distribution in the distance between where the ion passes close to a neutral. The effect of the collision is dependent on the type of collision which occurs. The probability that a hard sphere scattering occurs is constant with energy and is equal to the ratio of the hard sphere cross section to the total interaction cross section. In potential scattering, however, even though the total cross section remains invariant with energy, the scattering cross section decreases with increasing energy. Therefore it is increasingly likely that a 'null' event occurs and the ions' energy and trajectory remain unaffected.

For an elastic collision, the magnitude of the outgoing velocity was calculated from

$$|v'| = |v| \frac{1 + m_{rel}}{\sqrt{1 + m_{rel}^2 + 2m_{rel}\cos x}} \qquad \text{eqn 1.24}$$

where m_{rel} is the ion/neutral mass ratio, x is the scattering angle in the centre-of-mass frame (COM) of reference, v' is the outgoing velocity and v is the incoming velocity. With the assumption that the neutral is stationary before the collision (the ion energy being up to several eV and the neutral energy being 0.03 eV or so this is a valid assumption), the new velocity vector (in the LAB system) is at an angle of γ from the initial velocity vector where

$$\gamma = \cos^{-1}\left[\frac{m_{rel} + \cos x}{\sqrt{1 + m_{rel}^2 + 2m_{rel}\cos x}}\right] \qquad \text{eqn 1.25}$$

For elastic scattering with hard spheres, x has the simple distribution [84]

$$f(x) = (\sin x)/2 \qquad 0 \leqslant x \leqslant \pi \qquad \text{eqn 1.26}$$

and the scattering angle for each collision is given by

$$x = \cos^{-1}(1 - 2R) \qquad \text{eqn 1.27}$$

where R is a random number between 0 and 1 [85].

For the case where there is a continuous field between the ion and neutral, the deflection is a function of the energies, masses, form of the interaction potential and the impact parameter, defined as the distance between the closest approach of the incident velocity vector and the centre of the stationary neutral.

The potential used was for SF_5^+ in SF_6 and was of the form

$$V(r) = A_9 r^{-9} - A_6 r^{-6} - A_4 r^{-4} \qquad \text{eqn 1.28}$$

with the coefficients given by Brand and Jungblut [86]. The dependence of the scattering angle on the impact parameter was then calculated by the method given by Hirschfielder, Curtiss and Bird [87]. The third interaction model used was the 'isotropic shrinking sphere' model which assumes as in the hard sphere case that in the centre of mass frame, the scattering is isotropic, however, the collision cross section falls with increasing ion energy given by

$$47 \times 10^{-16} \varepsilon^{-\beta} \qquad \beta = 2/9 \qquad \text{eqn 1.29}$$

The final interaction model used was the 'anisotropic shrinking sphere' where the energy dependence of the cross section was the same as above but the scattering angle was approximated as having a linear relationship with the impact parameter.

The four interaction methods were compared by allowing them to travel well into a sheath in a D.C. field to allow them to evolve fully developed ion energy distributions. It was found that with appropriate scaling, the four models gave directionalities within 10% of each other and scaled average energies within 30% of each other. This is not a good approximation to the extent of scattering in an rf sheath between 10 and 90 mTorr, as fully developed distributions are more affected by charge exchange than elastic scattering and when fully developed, the IAD will not be expected to change as a function of the interaction potential. This paper has, however, caused others [88][89] to consider only hard sphere interactions. More recently, in a study by Phelps [90], it has been suggested that the 'hard-sphere' or isotropic component is only about 13 % of the momentum transfer cross section.

Liu *et al* [91] simulated argon IEDs and IADs at the grounded electrode of a reactor. The simulation included both charge exchange and momentum scattering events across a pressure range from 10 to 500 mTorr. A constant ratio of elastic to charge-exchange collision cross section of 0.82 was used, but it was accepted that this would not be a good assumption at low ion energy. The data for the total collision cross section was taken

from Cramer [92] and fits the following equation

$$\sigma(cm^2) = 9.64 \times 10^{-15}\varepsilon^{-0.131} \qquad \text{eqn 1.30}$$

The IEDs were compared with measured IEDs and found to be in good agreement. The maximum values of the energy attainable by the ions were predicted to be somewhat less than the measured values, however, and this was attributed to the neglecting of the floating plasma potential, using the uniform field approximation, inaccuracies in measuring the sheath thickness and approximations for the collision cross section. The ion angle distribution was also measured and compared with the predicted distribution but the correlation was not good.

Manenschijn and Goedheer [93] also followed the trajectories of the neutrals created by both elastic scattering and charge exchange. The results show that the contribution of the neutral flux contributes significantly to the predicted sputter yield of a surface based on the ion energy distribution and neutral energy distribution and the relative flux of neutrals per ion. The results also showed that the spread in the neutral and ion bombarding angles has a negligible effect on the sputter yield.

May *et al* [94] extended their previous work to include charge exchange and momentum transfer collisions for an argon plasma. They used the isotropic shrinking sphere model in their approach and calculated both ion and neutral energy and angle distributions. The results show very good agreement with published experimental distributions [95] and also show the importance of the neutral flux to the substrate.

This work was extended by Dickenson [96] to hydrogen plasmas where many different interactions between the three ions H^+, H_2^+ and H_3^+ were included. These interactions consisted of elastic scattering, charge transfers and various inelastic interactions, the cross sections of which had recently been published by Phelps [97]. Methane fragments were also included and allowed to undergo elastic scattering events. Though this work was a significant advance into the modelling of the sheath trajectories of more complex plasmas, the major problem was it was necessary to input the relative proportions of the different ion types assumed to be entering the sheath, information that cannot be gleaned from the cracking patterns [98], nor strictly from analysis of mass probe data at the anode, though this is probably a better estimate. An additional problem is the neglection of any electron induced ion creation in the sheath.

1.4 Surface modification - theoretical

1.4.1 Review of ion surface interactions

In rf discharges, ions are accelerated at near vertical angles of incidence from the plasma

and across the cathode sheath where they interact with the substrate in one of a number of ways summarised in figure 1.15 and generally categorized as chemical reactions, sputtering, which involves the physical removal of a target atom and implantation which involves the incident particle coming to rest within the lattice. Whichever event dominates is determined by the energies, angles and chemistry of incoming and target particles.

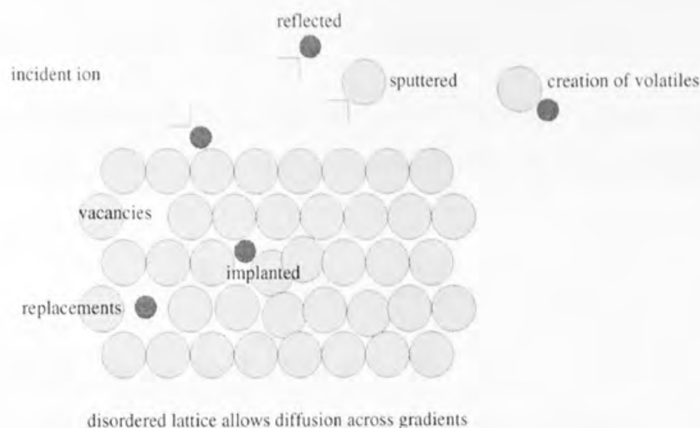

Figure 1.15 Summary of surface processes.

1.4.2 Sputtering theory and sputter yield

As energy is transferred from an incoming ion to a substrate, a collision cascade is set-up. If the number of target atoms set in motion is small in comparison with the number of atoms lying within the volume of the cascade, then the collisions can be treated as binary events and the collision cascade is said to be linear [99]. Linear cascades can then be described by linear Boltzmann transport equations and this approach results in the Sigmund theory of sputtering [100]. In his theory, Sigmund treats the target as an infinite medium and solves the transport equations for the cascade. Atoms which pass back through an imaginary plane in the infinite medium, representing the surface are considered to have been sputtered. Sigmund sputtering theory is the most widely used sputtering theory even though it neglects inelastic energy losses [101].

According to the theory, the sputter yield, defined as

$$Y = \frac{atoms\ sputtered}{atoms\ incident} \qquad \text{eqn 1.31}$$

is given by

$$Y = \Lambda F_D \qquad \text{eqn 1.32}$$

where Λ is a constant containing information about the substrate and the factor F_D is the energy deposited per unit depth at the surface and contains information about the incoming ion type, the substrate type and the density of substrate atoms. This can be rewritten as

$$Y = 0.042\alpha(M_2/M_1, \theta)S_n(E, Z_1, Z_2)/U_0 \qquad \text{eqn 1.33}$$

where M_1, M_2, Z_1, Z_2 are the masses and atomic numbers of the incident and target atoms respectively, E and θ are the incoming energy and angle, U_0 is the surface binding energy, S_n is the nuclear stopping cross section and the factor α is a dimensionless factor which represents the fractional energy available for sputtering.

The factor α has been found by Gries and Strydom [102][103] by solving the Sigmund formula and comparing with published sputter yields and binding energies. This results in the following

$$l = \log_{10}(M_2/M_1) \qquad \text{eqn 1.34}$$

$$\alpha = 0.12 \text{ for } l \leqslant -1.2 \qquad \text{eqn 1.35}$$

$$\alpha = 0.0857l^5 + 0.289l^4 + 0.402l^3 + 0.350l^2 + 0.22l + 0.189 \qquad \text{eqn 1.36}$$

$$\text{for} -1.2 \leqslant l \leqslant -0.144 \qquad \text{eqn 1.37}$$

$$\alpha = 0.0449l^6 - 0.107l^5 - 0.209l^4 + 0.313l^3 + 0.207l^2 + 0.156l + 0.183 \qquad \text{eqn 1.38}$$

$$\text{for} -0.144 < l \leqslant 1.8 \qquad \text{eqn 1.39}$$

The nuclear stopping cross section can be expressed as follows

$$S_n(\varepsilon) = 4\pi a Z_1 Z_2 e^2 \frac{M_1}{M_1 + M_2} s_n(\varepsilon) \qquad \text{eqn 1.40}$$

where ε is the reduced energy given by

$$\varepsilon = \frac{4\pi\varepsilon_0 a M_2}{Z_1 Z_2 e^2 (M_1 + M_2)} E \qquad \text{eqn 1.41}$$

with

$$a = \frac{0.8853 a_0}{(Z_1^{1/2} + Z_2^{1/2})^{2/3}} \qquad \text{eqn 1.42}$$

The factor $s_n(\varepsilon)$ is a function which depends on the approximation assumed for the repulsive nuclear potential. For the universal potential of Biersack and Ziegler [104] the universal stopping power is given by

$$s_n(\varepsilon) = \frac{0.5 \ln(1 + 1.1383\varepsilon)}{\varepsilon + 0.013218\varepsilon^{0.21226} + 0.91594\varepsilon^{1/2}} \qquad \text{eqn 1.43}$$

A correct value for the surface binding energy is the most difficult term in equation 1.33 to find. For elemental substrates, the surface binding energy can be approximated by the sublimation energy or the heat of atomization, which is the sublimation energy normalized to 273 K. For compound semiconductors, the surface binding energy is not at all obvious and will be considered in depth in section 1.4.5.

There are some important approximations to the Sigmund sputter yield formula discussed by Malherbe [105] and these are now considered. Zalm gives an approximation to the yield as [106]

$$Y(E) = \frac{5(Z_1 Z_2)^{5/6}}{9U_0} s_n(\varepsilon) \qquad \text{eqn 1.44}$$

with U_0 in eV. With approximations for the reduced nuclear stopping [107], Zalm gets

$$Y(E) = \frac{5(Z_1 Z_2)^{5/6}}{9U_0} \quad \text{for } \varepsilon \leqslant 0.03 \qquad \text{eqn 1.45}$$

and

$$Y(E) = \frac{5(Z_1 Z_2)^{5/6}}{27U_0} \quad \text{for } 0.1 \leqslant \varepsilon \leqslant 1 \qquad \text{eqn 1.46}$$

but these appear to give greater yields than experiment.

Smith [108] derived the following

$$Y(E) = \frac{20}{U_0} Z_1^2 Z_2^2 \frac{M_1}{M_2} \frac{E}{(E + 50Z_1 Z_2)^2} \qquad \text{eqn 1.47}$$

which gives values consistently lower than Zalm but which are also lower than experiment.

It is with these above theories that the sputter yield and therefore physical etch rate shall be calculated for the etching experiments. These equations, however, become less valid in the super low energy regime and here a different theory must be utilised.

1.4.3 Threshold sputter theory

For very low energies, the basic assumptions of the Sigmund model are no longer valid. Matsunami [109] derived an approximation of the Sigmund formula which agrees well with experiment

$$Y = Y_{SIG}[1 - (E_{th}/E)^{1/2}] \qquad \text{eqn 1.48}$$

where Y_{SIG} is the yield according to the Sigmund formula and E_{th} is the threshold energy for sputtering of about 20-25 eV for GaAs.

1.4.4 Preferential sputtering

It can be seen that finding an absolute value of the sputter yield is a difficult problem which is generally only approximate and semi-empirical. For compound semiconductors, the problem is eased by the need only to find the relative sputter rates of the two or more materials but complicated by the resulting inadequate knowledge we have of individual atomic binding energies in compounds. It is obvious from the above, that for atoms of different masses or binding energies, the yield will be different and this will result in the surface being depleted of one of the two elements until an equilibrium yield is reached.

The relative yield Y_1/Y_2 as a function of the relative surface binding energies, U_1/U_2 and masses M_1/M_2 is given by [110]

$$\frac{Y_1}{Y_2} = \frac{c_1}{c_2}\left(\frac{M_2}{M_1}\right)^{2m}\left(\frac{U_2}{U_1}\right)^{1-2m} \qquad \text{eqn 1.49}$$

where c_1/c_2 is the relative concentration of the two components and m is the power scattering parameter and is generally much less than 1. This has profound effects for semiconductor processing. Particle bombardment of InP always leads to phosphorous depletion [111], however, this is due to the extreme mass difference between In and P (114.82 and 30.97 a.m.u respectively). For the case of GaAs, the mass difference is small (69.72 and 74.92 a.m.u respectively) but the group V element is always preferentially removed. This has often been ascribed to the lower value of the surface binding energy for As, though this is not necessarily the case.

1.4.5 Surface binding energy

GaAs surfaces bombarded with inert ions tend to be depleted of As even though it is the heavier of the two elements. This has been attributed to the lower sublimation energy of arsenic than gallium [112][113]. The sublimation energies are as follows

Hs for As = 29 kcalmol^{-1} = 1.26 eV per atom

Hs for Ga = 64.9 kcalmol^{-1} = 2.82 eV per atom

and this gives the ratio $U_{As}/U_{Ga} = 0.45$.

Alternatively, for elemental substrates it is evaluated by correcting the heat of sublimation to 273 K to give the heat of atomization (most sputtered particles are single atoms rather than molecules [114]) and this gives the following

Ha for As = 302.5 $kJmol^{-1}$ = 3.141 eV

Ha for Ga = 277 $kJmol^{-1}$ = 2.876 eV U_{As}/U_{Ga} = 1.09

which implies an arsenic rich sputtered surface.

Malherbe *et al* [115] used Sigmund theory and applied it to the preferential sputtering of metal oxides. They found the surface binding energy by modifying the Pauling formalism [116] for the bond energies in a covalent bond to give the energy required to remove an oxygen atom as

$$U_0 = \frac{y}{x+y} D(O-O) + \frac{x}{x+y} D(M-O) + \frac{1}{2} (\varepsilon_m \varepsilon_o)^{1/2} \quad \text{eqn 1.50}$$

where D(O - O) and D(M - O) are the bond strengths of the diatoms and ε_m and ε_o are the metal and oxygen electronegativities. y/x is the ratio of oxygen to metal atoms in the molecule. The binding energy of the metal component is

$$U_m = H_s + 0.5 (\varepsilon_m - \varepsilon_o)^2 \quad \text{eqn 1.51}$$

where H_s is the sublimation energy of the pure metal. Using these equations with gallium representing the metal component and arsenic the oxide (GaAs bonding is mostly covalent with some ionic characteristics and Ga is the more metallic of the two elements) then with electronegativities of ε_{Ga} = 1.81 eV ε_{As} = 2.18 eV

U_{Ga} = 2.876 eV, U_{As} = 3.075 eV

and U_{As}/U_{Ga} = 1.07.

Yu [117] discusses problems associated Malherbe's model which make it physically unrealistic, especially when considering large changes from stoichiometry. He proposes the estimation of the average binding energy using the pair-bond model of Williams and Nason [118]. The model works by considering the nearest neighbour attraction in a two component system and calculating the bond strength on any one atom in terms of the attraction between like atoms and the attraction of unlike atoms. The resulting ratio of the binding energies of component *A* and *B* are as follows

$$\frac{U_A}{U_B} = \frac{C_A D(A-A) + C_B (A-B)}{C_A D(A-B) + C_B (B-B)} \quad \text{eqn 1.52}$$

where *D(i - j)* is the bond strength of the diatom *ij* and C_i is the relative concentration in the surface of component *i*. With bond strengths given by

Ga - Ga = 1.43 eV

As - As = 3.97 eV

As - Ga = 2.18 eV

then U_{As}/U_{Ga} = 1.7 for a stoichiometric surface. This model, unfortunately ignores the modification to the binding caused by the reduction in coordination number at the surface. An associated problem with all the above models is that they ignore the structure at the surface, Scandurra [119] for example found that the sputter yield increased with time with an equilibrium after 300 seconds which he attributed to the amorphization of the surface. Malherbe [120] emphasizes that the binding energy may change with the structure (*ie.* from crystalline to amorphous) and that the binding energies of similar atoms in different surface positions (*ie.* at a kink site) may vary considerably. Kelly [121] considered this problem and argued that sublimation of a material occurs from exposed kink sites or ledges, whereas sputtering is more likely to occur from a flat surface (which makes up most of the surface) and where the atom is constrained by more bonds. The surface binding energy is, therefore, somewhat higher than implied by the heat of sublimation.

It can be concluded that the relative surface binding energies of Ga and As are not known, but the consensus is that As is more tightly bound to the surface than Ga.

1.4.6 Gibbsian segregation

It has become increasingly apparent that the stoichiometry of a surface is influenced by the segregation of the different components at the surface. In the case of Gibbsian segregation, the surface configuration is of lower energy when proportionally more of the surface is occupied by one type of atom than another and this is due to a difference between two elements in exchanging a bulk atom with a surface atom. There is thus a temperature dependent thermodynamic drive toward the more stable surface summarised in the Langmuir-McLean equation [122]

$$\frac{(x_a / x_b)_s}{(x_a / x_b)_b} = \exp[-\Delta Q / kT] \qquad \text{eqn 1.53}$$

where x_i is the proportion of element i and the subscript s or b denotes the ratio at the surface or in the bulk. Q is known as the heat of segregation and is calculated from

$$\Delta Q = \gamma_a a_a - \gamma_b a_b \qquad \text{eqn 1.54}$$

where γ_i and a_i are the surface tension and the area created by atom i at the surface. The segregating species is then preferentially sputtered and this sets up a concentration gradient which leads to the subsequent diffusion of particles from high to low concentration. In a GaAs crystal, the diffusion coefficients of Ga and As are very low at room temperature and would not lead to diffusion but for the energy supplied by the bombardment and the disorder (*ie.* vacancies) created which aid the movement of atoms.

According to Kelly and Oliva [123] the composition of the outer surface is a function of the preferential sputtering, segregation and diffusion effects whereas the equilibrium sub-surface composition is only influenced by bombardment induced segregation and diffusion.

The use of the surface tension of the pure elements to find the surface energy of the atoms in a crystal suffers from the same problems as the use of the sublimation energy of the elements to find the surface binding energy of the atoms in a crystal, in that it takes no account of the structure of the lattice.

1.4.7 Codes

Computer codes are becoming increasingly popular for predictions of bombardment of surfaces due both to their availability and the reduction in computing time which comes from the continual advances is processing speed. All the codes, however, must make gross approximations in order to give answers for sputter rates, implantations *etc.* in a reasonable time. The Binary Collision Approximation (BCA) assumes the incoming ion interacts with only one target atom at a time and has completed the interaction before being influenced by the next target particle. The advantage of this approximation is that it allows the change in the velocity vectors of the incident and target particles to be solved exactly and quickly and even used in the form of look up tables. This approximation is most valid in the high energy regime (or for low density targets *ie.* gas). With a lower incident energy, the distance from which a target atom influences the incident atom increases until it overlaps the spheres of influence of neighbouring atoms and the approximation is no longer valid. Following particles using the Newtonian equations of motion increases the computational time by a factor of n^2 where n is the number of particles considered in the many body collision. With these codes, the forces are calculated from either spherically symmetric potentials based generally on the screened nuclear potential (which becomes increasingly inaccurate at low energies) or on a quantum mechanical treatment which plots the electron probability distributions and minimises the energy of the electron wave functions. This latter quantum treatment is considerably more time consuming than the former method. These codes take ions one at a time and follow their trajectories as they interact with atoms of the substrate. A brief description of three of the codes used plus the quantum mechanical code Hyperchem [124] follows.

1.4.7.1 SUSPRE

The SUSPRE code (Surrey University Sputter Profile) [125] is the simplest and fastest of the codes and can be used as a first order approximation. It uses a set of algorithms to calculate the energy deposition profile needed to find the sputter rate.

1.4.7.2 TRIM

Transport of ions in matter (TRIM) [126] is the most popular collision code. It uses the binary collision approximation and calculates not only sputters but displacements, replacements and vacancies. In common with SUSPRE it assumes the target particles are randomly distributed throughout the non-crystalline target.

1.4.7.3 MARLOWE

MARLOWE [127] was originally written to simulate the penetration of high energy (MeV) nuclei from fusion experiments into the walls of the reaction chamber. The interaction potential is screened coulomb, however, and applicable to much lower energies. The MARLOWE code uses the BCA in common with TRIM. In MARLOWE, however, the initial and subsequent positions of the target lattice are specified exactly and this allows the use of a crystal lattice. Use of a defined lattice allows effects such as channelling (where ions travel abnormally long distances into the crystal by scattering along crystal planes) to be simulated. It also allows the penetration depth profile to be better represented for low energies where the depth of penetration is only several times the lattice dimension. The disadvantage with MARLOWE is that the input files are difficult to set-up and the output files are difficult to interpret both for reasons of the quantity of information involved. This is the reason MARLOWE is used less than TRIM.

1.4.7.4 Hyperchem

One major disadvantage with all the above codes is that they model the bombardment of ions (essentially nuclei) with surfaces. This is obviously not sufficient for modelling of complex molecules (*ie.* methane). Additionally, none of the above codes take into account many-body interactions, which at low energies will be a closer approximation than binary collisions. The Hyperchem code can model polyatomic molecules interacting with a number of surface atoms concurrently, this is at the expense of computation time if the array of target particles is large. The code can be used with a choice of interaction potentials including a full quantum mechanical treatment. The quantum mechanical calculations, however, increase computation time by orders of magnitude.

1.5 Review of etching of III-V's

1.5.1 GaAs devices

As well as the group IV semiconductors Si and Ge, semiconductors made from combinations of elements from groups III and V of the periodic table are important in the microelectronics industry. Typical examples are InP, AlP and GaAs, the latter being one of the most useful semiconductors because of its use in infrared and visible solid state lasers. Because of the low effective electron mass (m_{eff} ~ .067 in comparison with Si

where m_{eff} ~ .98) and therefore high electron mobility, GaAs has applications beyond the 1-2 GHz operating range of silicon devices such as military radar and microwave telecommunications [128].

The operating principles behind III-V based microcircuits is the same as that for silicon based devices, however the method by which the microcircuits are manufactured is completely different due to the differing chemistry.

1.5.2 Etching chemistries

Chlorine based chemistries have traditionally been used in the dry etching of III-V semiconductors due to their excellent selectivity and high etch rate. Pure Cl_2 plasmas have been reported as giving smooth surface morphologies and controllable etch rates of GaAs [129] while the addition of Cl_2 into Ar plasmas reduces electrical damage to etched diodes [130]. $SiCl_4$ is a popular gas due to its low damage of GaAs and extremely high selectivity over AlGaAs (better than 10 000:1) [131] and extremely low residual damage when used in a mixture with SiF_6 [132][133].

The chlorine radicals are highly reactive and combine with both Ga and As (and other III-V's) to create the volatile etch products which are removed. However, Cl containing gases are all highly toxic and are corrosive to equipment. There is the additional problem of ozone depletion making all chlorine containing compounds unattractive.

This has led to interest into alternative gas chemistries for the RIE of GaAs. Initially, interest in methane and methane containing plasmas was stimulated by the need to produce smooth morphologies for InP, the surfaces of which are rough when etched with Cl [134] and Cl containing compounds [135][136][137] due to the relative involatility of indium chlorides [138]. Hydrocarbon alternatives to chlorine were also found to successfully etch GaAs [139][140][141] with etch rates lower and more controllable than those with chlorine mixtures. The role of CH_4 is to remove the group III (A) species as $(CH_3)_mA_n$ while the H_2 removes the group V species (B) as BH_3. This results in very smooth morphologies as long as the CH_4/H_2 ratio is kept within th range 0.1-0.4. At the low end of the range, the group V element is preferentially removed, leading to rough surfaces, whilst at the high end of the range polymer deposition becomes excessive [142][143].

1.5.3 Hydrocarbon etching of GaAs

In the search to find an environmentally benign, controllable and damage free etch for GaAs, mixtures of methane and hydrogen were studied. They were initially used to overcome rough etching on InP [144] but were found to etch GaAs also. The methane reacts with the gallium to form trimethyl gallium ($(CH_3)_nGa$)) and the hydrogen reacts with the arsenic to form arsine (AsH_3) both of which are volatile at room temperatures[145].

As three CH_4 precursors are needed for the removal of one Ga, and these easily polymerize, then it is necessary to run the methane etch in an excess of another gas to remove the polymer build up [146]. The excess gas can be inert in which case the polymer is prevented by physical sputtering, or hydrogen in which case it is chemical. The advantage of hydrogen is that it will not etch into the polymethyl methacrylate (PMMA) mask and methane/hydrogen mixtures, therefore offer the best selectivity [147]. Cheung[148] suggests that the CH_3 fragment is necessary for the etch, however, since the hydrogen/ carbon bond is of the order of 4-5 eV, it is expected that ions striking the surface with energies of several hundred eV will be dissociated [149]. The etch rate was found to increase with the methane concentration [150] until a maximum, found by Cheung *et al* [151] at 20 % methane in hydrogen. Increasing the CH_4 percentage caused a decrease in etch rate and eventually deposition, this change being sharp for Semu *et al* [152]. Many authors have found an increase in etch rate with power [153][154][155]. Thoms [156] found CH_4/H_2 gave an etch rate 10 times smaller than $SiCl_4$ with a very smooth finish. He suggests etching with CH_4/H_2 is metallo organo vapour deposition (MOCVD) in reverse (*ie.* the process by which GaAs is grown). Werking [157] found, not that the etch rate was proportional to the power but to the D.C. bias (approximately the square root of the power) and increases with pressure in the range 10 - 40 mTorr (after which deposition occurs).

Some authors have used mixtures of methane/hydrogen with inert gases [158][159] and found that the inert gas enhances the etch rate and aids plasma ignition and stability or delays the onset of polymerization. Law [160] found the etch rate to be proportional to the mass of the inert mixant.

The loss of active components in the plasma appears to be important for the etch rate as found by Pearton [161] who found it necessary to season the walls of the reactor before getting consistent etch rates (the walls constitute a loss mechanism for methane radicals). Similarly Law [162] found the etch rate to scale with the inverse of the wafer area.

In general it has been found that the etch rate is a function of the rate of removal of the metal component [163][164] and that attempting to increase this by increasing the flux of methane to the surface works up to a point where it causes deposition of a polymer. This point can be delayed by concurrently etching the polymer with hydrogen or an inert gas.

Etching of GaAs with methane/hydrogen is also found to be unaffected by relatively large amounts of water vapour [165], rendering the process robust industrially.

1.5.4 Stoichiometry change

1.5.4.1 Inert

Inert ion bombardment effects must be studied separately in order that the chemical effect on the surface can be attributed to the chemistry rather than merely the physical effect. There have been many studies of inert ion bombardment of III-V surfaces, all of which find depletion in the group V element, though in the case of InP this is attributed to its low mass [166]. In a high energy study of 20-100 keV Ar and Se on GaAs, Singer *et al* [167] found As depletion to a depth given by the bombarded region and attributed this to As preferential sputtering. Malherbe [168] found similar As depletion for lower energy Ar ions (0.65 - 3 keV) and found that the extent of the depletion increased with energy. This was also attributed to As preferential sputtering explained by the lower sublimation energy of As than Ga. Padeletti [169] *et al* also found preferential removal of As from $Al_xGa_{1-x}As$/ GaAs from 5 keV Ar. Scandurra [170] used a variety of low energy inert gases and oxygen on GaAs and found in all cases, As depletion. In the Ar ion bombardment of GaAs (3 keV), Sullivan *et al* [171] found As depletion but also As enrichment of the outer layer and this was explained by Gibbsian segregation and diffusion. Aoyama [172] found a similar result with 1, 2 and 3 keV Ar and Xe ions and also that the surface segregation effect is independent of temperature, implying the Gibbsian tendency is strongly influenced by ion bombardment. A range of low energies (1-5 keV) Ar ions used by Pan [173] showed Ar depletion which was more extreme on the surface at 1keV and less extreme on the surface at 5 keV. At 3 keV there appeared to be a homogeneous As depleted layer. This implies that the two opposing processes of preferential sputtering and radiation enhanced segregation/diffusion are competing at these energies.

Weegels [174] with a low energy ECR plasma found an altered layer depleted in arsenic. The depth of this altered layer was found to be

$$d\,(\mathrm{nm}) = 0.91 + 0.021U\,(\mathrm{eV}) \qquad \text{where } U > 11\ \mathrm{eV} \qquad \text{eqn 1.55}$$

with a threshold of 14 eV for any damage which is close to the energy required to knock an As out of the lattice.

1.5.4.2 Hydrocarbon

There has been considerably less investigation into the stoichiometry changes of III-V's subject to methane/hydrogen plasma etching or ion bombardment and most of this has been concerned with InP. Pure hydrogen plasma treatment of GaAs subject to XPS by Debiemme-Chouvy [175] showed arsenic depletion which increased with the applied power, a result confirmed by Sullivan *et al* [176]. Additionally it was found that there was no oxidation of arsenic on subsequent exposure to air. This implied that either the As atoms were buried beneath a Ga surface film, or that the chemical reactivity of the surface

is changed by strong incorporation of hydrogen into the upper lattice. Mclane, [177] using a methane/hydrogen/argon admixture, reports As deficiency in the first 10 nm and that this deficiency increased with the amount of Ar. Pearton [178] also found with a high power methane/hydrogen/argon mixture that there was a loss of arsenic.

Meharg [179] in a study involving the bombardment of very low energy (20 - 500) eV carbon ions onto GaAs found that the removal of As was proportional to the ion energy and that even at energies as low as 20 eV there was substantial subsurface damage due to both chemical and physical effects. This damage was reduced by exposure to a hydrogen plasma (though not damage due to depletion of As). In another paper [180] he concluded that even at 20 eV there was a damaged C-GaAs layer of 8 Å.

1.6 Research Programme

This research project was run in concurrence with an ongoing research project at Aston University which is etching GaAs in hydrogen and mixtures of methane/hydrogen. The XPS results are obtained by Dr Sayah Saied. The timetable of research was split into three main areas. Firstly, the modelling of the plasma in terms of the fluxes of ion and neutral particles to the surface. Secondly, modelling of the particle surface interactions and thirdly, the gathering and interpretation of the XPS results in the light of the above.

1.6.1 Plasma

Initially, it was necessary to know the angle and energy distributions of all particles at the surface of the sample. To this end, a model was devised based on a 1-D interpretation of the plasma. The model followed electron motion in the plasma and all electron interactions with the background gas. This allowed the ionisation profile to be determined and qualify the extent of ionisation in the sheath, the existence of which invalidates purely sheath models. Use of the correct ionisation cross sections allowed the mass breakdown of the background gas to be determined and this was compared to the measurements of the mass probe. Other plasma parameters which arose from the modelling such as the electron energies were compared with results of the Langmuir probe.

Ion motion was followed and as many interactions with neutrals were included as there was available cross section data for.

It was necessary to follow neutral cascades as they comprise a significant flux of energy to the surface. In following neutral cascades, there is a rapid increase in computation time as the pressure (and number of collisions) increases. Therefore, it was necessary to write the code in a relatively fast language which is portable thereby allowing it to be run remotely. The language chosen was C and the codes were run in the background (so as not to require sole use of any machine) on a number of SUN multi-tasking workstations.

Special care was taken in the form of elastic scattering used in the simulation. It is likely that the hard sphere approximation is too simplistic a model for the scattering of polyatomic particles. The scattering of these particles was therefore studied with both self-developed codes and the commercial Hyperchem code.

The code used was not required to be self-consistent because we have knowledge of the potentials across the plasma. These, determine the energy of the bombarding ions, which being the most important plasma parameter, can be found experimentally.

1.6.2 Surface interactions

It has been seen that both the inert and methane ion bombardment of GaAs leads to arsenic depleted surfaces. It was not known, whether the methane bombardment of GaAs at reactive ion etching energies leads to unstoichiometric surfaces due to purely physical or chemical effects or a mixture of the two. Attempts were made, therefore, to isolate the two effects by the comparison of etching due to methane/hydrogen and the inert gas neon. Attempts were made to predict the physical effects at the surface with recourse to the particular crystal structure in terms of preferential sputtering and Gibbsian segregation because at these low energies it is possible that the surface is not amorphous [181]. Use of binary collision codes helps in determining the damage layer and the layer affected by bombardment enhanced segregation.

These effects will allow us to make predictions about the composition of the surface which can be experimentally determined with XPS.

1.6.3 XPS

The experiments were run over the matrix of pressure, power and methane concentrations and in addition, some experiments were performed with neon and neon/hydrogen mixtures.

It is possible to quantitatively interpret XPS results in terms of either fixed elemental concentrations and variable layer thicknesses or fixed layer thicknesses with atomic concentration gradients. In this study it was decided to interpret the XPS data in terms of variable layer thicknesses, each layer containing a fixed concentration of elements. A code was devised to allow easy interpretation of the XPS results based on this model. The code predicts the relative atomic concentrations of each element as a function of the angle of investigation and incorporated a user interface allowing user defined changes in layer thicknesses to give corresponding changes in predicted XPS results in real time. These predictions were compared against the extensive experimental results that were produced.

Chapter 2. Modelling of ion energies

The model presented will be explained sequentially beginning with the simplest collisionless approach. The model will be expanded for the simple case of argon, followed by the numerous interactions involved in hydrogen and methane/hydrogen. At each stage predictions will be compared with experimental results. Finally, the assumption of the mass distribution of particles in the plasma will be replaced by an electron model, the spatial and mass distribution of the ionisations from which will be the starting point of the ions in the ion trajectory model. The final model (the code for which is in appendix I), which combines both aspects, will be discussed along with the form of the results output.

2.1 The general collisionless model

2.1.1 Ion trajectories

The following is a description of the basic collisionless model used to predict ion energy distributions at the electrodes of an asymmetric rf reactive ion etcher. Later collisions will be introduced for the simple case of argon in order to compare the model predictions with experimental results. The model will then be extended for the more complicated cases of hydrogen and methane/hydrogen mixtures. The collisionless model is justified at pressures below several mTorr and can therefore be applied to many different plasma gases. The program was based on a code by Wronski [182] for predicting ion energies in a D.C. discharge.

The program was originally written in BBCBasic on an Archimedes A5000, but was later converted into C which improved the efficiency by orders of magnitude and allowed the program to be run remotely on SUN workstations so that many simulations could be run simultaneously.

The simulation proceeds by taking ions which have crossed the boundary between the plasma and the sheath and applies forces which are given by the instantaneous electric field at the present ion position. The subsequent trajectory of the ion is followed until it strikes the electrode, when its energy and angle are recorded in an array. At any time, the ion trajectory is defined by the energy, velocity, position, direction cosines with respect to cartesian x, y and z axes and velocity components parallel to these axes.

2.1.2 Entering the sheath

The ion energies in the plasma are similar in magnitude to that of the background gas, being a weakly ionized plasma. The primary ion, on crossing the sheath boundary is

given a component of velocity in the x, y and z directions (the x vector being perpendicular to the cathode we only allow the x component of velocity to be towards the cathode) which is randomized within the constraint that the distribution function is Boltzmann. *ie.*

$$P(v_x, v_y, v_z) \propto \exp\left[-m_i\left[v_x^2 + v_y^2 + v_z^2\right] / 2kT_i\right] \qquad \text{eqn 3.1}$$

where $P(v_x,v_y,v_z)$ is the probability that at ion temperature T_i, an ion of mass m_i has velocity components v_i.

The velocity is found by randomizing v_x, v_y, v_z and calculating the probability of the ion having this energy, $P(v_x,v_y,v_z)$ which is then compared to a random number between 0 and 1. If $P(v_x,v_y,v_z)$ is greater than this random number and $v_x >= 0$ then we accept this and the ion proceeds into the sheath. In order to reduce computation time, the initial range of velocity values was limited, ignoring those velocity values with very small probabilities which are generally rejected. The range of velocity values was limited in order to save time by reducing the number of energies which are by the above method rejected for being anomalously high. The maximum velocity (positive or negative) is then given by

$$v_{i\,max} = 3 \times \sqrt{\frac{2E_{i\,av}}{m}} \qquad \text{eqn 3.2}$$

where the average energy in each orthogonal direction is given by

$$E_{i\,av} = \frac{1}{2}kT_i \qquad \text{eqn 3.3}$$

The result is a compromise between reducing computational time and the need to have a full initial energy distribution function.

The phase at which the ion enters the sheath is also randomized between 0 and 2π with a uniform probability distribution.

2.1.3 The plasma and sheath potential

As has been discussed in section 1.2.3.4 and 1.3.4.1, the consensus of opinion is that the plasma potential follows the positive part of the cathode potential in some way that differs slightly depending on whether the sheath displays dominantly resistive or capacitive behaviour. This difference is small and less important than the magnitude of the rf component of the plasma potential, a value given by the D.C. bias, the driving potential and the floating potential. In this study plasma potential is represented by a sinusoid with a minimum value given by the floating potential and a maximum by the maximum of the cathode potential plus the floating potential.

The sheath potential is given by the difference between the plasma potential and the cathode potential (with the assumption that they are in phase) and the anode sheath

potential is given by the plasma potential.

Similarly, the exact nature of the electric field between the plasma/sheath boundary and the cathode has only a small effect on the IEDs and in this study was used in the form given by the Child-Langmuir space charge limited current.

2.1.4 Equations of motion

If the ion at time t is within the extent of the sheath then it undergoes an acceleration given by

$$\frac{d^2r}{dt^2} = (-e/m_i)\frac{\partial V(r,t)}{\partial r} \qquad \text{eqn 3.4}$$

then with the assumption that the field is plane parallel with the electrode, the equation of motion for the ions is

$$\frac{d^2r}{dt^2} = -\frac{4}{3}\left(\frac{e}{m_i}\right)\left[\frac{V_{pe}(t)}{l(t)}\right]\left[\frac{l_{max}-x}{l(t)}\right]^{1/3} \qquad \text{eqn 3.5}$$

for the collisionless Child-Langmuir potential.

The program employed small time steps for the simulation, with the requisite that the time step is considerably smaller than the time for 1 RF cycle. The new velocity component in the x direction (y and z being unchanged in a plane parallel field) is calculated each time step from the equation of motion. For argon it was found that a time step equal to .01 of a radian at 13.6 MHz was sufficiently small but for hydrogen a smaller time step was required due to its lighter mass.

2.1.5 Results

On arrival at the cathode the ion has its energy and angle recorded in an array which has variable energy bin sizes that are usually set to 1 eV which approximately corresponds to the resolution of most mass spectrometers. The angle bins were sized at 2 degrees and the number of ions recorded in each angle bin was normalized (to give ion current) by dividing by cos θ, where θ is the angle between the ion direction and the normal to the surface. This process is repeated for as many particles as is deemed statistically necessary which is dependent on the number of energy bins. *ie* in order to keep statistical error below 5 % we need at least 400 particles per bin.

2.1.6 Comparison with published results

The simulations performed in this work will be compared to the experimental data reported by Kuypers [183] because it is relatively recent data performed at low pressure. This data has already been compared to simulations made by Field *et al* [184].

Figure 2.1a shows the result of the ion energy distribution (IED) for oxygen. The parameters supplied to the program were kT_e = 2 eV, kT_i = .05 eV, V_0=488 V and l_{max} = 6.23 mm. The ratios of O and O_2 are arbitrary. The IED shows the classic saddle structure as expected, with the heavier molecule having the narrower peak separation.

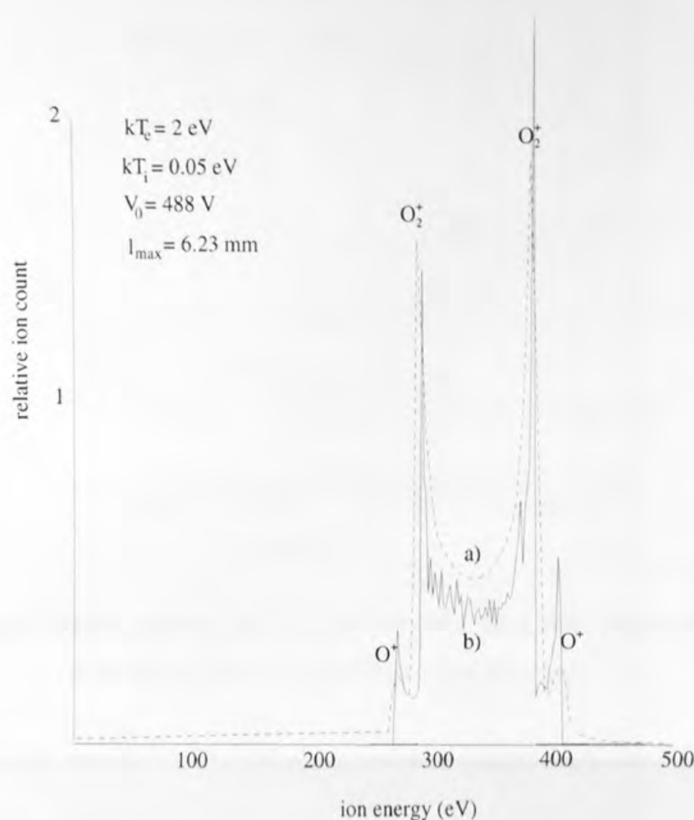

Figure 2.1 Comparison of a) predicted and b) experimental results for the IEDs at the cathode of an rf oxygen plasma.

Figure 2.1 b) shows the experimental results of Kuypers and it can be seen that the peaks are well reproduced. The experimental results are not supplied with the parameters of the discharge and therefore those inferred by Field *et al* are used in the fitting.

It is felt justified to fit the parameters by trial and error because of the different ways in which they affect the modelled IED. For instance, the peak separation is affected only by the frequency, the ion mass and the maximum sheath width l_{max}, so this gives a good measure of l_{max}. Similarly, the average ion energy is given by the peak voltage at the cathode.

An important point to stress is that the value of A_c/A_a used in the calculation is 0.4, which was obtained from the measurement directly of V_0 and V_{DC} and is substantially different from the real value of A_c/A_a. *ie.* this value is the effective area ratio of the cathode and anode and is the geometric ratio modulated by some effect of the geometry. The difference arises because some parts of the cathode or anode may be more or less effective

in affecting the plasma depending on their exact location in the chamber.

Figure 2.2 shows the predicted and measured IEDs at the cathode for an argon hydrogen mixture using the parameters shown. Again the peaks are well reproduced.

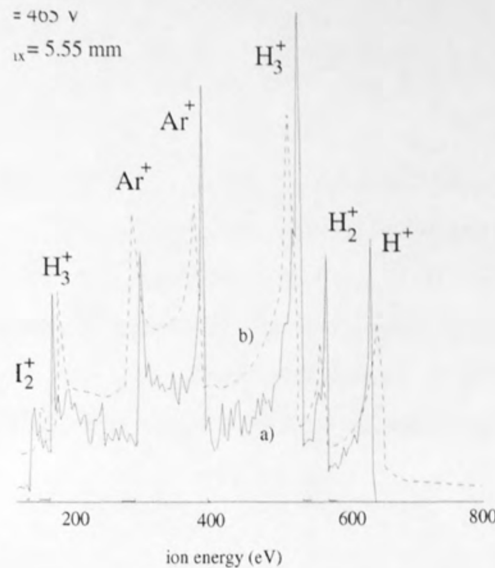

Figure 2.2 Comparison of a) predicted and b) experimental results for the IEDs at the cathode of an rf argon/hydrogen plasma.

Finally diagram 2.3 shows the results of calculation and experiment for CF_4 discharge.

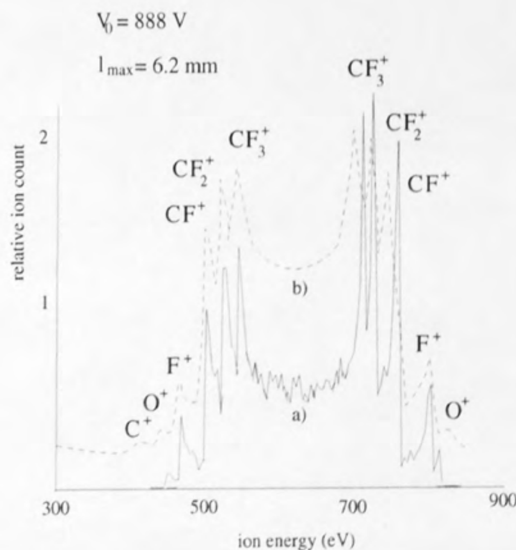

Figure 2.3 Comparison of a) predicted and b) experimental results for the IEDs at the cathode of an rf carbon tetrafluoride plasma.

The values of kT_i and kT_e hardly affect the distributions and their values remain fixed throughout the study.

In all the experiments, the pressure was 3 mTorr which is sufficiently low that collisions in the sheath are negligible and the mean free path of ions in the sheath is of the order of the maximum sheath width or greater. The next stage is to introduce collisions into the model in order that higher pressure plasmas may be modelled.

2.2 Argon collisions

2.2.1 Cross sections

The next stage in the generation of the model is to include collisions in the sheath. Figure 2.4 after Phelps [185], shows the main processes for Ar^+ ions (the major ionic component of the plasma) with neutral argon (*ie.* the background gas in the sheath). In the diagram, Q_m is momentum transfer, or scattering, Q_{CT} is charge transfer, $Q_{(UV)}$ is the UV resonance line, $Q_{(e)}$ is ionization, and $Q_{(811)}$ and $Q_{(488)}$ are excitation lines. In the lower energies encountered in reactive ion etching only momentum transfer and scattering need to be considered.

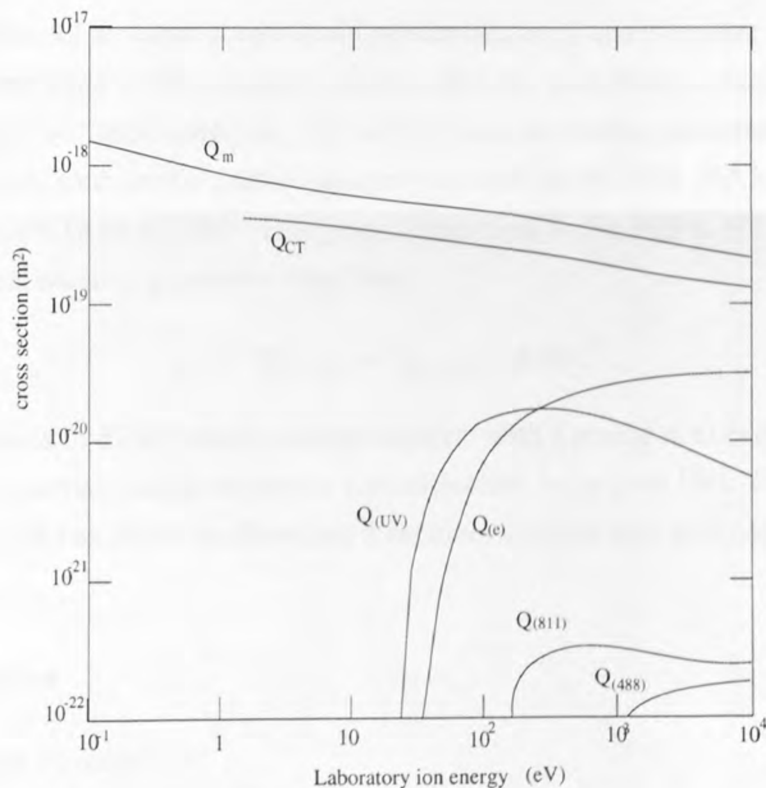

Figure 2.4 Cross section data for Ar+ collisions with Ar.

2.2.2 Randomization of a collision event

For the case of argon, the two interactions of any consequence are momentum transfer and charge transfer. This has led previous authors to use the principle of a total cross section and the probability ratio between the two interactions. With the numerous interaction channels available for methane/hydrogen, it was considered the simplest method to find

the cross section for each and treat them as independent processes. This is a valid approximation if the distance step dx moved by the ion each time is small and therefore the probability of any interaction is small. This is the approach followed in this work.

dt is small as is the change in energy ΔE, and since the cross section is recomputed at every time step, this method allows the cross section for any event to vary very smoothly with the energy of the interacting particle.

Assuming the background gas atom is stationary with respect to the incoming ion, the probability of an event is given by

$$P = \exp(-dxQ) \qquad \text{eqn 3.6}$$

where Q is the macroscopic cross section, $q.N$ where q is the microscopic cross section and N is the particle density. If a random number between 0 and 1 exceeds 1 - P then the event has taken place. In the program, the cross sections for each event are stored in an array which is looked up at each step.

As the probability of an event is very small in each time step, the computer is comparing a number between 0 and 1 with a number almost 1 then the discreetness of the generated random numbers becomes important. The default random number generator on the workstations used calculates a random integer between 0 and RAND_MAX where RAND_MAX is a 16 bit number. This gives discreetness in the region of 1 part 10^4. This program uses an additive generator of the form

$$X_n = (X_{[n-24]} + X_{[n-55]})\ \mathrm{MOD}\ 2^{31} \qquad \text{eqn 3.7}$$

This gives a series of 32 bit pseudo random numbers with a period in excess of 2^{55} whose randomness properties, though unproven are conjectured to be good [186]. Empirical testing since 1958 has shown no flaws and it becomes discreet only at the level of 1 part in 10^9.

2.2.3 Collisions

2.2.3.1 Charge transfer

Charge transfer involves the exchange of an electron between incoming and target particles with negligible transfer of momentum. The process of charge exchange is very different at low than high incident energies. In the former case a collision complex is formed and the resulting charge exchange possibility on rearrangement is high, in the latter, the kinematics of the reaction are very restrictive and the possibility falls very quickly with increasing energy [187]. It results in the neutralisation of the incoming ion and the ionization of the background neutral. The program stores the position of the newly formed ion in an array and later allows it to be accelerated in the field to the

cathode where the charge exchange process may be repeated. The fast atom created is unaffected by the field and carries on towards the cathode unless it is involved in a momentum scattering event.

2.2.3.2 Momentum scattering

For hard sphere scattering, the collision cross section is well defined as a sphere centred around the particle. For scattering involving a potential field, the scattering cross section is essentially infinite. When analysed quantum mechanically, there is in fact a maximum distance of approach of the two bodies which will lead to a change in velocity vector, but for the purpose of this study, we will define the scattering cross section as that where scattering of the incoming particle is at least 2°. The reason for this is that shallower angle scattering than this is not deemed relevant, but more importantly, the experimental cross sections used are taken from a range of different experiments with different errors and definitions of relevant scattering and so without recourse to the individual experiments, this cut off is a useful one.

Figure 2.5 shows the mechanics of the interaction used

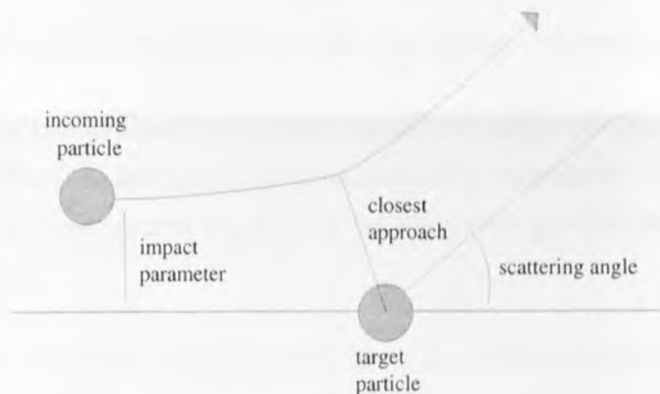

Figure 2.5 Schematic of the interaction of a pair of particles via a central potential.

The solution for the final scattering angle involves solving for the closest approach of the centres of the two spheres. A good explanation is given by McDaniel [188].

The final scattered angle (when the distance between the two spheres is infinite) is given by

$$\Phi(v_0, b) = \pi - 2b \int_{r_a}^{\infty} \frac{dr}{r^2\left[1 - \frac{V(r)}{E_0} - \frac{b^2}{r^2}\right]^{1/2}} \qquad \text{eqn 3.8}$$

where r is the separation of the centre of the two spheres, $V(r)$ is the central force, r_a is the distance of closest approach and E_0 is the initial kinetic energy of the incoming particle. r_a is found from where the bottom half of the right hand side of the above equation is zero.

After finding the angle through which the particle has been scattered, it must have its velocity components changed as indicated in figure 2.6.

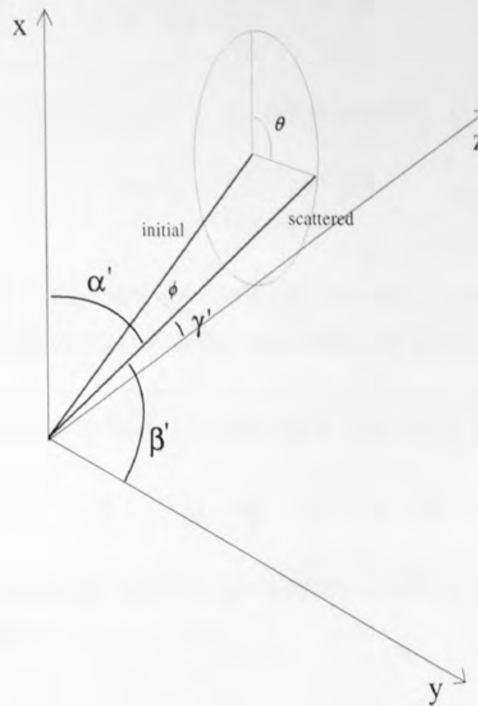

Figure 2.6 Schematic of the angle change of a scattered particle.

If a scattering event occurs when the particle interaction radius is r, then the impact parameter b is randomized from 0 to r and the scattering calculated. The randomization is weighted as a square root so as to account for the number of possibilities of b being proportional to b^2.

The potential of the interaction is assumed to be a Coulomb potential modified by the screening function $\chi(r)$ [189] *ie.*

$$V(r) = Z_1 Z_2 e^2 \frac{\chi(r)}{4\pi\varepsilon_0 r} \qquad \text{eqn 3.9}$$

where Z_2 and Z_2 are the proton numbers of the interacting nuclei.

Figure 2.6 shows the initial and the scattered velocity vector. The scattering angle is equal to ϕ and this vector must be randomized about the axis of the original direction of travel (the potential field is isotropic and only the magnitude of the impact parameter was randomized, not its relative position) between 0 and 2π.

If the direction cosines associated with the x, y and z axes are α, β and γ respectively, then they change according to the expressions below [190] where ϕ is the scattering angle and θ is the randomized angle about the initial velocity vector.

$$\alpha_0 \rightarrow \alpha_1 = \arccos[\cos\alpha_0 \cos\phi - \sin\alpha_0 \sin\phi \cos\theta] \qquad \text{eqn 3.10}$$

$$\beta_0 \rightarrow \beta_1 = \arccos[\cos\beta_0 cos\phi - \sin\beta_0 \sin\phi (\cos\theta P_b - \sin\theta (1 - P_b^2)^{1/2})] \text{eqn 3.11}$$

$$P_b = -\frac{\cos\alpha_0 \cos\beta_0}{\sin\alpha_0 \sin\beta_0}$$

$$\gamma_0 \rightarrow \gamma_1 = \arccos[\cos\gamma_0 cos\phi - \gamma_0 \sin\phi (\cos\theta P_g + \sin\theta (1 - P_g^2)^{1/2})] \text{ eqn 3.12}$$

$$P_b = -\frac{\cos\alpha_0 \cos\gamma_0}{\sin\alpha_0 \sin\gamma_0}$$

In practice, the third angle is worked out from the first two, in order that the final direction is physically possible (small computer error may build up in the coordinates).

The energy of the incoming particle is also changed according to

$$E_0 \rightarrow E_1 = E_0(1 - (1 - ((M_t/M_i - 1)/(M_t/M_i + 1))^2 \sin^2(\psi/2))) \text{ eqn 3.13}$$

where M_t/M_i is the ratio of target mass to incident mass and ψ is the scattering angle in centre of mass coordinates.

The velocity and direction of the target particle is calculated from conservation of momentum considerations.

2.2.4 Neutral cascades

It can be seen that one initial ion can cause a cascade of fast neutrals which in turn scatter more neutrals. This causes the program to operate much slower at high pressures than low pressures.

The scattering for a neutral is taken to be the same as the scattering of an ion. Both incident ion and target atoms are followed until they either reach the cathode, or in the case of the neutrals, they are reflected back toward the plasma in a scattering event or their energy falls below some minimum where they are effectively indistinguishable from the thermal neutrals. This minimum is taken to be 0.1 eV.

2.2.5 Comparison with published data for argon

2.2.5.1 At the cathode

Good experimental cathode IEDs have been produced by Kuypers [191] for a collisional sheath of visual extent 4-5 mm at a pressure of 39 mTorr, as shown in figure 2.7. The computer prediction is shown for comparison with the program parameters.

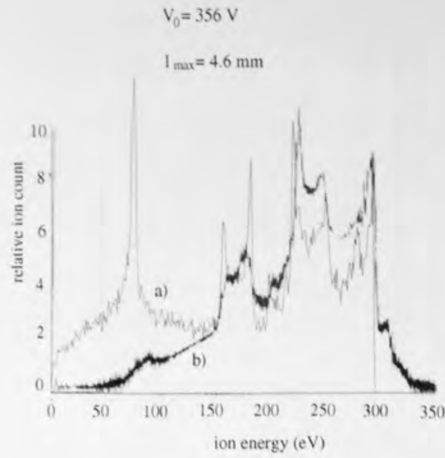

Figure 2.7 Comparison of a) predicted and b) experimental results for the IEDs at the cathode of argon rf plasma.

It can be seen that the main difference is below 100 eV where the sensitivity of the probe is reduced, probably due to space charge effects at the orifice. We also find as others have [192] that in fitting the data we require only half the pressure. This is due either to initial experimental error or inaccurate cross-section data. It was also confirmed that the high pressure Child-Langmuir approximation to the electric field and the linear electric field gave a distribution indistinguishable from the original, as does the addition of 2 eV to account for the Bohm criterion.

2.2.5.2 At the anode

Using the expressions derived above, the predictions for the IEDs are shown with the experimental data of Liu *et al* [193] in figures 2.8 and 2.9 for pressures of 10 mTorr and 50 mTorr respectively.

In figure 2.8, the predicted IED correctly estimates the extent of the 'smearing' of the peak to lower energy values. There is no peak splitting due to the rf field because the relatively large sheath width over the anode which occurs in parallel plate systems has increased the average number of cycles it takes an ion to cross the sheath until the difference between the maximum and minimum energy attainable by the ion is negligible. In figure 2.9, the ion energies are reduced still further. In common with Liu *et al* we find that the predictions for ion energies at 500 mTorr underestimate the experimental energies and this is due to an overestimate of the true sheath width.

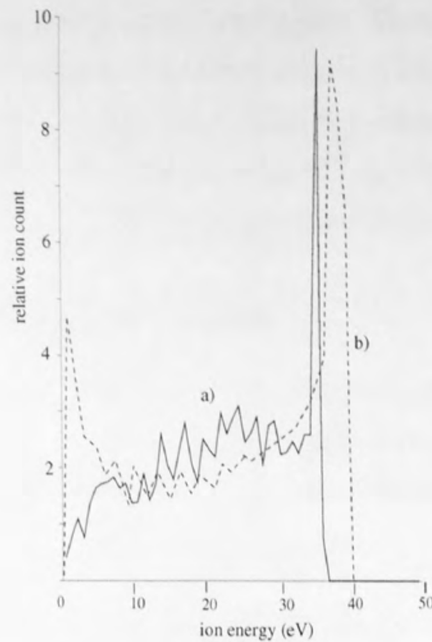

Figure 2.8 Comparison of a) predicted and b) experimental results for the IEDs at the anode of argon rf plasma. Pressure = 10 mTorr.

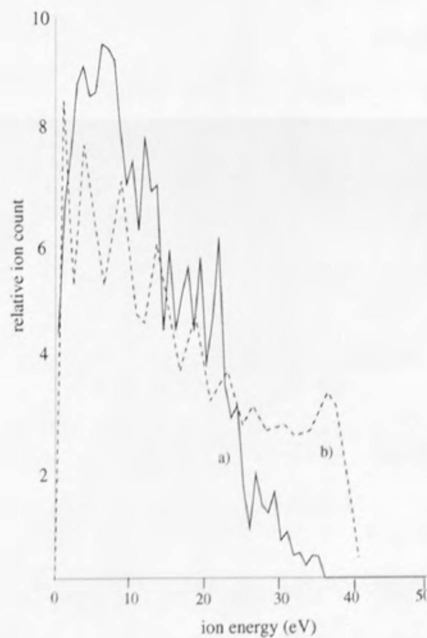

Figure 2.9 Comparison of a) predicted and b) experimental results for the IEDs at the anode of argon rf plasma. Pressure = 50 mTorr.

2.3 Complex molecule scattering

In the argon case, the scattering was modelled using an interaction potential based upon the screened nuclear coulomb repulsion. For the case of extending the code to hydrogen and methane, the hard sphere model becomes less valid, but using a central potential for a polyatomic molecule likewise appears an oversimplification. Phelps [194] presents data on

ASTON UNIVERSITY
LIBRARY & INFORMATION SERVICES

the scattering of hydrogen ions with neutral hydrogens. These data are, however, only some approximated values interpolated between very high energies and thermal energies. It is also necessary to know the angular distribution of scattered particles. To this end, the scattering of complex molecules was studied using self-developed codes and the commercial code Hyperchem [195], with the results to be used in the plasma model.

2.3.1 The choice of interaction potentials

In this study we use two approaches to model the scattering of hydrogen molecules. The first regards each molecule as a single point with a spherically symmetric potential distribution. The second approach solves for the forces between each atom in the collision complex.

In the first case, we have used two different forms of the intermolecular potential. Firstly, theory suggests that molecules interact with an exponentially decreasing potential of the form

$$V(r) = A\exp(-\beta r) \qquad \text{eqn 3.14}$$

where A and b are coefficients which have been calculated by Radcig *et al* [196] for a number of molecule/molecule combinations (model 1). The second form of the potential is that given by the screened coulomb repulsion of Firsov as follows

$$V(r) = \frac{Z_1 Z_2 e^2}{4\pi\varepsilon_0}\frac{1}{r}\left[0.35\exp\left(-0.3\frac{r}{a_s}\right) + 0.55\exp\left(-1.2\frac{r}{a_s}\right) + 0.1\exp\left(-6\frac{r}{a_s}\right)\right] \qquad \text{eqn 3.15}$$

where

$$a_s = 0.885 a_0\left(\sqrt{Z_1} + \sqrt{Z_2}\right)^{-2/3} \qquad \text{eqn 3.16}$$

and a_0 is the Bohr radius. Here we regard each molecule as a single atom, the nucleus of which contains all the protons of the molecule (model 2).

In the polyatomic molecular model, theory suggests that the atoms of a parent molecule interact by the force field whose potential is described by the Lennard-Jones formula

$$V(r) = c_1 r^{-m} + c_2 r^{-n} \qquad \text{eqn 3.17}$$

where c_1, c_2, m and n are constants. In this study, m and n are taken to be 8 and 4 respectively and c_1 and c_2 are fixed by the use of the interatomic potential minimum and the equilibrium atomic separation, both of which are well known [197]. The atoms in molecule 1 interact with the atoms in molecule 2 by either the screened coulomb repulsion (model 3) or the interatomic force (model 4). The four potential distribution functions are shown in figure 2.10.

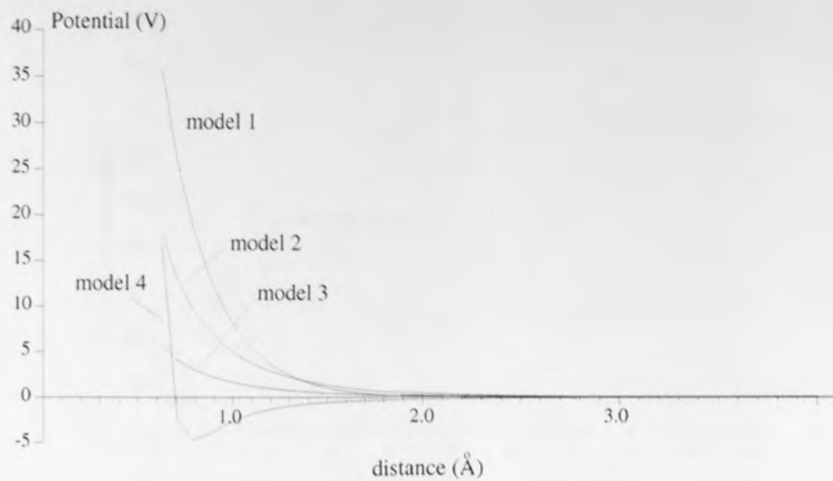

Figure 2.10 The four interaction potentials used to model polyatomic scattering.

2.3.2 The model

The model proceeds by taking a target H_2 molecule and an incident molecule at positions x, y, z such that $x_{inc} \sim x_{tar}$ -10 Å, $z_{inc} = z_{tar},$ and $y_{inc} = y_{tar} + b$ where b is the impact parameter. The molecular orientations in space are randomized and the incident molecule is given an initial velocity v_{inc} which is associated with the interaction energy E. The trajectories of both particles are then followed with the Newtonian equations of motion being applied at each time step Δx. The program, written in C and contained in appendix II, outputs the final energies, velocities, angles *etc.* of the particles when the final separation between them has reached some large value (say 10 Å). For each of the four models, the matrix of scattering angle versus energy and impact parameter was calculated.

2.3.3 Predictions for scattering angles

Figures 2.11, 2.12, 2.13 and 2.14 show the scattering angle against the impact parameter for models 1 to 4 respectively for the range of energies from thermal to 1000 eV, the highest energy likely to be gained by an ion in an rf plasma.

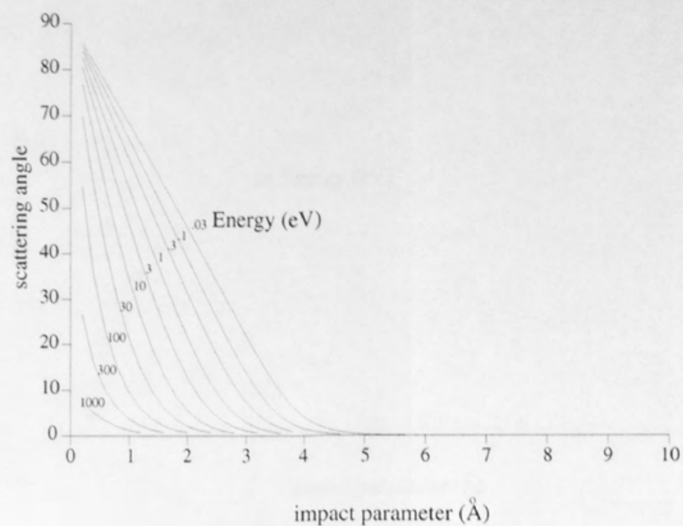

Figure 2.11 Results of model 1.

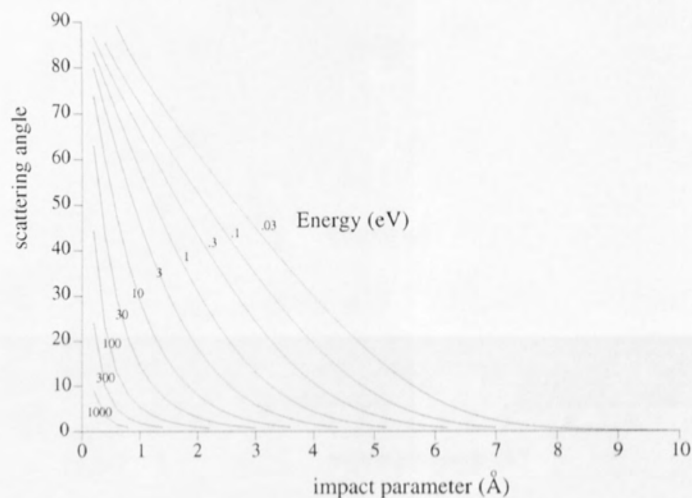

Figure 2.12 Results of model 2.

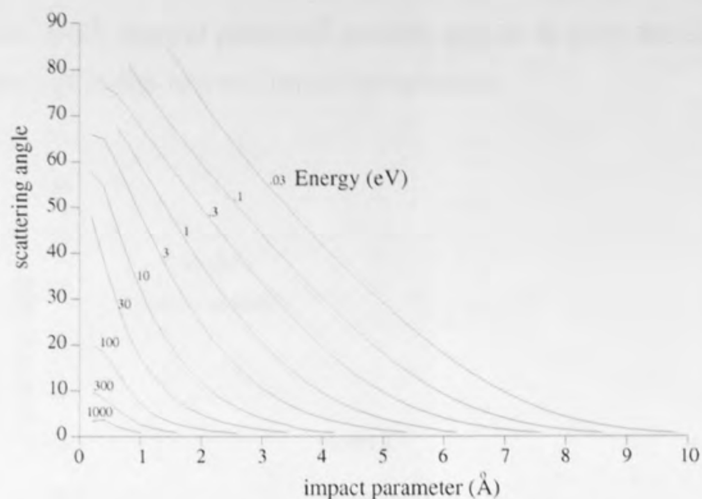

Figure 2.13 Results of model 3.

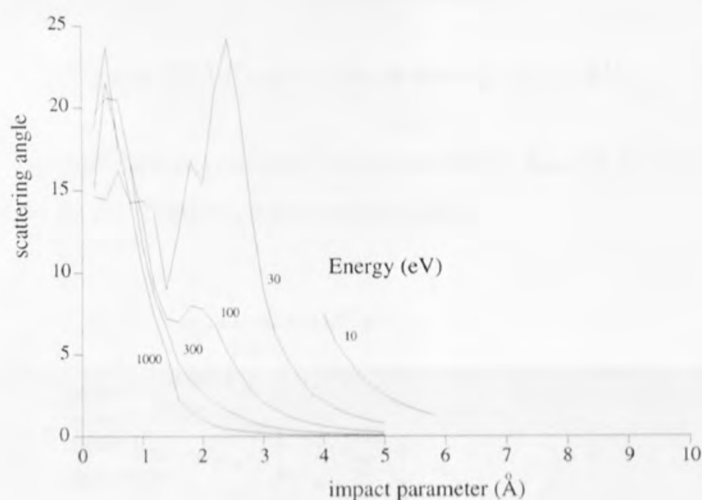

Figure 2.14 Results of model 4.

It can be seen that the models 1 and 2 with central potentials are similar for the highest energies, but at low energies, the slow decline to zero of the screened coulomb potential in comparison with the exponential potential gives model 2 greater scattering at high impact parameters. The polyatomic model 4 gives spurious results when the interaction energy is of the same order as the bond energy and is quite unsuitable for this energy regime. The polyatomic screened coulomb potential (model 3) shows similar results to models 1 and 2 but with higher scattering in every case.

The Hyperchem code, being computationally expensive was only used around the scattering threshold except for 10 eV where it was used across the range of impact parameters.

Figure 2.15 shows the scattering for the four models plus Hyperchem on the same graph for an energy of 10 eV. All the model results are similar except those from model 4. The results from models 1 and 2 cross over due to the crossing over of their potentials as a

function of distance. Both central potential models appear to give the closest match to the Hyperchem code except at the lowest impact parameters.

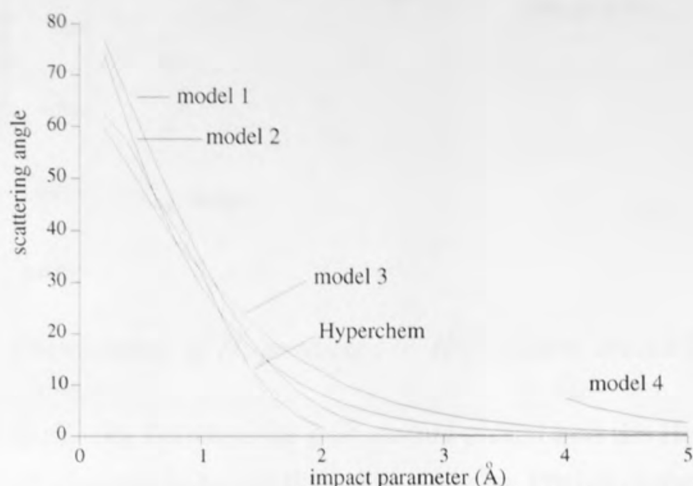

Figure 2.15 Results for an energy of 10 eV.

The results of the cross sections associated with scattering $\theta_{\min}$ (= 2°) are shown in figure 2.16 and are compared to the Phelps cross section data.

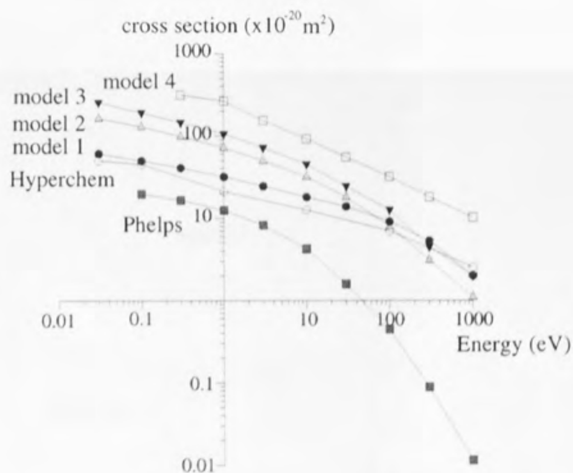

Figure 2.16 Cross sections associated with scattering of θ_{min} (= 2°).

All the models including Hyperchem show cross sections considerably larger than those given by Phelps. Due, however, to the different rates at which the potentials drop to zero at large r, the cross section is probably not the best method of comparison of the different models.

Figure 2.17 shows the results of the cross section for dissociation of H_2 by collision with H_2. The Hyperchem results are displayed with the results of the screened polyatomic model and the data of Phelps.

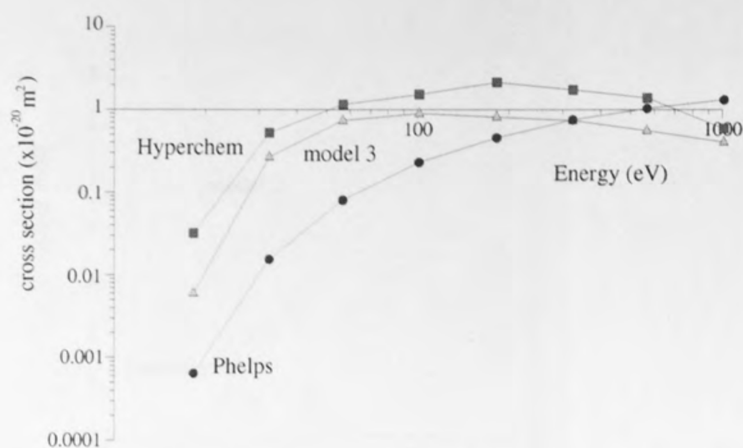

Figure 2.17 Dissociation of H_2 predicted by Hyperchem, model 3 and Phelps.

The results show a similarity between the polyatomic model and the Hyperchem results with a cross section considerably larger than that given by Phelps at the lower energies.

Radcig [198] does not supply coefficients for the potential for methane/hydrogen interactions and so we have compared the results of the central screened potential (model 2) with those from Hyperchem in figures 2.18 and 2.19. The screened coulomb potential appears to overestimate the scattering in comparison to the Hyperchem model, though the Hyperchem model is not necessarily more accurate.

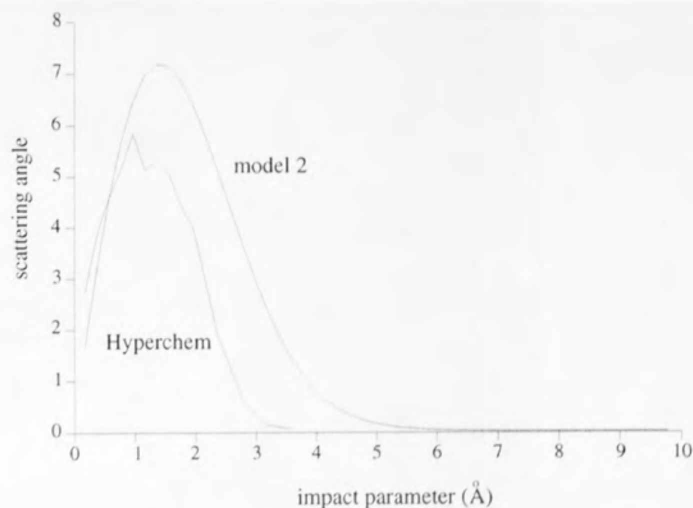

Figure 2.18 Scattering of CH4 from H2 - interaction energy 10 eV.

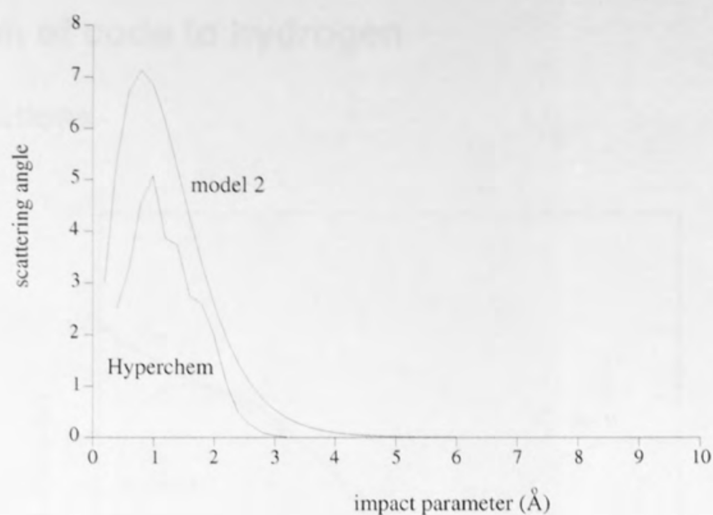

Figure 2.19 Scattering of CH_4 from H_2 - interaction energy 100 eV.

Model 2 was taken as the scattering potential for all subsequent work, due the closeness between its predictions and those of both model 1 and Hyperchem. In addition the potential is easy to use because its generality allows it to be applied to any molecules. The inclusion of some of the physics of the interaction necessarily makes it more correct than the hard sphere approximation. Unfortunately, this central potential is isotropic and does not reflect the non-spherical shape of hydrogen molecules and therefore the non-isotropic scattering that would result. However, the polyatomic codes used did not agree well and showed much greater scattering.

2.4 Extension of code to hydrogen

2.4.1 Cross sections

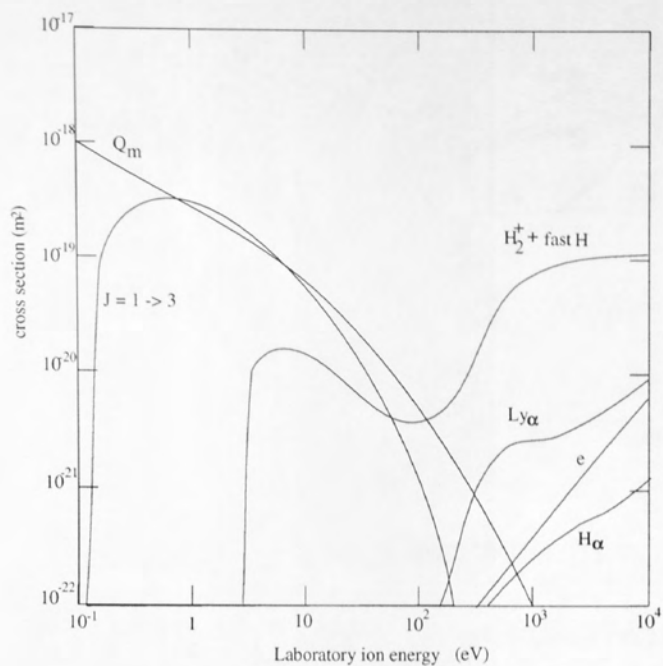

Figure 2.20 Cross sections for $H^+ + H_2$.

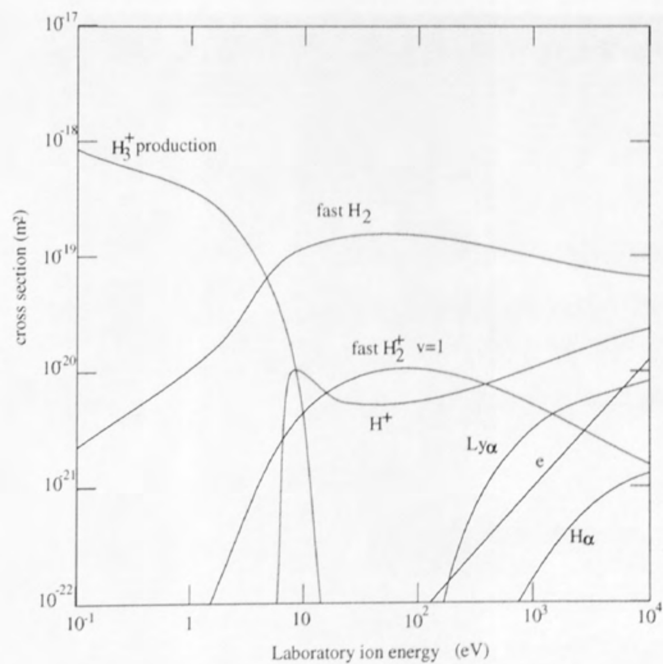

Figure 2.21 Cross sections for $H_2^+ + H_2$.

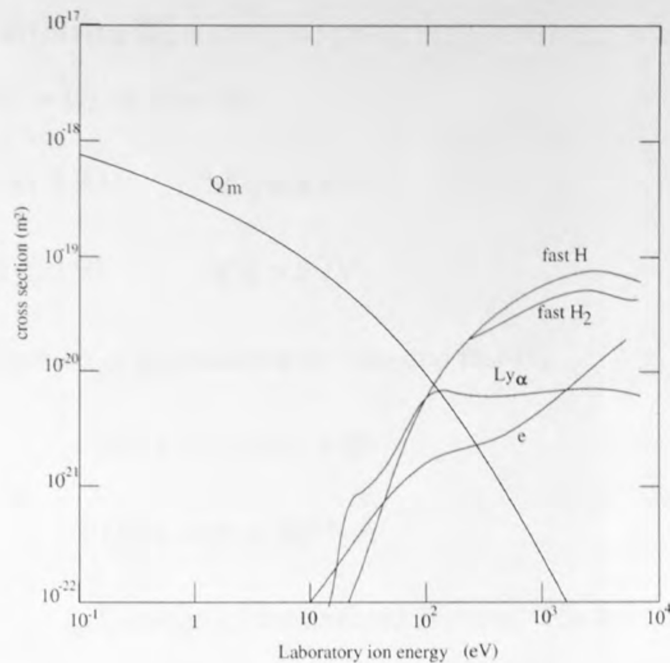

Figure 2.22 Cross sections for $H_3^+ + H_2$.

Figures 2.20, 2.21 and 2.22 show the cross sections for scattering on H_2 of H^+, H_2^+ and H_3^+ (after Phelps [199]). Much of the data involves extrapolations from higher or lower energies. The range 1 eV to 100 eV is not well known experimentally.

It can be seen that the major reaction which occurs up to several tens of volts (apart from excitations) are momentum scattering, charge transfer between H_2^+ and H_2 and the exothermic reaction

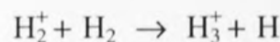

$$H_2^+ + H_2 \rightarrow H_3^+ + H$$

which was considered by Dickenson [200] to have a threshold activation energy of several eV, but is considered by Phelps and others [201] to proceed at negligible energies. There is evidence, however, that the cross section for the dissociation of H_3^+ is of the order of 40 times larger than that given by Phelps and this may become important at the higher pressures [202].

The collisions and cross sections considered in hydrogen plasmas are summarised below, with the interaction energy E in electron volts.

2.4.1.1 Collisions involving H^+.

Creation of H_2^+ $\quad H^+ + H_2 \rightarrow H + H_2^+$

Cross section $\quad 0.6\ Å^2$ if $E > 3$ eV

Result $\quad$ Creation of thermalized H_2^+ ion and fast H

2.4.1.2 Collisions involving H_2^+

Charge transfer $H_2^+ + H_2 \rightarrow H_2 + H_2^+$

Cross section $E \times 1.4$ Å^2 if $E < 8$ eV

$11 - E/150$ if $E > 8$ eV

Result Creation of thermalized H_2^+ ion and fast H_2

Conversion to H_3^+ $H_2^+ + H_2 \rightarrow H_3^+ + H$

Cross section $110 \times \exp(-1.5E^{0.6})$ Å^2

Result Creation of thermalized H_3^+ ion. The low energy H is ignored.

2.4.1.3 Collisions involving H_3^+

Charge transfer $H_3^+ + H_2 \rightarrow H_2 + H + H_2^+$

Cross section 3.45 Å^2 if $E > 15$ eV

2.25 Å^2 if $E > 25$ eV

0.95 Å^2 if $E > 35$ eV

Result Creation of thermalized H_2^+, fast H_2 and H with velocity equal to initial velocity of H_3^+.

Creation of fast H^+ $H_3^+ + H_2 \rightarrow H^+ + H_2 + H_2$

Cross section 0.5 Å^2 if $E > 15$ eV

1.2 Å^2 if $E > 35$ eV

1.45 Å^2 if $E > 45$ eV

1.7 Å^2 if $E > 65$ eV

Result Creation of fast H^+ with velocity equal to the initial velocity of H_3^+, 2 H_2's with remaining energy shared.

2.4.2 Comparison with published data for hydrogen

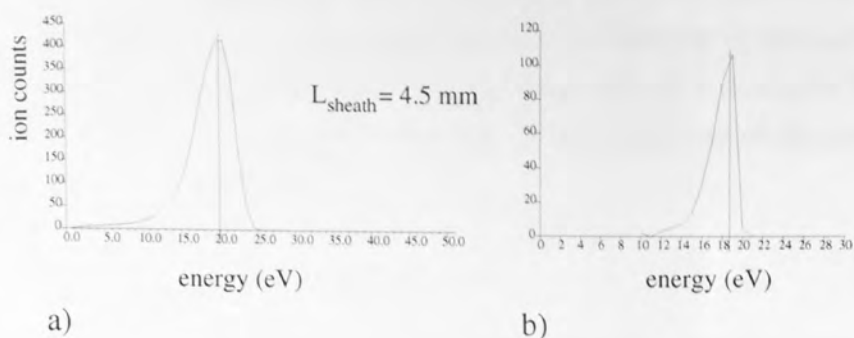

Figure 2.23 Comparison of a) Predicted and b) Experimental results for the IEDs at the anode of hydrogen rf plasma. Pressure = 9 mTorr.

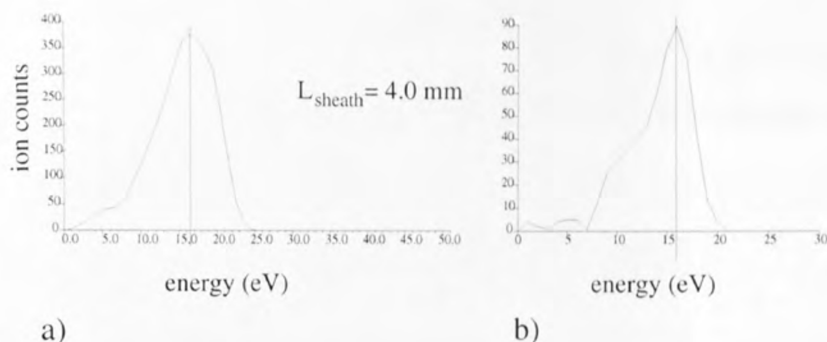

Figure 2.24 Comparison of a) Predicted and b) Experimental results for the IEDs at the anode of argon rf plasma. Pressure = 27 mTorr.

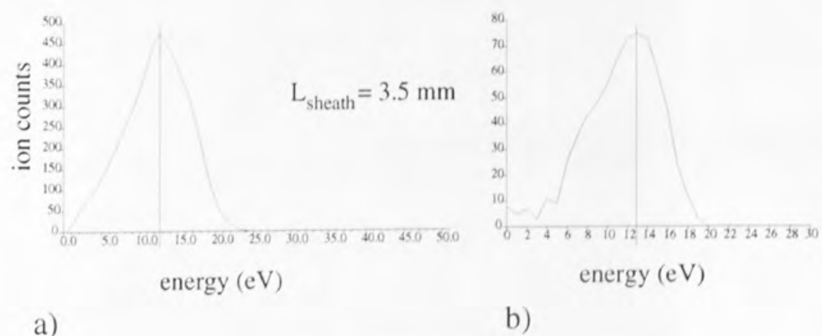

Figure 2.25 Comparison of a) Predicted and b) Experimental results for the IEDs at the anode of argon rf plasma. Pressure = 65 mTorr.

Dickenson [203] has produced mass probe data for a hydrogen plasma at the anode. Unfortunately, his analyser could not discriminate between the different hydrogen ions. His IEDs and the corresponding simulations are shown in figure 2.23, 2.24 and 2.25 for pressures of 9, 27 and 65 mTorr respectively. The simulation IEDs are for H_3^+ ions which are the dominant species from an initial mass distribution of 1:1:1 for H^+, H_2^+:H_3^+.

Though it appears there is a greater energy spread in the predictions, the peak is correctly reduced as the pressure is increased (in the model this is purely by collisional processes). It is also possible that part of the difference could be accounted for by the inclusion of H^+ which has a greater spread in energy due its lighter mass, though it would be difficult to include H^+ and H_2^+ because we have no knowledge of the sensitivity of the probe used with respect to the three ion species.

2.5 Extension to methane fragments

With the inclusion of methane in the mixture, we have the associated reactions of the methane fragments with neutral H_2 as well as the reactions of all particles with neutral CH_4. The cross section used in calculation is given by

$$Q_{mac} = Q_{mic} N_s P_{H_2,CH_4} \qquad \text{eqn 3.18}$$

where Q_{mac} is the macroscopic cross section, Q_{mic} is the microscopic cross section, N_s is the number of particles occupying unit volume at 1 Torr and P_i is the partial pressure of the background gas molecules CH_4 or H_2.

Below are the additional collisions which are taken into account.

2.5.1 Collisions involving H_2^+

The following reactions are taken from Glosik [204].

Creation of CH_3^+	$H_2^+ + CH_4 \rightarrow H_2 + H + CH_3^+$
Cross section	$19.2 \times E^{-0.5}$ Å^2
Result	Creation of thermalized CH_3^+ and fast H_2 with velocity equal to initial velocity of H_2^+.
Creation of CH_5^+	$H_2^+ + CH_4 \rightarrow H_2 + CH_5^+$
Cross section	$13.4 \times E^{-0.5}$ Å^2
Result	Creation of thermalized CH_5^+ and fast H_2 with velocity equal to initial velocity of H_2^+

2.5.2 Collisions involving CH_3^+

The following reactions are taken from Clow [205].

Creation of $C_2H_3^+$ $CH_3^+ + CH_4 \rightarrow C_2H_3^+ + H_2 + H_2$

Cross section $1.36 \times (E/6)^{0.5}$ Å^2 if $E < 6$ eV

$1.36 \times (E/6)^{-0.5}$ Å^2 if $E > 6$ eV

Result Creation of thermalized $C_2H_3^+$.

Creation of $C_2H_5^+$ $CH_3^+ + CH_4 \rightarrow C_2H_5^+ + H_2$

Cross section $23.1 \times (E/6)^{-0.5}$ Å^2 if $E < 6$ eV

$23.1 \times (E/6)^{0.5}$ Å^2 if $E > 6$ eV

Result Creation of thermalized $C_2H_5^+$

2.5.3 Collisions involving CH_4^+

The following reactions are taken from McIver *et al* [206] and Giardini-Guidoni [207].

Creation of CH_3^+ $CH_4^+ + CH_4 \rightarrow CH_4 + H + CH_3^+$

Cross section $3 \times (E/16)^2 \exp(-(E/16)^2)$ Å^2

Result Creation of thermalized CH_3^+ and fast CH_4 with velocity

equal to that of initial velocity of CH_4^+.

Creation of CH_5^+ $CH_4^+ + CH_4 \rightarrow CH_3 + CH_5^+$

Cross section $34.2 \times E^{-0.5}$ Å^2

Result Creation of thermalized CH_5^+ and fast CH_3 with velocity

equal to that of initial velocity of CH_4^+.

This concludes the heavy particle interactions. It is not possible to predict the mass breakdown of the heavy particles crossing the plasma/sheath boundary nor the phase and therefore, the creation of the ions must be modelled. This involves following electrons throughout the plasma and sheath and allowing them to ionise H_2 or CH_4 molecules. The created ion is then followed to the cathode or anode as previously described in order to build up the IEDs and IADs. The modelling of electrons is described below.

2.6 Extension to include ion creation processes

2.6.1 Electron motion and randomization

Electrons are initially given a position randomized between the cathode and the anode. The velocity of the electron is randomized in the same way as that for ions in section 2.1.2 but with the higher electron temperature of 2 eV. The velocity of the electron is not restricted such that v_x is towards the cathode and the electron can wander between the sheaths at either electrode and through the field free plasma. The electron gains energy by the 'wave riding' mechanism discussed in section 1.2.2.6. The time step used in the calculations is much smaller than for the ion case due to the relatively large electron velocities. Due to the large distance (in this case ~10 cm) that the electron travels between the two sheaths, undergoing no acceleration, the time step was made variable, such that the distance travelled in the x direction by the electron in each step was .001 m in the plasma (with an upper limit of 0.1 of a rf cycle) and .0001 m in the sheaths (with an upper limit of .01 of an rf cycle).

The electron will repeatedly travel between each electrode, gaining energy in the sheath and losing energy in inelastic collisions until it gains enough energy at one sheath to overcome the potential hill at one of the electrodes. If this occurs then the electron hits the electrode and is lost.

The electron is allowed to undergo a variety of collisions, elastic scattering from, ionisation and excitation of neutral molecules. Due to the low degree of ionisation, it was assumed that the only molecules available for collisions with electrons are H_2 and CH_4. This also assumes that the breakdown of the background gas is negligible.

In all the following collisions except scattering, the electron retains its original direction of motion with a reduced velocity given by the energy loss indicated for each event.

2.6.2 Scattering

Elastic scattering is the major collision process between electrons and molecules in a gas. The electrons change direction without loss of energy.

The cross section for elastic scattering by a gas molecule was approximated by the formula

$$Q_e = Q_0 E_n \qquad \text{for } E_n < 1 \qquad \text{eqn 3.19}$$

$$Q_e = Q_0 (E_n)^{-Q_1} \qquad \text{for } E_n > 1 \qquad \text{eqn 3.20}$$

where $E_n = E/E_{max}$ where E_{max} is the energy at which the peak of the distribution occurs and Q_0 and Q_1 are constants. This approximation was worked out from data given by

Csanak [208] and Lohmann *et al* [209] and is shown in figure 2.26. This, however, does not give a good approximation at very low energies where the cross section rises sharply below 0.5 eV or so [210].

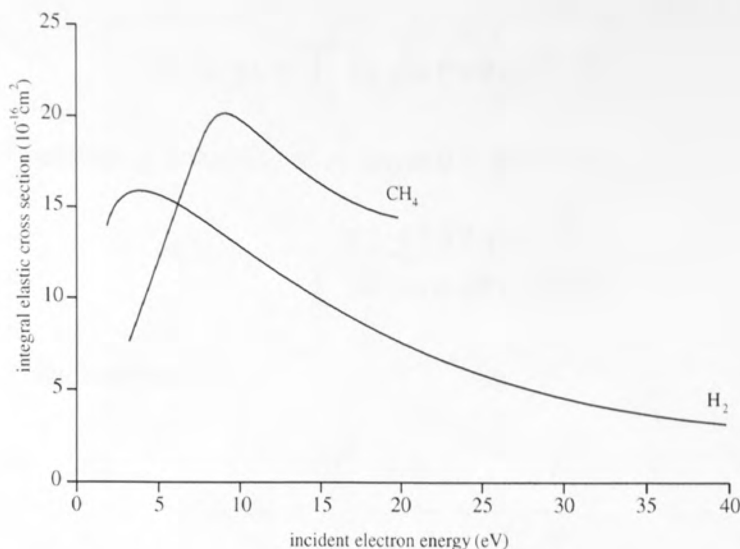

Figure 2.26 Cross section for electron scattering from H_2 and CH_4.

Fitting the data to equations 2.18 and 2.19, then for hydrogen,

E_{max} = 5, Q_0 = 16 and Q_2 = -0.75

and methane,

E_{max} = 8, Q_0 = 20 and Q_2 = -0.4

There is a complex dependence of the differential cross section on the scattering angle which is explained below with reference to figure 2.27.

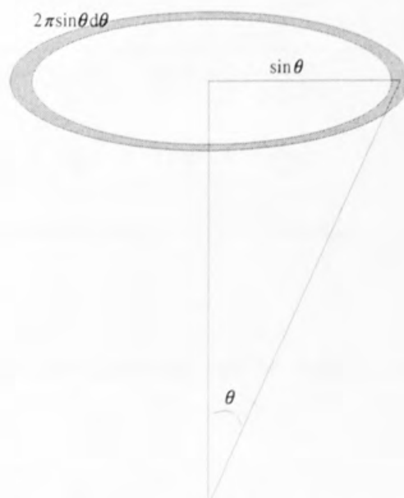

Figure 2.27 The scattering of an electron by an angle $\boldsymbol{\theta}$.

The measured flux of electrons scattered at an angle θ is given by

$$I(E, \theta) = 2\pi \sin\theta \, d\theta \, q(E, \theta) \qquad \text{eqn 3.21}$$

and the total flux is given by

$$I(E, \theta) = \int_0^{\pi} 2\pi \sin\theta \, d\theta \, q(E, \theta) \qquad \text{eqn 3.22}$$

Therefore the probability of scattering at an angle θ is given by

$$P(E, \theta) = \frac{2\pi \sin\theta \, d\theta \, q(E, \theta)}{\int_0^{\pi} 2\pi \sin\theta \, d\theta \, q(E, \theta)} \qquad \text{eqn 3.23}$$

If we now define the function

$$P(E, \theta) = \frac{\int_0^{\theta} \sin\theta \, d\theta \, q(E, \theta)}{\int_0^{\pi} \sin\theta \, d\theta \, q(E, \theta)} \qquad \text{eqn 3.24}$$

this function goes from 0 to 1 as the angle goes from 0 to π and is equal to the probability of the electron scattering between 0 and θ. If we randomize a number between 0 and 1 then the value of θ this corresponds to is the scattering angle.

From the experimental data, the integral in the equation can be found and fitting a polynomial to the function such that

$$\theta = \sum_{i=1}^{4} a_i P^i \qquad \text{eqn 3.25}$$

then

	a_1	a_2	a_3	a_4
for H_2	-3.32	212	-357	309
for CH_4	1.36	117	-252	310

2.6.3 Ionisation

The cross section for ionisation by electrons can be approximated by the following formulas [211]

$$Q(E_n) = Q_{01} \frac{E_n^2}{E_n^2 + 1} \exp\left(-p_1 E_n^2\right) \quad \text{for } 1 < E_n < E_{nmax} \qquad \text{eqn 3.26}$$

$$Q(E_n) = Q_{02}\frac{1}{E_n}\ln(p_2 E_n) \quad \text{for } E_n > E_{nmax} \qquad \text{eqn 3.27}$$

where Q_0 and Q_1 are coefficients, $E_n = E/E_{th}$ where E_{th} is the threshold energy of ionisation and $E_{n,max}$ is the energy at which the maximum in the cross section occurs.

The coefficients used are summarized below.

ion/neutral	E_{th}	Q_{01}	Q_{02}	p_1	p_2
H^+/H_2	17.1	.00226	.086	.00714	.66
H_2^+/H_2	15.4	1.04	3.92	.00478	.599
H^+/CH_4	13.6	.136	.6666	.0021	.4891
H_2^+/CH_4	15.1	.027	.0905	.000102	.5825
CH_3^+/CH_4	14.3	1.367	8.75	.000836	.3914
CH_4^+/CH_4	12.6	1.54	11.5	.000504	.3425

The cross section for production of CH_2^+, CH^+ and C^+ are considerably lower and are not included. The energy of the ionisation is subtracted from the energy of the incident electron. The remaining energy is then shared between the primary electron and the electron newly created, the parameters of which are stored in an array.

When the original electron is lost, any ionisation electrons it has created are followed in the same way starting from the position at which they are created. Any subsequent electrons created are also stored and have their trajectories followed until all electrons resulting from one initial electron are lost. The program then moves to the second initial thermal electron at a random position between the electrodes.

2.6.4 Excitation

For simple molecules, the interaction of electronic, vibrational and rotational excitations is extremely complicated. The three kinds of motion are so different, however, that they can be treated as separate reaction channels [212].

2.6.4.1 Electronic

Collisions which raise an electron in an atom from one bound state to a higher energy bound state are known as electronic excitations and these are a major energy loss mechanism for electrons travelling through a gas.

Electronic excitation of H_2 [213]

Cross section	$(E/11)^{-0.3}$ Å^2	if E > 11 eV

Below 100 eV, this cross section represents the sum of the six lowest electronic states and above 100 eV this represents the estimated sum of all electronic excitation cross sections. The average energy loss per collision is given as 10 eV which approximates to the average of the lowest six transitions.

Electronic excitation of CH_4

Cross section	0.7 x ((E-10)/5) Å^2	if E > 10 eV

0.7 x $(E/15)^{-1}$ Å^2 if E > 15 eV

The cross section was computed by Winstead *et al* [214] and agrees well with summed experimental data from Vuskovic [215] representing energy losses of 7.5 to 10.5 eV. The energy loss due to the excitation is taken as 9 eV.

2.6.4.2 Vibrational

Typically, rotational levels are spaced several meV apart and vibrational levels are separated by 0.1 eV or so, however, though the loss per collision is small, the large cross sections at low energies can make their effect significant.

Vibrational excitation of H_2

Cross section	(0.3 x E) - 0.2 Å^2	if E >1 eV
	(-.086 x E) + 0.96 Å^2	if E >3 eV
	0 Å^2	if E > 10 eV

This results in an energy loss of 0.1 eV.

Vibrational excitation of CH_4

Cross section	1.4 x (E/8) Å^2	if E > 1.5 eV
	1.4 x $(E/8)^{-1.5}$ Å^2	if E > 3 eV

This cross section was taken from Shyn [216] who measured differential cross sections significantly higher than the extensive measurements made by Tanaka [217]. The results of measurements made my Mapstone *et al* [218] more recently, agree substantially with those

of Shyn. The measurements are of the $\upsilon_{2,4}$ and the $\upsilon_{1,3}$ vibration modes, representing energies of approximately 177 meV and 368 meV respectively. The energy lost by the electron is taken to be the average *ie.* 0.3 eV.

2.6.4.3 Rotational

The rotational cross section is taken from Trajmar [219] and results in the electron losing 15 meV, a value which is uniquely large for hydrogen. For methane, rotational excitation is ignored due to a lack of data.

Rotational excitation

Cross section	$(0.68 \times E) - 0.036$ Å^2	if $E > 0.1$ eV
	$(-.143 \times E) + 2.43$ Å^2	if $E > 3$ eV
	0 Å^2	if $E > 10$ eV

2.6.5 Electron recombinations

Another way for electrons to be lost other than by collisions with the walls is by electron ion recombination. Assuming the major ionic species within the plasma is H_3^+, then we can estimate the cross section from data for the dissociative recombination of H_3^+.

Dissociative recombination	$e + H_3^+ \rightarrow H_2^+ + H^-$
Cross section	$(10/E)$ Å^2

The cross section increases rapidly as the energy falls from 1 eV to about .001 eV from 10 Å^2 to 100 Å^2 or so and there is a large discrepancy between the published data of more than an order of magnitude [220][221][222][223]. Above 1 eV, the cross section is approximately 2×10^{-22} Å^2 and is considered negligible [224]. The fit used is a compromise between these data sets. An added uncertainty is the number density of ions in the plasma required to give the macroscopic cross section for the reaction. This number is estimated as 10^{-5} of the neutral gas pressure.

2.6.6 Electron induced secondary electrons

In their particle simulations, Surendra and Graves [225] use a fixed value of 0.25 [226] for the probability of an electron being reflected from the electrodes. More recently, however, the secondary electron emission by electron impact coefficient δ has been calculated by Ordonez [227] for a variety of surfaces. All the relationships calculated have δ rise almost in proportion with the electron temperature. *ie.* at 100 eV, carbon has a δ value of 0.8 - 1 whereas aluminium has a value of 1.7 and silicon 1.5. In an experiment, the surface will

be quartz and aluminium covered with a layer of carbon. The energy dependence of δ used reflects this and is given as δ = E/120. The electrons are reflected without loss of energy and with only the velocity vector v_x reversed.

2.6.7 Ionisations used as source of ions

At an ionization event when an electron ion pair is created, the ion is taken and has its trajectory followed until it leaves the plasma and is accelerated by the sheath at either the anode or the cathode. The ion has variable time steps such that the x distance travelled is equal to 1 mm in the plasma with a maximum time step of 0.5 of an rf cycle and .1 mm in the sheath, with a maximum time step of .01 of an rf cycle. The ion is discarded if the simulation time exceeds 2000 rf cycles.

2.6.8 Ion induced secondary electrons

When ions impinge on a surface, there is a probability that an electron will be ejected. In radio frequency discharges this probability is dependent on the contributions of ions, fast neutrals, metastables and photons impinging on the electrode as well as the properties of the electrode. Measurements by Bohm and Perrin [228] have shown this global emission coefficient to be up to 10 times larger than simply ion induced electron emission. Values in the range of 0.1 to 1 have been found for aluminium, silicon, steel and copper, being at the high end of the range when the contribution of metastables is important. In this study, the value of 0.3 was taken, being similar to the values found for low pressure hydrogen plasmas at similar driving potential. The electron is ejected with a low (thermal) energy and is quickly accelerated by the field into the plasma.

2.6.9 Electron cascades

The initial electrons, usually 50 in number, are created at a random phase within the first cycle of the simulation. Some are lost to the walls or recombinations, but some create secondary electrons which themselves can be lost or create further electrons in a cascade. The condition required for a stable plasma is that for each electron lost, one electron is created and therefore each electron produces on average one electron before being lost. In the real device, this condition is provided by the feedback inherent in the system. For example, the ability of electrons to escape from the plasma is partly given by the plasma potential. A decrease of electrons in the plasma will cause the plasma potential to increase, thereby increasing the potential barrier to the electrons, increasing free electron residence time and therefore increasing the average ionization per electron. In the program, electron cascades are created and sometimes fizzle out. If the average production per electron is less than 1, the floating potential can be increased. If the cascade tends to 'runaway' the floating potential can be decreased to bring the average electron production back to unity. The simulation is halted after 2000 cycles, by which

time ideally there would be the same number of electrons as were initially created, however, the simulation has either already run out of electrons or there are some electrons left. 2000 cycles is considered a long enough time to get the average production of electrons close to unity, taking into account the statistical nature of the process.

2.6.10 Data output

The angle and energy distributions for all species arriving at the cathode and anode are saved as CSV files. Extra information saved is detailed below.

2.6.10.1 Text file

With each simulation is output a data file in the following form.

1 pressure = 0.040000
2 Lcfmax = 0.010000
3 Vf = 12.000000
4 Vdc = 90.000000
5 Vo = 100.000000
6 No electrons = 50

At the cathode
7 H1ions 2 (5.128205) H2ions 12 (30.769231) H3ions 13 (33.333333)
8 CH3ions 3 (7.692308) CH4ions 7 (17.948718) CH5ions 2 (5.128205)
9 C2H3ions 0 (0.000000) C2H5ions 0 (0.000000)

10 eH1ions 80.220321 eH2ions 50.976482 eH3ions 97.094130
11 eCH3ions 91.825229 eCH4ions 98.394172 eCH5ions 80.550148
12 eC2H3ions 0 eC2H5ions 0

13 H2neuts 30 (76.923077) CH4neuts 8 (20.512821)
14 eH2neuts 18.784583 eCH4neuts 4.318801

15 neuts/ions 0.974359

At the anode
16 H1ionsa 1 (3.571429) H2ionsa 4 (14.285714) H3ionsa 13 (46.428571)
17 CH3ionsa 1 (3.571429) CH4ionsa 6 (21.428571) CH5ionsa 1 (3.571429)
18 C2H3ionsa 0 (0.000000) C2H5ionsa 2 (0.051282)

19 eH1ionsa 12.049685 eH2ionsa 6.873819 eH3ionsa 10.149472
20 eCH3ionsa 11.748561 eCH4ionsa 10.474377 eCH5ionsa 10.804816

21 eC2H3ionsa 0 eC2H5ionsa 0.175227

22 ionisation ratio 1.340000
23 elecperelecall 0.595420

24 ionisations 67
25 ions at cathode 39
26 ions at anode 28
27 ions unaccounted 0

28 electrons at cathode 74
29 electrons at anode 49
30 electrons too long 6
31 electron recombinations 1

Lines 1-6 give some of the basic data of the discharge plus the number of initial electrons considered.

Lines 7-9 give the number (and percentage of the total flux) of each different ion species to the cathode and lines 10-12 give the average particle energies.

Line 13 gives the neutral fluxes and line 14, their average particle energies.

Line 15 gives the ratio of neutrals to ions at the cathode (neutrals which have minimum 1 eV energy).

Lines 16-21 give the fluxes and energies of ions at the anode.

Line 22 is the number of ions created divided by the number of initial electrons.

Line 23 is the average number of electrons created by each electron before it is lost to the walls or a recombination event.

Line 24 is the total number of ionisations, broken down into the number arriving at the cathode (line 25), the anode (line 26) and the number who exceed the maximum time (line 27).

Line 28 and 29 give the number of electrodes arriving at the cathode and anode respectively and lines 30 and 31 give the number of electrons which exceed the simulation time and the number lost in recombinations respectively.

2.6.10.2 Energy and angle distributions

The angle and energy distributions for all species arriving at the cathode and anode are saved as CSV files

2.6.10.3 EEDF

In order to extract the electron energy distribution function (EEDF) from the simulation, each time an electron crosses a position midway between the electrodes, it has its energy and angle added to an array to give $F(\varepsilon,\alpha)$ which on integrating between 0 and π gives $F(\varepsilon)$.

2.6.10.4 Ionisation and excitation profiles

The ionisation and excitation profiles are stored as CSV files by counting the ionisations and excitations as a function of position between the electrodes.

2.6.10.5 Number density profile of electrons and ions

At each time step, the position of the electron or ion is added to an array to create the electron and ion density profile. The contribution the particle makes to the profile is in proportion to the time step (*ie.* the time it has spent at that position).

Chapter 3. Plasma Surface Interaction

3.1 Hyperchem

As has been discussed previously, many body simulations are computationally expensive, so it would be preferable to model the particle surface interactions as binary collisions using codes such as TRIM [229]. These codes have problems associated with the validity of the binary collision approximation at low energies and also in this case have the additional problem of attempting to model polyatomic methane fragments as single nuclei. At high energies it is likely that the methane fragments will dissociate at the surface due to the carbon-hydrogen bond energy being small in comparison to the interaction energy (100's of eV), and the impact resembles the normal binary collision of a carbon ion with the surface. To investigate this the Hyperchem code was used in a quantum mechanical treatment described below.

3.1.1 The simulation

Using Hyperchem, an attempt was made to model the interaction of a methane molecule with a unit of GaAs for a range of energies. Due to the limited computing power available and the fact that the computation time increases as n^2 where n is the number of particles involved in the simulation, it was necessary to use the smallest number of particles possible, while still adequately representing a collision with a GaAs lattice. The number of particles used was 18 and fixing the positions of atoms within this cluster was deemed unrealistic for such a small number of atoms. The GaAs structure is of the Zincblende type, with each Ga atom being tetrahedrally connected to four As atoms and vice versa as shown in figure 3.1 for an arrangement of 9 Ga and 9 As atoms. Figure 3.2 shows the same arrangement from a different perspective and figure 3.3 shows the structure with the atoms represented as spheres with a molecule of methane also shown to scale for comparison. One disadvantage of this method was that the non-fixing of the coordinates of atoms in the GaAs cluster allowed it to recoil somewhat, whereas in reality the energy would be transferred further into the lattice or back to the incident methane molecule.

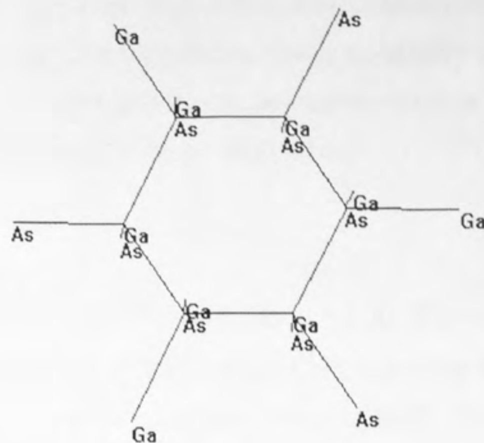

Figure 3.1 9 Ga and 9 As atoms in a stable arrangement

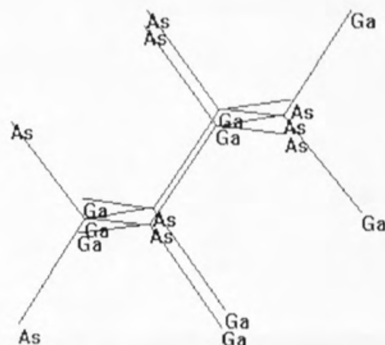

Figure 3.2 The arrangement in figure 3.1 from a different perspective

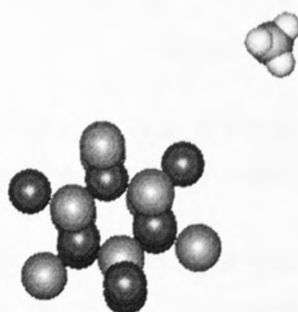

Figure 3.3 Comparison of GaAs and methane molecule

The simulation involved taking the GaAs structure and striking it with the methane molecule at a large number of orientations both of incident and target and averaging the results for each interaction energy, using the quantum mechanical PM3+ electron wavefunction determination method.

The quantum mechanical method predicts when dissociations occur, but does not register them as such. In order to interpret the results, it was necessary to output from the program the positions of the four hydrogen atoms and the carbon atom at the end of the simulation. From this the extent of dissociation can be worked out.

3.1.2 Result

The equilibrium bond length of C-H in methane is 1.1 Å. The simulations finish after a predetermined length of time and if the distance C-H is greater than some designated distance, then the C-H bond is deemed to have been broken. The extent of this distance x_{sep} is such that it can effectively be regarded as infinite without unduly lengthening the simulation time. A more rigorous approach would calculate the relative kinetic energy of the particles and add this to the mutual potential energy and assume the bond is broken if $E_{tot} > 0$. Figure 3.4 shows the proportion of the four hydrogen bonds which exceed a certain length at the simulation end as a function of the impact energy of the methane molecule.

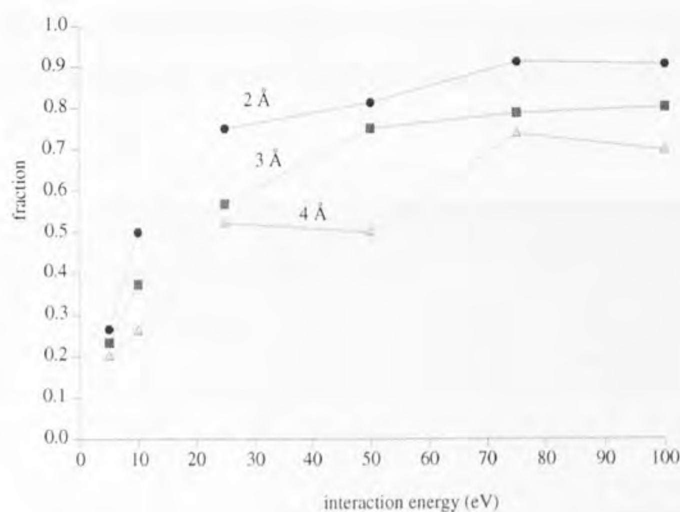

Figure 3.4 Average fraction of C-H bonds exceeding certain lengths at the simulation end as a function of interaction energy

A separation of 4 Å is a definite dissociation, but ignores some bonds with lower final separations which would dissociate with an increased simulation time. The true fractional dissociation can be estimated from the envelope given by the three curves above. It can be seen that at energies of 100 eV and above, the methane molecule is on average 75 % dissociated (*ie.* is a CH). The assumption of total dissociation is therefore only partially true at these energies, though the point is illustrated.

3.2 Sputter yield

By finding the sputter yield and calculating the flux of particles incident on the sample

surface, it should be possible to predict the etch rate based upon physical sputtering alone. An estimate is therefore needed for the sputter yield of a carbon atom on GaAs and various predictions for this value are discussed below.

Zalm (equations1.45 and 1.46) predicts a sputter yield of 1.65 GaAs molecules per incident argon ion at 1000 eV and 1 GaAs molecule per incident argon ion at 500 eV. From his theory, the sputter yield from carbon is 10 % less. Smith (equation 1.47) predicts a sputter yield at 1000 eV of 0.7 molecules and 0.3 molecules at 500 eV. The predicted yield for carbon is some 50 % less than that from argon. From his low energy approximation, Matsunami gives a yield of 1.2 molecules from 1000 eV argon, 0.7 molecules at 500 eV and 0.2 molecules at 100 eV.

The TRIM code gives sputter yields as shown (in terms of atoms/ion) in figure 3.5 for carbon bombardment. The yield of Ga and As is almost the same (the binding energy used is the average of the sublimation energies). For comparison, the prediction from SUSPRE is shown. The results from SUSPRE show the total number of atoms sputtered per ion whereas the results from TRIM show the number of each atom type per incident ion. The sputter yield predicted from TRIM is therefore much greater than that from SUSPRE. Both codes predict the sputtering yield from hydrogen to be negligible.

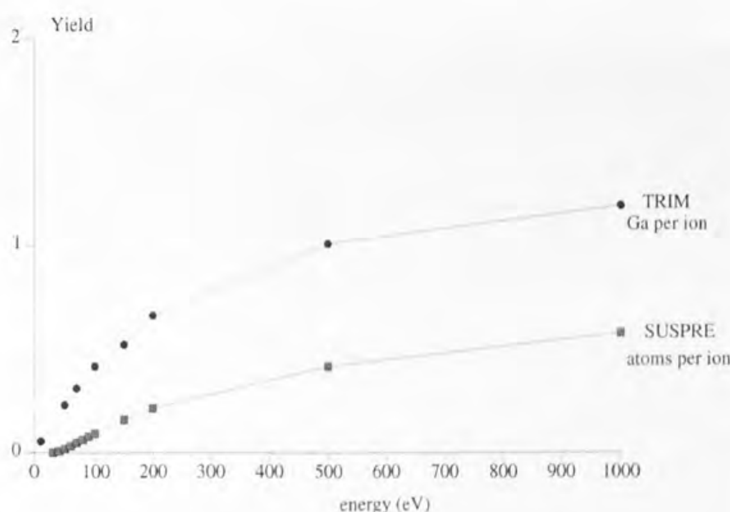

Figure 3.5 Comparison of sputter yields predicted for C into GaAs from the codes TRIM and SUSPRE

The sputter yield is a strong function of the binding energy as shown for the TRIM simulation in figure 3.6. The results from TRIM are therefore subject to errors in the estimation of the surface binding energy. The binding energy in TRIM is estimated from the average sublimation energy of Ga and As of 2.72 eV. Malherbe [230], however, recommends a surface binding energy of 6.72 eV per molecule or 3.36 eV per atom.

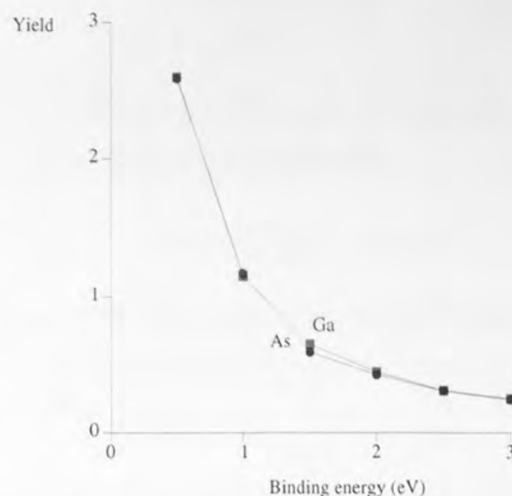

Figure 3.6 Sputter yield as a function of the binding energy for 100 eV C onto GaAs

As a function of incident ion mass, TRIM gives the yield in atoms per incident ion for Ar, Ne and C as 1.77, 1.53 and 0.97 respectively at an incident energy of 500 eV when using 3.36 eV as the binding energy.

Some experimental values of the sputter yield of GaAs summarised in the review paper by Malherbe are as follows

Ion	Energy (eV)	Sputter yield (molecules per ion)
Ar	50	0.011 - 0.015
	200	0.25 - 0.61
	500	0.2 - 1
	1000	1 - 1.5
Ne	500	0.1

The low value of 0.1 found with neon was in the same study that found a value for argon of 0.83 at 500 eV [231]. It seems reasonable, therefore, that at 500 eV, the value of 0.7 molecules of GaAs given by Matsunami is a good estimate for argon, this figure being somewhere in the middle of the experimental data. If the yields for carbon and neon are taken from this value, scaled by the amount inferred by TRIM then at 500 eV, an estimate for neon of 0.6 molecules and for carbon, 0.4 molecules per ion is arrived at. The estimate for neon is considerably higher than the experimental results, however.

3.2.1 Etch rate

To estimate the physical etch rate, the flux must be estimated. At 150 W, over 400 cm^2 of cathode, with a bias voltage of 400 V, the current is

$$6 \times 10^{-4} \times eff \text{ A cm}^{-2} \qquad \text{eqn 3.1}$$

where *eff* is the efficiency of the discharge (proportion of total energy given to bombarding ions). Assuming the efficiency of the discharge is 20 % [232] then the current density is given by 1.2 x 10^{-4} A cm^{-2}.

Alternatively, using the Child-Langmuir law, the sheath width can be written as follows

$$S = 0.793\, \varepsilon_0^{1/2} \, (e/M)^{1/4} \, V_{dc}^{3/4} J_i^{-1/2} \qquad \text{eqn 3.2}$$

where S is the sheath width, M is the ion mass, e is the ion charge and J_i is the current density to an rf electrode [233], then

$$J_i^{1/2} = \frac{0.793}{S} \varepsilon_0^{1/2} \, (e/M)^{1/4} \, V_{dc}^{3/4} \qquad \text{eqn 3.3}$$

which for a D.C. bias of 400 V and a sheath width of 2 cm yields a value for the current density at the cathode of between 0.4 and 1.6 x 10^{-4} A cm^{-2} (assuming the average ion mass is between the extremes of 16 amu and 2 amu respectively) which is in agreement with the previous estimate.

Using a current density of 1.2 x 10^{-4} A cm^{-2}, this gives the number of ions bombarding the surface per second (flux density) as 7.5 x 10^{14} cm^{-2}. For the density of GaAs, ρ= 5.8 g cm^{-3}, there are 5 x 10^{22} atoms per cubic centimetre. Hence, the etch rate

$$er = Y\,(atoms\ per\ ion) \times flux\ density / 5 \times 10^{22} \qquad \text{eqn 3.4}$$

is equal to 1.8 x 10^{-8} cm s^{-1} = 0.18 nms^{-1} for a 150 W neon plasma. Substituting the yield for carbon and the change in flux due to the change in average ion mass gives predictions for etch rates as a function of methane concentration, when the methane partial flux is known from the modelling. The values obtained are what is expected for purely physical etching of GaAs and when compared with the real value of the etch rate, will give some idea of the relative importance of physical and chemical removal of the substrate.

3.3 Damage

3.3.1 Penetration depth

The penetration depth of ions into the substrate can be estimated from the binary codes SUSPRE and TRIM, both of which give similar results as shown in figure 3.7. At

energies up to 500 eV, the carbon atoms only penetrate an average of 20 Å, equivalent to 8 atomic layers or so. At the lower energies, these codes are expected to underestimate the true penetration depth due to effects such as channelling and the effect of the discrete nature of atoms in the lattice which are not accounted for in the SUSPRE and TRIM codes. Preliminary work with MARLOWE which accounts for the crystal nature of the target, however, gives similar penetration depths [234].

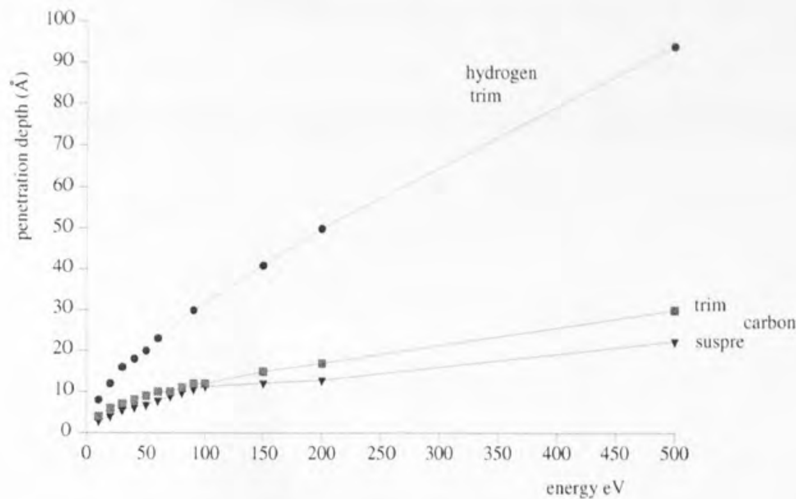

Figure 3.7 Average penetration depth of hydrogen and carbon into GaAs

3.3.2 Depth of damage

The penetration depth profile of ion species impingent on a sample surface is not a true reflection of the damage depth profile, given that on arrival at a certain depth, an ion requires a non-zero amount of energy in order to cause damage, be it via vacancy creation, displacement or replacement. In order to create a displacement approximately 15 eV is required for semiconductors. This results in a vacancy if the incoming atom has sufficient energy after the collision. The depth distribution of vacancies and displacements is shown if figures 3.8 and 3.9 to be essentially the same function for a 200 eV carbon atom. The depth of the damaged layer is an important parameter which is equivalent to the depth from which particles can be removed, whether via diffusion, segregation or physical impact.

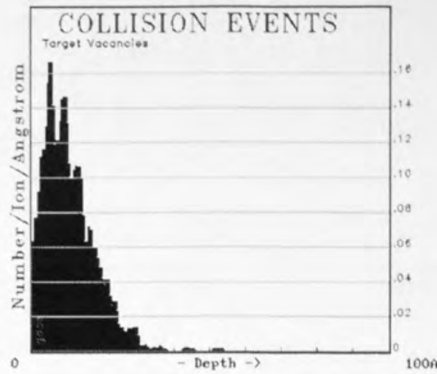

Figure 3.8 Depth profile of target vacancies in GaAs due to 200 eV carbon atom

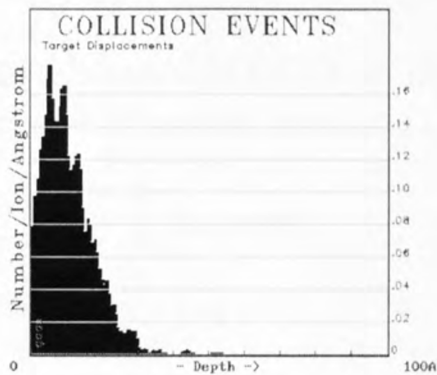

Figure 3.9 Depth profile of target displacements in GaAs due to 200 eV carbon atom

3.3.3 Depth of damage in equilibrium

The above simulations showed the depth of damage created by a finite number of particles impacting upon a GaAs surface whose surface is stationary. This does not reflect the true depth of damage, due to the action of sputtering which clears up and limits the depth of damage by etching away the surface. Over long periods of time, a constant damaged layer will be established, the extent of which depends on the etch rate, the damage rate and the damage depth profile. Simplifying the damage depth profile as $f(x)$ where

$$\int_0^\infty f(x)\, dx = 1 \qquad \text{eqn 3.5}$$

as in figure 3.10 the parameter of interest is the damage at point x below the surface as the surface recedes.

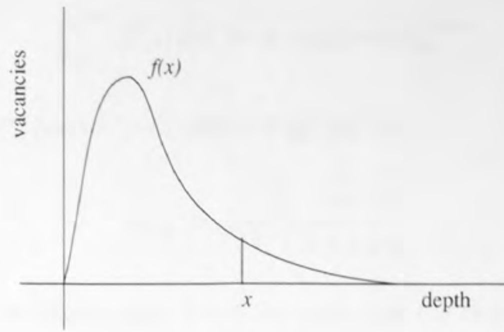

Figure 3.10 The vacancy creation function f(x)

The number of vacancies per m² produced at depth x in time dt is given by

$$n = f(x)\,\phi\,v\,dt \qquad \text{eqn 3.6}$$

where v is the number of vacancies created per ion and ϕ is the particle flux in ions per m² per second. Therefore, the number of vacancies produced at x by time t is given by

$$\int_0^t f(x)\,\phi\,v\,dt \qquad \text{eqn 3.7}$$

and as $dx = -r\,dt$ where r is the etch rate, then

$$n = -\int_\infty^x f(x)\,\phi\,v\,dx\,/\,r \qquad \text{eqn 3.8}$$

Now, $r = Y s \phi/a$ where Y = sputter rate (atoms/ion)

s = atomic layer separation

a = atoms per square metre

Therefore,

$$n = -\frac{v\,a}{s\,Y}\int_\infty^x f(x)\,dx \qquad \text{eqn 3.9}$$

or the fraction of atoms vacant in the layer is given by

$$N_f = -\frac{v}{s\,Y}\int_\infty^x f(x)\,dx \qquad \text{eqn 3.10}$$

So for some slightly disordered layer where $N_f = 0.1$

$$-0.1\frac{s\,Y}{v} = \int_\infty^{x_{10\%}} f(x)\,dx \qquad \text{eqn 3.11}$$

If $f(x) = 1/\lambda \exp[-x/\lambda]$ where λ is some parameter describing the characteristic depths to which defects are created [235] then

$$\int_{\infty}^{x_{10\%}} f(x)\,dx = -\exp[-x/\lambda]_{\infty}^{x_{10\%}} \qquad \text{eqn 3.12}$$

and the depth to which we get 10 % disorder is given by

$$x_{10\%} = \lambda \ln\left[\frac{\nu}{0.1\, s\, Y}\right] \qquad \text{eqn 3.13}$$

In the absence of diffusion of damage, it can be seen that the depth of the damaged layer is given by the characteristic depth of the damage λ and the ratio ν/Y. The function λ increases with the velocity of the incoming particle *ie.* $E^{1/2}$. The dependence of ν/Y on the energy can be found from TRIM and shows there is a moderate increase in $\ln\left[\frac{\nu}{0.1\, s\, Y}\right]$ over the energy range 0 to 500 eV.

The implication is that as the energy increases, the depth of damage increases as a strong function of the incident ion energy. It is from this layer that we expect diffusion and segregation effects. It is likely therefore, that at high energies diffusion and segregation dominate, whereas at lower energies preferential sputtering of the segregated layer dominates. This leads to the result that the segregating species (As) is depleted but enriched at the extreme surface for high energies [236] but depleted throughout the layer at the lower energies encountered in RIE [237].

3.4 The crystal structure of GaAs

3.4.1 The GaAs structure

From the discussion in section 1.4.5, it can be seen there is no consensus on either the absolute or the relative surface binding energies of Ga and As in a GaAs lattice. The crystalline nature of GaAs invalidates the assumptions used when trying to find the surface binding energy from the heat of sublimation or the surface energy from the surface tension of the pure elements. Malherbe's model [238] was established for metals and oxides which are generally ionic compounds. Gallium appears more metallic than arsenic, though GaAs bonding is essentially covalent with little ionic characteristics, making the pair bond model more theoretically accurate. Study of the explicit crystal structure of GaAs should, however, be more accurate still [239].

The following discussion attempts to do this in order to investigate the true bonding of Ga and As and to investigate how the surface configuration contributes to preferential As sputtering.

3.4.2 Surface binding energy and preferential sputtering

Feng et al [240] used quantum mechanical simulations to find the binding energies of small GaAs clusters (*ie.* Ga_nAs_m). The following shows some of their results in terms of the total binding energy and the binding energy per atom.

energy of Ga_2As_2 = 14.4 eV per atom = 3.6 eV

energy of Ga_2As_1 = 8.25 eV per atom = 2.75 eV

energy of Ga_1As_2 = 10.47 eV per atom = 3.49 eV

energy of Ga_3As_1 = 13.76 eV per atom = 3.44 eV

energy of Ga_1As_3 = 15.36 eV per atom = 3.84 eV

Although only a crude approximation to a lattice, the implication is that As is bound to the clusters with an energy of 4.89 $\rightarrow$ 6.15 eV whereas Ga is bound with 3.93 $\rightarrow$ 5.51 eV. This gives a ratio of the surface binding energies U_{As}/U_{Ga} of around 1.6 for Ga_2As_2 to Ga_1As_2 or Ga_2As_1. Therefore we should expect greater sputtering of Ga and the lower sublimation energy of As cannot explain preferential As sputtering which is better described by using segregation and diffusion effects.

3.4.3 The (100) surface and relaxation

As for the surface binding energy calculations, it appears inaccurate to use the surface energy derived from the elemental form of Ga and As to predict the surface energy for each of the species in a GaAs lattice. Much work has been performed, however, on both the experimental and theoretical aspects of GaAs surface relaxation and reconstruction and the following describes how the behaviour of the GaAs surface can explain the increased sputtering of As in terms of the lattice.

Quantum mechanical calculations made by Feng et al [241] for the (110) surface and by Qian et al [242] for the (100) surface of GaAs predict the relative movements of Ga and As atoms within the surface.

Figure 3.12 shows how the normal structure of GaAs deforms when it is forced to make up the (110) surface. The As forces itself out of the surface and the Ga sinks into the lattice. This leaves the As more susceptible to being sputtered. The effect with the (100) surface is even more extreme as shown in figure 3.13. a) shows the original surface from above and b) shows how the Ga relaxes into the As layer. c) shows the behaviour of the surface As resulting from the surface shown in a) with Ga and As reversed.

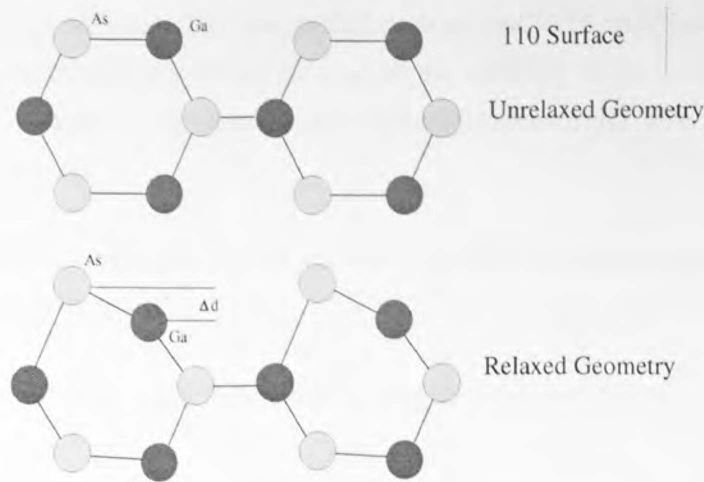

Figure 3.12 Relaxation of the (110) surface of GaAs

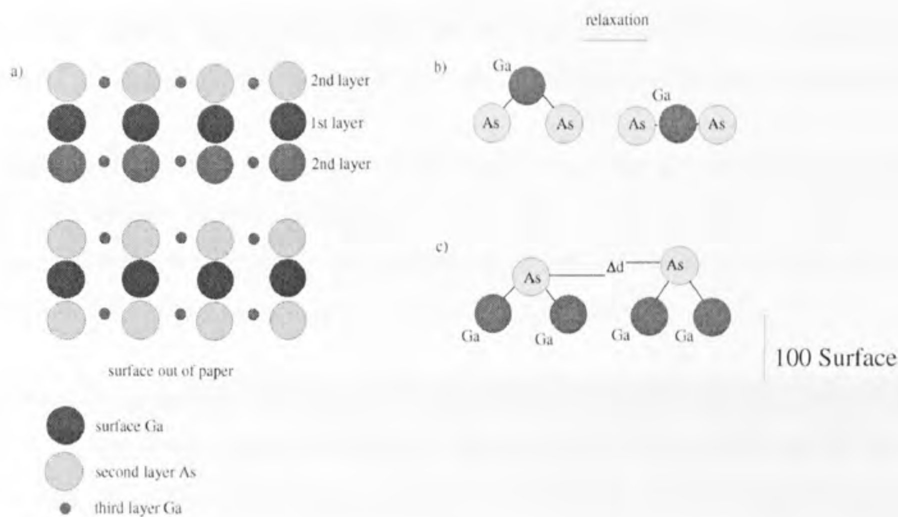

Figure 3.13 Relaxation of the (100) surface of GaAs

Initially the surface will resemble a (100) surface but after bombardment and the segregation and sputtering effects mentioned above, it will begin to resemble something between polycrystalline and amorphous and the As will rise above the surface in order to minimise the free energy as described. It is also energetically favourable for arsenic to move to the surface from the bulk as shown by Qian *et al* [243]. This is an energy minimising surface effect and explains how arsenic preferentially occupies surface positions whilst taking account of the lattice structure. This phenomenon causes enrichment of arsenic in the first layer which leads to preferential arsenic sputtering, aspects of which for the simple case of the surface are outlined below.

3.4.4 Preferential sputtering

The phenomena of the As atoms rising out of the surface and the Ga collapsing into the plane of the (100) GaAs surface has the possible effect of increasing the sputtering of arsenic by two mechanisms, each of which will be discussed in turn for the simplified case

of a plane crystalline surface. This assumption is accepted to be only partially true after sufficient surface bombardment but in the case of the inability to study the real scenario, the oversimplified version is still expected to reveal some insights. The two mechanisms studied are as follows...

1) increased probability of direct recoils where the surface arsenic atom which is struck is the atom which is sputtered

2) increased probability of a cascade releasing a surface arsenic atom

3.4.4.1 Direct knock-on

It is obvious that the probability of sputtering of a raised arsenic atom is increased from the value of an atom in the plane of the surface. This increase is due to the possibility of it being glancingly struck and recoiling from the surface with sufficient energy to break its surface bonds. This probability is in addition to all other possible sputtering mechanisms.

This was modelled by a two part simulation which calculates the energy and angle distribution of a surface arsenic atom immediately after being struck by a carbon atom and proceeds to follow the trajectory of the arsenic atom and its interaction with the surface. It is assumed that the carbon atoms strike the surface normally.

On being struck by a carbon atom (using the screened coulomb potential described in section 2.2.3.2), the arsenic atom recoils in a direction which is a function of the impact parameter. The majority of scattering angles for the arsenic will be large because most collisions from the incident particle's point of view are glancing.

In order to find the probability of scattering in a certain direction, it is necessary to plot $p = f(\theta)$ where p is the impact parameter. A plot of $p^2 = f(\theta)$, normalized, gives the scattering angle as a function of the probability of scattering at an angle between 0 and θ.

The final energies of the carbon and the arsenic atoms are plotted in figure 3.14 with the total as a consistency check for an initial energy of 1000 eV. It can be seen that at the high scattering angles, the energy of the arsenic atom is low. There is therefore a trade-off between the scattered arsenic atom having a large angle making it likely to leave the surface, and having a high energy making it likely to break its surface bonds. If the scattering angle is low, the probability of the arsenic atom leaving the surface becomes very small because the similarity in the masses of gallium and arsenic means that most of the energy of the arsenic will be lost to atom(s) in the direction of scatter.

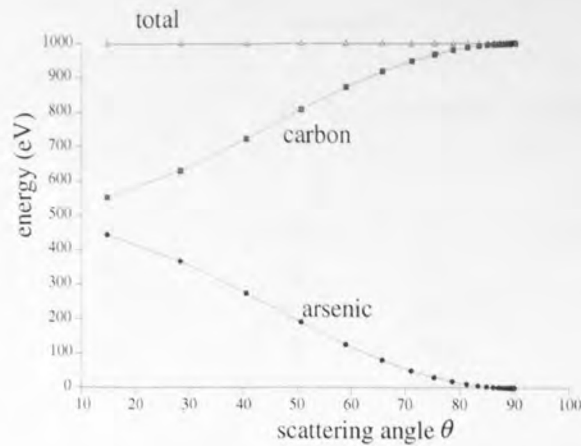

Figure 3.14 The energies of incident carbon atom and scattered arsenic atom as a function of angle for initial energy of 1000 eV

The true probability of the arsenic leaving the surface when scattered with a specific angle and energy depends on the specific arrangement of neighbouring atoms from which the arsenic subsequently scatters. It can, however, be estimated by use of the TRIM code which predicts backscatters when the particle which initially hits the surface returns with an energy greater than the surface binding energy. After finding the dependence of the angle and energy of the arsenic atom as a function of the energy and impact parameter of the carbon atom, these can be used as inputs to the TRIM code where the arsenic is subsequently followed in its interaction with the surface.

The probability of the atom backscattering (*ie.* being sputtered from the surface) is predicted to increase with energy and angle. To combine the two to find the probability of an As sputtering from a surface after being struck by a carbon atom it is necessary to randomize the collisions of carbon atoms with arsenic and use the results as input parameters to TRIM.

Below is a table of various initial energies of carbon atoms and numbers between 0 and 1 which represent the randomization of the impact parameter (with the probability of the impact parameter being between 0 and r proportional $\sqrt{r}$) up to 5 Å. The scattering angle of the arsenic, its energy and from TRIM, the probability of escape are in subsequent columns. Only numbers corresponding to scattering above the minimum energy of 3 eV necessary to break the surface bond are shown.

Carbon		Arsenic		
RND	θ	E	prob	**cross section**
1000eV				
0.1	50	191	0.2	14 Å^2
0.2	66	80	0.4	
0.3	71	50	0.5	
0.4	78	18	0.35	
0.5	81	11	0.3	
300eV				
0.1	49	61	0.2	9.5 Å^2
0.2	61	33	0.36	
0.3	70	16	0.3	
0.4	74	10	0.25	
0.5	79	4.5	0.1	
100eV				
0.1	48	21.2	0.15	4 Å^2
0.2	57.8	13.5	0.2	
0.3	66.3	7.7	0.15	
0.4	73	4	0.05	
30eV				
0.1	45.6	7	0.03	0.3 Å^2
0.2	57.6	4	0.02	

It can be seen that for a carbon atom of 1000 eV, half of the interactions within 5 Å result in an average sputter probability of about 0.35 whereas at 100 eV only 4 out of 10 of the interactions result in a scattering above threshold energy but with an average sputter probability of only 0.1375. For a carbon atom with incident energy of only 30 eV, the probability of a direct recoil leaving the surface is almost zero. The above simple analysis leads to an effective cross section for scattering by this method which is shown in the final column. For the higher energies, these are significant cross sections in comparison with the actual atomic cross sections at the surface of 7 Å^2.

In conclusion, exposed surface atoms are directly sputtered with a cross section which increases with energy. This cross section is in addition to the sputtering caused by linear cascades. As the surface As is scattered, to have a high chance of being ejected, it must have a high angle, which consequently means low energy. This means that the probability drops very quickly as the energy decreases, *ie.* at low energies the contribution from direct recoils is small. At higher energies it is a significant contribution and will lead to the preferential sputtering of arsenic.

The simulation probably underestimates the backscattering due to the way TRIM randomizes the scattering angle of the incident particles such that they scatter 'into' or 'out

of the surface with equal probability. In reality, for the most glancing angles, the backscatter probability would probably approach unity as the atoms on the surface layer start to overlap in the line of sight of the scattering atom. A further simulation would have to take account of the crystal structure of the matrix.

For a similar situation where one of the atoms has considerably less mass than the other atom (unlike for GaAs) this effect could become important as a larger range of scatters of the lighter target particle could produce recoils away from the surface (*ie.* in the scattering of InP).

3.4.4.2 Increased surface release

The more important effect of the behaviour of As at the surface is to facilitate the atom's release if it gains energy in a collision cascade which returns to the surface. If a collision cascade donates energy E at some angle θ to the surface, then for an atom raised above the surface, the probability of escape (*ie.* being sputtered) is equal to 1 if $E>U_0$ where U_0 is the binding energy.

In the case that the atom lies within the surface layer, then it will donate energy to its neighbours, reducing the probability of escape. It is possible to evaluate the reduced probability of escape by a surface atom by simply analysing the energy shared with its neighbours as a function of the angle and energy of its initial escape trajectory. Figure 3.15 shows the final angle of a Ga atom from the normal as a function of the initial angle. The distance from the centres of the atoms has been taken to be 2.45 Å or the average interatomic spacing in the GaAs lattice. It can be seen that as the atom leaves, its trajectory is forced to near vertical, losing most energy at the initially shallow angles.

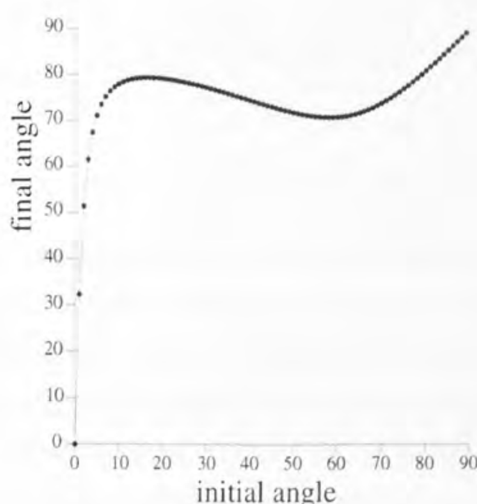

Figure 3.15 The final angle of a gallium atom with initial energy 10 eV leaving the surface as a function of its initial angle

If the final energy is above U_0 then the atom escapes. For an initial energy of 10 eV, the atom in figure 3.15 escapes at any initial angles above about 25°. When the simulation is performed for the full range of energies, the resulting graphs of energy versus initial angle all have the same shape, scaled with the initial energy. This results in the probability of escape being given by

$$P(E) \approx \left(1 - \frac{U_0}{E}\right) \qquad \text{eqn 3.14}$$

The energy of escaping particles follows the well known and experimentally verified law

$$\frac{dY}{dE_s} = k\frac{E_s}{(E_s + U_0)^{3-2m}} \qquad \text{eqn 3.15}$$

where k is a constant, E_s is the energy of sputtered particles and $m << 1$ [244]. Then it can be assumed that the energy of particles returning to the surface follows the relationship

$$\frac{d\phi}{dE} \propto \frac{1}{E^2} \qquad \text{eqn 3.16}$$

For an isotropic distribution, the probability of escape from the bulk

$$prob = \frac{\int_{U_0}^{\infty} f(E)P(E)dE}{\int_{U_0}^{\infty} f(E)dE} \qquad \text{eqn 3.17}$$

$$= U_0 \int_{E_b}^{\infty} \frac{1}{E^2}\left(1 - \frac{U_0}{E}\right)dE \qquad \text{eqn 3.18}$$

$$= U_0\left[-\frac{1}{E} + \frac{EU_0}{2E^2}\right]_{U_0}^{\infty} \qquad \text{eqn 3.19}$$

$$= U_0\left[\frac{1}{U_0} - \frac{U_0}{2U_0^2}\right] \qquad \text{eqn 3.20}$$

$$prob = \frac{1}{2} \qquad \text{eqn 3.21}$$

This implies that when an atom of the surface is given energy from a cascade, it has a finite probability of leaving the surface which is less than the probability of an atom leaving which is raised above the surface. This is similar to saying the effective binding energy of a surface atom is more than that of an exposed or 'kink-site' atom. Kelly [245] used this argument and claimed that the surface binding energy of a surface atom is 33 % higher than that of a kink-site atom (leading to a sputter increase of 33 % for kink-site atoms).

In conclusion, this implies that the probability of sputtering of an As atom raised above the surface is significantly higher than that of an atom lying within the plane of the surface

and segregating As atoms can be expected to sputter more readily than Ga. At higher energies, however, the vacancy creation rate and radiation enhanced diffusion effect will be large and the movement of arsenic to the surface may overwhelm the preferential sputtering effect, leading to depletion of arsenic through an extensive layer, though enrichment at the immediate surface.

3.5 Chemistry

Figure 3.16 shows the relative sizes of the etch products, arsine and tri-methyl gallium in comparison with a section of the GaAs lattice. The penetration depth of hydrogen into the lattice is high and so is the rate at which hydrogen can diffuse through the structure, so it is expected that the surface is saturated with hydrogen, some of which combines with As to form arsine. The methane will not diffuse with the same ease due to its size, however, it is expected that the first few layers should be saturated with methane fragments.

Additionally, it can be expected that any arsine created below the surface diffuses more rapidly than the tri-methyl gallium because of its size.

The diffusion rate of Ga, As and Ga and As vacancies is very low and the extent to which diffusion occurs will be given by the depth of the layer under bombardment which will be determined by the energy and the etch rate as discussed in section 3.3.3.

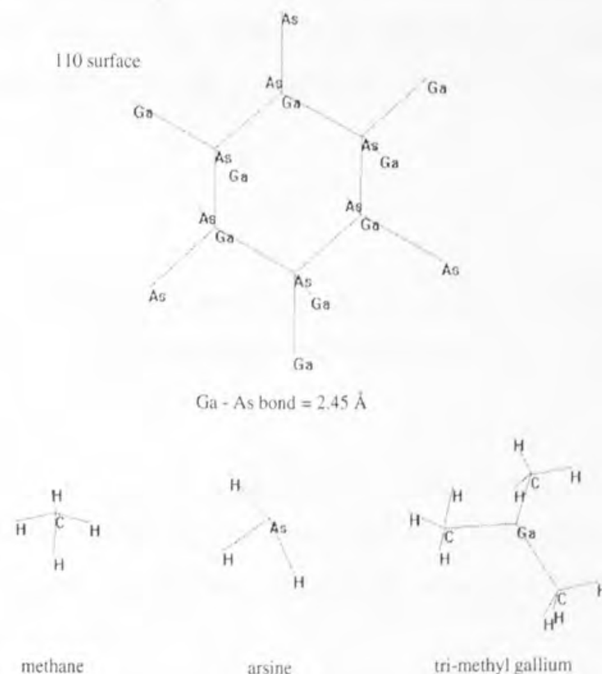

Figure 3.16 The relative sizes of the etch products arsine and tri-methyl gallium in comparison with a part of the GaAs lattice and a methane molecule

3.6 Summary and predictions

3.6.1 Summary

Inert ion etching of GaAs surfaces causes preferential loss of arsenic due to Gibbsian segregation and preferential sputtering in conjunction with radiation enhanced diffusion of arsenic from the damaged layer toward the surface. At low energies the damaged layer is shallow and diffusion of arsenic small, resulting in a surface depleted in arsenic. At higher energies, the damaged layer is deeper and there is a higher rate of arsenic movement toward the surface. In conjunction with Gibbsian segregation and preferential sputtering this leads to a surface depleted in arsenic but with arsenic enhancement at the outermost layer. The depth of the depleted layer is a function of the energy of the bombarding ions, the etch rate and the rate of bombardment enhanced diffusion.

In the case of methane/hydrogen etching of GaAs, there are the physical effects of carbon ion bombardment discussed above and in addition, the preferential removal of As due to the excess hydrogen in the gas mixture, the increased penetration of hydrogen ions and the increased ability of the arsenic etch product over the gallium etch product to move through the lattice. The chemistry also leads to a higher etch rate and consequently shallower damaged layer in comparison to purely physical etching at the same energies.

3.6.2 Predictions

Below is a summary of the expected results from methane/hydrogen etching of GaAs if the process is predominantly physical or chemical. The physical predictions additionally apply to neon etching.

3.6.2.1 Physical

It is expected that the etch rate increases with the power (due to both increased flux and yield per particle) and increases with methane proportion (due to the high yield of methane in comparison to hydrogen).

The etched surface will have arsenic segregating to the outermost layer but whether there is increased arsenic at the surface will be dependent on the energy (*ie.* the sputter rate and depth to from which arsenic can diffuse). At 500 eV and below there will probably be no surface enrichment of arsenic.

The depth of the arsenic depletion layer will be given by the depth to which damage occurs, the diffusion rate and the sputter rate. *ie.* the damaged layer depth is a function of the energy. If the radiation enhanced diffusion is fast, then the depletion layer will correspond to the damaged layer, otherwise the depletion layer will be less extensive than the damaged layer. The depletion layer should therefore increase with the power (due to

the ion energies). The depletion layer should also be invariant with the methane concentration because this should not effect the damage layer (unless the depletion is limited by the diffusion rate in which case it is expected that the depletion layer decreases with increasing etch rate).

3.6.2.2 Chemical

For a predominantly chemical etch, the etch rate would be expected to increase with the power as the flux of precursor molecules to the surface increases as does the energy supplied to the surface which is available for bond breaking. The etch rate would also be expected to increase with the methane proportion as the number of precursor molecules increases.

The depth of arsenic depletion will be given by either the extent of the damage layer (*ie.* the depth to which it is possible to remove arsenic) or the penetration depth of the hydrogen ions. Again, the damage layer is a function of the damage profile, the vacancy creation rate and the etch rate; however, in this case the etch rate is greater than the sputter rate and so the damage layer will be smaller than that in the physical case. The extent of the depletion layer as a function of power is thus a trade off between higher damage and a higher etch rate. The depletion layer should in either case either be invariant or decrease with increasing methane concentration. If the arsenic is removed from a depth given by the hydrogen ion penetration then the depletion layer would be expected to increase with the power and decrease with the methane concentration.

3.7 Reconstruction of the subsurface

3.7.1 Computer code

Reconstruction of a subsurface from XPS data is extremely difficult owing to the infinite number of solutions available and the tendency for maximum entropy codes to find solutions which are physically unreasonable. It has been decided, therefore, in this study to compare the results of the XPS data with predicted results given by a code which simulates a layered subsurface. The control of the layer thicknesses and compositions is thus in the hands of the operator.

The contribution to the spectrum from an atom type at depth x is given by

$$dS = n(x)\exp\left(-x/L_e\right)dx \qquad \text{eqn 3.22}$$

where $n(x)$ is the atomic concentration and L_e is the mean free path of the electron through the solid. The total signal from atoms of this type is then given by

$$S = \int_0^\infty n(x)\exp\left(-x/L_e\right)dx \qquad \text{eqn 3.23}$$

In the case of the angle of detection of the emitted electrons being away from the vertical, the expression becomes

$$S = \int_0^\infty n(x) \exp\left(-s / L_e\right) ds \qquad \text{eqn 3.24}$$

where s is the distance travelled by the electron through the material and is equal to

$$s = \frac{x}{\cos\theta} \qquad \text{eqn 3.25}$$

where θ is the angle from the normal to the surface.

In the simplest case a number of layers can be set up, each with a constant value of $n(x)$ for each atom type where $n(x)$ is a relative concentration such that $n_a(x) + n_b(x) + ... = 1$, where *a,b...* are the atom types. The concentrations in each layer are normalized such that $n_a(x)m_a + n_b(x)m_b + ... = r(x)$. Where m_i are the atomic masses and $r(x)$ is the material density at depth x. Computing the integrals for different values of θ gives ARXPS data which can be directly compared to that gained experimentally.

Several codes were written in order that the relative concentrations of the elements in each layer and the layer depths could be changed with the results displayed on the screen in real time. The most successful and usable of these codes (mainly because of its speed) was the code written in WimpBasic Version 1.1[246] and run on a StrongArm RISC processor. The part of the code involved in the calculations is given in a Basic version in appendix III.

The interface was as shown in figure 3.17, with the user able to input the depths and concentrations or merely scroll up and down through them at user defined intervals. The program calculates and redraws the XPS profile in approximately 0.1 seconds.

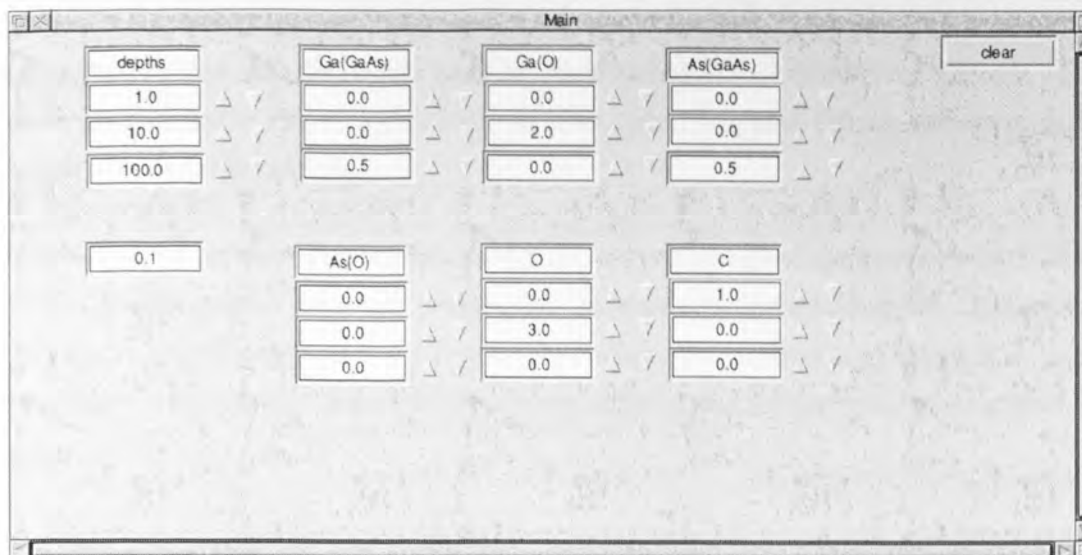

Figure 3.17 Front end for program to predict ARXPS results from standard layered structure

3.7.2 The inelastic mean free path

Additional problems involved in using angle resolved XPS rather than just XPS are numerous. These include problems due to the surface roughness and shadowing, elastic scattering of the electrons and electron refraction at the surface [247] (fig 3.18).

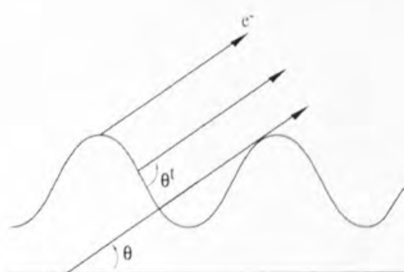

Figure 3.18 problems of shadowing in ARXPS

These tend to have the affect of making the shallow angle results much more subject to error. It is also expected that for a crystalline surface, the crystallographic direction relative to electron direction will be important. For crystalline samples the inelastic mean free path (and elastic mean free path) is not isotropic. Unfortunately, these effects cannot be accounted for in a simple program, though it is expected that for the samples in this study the surfaces will be very smooth.

Another source of error will be the value taken for the inelastic mean free path of electrons in the surface. Ignoring effects of crystallographic direction, the highly bombarded surface of a semiconductor sample consisting of implanted ions, vacancies *etc.* will not be

expected to have the same inelastic mean free path as the bulk material. It is because of these complications that the results must be mainly viewed in a qualitative manner. The layer depths are some values which scale with the mean free path but are not necessarily absolute values in themselves.

Additionally, by representing the structure as layers with constant proportions of different elements, concentration gradients are ignored. However, at the small depths considered, the surface cannot be regarded as a continuum and any concentration gradient is in fact the averaging of a probability distribution for some element and not the true microscopic structure of the surface.

There has been considerable work undertaken in recent years in attempting to find the values of the inelastic mean free path (IMFP) for different elements, and compounds. Tanuma et al [248] give a value of 44.4 Å for GaAs from optical data and 28.6 Å calculated from an equation modified from the Bethe equation [249]. Though they do not give values for oxides of arsenic or gallium, they give values of 27.9 and 27.4 Å for the two different methods above for Al_2O_3. Seah and Dench [250] collected data for a number of inorganic compounds and fitted a curve with the following formula

$$\lambda_m = 2170\, E^{-2} + 0.72\,(aE)^{1/2} \qquad \text{eqn 3.26}$$

where E is the energy of the electron in eV above the Fermi level and a is the monolayer thickness. This results in an IMFP in GaAs of 38 Å.

Chapter 4. Experimental set-up and diagnostic tools

4.1 The etching chamber

The etching experiments were carried out in an asymmetrical industrial OPT Plasmalab 100 system outlined below.

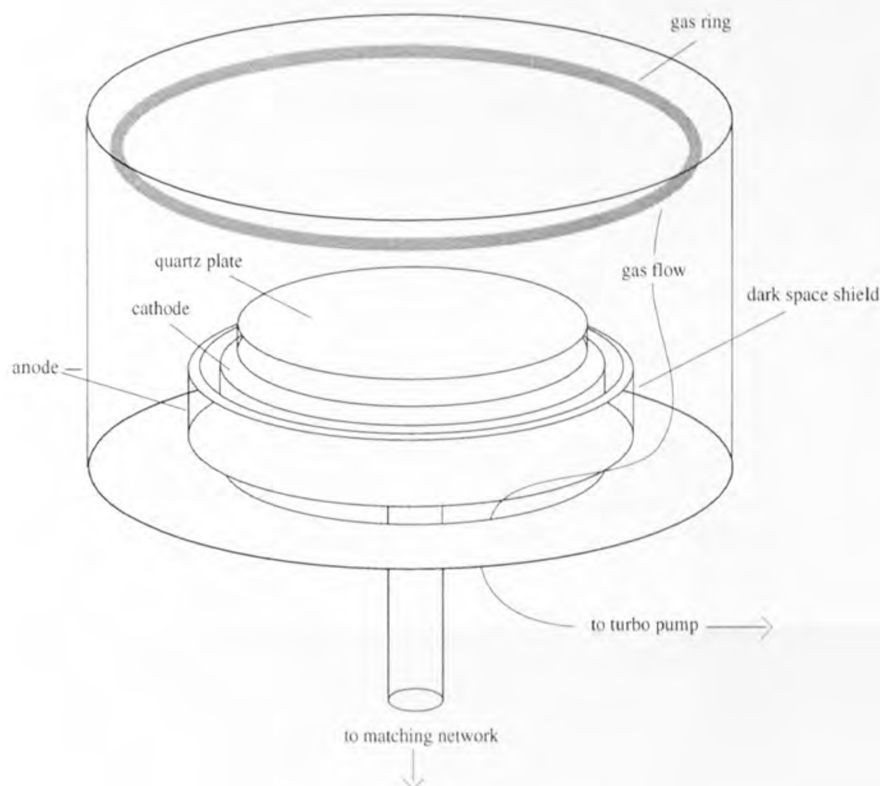

Figure 4.1 The etching chamber.

The grounded anode (which included the chamber walls) was much larger than the driven electrode which had an area of 400 cm^2. The grounded dark space shield prevented the formation of any plasma around the sides of the cathode, and kept the equipotentials closer to parallel to the surface of the cathode. A matching network was used to match the impedance of the plasma and sheaths to the external controllable impedance in order to maximise the energy input. The pressure was controllable between 8 and 95 mTorr and this was achieved automatically by measurement of the pressure via a capacitance manometer (CM) gauge and a throttle valve. A number of different gases could be allowed into the chamber at a rate governed by a set of mass flow controllers which measure the flow by heating the gas and measuring its temperature rise. The flow rate was measured in cubic centimetres per second at standard temperature and pressure (sccm). The range of powers available was approximately 0 - 300 W, but problems with overheating of the generator at high powers and instability of the plasma at low pressures reduced this range to 25 - 150 W. The apparatus was controlled from a 486 DX33 PC.

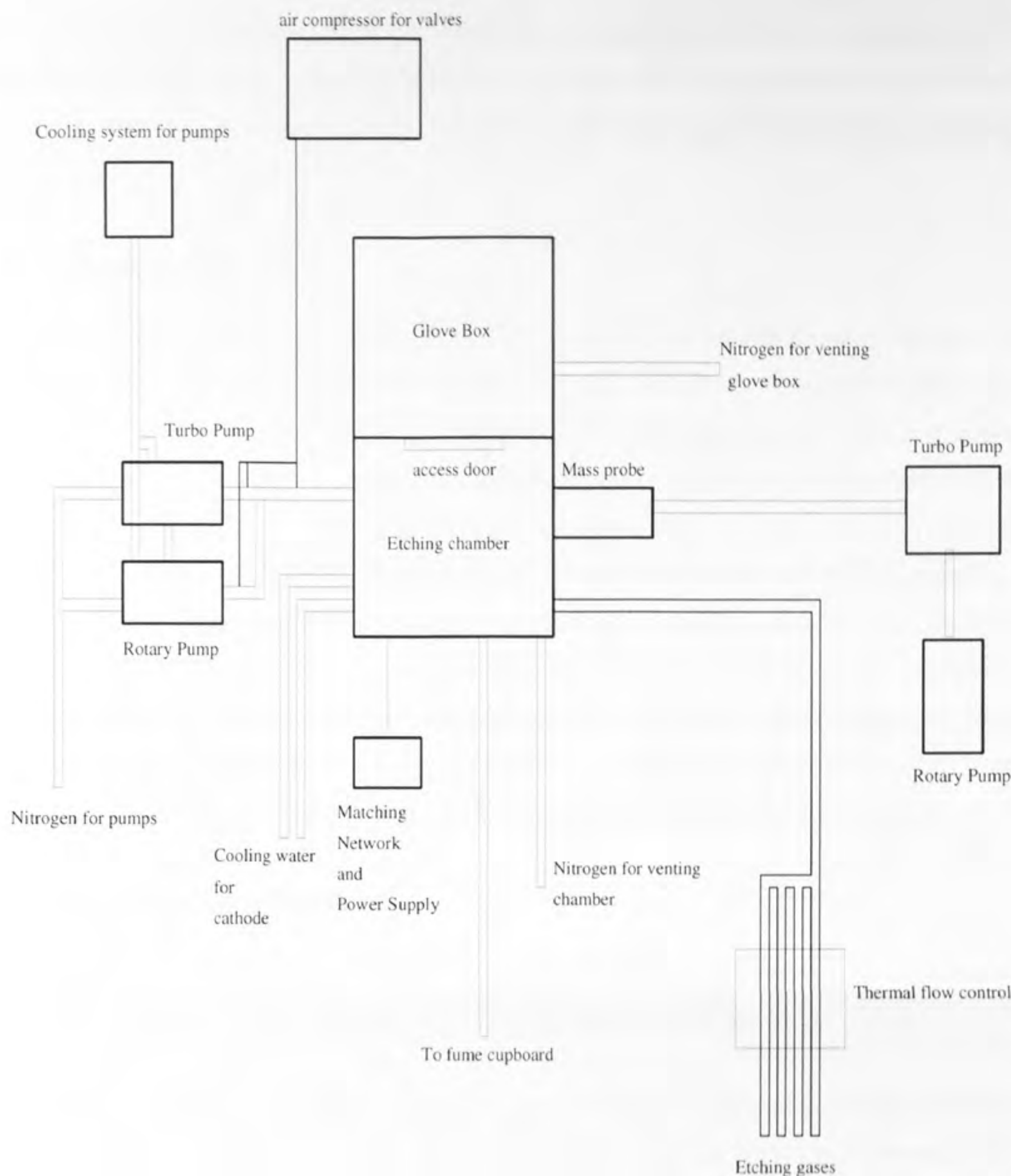

Figure 4.2 Schematic of the etching apparatus.

The schematic diagram in figure 4.2 shows the total pumping, cooling and gas flow.

4.1.1 Chamber cleaning

Polymer deposition caused by the methane/hydrogen plasmas built up and eventually caused shorting between the dark space shield and the cathode. This had the effect of lowering the D.C. bias. In order to remove this polymer, it was necessary to clean by running an oxygen plasma. The chamber was considered clean when the light emission from the plasma changed from white (signifying carbon monoxide) to green (oxygen plasma). Mechanical cleaning using hydrocarbons and abrasives were sometimes used before the oxygen plasma. The oxygen plasma was followed by a hydrogen plasma in the case of methane/hydrogen etching to remove any oxygen [251]. It has been suggested in the case of InP etching, that some amount of 'seasoning' of the chamber is necessary in

order to obtain reproducible results [252] and this is a general standard in industry [253]. In this study a 1/2 hour O_2 plasma followed by a 1/2 hour H_2 plasma preparation was used but later on this was changed to allow the polymer to build up. The results were compared for consistency.

4.1.2 Sample preparation

For each experiment, three polished GaAs (100) samples and three masked samples were used. The mask consisted of polymethyl methacrylate (PMMA) which after etching was removed in acetone and iso-propyl alcohol (IPA) to reveal the etch pits which could then be measured. The polished samples were ultrasonically cleaned in acteone and IPA for 15 minutes each, finally blow drying in inert gas to prevent any contamination from settling out of the IPA as it evaporated. More extensive cleaning methods were investigated, including increasing the time of the ultrasonic bath and including an ultrasonic cleaning stage in methanol between the acetone and the IPA. These did not have a significant effect, except that the brittle samples were more likely to break when cleaned for longer periods. The most likely source of contamination was atmospheric dust particles settling either on samples exposed to air on in the beakers containing the hydrocarbons.

4.1.3 Experimental procedure

The semiconductor samples were passed into the chamber on a piece of 12 mm thick quartz plate upon which the sample stayed for the duration of the etch.

The chamber was pumped down to 2×10^{-6} mbar before the beginning of each etching experiment. The time taken to reach this pressure and also the final base pressure after some hours pumping is a good indicator of any leaks. Upon completion of the etch, the chamber was vented with pure nitrogen.

The experiments performed consisted of a matrix defined by the parameters, pressure, power and percentage of methane in hydrogen. The total gas flow remained fixed at 30 sccm with the ratio of methane to hydrogen increasing as CH_4:H_2 = 0:30, 1:29, 2:28, 3:27, 4:26, 5:25 and 6:24. The powers of 15 W, 25 W, 50 W, 100 W and 150 W were used with pressures of 10 mTorr, 20 mTorr, 40 mTorr and 80 mTorr. This consists of a large number of individual experiments, but deposition over much of the conditions reduces the work considerably.

Additionally some experiments were performed with pure neon at the higher powers of 100 W and 150 W to compare purely physical etch rates with the chemically assisted etch rates of the methane/hydrogen experiments.

4.2 Plasma diagnostic tools

The set-up of the diagnostic tools is shown schematically in figure 4.3.

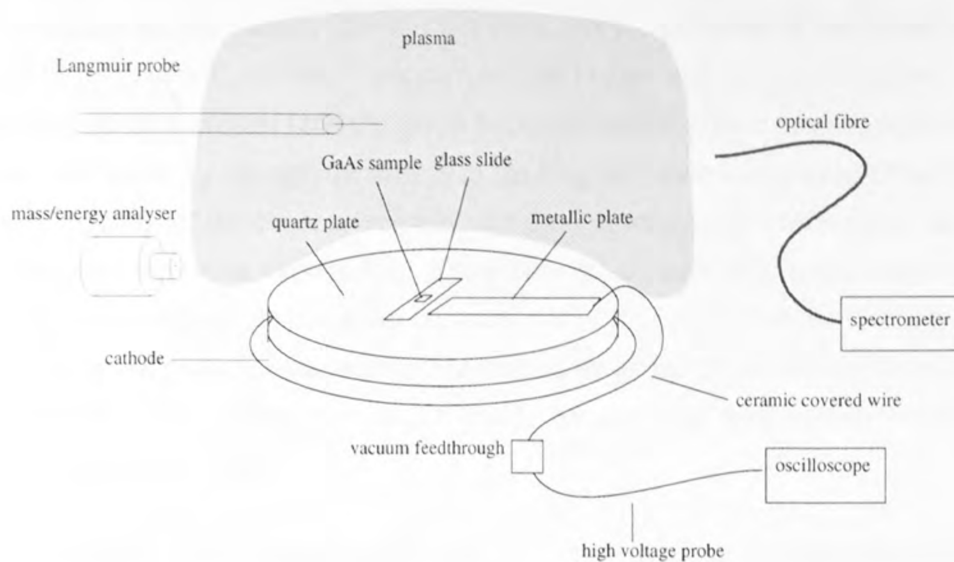

Figure 4.3 Schematic of the set-up of the diagnostic tools.

4.2.1 Langmuir Probe

The electrical probe used was the Hiden Analytical Langmuir probe which was inserted into the middle of the plasma as shown in figure 4.3. In the most primitive type of probe, the voltage at the tip is swept from say -100 V to +100 V and the current-voltage information is displayed graphically. Figure 4.4 shows a typical probe current-voltage characteristic with the probe current being the negative or electron current [254] .

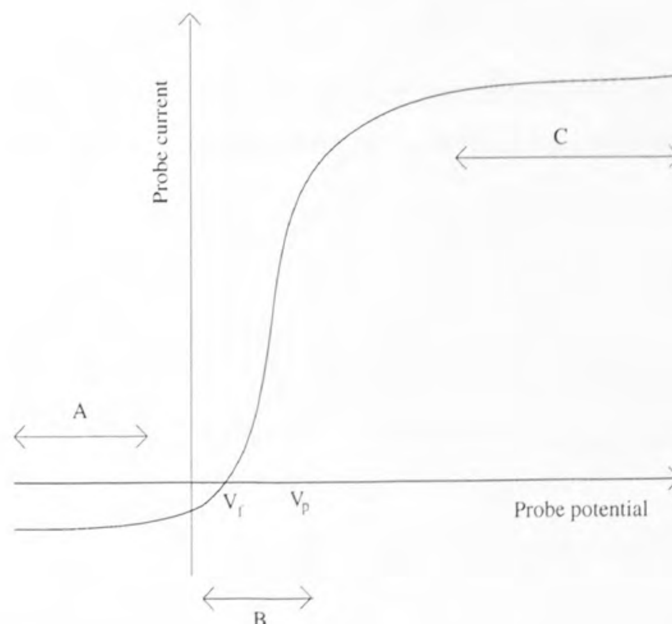

Figure 4.4 Typical Langmuir probe characteristic.

Referring to figure 2.4, the graph may be obtained continuously in a steady discharge, in pulses, or as in our equipment the entire curve obtained in a sweep of several milliseconds. At point V_p, the potential of the probe is equal to the potential of the plasma and no field exists around the probe tip. Ions and electrons migrate freely and due to their higher mobilities the net current drawn is negative. As the potential of the probe is increased through area C, the small ion current falls to zero and the probe reaches saturation of electron current (and the graph becomes linear). If the probe potential is decreased relative to V_p through the area B in the diagram, then it begins to attract ions and repel electrons. If the electron velocity distribution were truly Maxwellian then this area of the graph would be exponential. Eventually the current falls to zero as the ion and electron fluxes are equal. At this point the potential of the probe is at the floating potential, V_f, or the potential that would be assumed by an insulated object placed in the plasma. As the probe is made more negative still, we move through area A, which is the ion current saturation region.

Care must be taken when using the probe not to have too high an electron saturation current since this will result in the end of the probe glowing orange. If the current is increased further the tip will melt.

The software supplied with the probe can either automatically analyse the data or allow more careful manual analysis. The shape of area B gives the electron temperature and the magnitude of the electron saturation current gives the plasma density. The floating potential, V_f, is given by the point at which the probe current is zero. If the EEDF is Maxwellian then a plot of the logarithm of the probe current versus the probe potential will yield a straight line for this part of the graph with the gradient being e/kT_e *ie.*

$$\ln(-I_p(V_p)) = \frac{eV_p}{kT_e} \qquad \text{eqn 2.1}$$

The automatic analysis with the software finds the plasma potential by extrapolation of this part of the graph with electron saturation part and finds the crossing point as shown in figure 4.5.

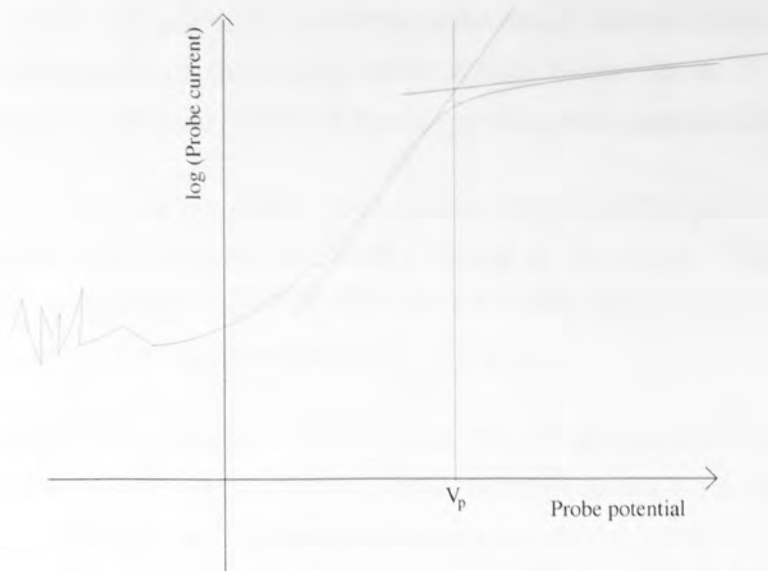

Figure 4.5 Method for finding the plasma potential.

The plasma potential, however, is not as well defined as the floating potential and other methods of estimating its numerical value exist. If one is to calculate the second differential of the ion current with respect to the probe potential, d^2I/dV^2. *ie.* it can be shown that

$$\frac{d^2 I_e}{dV_p^2} = -A_p 2e\pi \left(\frac{e}{m_e}\right)^2 [f(E)]_{E=-eV_p} \qquad V_p < 0 \qquad \text{eqn 2.2}$$

and therefore,

$$[f(E)]_{E=-eV_p} = -\frac{1}{A_p 2e\pi}\left(\frac{m_e}{e}\right)^2 \frac{d^2 I}{dV_p^2} \qquad V_p < 0 \qquad \text{eqn 2.3}$$

where $f(E)$ is the velocity distribution. As the energy distribution

$$f(E)dE = 4\pi c^2 f(E)dc \qquad \text{eqn 2.4}$$

and

$$E = \frac{1}{2}m_e c^2 \qquad \text{eqn 2.5}$$

then

$$[f(E)]_{E=-eV_p} = -\frac{4}{A_p e^2}\left(\frac{-m_e V_p}{2e}\right)^2 \frac{d^2 I}{dV_p^2} \qquad V_p < 0 \qquad \text{eqn 2.6}$$

The point at which this is equal to zero, or the maximum of this function can be taken to be the plasma potential. These methods can yield similar values for the plasma potential, though not exclusively.

The above is a simple account of the use of the probe which assumes the plasma parameters are stationary over the duration of the voltage sweep. In an RF plasma this is not true as the plasma potential follows in some way the driving potential at the cathode.

An attempt to overcome the problem is to compensate the end of the probe by driving it at the same frequency and hopefully at the same potential as the plasma. This method has been extensively researched [255] [256] [257] [258] and the results show that the current-voltage characteristics can then be interpreted as in the DC case.

When there is any hydrocarbon in the gas mixture, this results in deposition on the probe tip and a degradation of the signal. This occurs with contaminants when running a pure hydrogen plasma and the probe tip must be cleaned between data acquisition by holding the probe at a high negative value (*ie.* 60 V) which sputter cleans the tip with hydrogen ions.

4.2.2 Mass/energy analyser

Figure 4.6 shows the layout of the mass probe which is bolted onto the side of the etching chamber and is differentially pumped with both a rotary and turbo pump. The pressure attained in the probe is of the order of 10^{-6} mbar or better. The mass/energy analyser used was a Hal Hiden EQP plasma diagnostic system which was run from a PC using WINDOWS MASsoft software. The mass probe can be operated in residual gas analysis mode (RGA) to check for leaks and contaminants and also to monitor the mass distribution of the particles in the buffer gas or in SIMS mode to sample ions from the plasma.

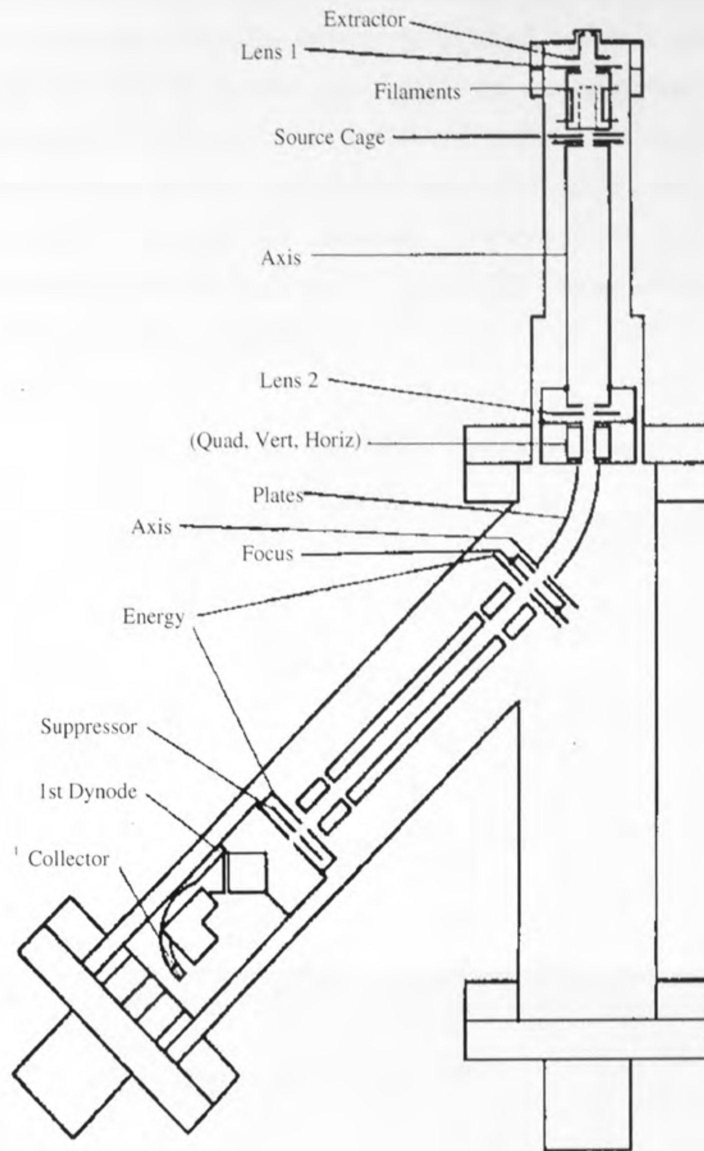

Figure 4.6 The mass/energy analyser.

The outer casing of the mass probe was bolted onto the earthed chamber wall in which is a large (5mm) orifice. Behind this is the extractor which can be set at a potential between -100 V and +100 V where there is the much smaller orifice in the form of a hole (tapering outwards away from the plasma) in a thin piece of foil which is spot welded to the end as shown in figure 4.7.

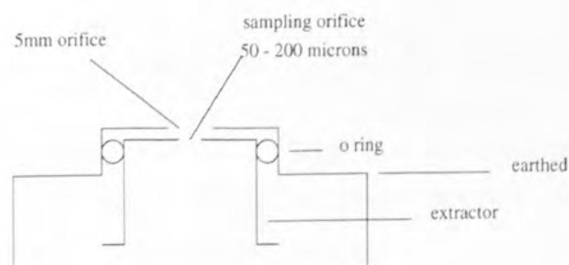

Figure 4.7 The mass probe orifice.

The foil is considerably thinner than the width of the orifice in order to ensure that the ion doesn't 'see' a tunnel. From the orifice the ion travels to lens 1 which is another orifice at a user defined potential, the value of which is set to maximise the count rate. The energy of the particles is selected on travel through the electrostatic plates at 45^0 to the main flight axis from where the ions enter the mass quadrapole which through the use of D.C. and rf fields allows only particles of a certain mass through. The ions finally reach the detector which is an off axis mounted electron multiplier. The energy change of the ions as they travel through the probe is plotted in figure 4.8.

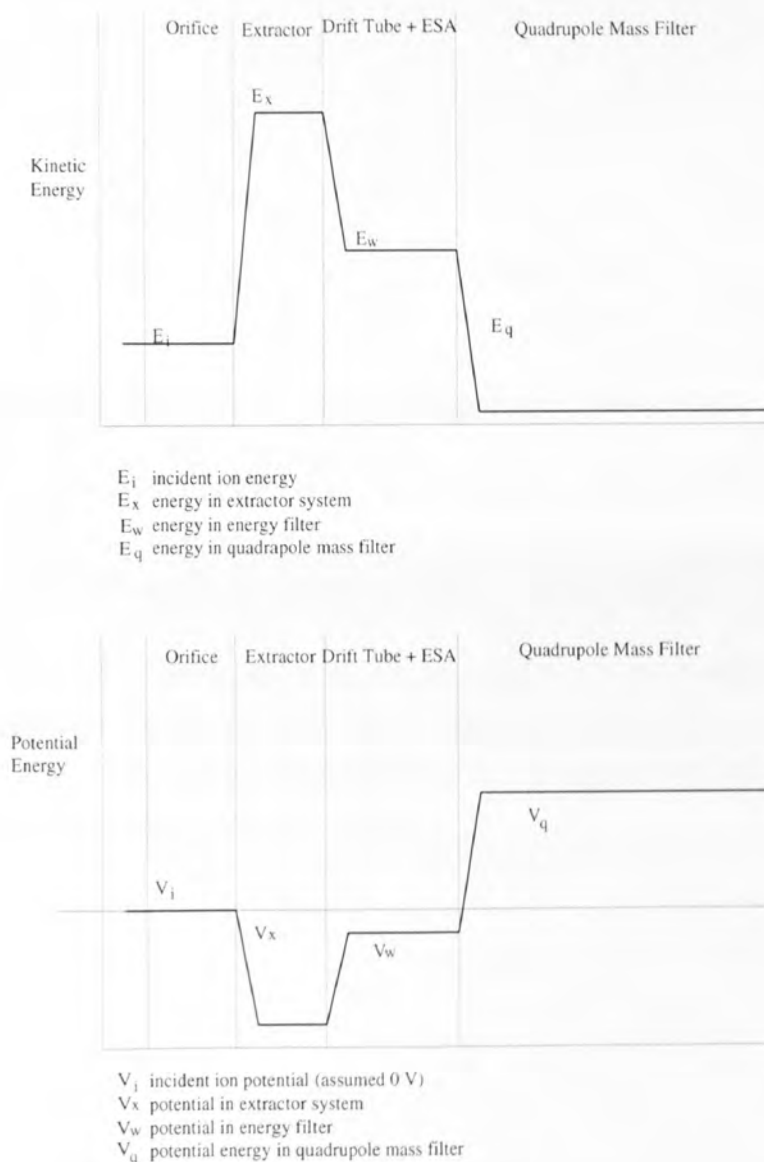

Figure 4.8 Energy change of ions traversing the mass/energy analyser.

This work by Howling [259] implies the true energy is some 4 eV higher than the measured energy and this can be seen when analysing the energy spectrum of the residual gas atoms where the minimum energy is approximately -4 eV.

There are two modes in which the probe can operate.

1) Residual Gas Analysis (RGA)

2) Secondary Ion Mass Spectrometry (SIMS)

The probe has an effective acceptance angle for incoming ions as illustrated in figure 4.9.

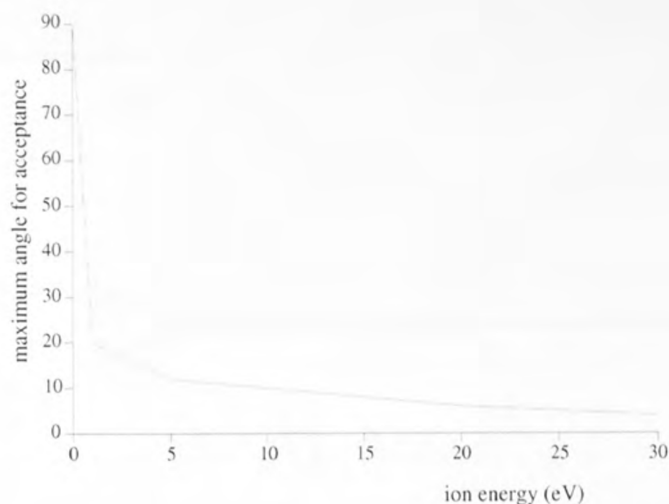

Figure 4.9 Angle of acceptance for ions entering the probe orifice.

This is, however, an oversimplification and work recently announced [260] implies that the interaction between the extractor and lens 1 can introduce a double peak into a monoenergetic ion beam due to an optical type effect outlined below.

Depending on the relative potentials of the extractor and lens 1, the beam, represented by the grey wedge in figure 4.10 will either focus before, after or in the plane of lens 1. In the former two cases, ions entering the extractor orifice at angles more extreme than those shown will not pass through the second orifice.

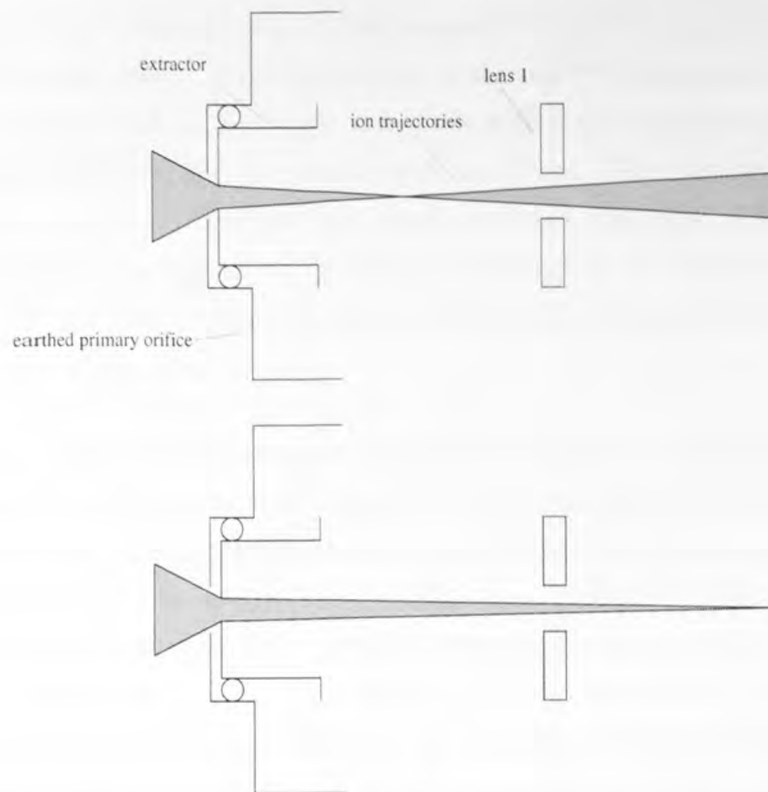

Figure 4.10 Ion trajectories between the orifice and lens 1.

There also appears to be discrimination against low energy ions in this type of probe first noticed by Davis and Vanderslice [261] and more recently in a study of off-axis probes [262] where no ions below 6 eV were recorded.

Results are generally presented as the number distribution of ions entering the orifice as a function of energy for a specific ion, or as the number distribution of ions with different masses which enter the orifice at some fixed energy.

As with the Langmuir probe, this technique suffers from the build up of polymer around the orifice which with time gives unreliable results. Cleaning in an oxygen plasma helps but it is sometimes necessary to dismantle and mechanically clean the orifice with solvents.

4.2.3 Measurement of sample potentials

The system used in this research includes an optional quartz plate approximately 12 mm thick on which the sample is placed. Quartz was chosen because it does not readily increase contamination in the chamber through sputtering and has the added advantage that if it was incorrectly placed in the middle of the electrode then it would not interfere with the creation of the plasma by shorting out between the electrode and the dark space shield. However, as later work shows, this has several disadvantages when it comes to modelling as it changes the potentials and the form of the field over the cathode.

Generally the powered electrode in a dry etch system consists of a target plate, backing plate and a dark space shield. Work by de Vries and Hoek [263] has shown that the measurement of the D.C. bias, V_{dc} is not straightforward if the target plate is an insulator and the backing plate is not in direct contact with the plasma. This situation often occurs with aluminium electrodes which have been anodized when used with chlorine chemistry plasmas. The D.C. bias is a result of the build up of charge on the target plate and measurement of V_{dc} is only possible if there is some leakage current from the top of the insulator to the backing plate.

In the apparatus used here the quartz plate incompletely covers the cathode such that a ring 2 or 3 mm wide of the cathode is exposed to the plasma around the circumference of the quartz. This complicated geometry means that the potential at the surface of the quartz is not obvious and cannot be inferred from the D.C. bias. An attempt was made, however, to measure directly the potential at the surface of the quartz using an oscilloscope connected via a high voltage probe to a 1 mm x 1cm x 3cm metal plate which lay on the surface of the quartz and at equipotential with the samples to be etched. Being an insulator, it was expected that the potential across the surface may not be uniform, but this measurement would give us a good estimate of the true potential the ion experiences as it crosses the sheath. Any problems associated with this method were expected to come from the exposed wire leading from the metal plate through the cathode sheath to the vacuum feedthrough, though this is unavoidable. The potential at the cathode was directly measured using an oscilloscope.

4.2.4 Optical measurements

Visual measurements of the extent of the sheath were taken using a travelling microscope. Although there is evidence that the visual sheath width may not be representative of the electrical sheath width at high pressures [264] [265], below 100 mTorr it is thought to be similar. These measurements were complicated by the tenuous nature of the plasma/ sheath boundary especially at low pressures and powers. The sheath width measured was the distance from the cathode to where the dark space gave way to the bright head of the plasma, some distance shorter than the brightest part of the plasma.

4.3 Surface techniques

4.3.1 X-ray photoelectron spectroscopy (XPS)

X-ray photoelectron spectroscopy and angle resolved X-ray photoelectron spectroscopy were used to analyse all treated surfaces.

4.3.2 Atomic force microscopy

For the small etch depths to be measured accurately and to investigate the smoothness of

the resulting etched surface, it was necessary to use an atomic force microscope (AFM). As the semiconductor surface is quite hard it was possible to use the instrument in contact mode. This involves the scanning tip head being dragged across the surface of the sample where changes in topography change the angle of the cantilever upon which the head is mounted.

A laser reflected from the cantilever records changes in the angle and a feedback mechanism uses piezoelectric crystals to raise or lower the entire cantilever in order that the angle remains constant. A conversion factor for the piezoelectrics converts the voltage into height changes and as lines are scanned adjacently, an image of the surface is built up.

Another method for looking at the topography on very smooth surfaces involves turning off the feedback mechanism and just recording the change in angle of the cantilever. This method, whilst more accurate, is difficult to convert to real topographic heights.

Chapter 5. Model Results

5.1 Electron model

The electrons travel between the anode and the cathode sheath, gaining energy, scattering and causing ionisations and excitations. The electrons gain energy as the sheath is expanding and therefore, reach the threshold for ionisation at specific phases of the rf cycle. For the following simulations, the anode/cathode distance was fixed at 10 cm and the cathode sheath width and anode sheath width at 1 cm and .5 cm respectively. Figure 5.1 shows the total number of ionisations as a function of position between the electrodes and the phase of the rf cycle for a 90 mTorr hydrogen plasma. Maxima occur near the plasma/sheath boundary at cathode and anode corresponding to where the electrons are supplied with energy. The maximum ionisation rate occurs at a phase of π radians, where the sheath is at its maximum potential and extent.

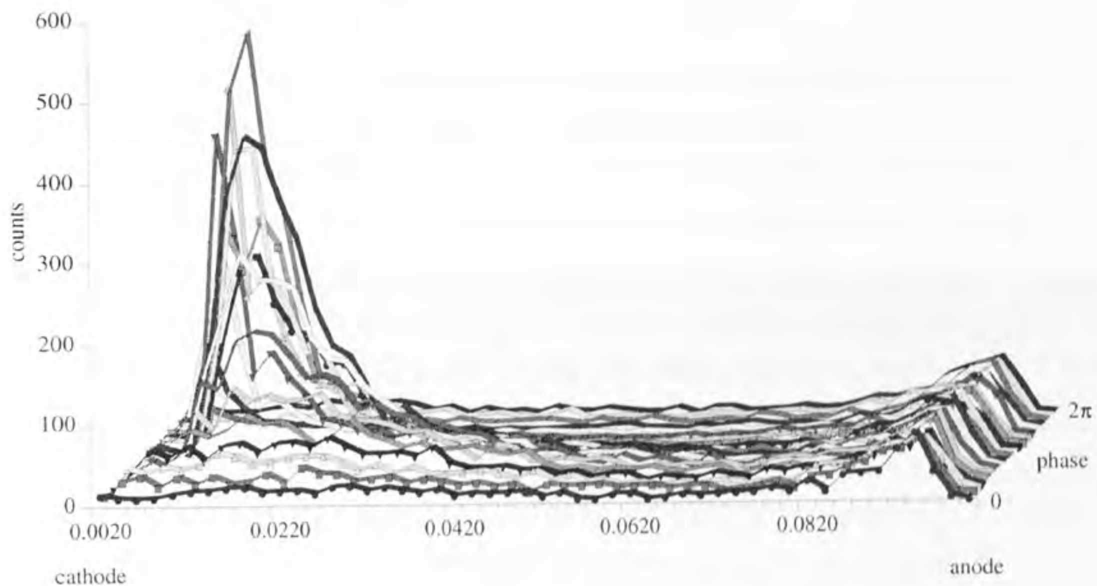

Figure 5.1 Ionisation profile in position and phase space.

Transposing the x and y axes enables a second peak to be seen at a later phase in the cycle when the sheath is contracting. This secondary peak is closer to the cathode as shown in figure 5.2 and is apparent in all of the simulations to an extent. The effect is due to the ionisations occurring when the sheath potential is either at a maximum or for some time after when the sheath is contracting. The secondary peak is not therefore an isolated phenomenon but is the primary peak smeared in time and space. This should not be confused with the secondary peak in the optical spectrum close to the cathode at a phase corresponding to the minimum sheath potential seen by Mahoney *et al* [266][267]. When the ionisation spectrum is integrated across the phase, the double peak is not evident, the main peak is merely broader.

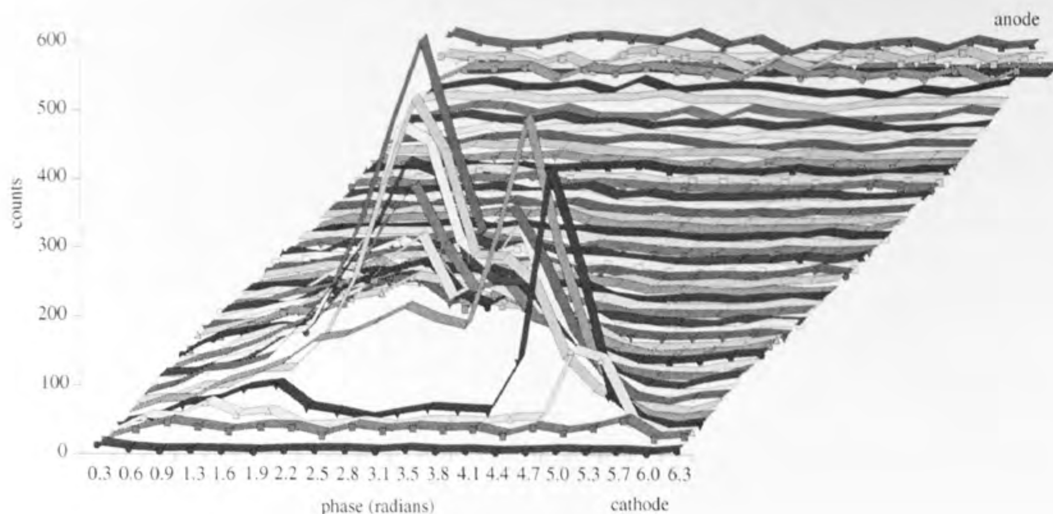

Figure 5.2 Ionisation profile in position and phase space with x and y axes transposed.

5.1.1 Effect of a change in V_f

The ability of an electron to escape from the plasma is governed largely by the floating potential, V_f. The lowest value of the sheath potential over the anode or the cathode is given by V_f and the energy required by an electron to surmount this potential barrier must be greater than V_f (the sheath potential is at this value instantaneously). If V_f is higher than the electron ionisation threshold, then the electron will have a high probability of losing energy in an ionisation event and will find it difficult to leave the plasma especially at higher pressures. If the floating potential is lower than the ionisation threshold, then any electrons gaining kinetic energy greater than V_f can remain at this energy for a considerable time. The energy loss through rotational and vibrational excitation being small, and negligible near the ionisation threshold, the electron will have a large chance of escaping. The multiplicity m_e, the number of electrons created on average per electron is therefore highly sensitive to the value of V_f. This is illustrated in figure 5.3 which plots the multiplicity against the floating potential for a 40 mTorr hydrogen plasma.

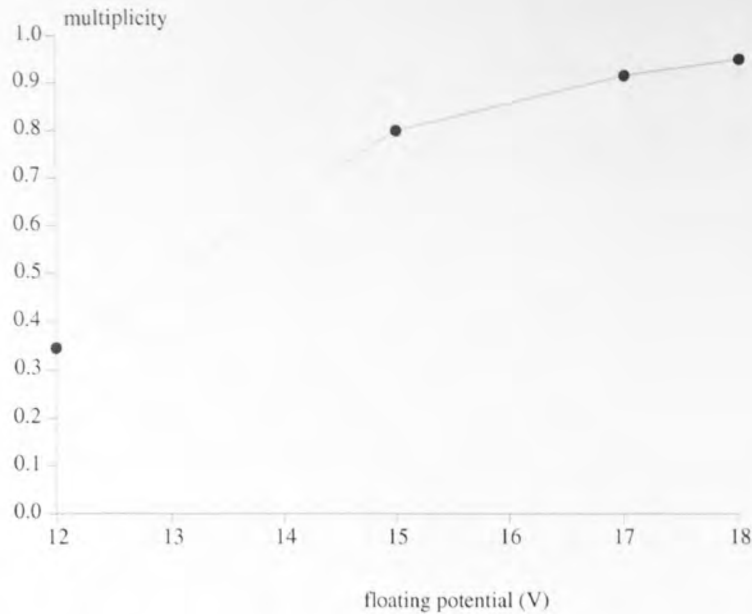

Figure 5.3 The multiplicity m_e as a function of the floating potential for a 40 mTorr hydrogen plasma.

As the value m_e tends to 1, the total number of electrons created tends to

$$\frac{1}{1 - m_e} \qquad \text{eqn 5.1}$$

but is limited by the finite time taken between an electron being created and causing an ionisation and the total length of the simulation, electrons being discarded if they still exist after the length of the simulation. Choosing a value of V_f for each simulation involves a trade off between having enough electrons generated to give good statistics in the results and having V_f too high such that an inordinately high number are discarded at the end of the simulation. The resultant choice of V_f gives added information about the simulation.

5.1.2 Effect of a change in pressure

The following simulations are performed for pure hydrogen, floating potential 17 eV in order to demonstrate the effect of a change in pressure on the simulated discharge. For clarity, even though a change in pressure causes a change in sheath width, this is ignored and now and for the later simulations, the plasma parameters are treated as independent variables.

5.1.2.1 The floating potential

As the pressure increases, the electron mean free path falls and electrons tend to be retained in the plasma. This has the effect of increasing m_e as shown in figure 5.4.

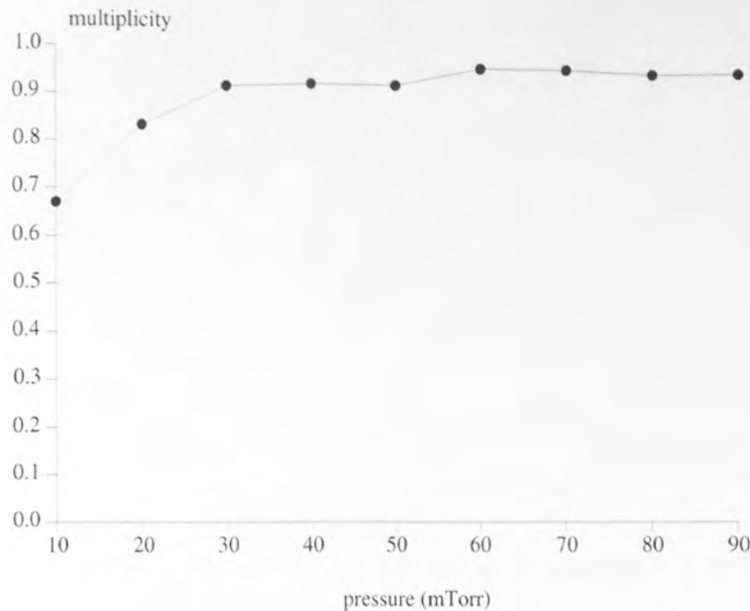

Figure 5.4 The multiplicity m_e as a function of pressure for a hydrogen plasma with V_f = 17 V

Another effect is that the number of electrons which exist for times exceeding the length of the simulation increases as shown in figure 5.5.

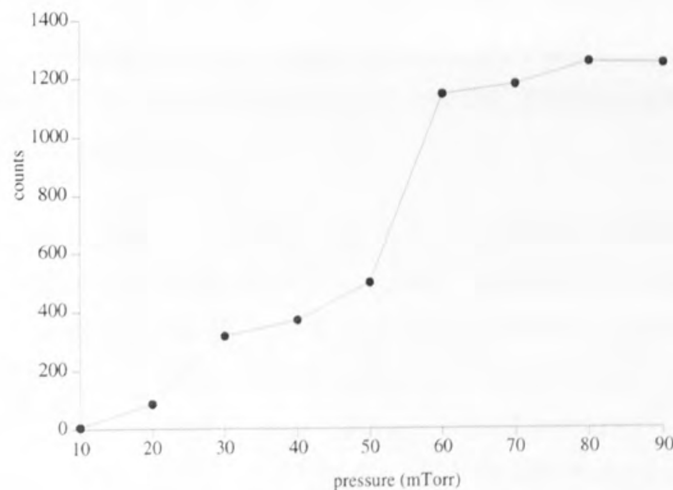

Figure 5.5 The number of electrons exceeding the simulation length as a function of the pressure, V_f = 17 V, hydrogen plasma.

In order to find the level at which the plasma is in equilibrium, the simulations were repeated for a number of values of V_f. As the multiplicity is highly dependent on the floating potential, we can adjust the floating potential to give a fixed value for the multiplicity.

The resulting values for the floating potential versus pressure are shown in figure 5.6.

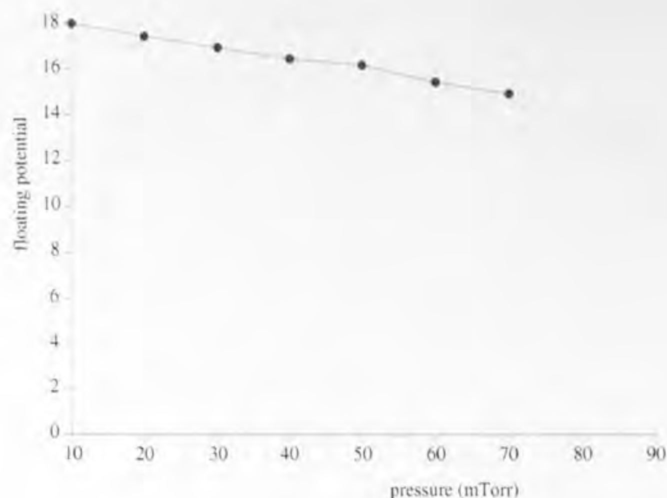

Figure 5.6 The value of the floating potential necessary to give a value of the multiplicity of 0.95.

At 80 mTorr and 90 mTorr, the multiplicity does not reach 0.95 at any level of V_f (though it is possible given different random numbers). This implies the electron residence time is approaching the simulation time and the simulation time should be extended.

5.1.2.2 The ion and electron distribution functions

Figures 5.7 and 5.8 show the spatial distribution of ions and electrons for the extreme cases of 10 mTorr and 90 mTorr. The sheaths at both anode and cathode tend to be free of charged particles due to the fact that electrons are repelled from and ions are quickly accelerated through the sheaths.

The ions are more equally distributed in the case of low pressure than high pressure when they tend to exist in greater numbers near the cathode, and this reflects the spatial dependence of the ionisation frequency. The electrons, however, are very equally distributed in both cases throughout the entire plasma and this reflects the higher velocity of the electrons and the fact that they make multiple journeys through the plasma from sheath to sheath. In a self-consistent plasma, the effect of this bunching of ions would be to affect the potentials and this would in turn affect the charged particle distributions. The direct comparison of the number density of the ions and electrons from this simulation is not valid because even very weak fields in the plasma bulk would radically change the spatial distributions of ions and electrons. With zero field, the ions must leave by crossing the plasma/sheath boundary due to Brownian motion alone, whereas the real effect of the leaking of the sheath field into the plasma will significantly increase the ion flux there.

In figure 5.8 for example, the apparent abundance of ions at the cathode plasma/sheath boundary would have the effect of increasing the plasma potential there, attracting electrons and repelling ions and thereby attempting to reduce the positive plasma anomaly. The equilibrium field and ion distribution is therefore not obvious.

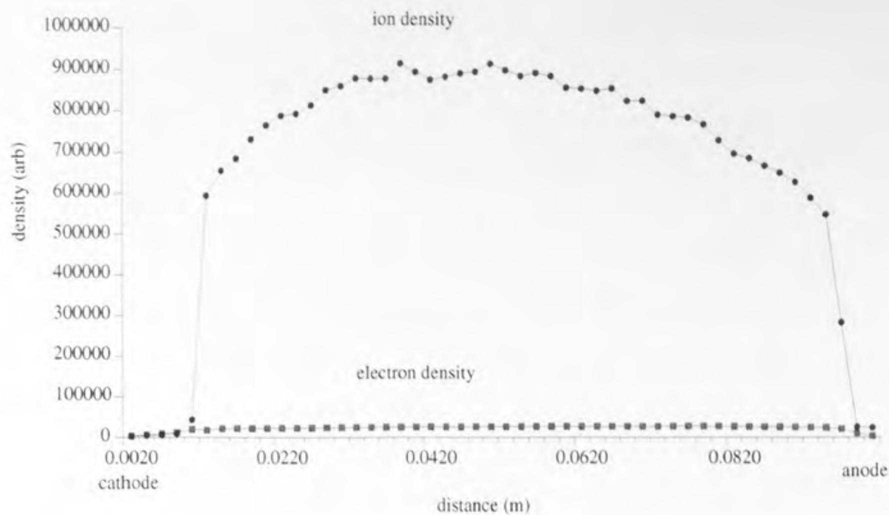

Figure 5.7 The spatial number density of ions and electrons, 10 mTorr.

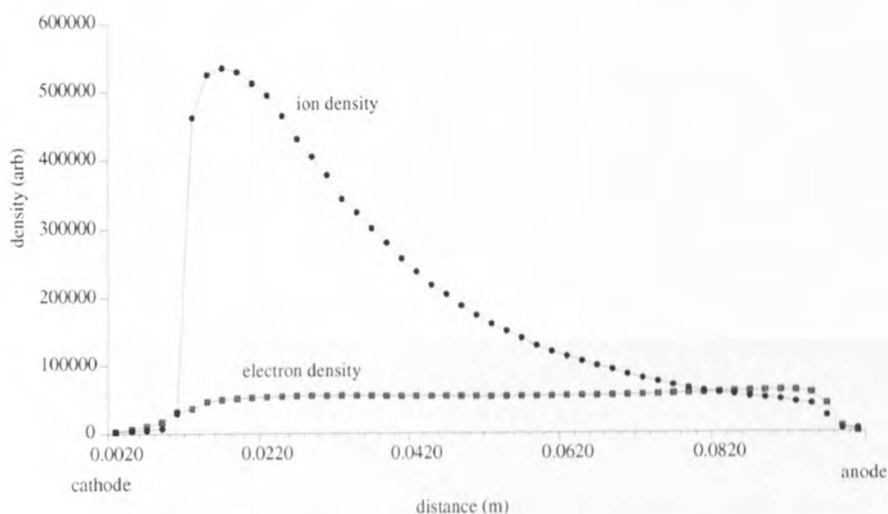

Figure 5.8 The spatial number density of ions and electrons, 90 mTorr.

5.1.2.3 The ionisation profile

The ionisation profile changes as the pressure increases according to diagrams 5.9 and 5.10. The major method by which electrons gain energy is by interacting with the sheaths and as the pressure increases, so too does the elastic scattering of the electrons from neutral molecules. This 'random walk' by the electrons through the plasma increases the probability of an ionisation or excitation event greatly and consequently reduces the probability of an electron having a high energy mid-way between the electrodes. The result is that the ionisation profiles tend to be bunched at the sheath edges.

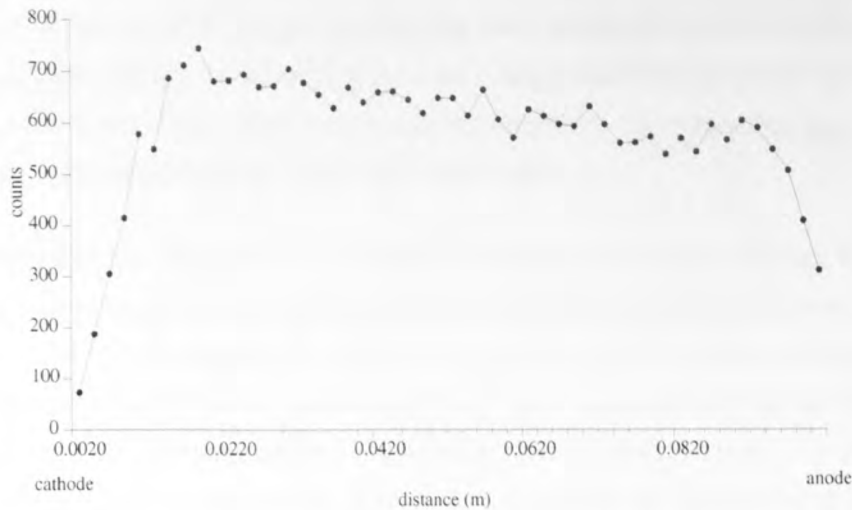

Figure 5.9 The ionisation profile, 10 mTorr.

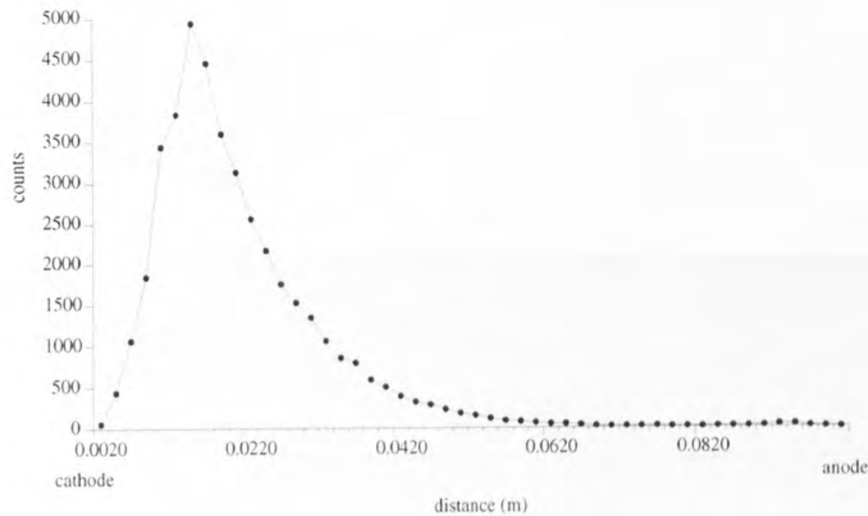

Figure 5.10 The ionisation profile, 90 mTorr.

It can be seen that there is considerable ion creation in the sheath, especially at the higher pressures. This invalidates the assumption that all ions are created in the plasma and drift into the electric field in the sheath.

The excitation profile is in general very similar to the ionisation profile.

5.1.2.4 The electron temperature

Another result of higher pressures is that the peak in the EEDF is shifted to lower energies. Figures 5.11, 5.12 and 5.13 show the EEDF for 10 mTorr, 40 mTorr and 90 mTorr respectively. It can be seen that the high energy tail of the electron distribution is longer at low pressures. At higher pressures the high energy electrons have a greater probability of causing ionisations and excitations and are consequently reduced. It must

be stressed that the electron energy distributions used are those obtained in the centre of the plasma and would not necessarily reflect the energy distribution in the the sheath or at the plasma sheath interface. The position midway between the electrodes was chosen to best represent the sampling area of the Langmuir probe.

It was thought that the apparent lack of a high energy tail could alternatively be due to statistical discrimination against the higher energy secondary electrons which are created by ion impact on the electrodes. This occurs to a similar extent throughout the rf cycle and therefore results in electrons with energies up to the maximum of the sheath potential, unlike secondary electrons created by electron impact which tend to occur at times when the sheath potential is at a minimum. The longer time taken for ions to reach the electrodes could therefore result in the electrons created being discriminated against due to the finite simulation time. Taking this into account, both by increasing the simulation time and resetting the creation time of the resultant electron to T=0 does not affect the EEDF and this explanation can be discounted.

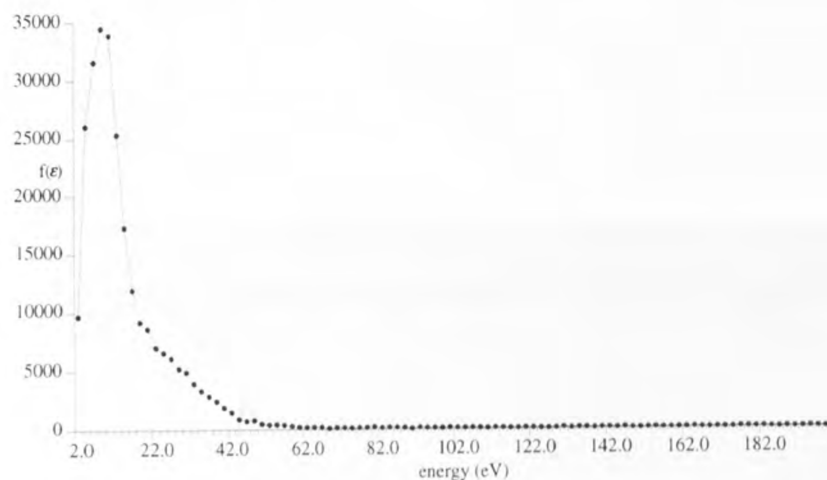

Figure 5.11 The EEDF, 10 mTorr.

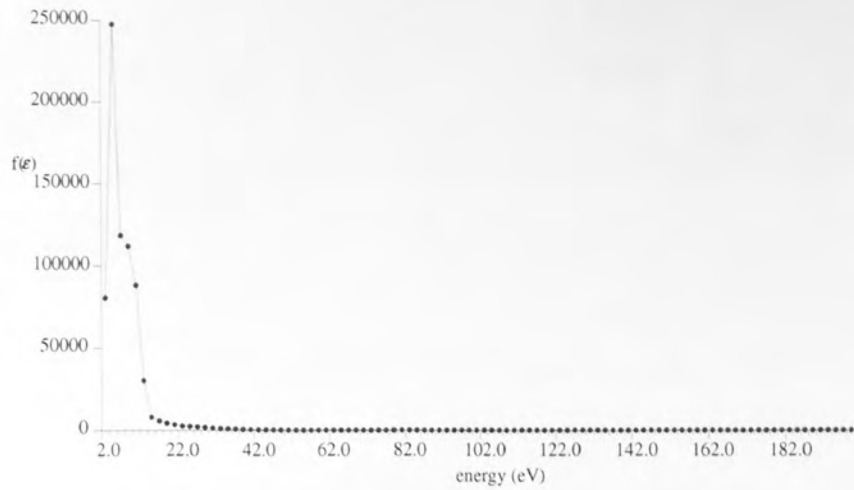

Figure 5.12 The EEDF, 50 mTorr.

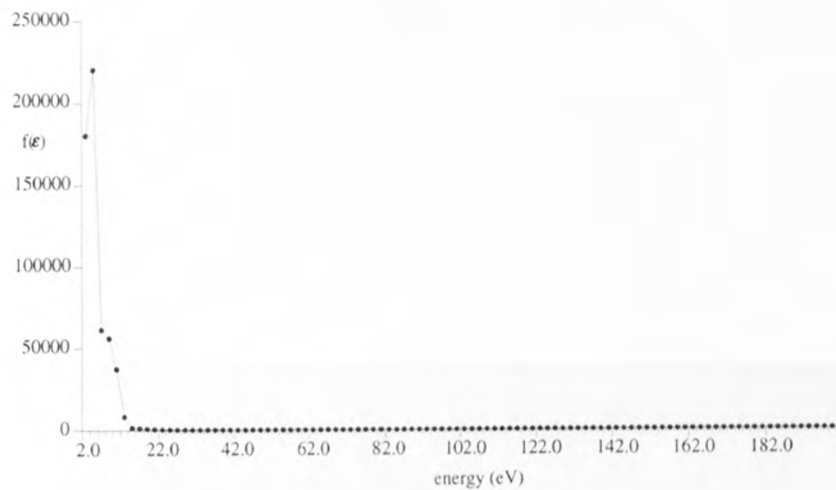

Figure 5.13 The EEDF, 90 mTorr.

For a Maxwellian distribution of electron energies $f(\varepsilon)$, we expect

$$f(\varepsilon) \propto \sqrt{\varepsilon} \exp\left(\frac{-\varepsilon}{kT_e}\right) \qquad \text{eqn 6.1}$$

Hence a plot of $\ln(f(\varepsilon)/\sqrt{\varepsilon})$ versus energy should yield a straight line. These predicted distributions are shown in figures 5.14, 5.15 and 5.16 for 10 mTorr, 40 mTorr and 80 mTorr respectively. The plots show in greater detail the reduction in the high energy tail with increasing pressure and henceforth the term EEDF will refer to the distribution plotted as $\ln(f(\varepsilon)/\sqrt{\varepsilon})$. It can be seen that the plots are distinctly non-Maxwellian and it is better to refer to the EEDF than to attempt to extract an electron temperature, as suggested by Surendra and Graves [268].

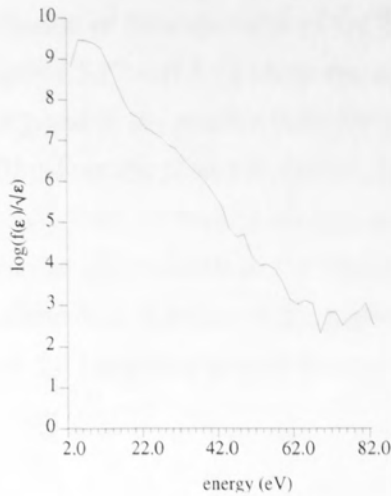

Figure 5.14 A plot of $ln(f(\varepsilon)/\sqrt{\varepsilon})$ against electron energy for a plasma at 10 mTorr.

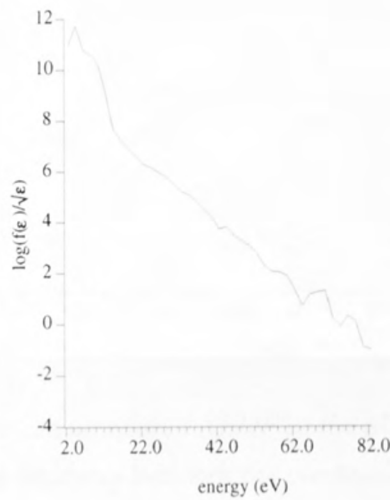

Figure 5.15 A plot of $ln(f(\varepsilon)/\sqrt{\varepsilon})$ against electron energy for a plasma at 40 mTorr.

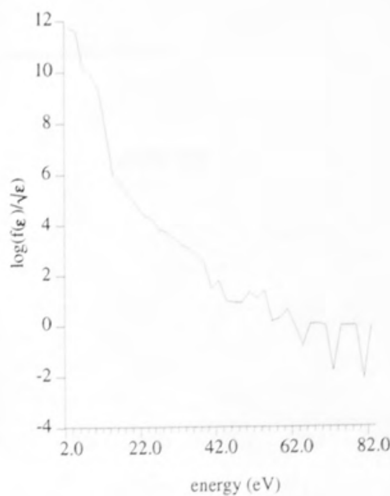

Figure 5.16 A plot of $ln(f(\varepsilon)/\sqrt{\varepsilon})$ against electron energy for a plasma at 80 mTorr.

As a result of the inhomogeneous power input to the plasma as witnessed by the ionisation

profile, a change in the position of measurement of the EEDF changes drastically the resulting distribution. Figures 5.17 and 5.18 show the superimposed EEDFs simulated at the plasma/sheath boundary and in the plasma bulk for pressures of 10 mTorr and 90 mTorr respectively. At 10 mTorr the plots are similar, but at the plasma/sheath boundary the function falls more slowly with increasing energy, whereas at 90 mTorr the EEDFs are completely different. It can be inferred that at the lowest pressures, the EEDF is relatively homogeneous over the plasma bulk whereas at the highest pressures, the position of measurement (*ie.* the tip of the Langmuir probe) is crucial to the final form of the distribution function.

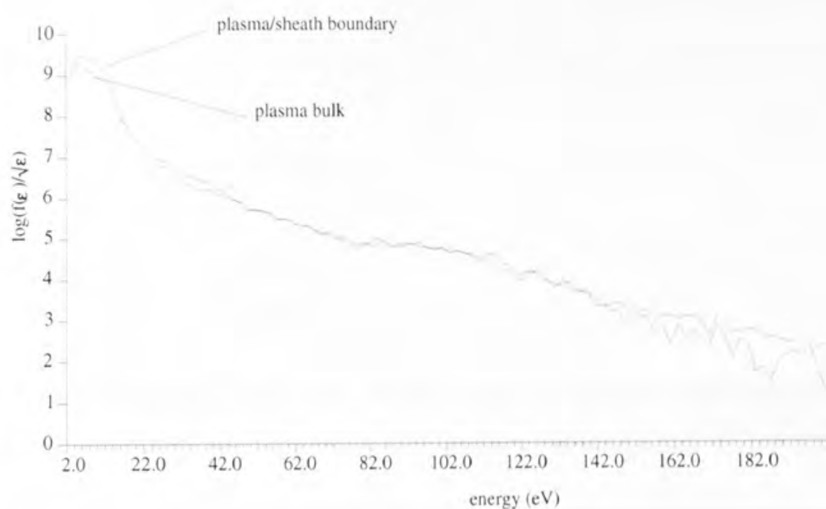

Figure 5.17 Comparison between simulated EEDF at the plasma/sheath boundary and in the plasma bulk (midway between the electrodes) at 10 mTorr.

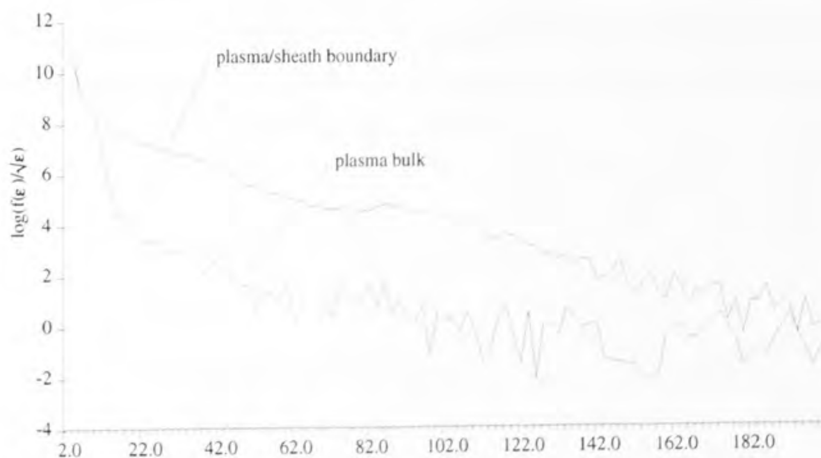

Figure 5.18 Comparison between simulated EEDF at the plasma/sheath boundary and in the plasma bulk (midway between the electrodes) at 90 mTorr.

The importance of the rotational and vibrational modes of excitation can be seen in figure

5.19. The contribution from rotational excitations appears negligible, but the contribution from vibrations appears substantial over the energy range where its cross section is effective (*ie.* <10eV). The resulting mass breakdown of the ionisation products will be unaffected, however, as most electrons which cause ionisation have energies greater than this.

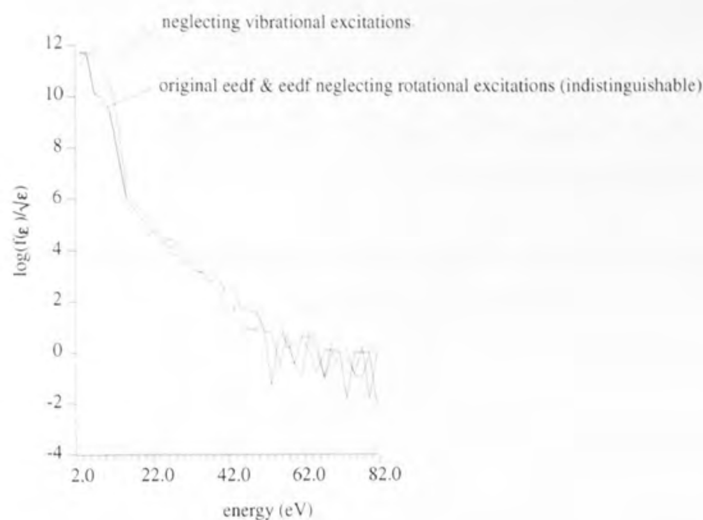

Figure 5.19 Simulated EEDF with EEDFs neglecting rotational and vibrational excitations superimposed, pressure = 90 mTorr, measured in the plasma bulk.

5.1.3 The effect of addition of methane

5.1.3.1 The floating potential

The addition of small amounts of methane drastically changes the electron ionisation probability. The lower ionisation threshold of methane (~12 eV compared to ~17 eV for hydrogen) increases the rate of ionisation and the electrons tend to cascade. Figure 5.20 shows the number of electrons which run for longer than the simulation time for different ratios of methane/hydrogen. The result is a lowering of the floating potential conducive to a multiplicity factor of 0.9 as shown in figure 5.21.

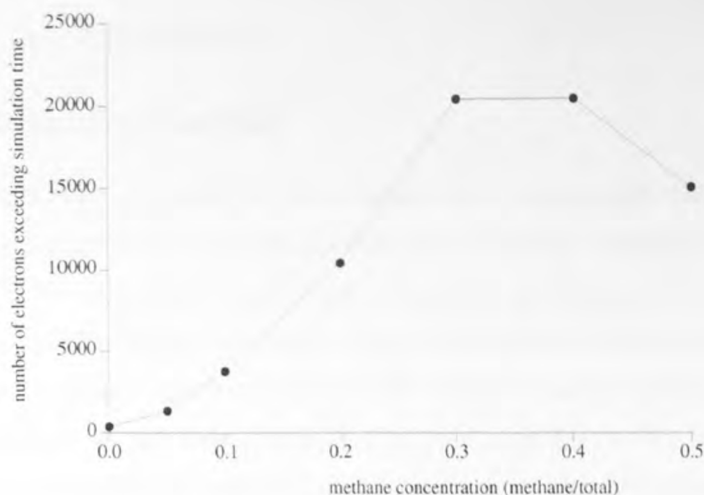

Figure 5.20 Number of electrons exceeding the simulation time as a function of the methane concentration.

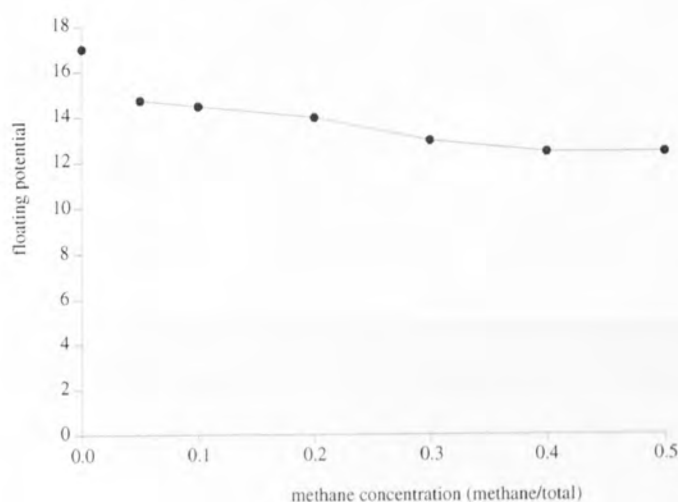

Figure 5.21 Floating potential as a function of the methane concentration.

5.1.3.2 The ion and electron distribution functions

An increase in methane concentration has a similar effect to that of an increase in pressure. The spatial distribution of the ions becomes more concentrated at the plasma/ sheath boundary where the ionisation increasingly takes place though to a lesser extent than a change in pressure over the range would cause.

5.1.4 Change in pressure of methane/hydrogen

Predictably, an increase in the pressure of a methane/hydrogen plasma (ratio 1:1) leads to an increase in the number of ionisations per electron in a similar way to that for pure hydrogen, though to a greater extent. The floating potential required to give an approximate electron balance therefore decreases as the pressure increases. The ion and electron distribution functions, ionisation profile, EEDFs *etc.* all behave as in the increase

in pressure in the pure hydrogen case.

5.1.5 Change in driving potential

An increase of the driving potential in the simulation has a profound effect. The preceding simulations were for a 150 W plasma with a driving potential, V_0 of approximately 500 V. Lower power plasmas with lower sheath potentials have decreased energy available to electrons and this causes fewer ionisations per electron and a consequent need to increase the floating potential. This decreased energy is mainly apparent at the cathode sheath with the result that the ionisation profile becomes increasingly symmetric as the driving potential decreases as shown in figure 5.22. The effect is almost identical in the hydrogen and the methane/hydrogen case.

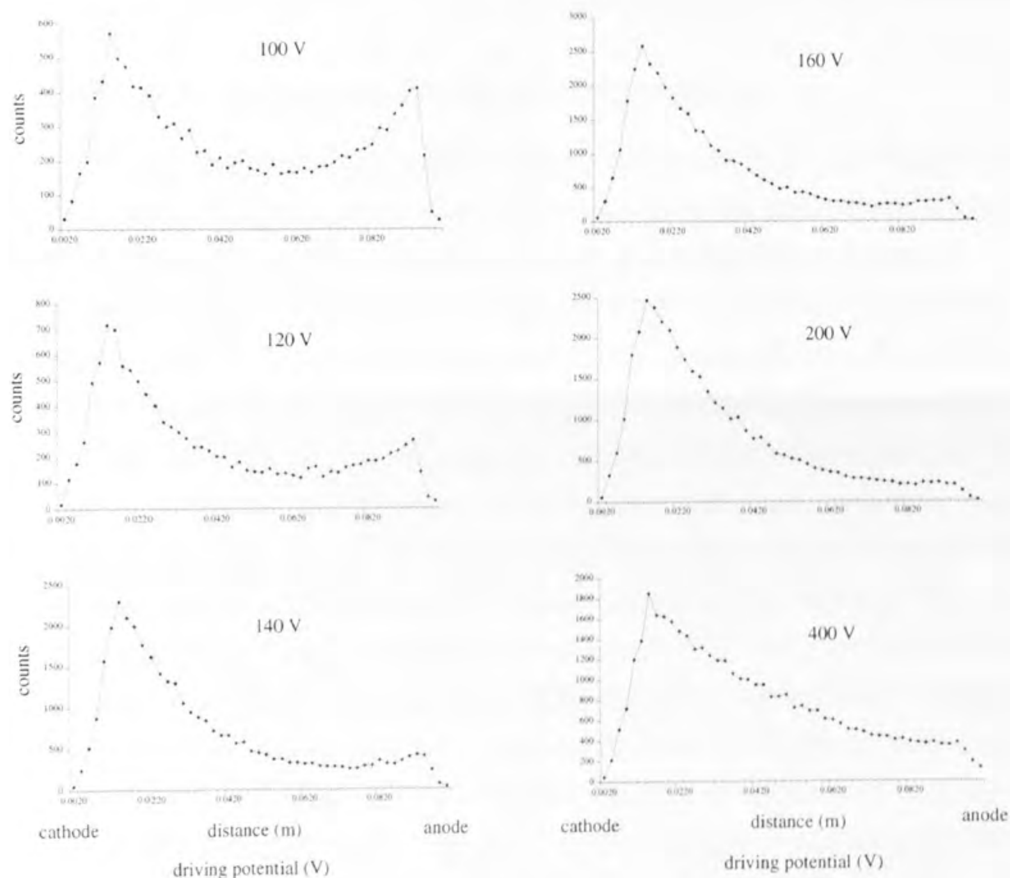

Figure 5.22 The ionisation profile, pure hydrogen, 40 mTorr, for a range of cathode driving potentials, V_0.

Figure 5.23 shows the simulated EEDFs for powers of 50 W, 100 W and 150 W. The plots are scaled such that their peaks are of equal height. It can be seen that there is a significant difference in the distribution especially below 100 eV where the statistics are good, the difference though is small and not expected to be resolvable with the Langmuir probe.

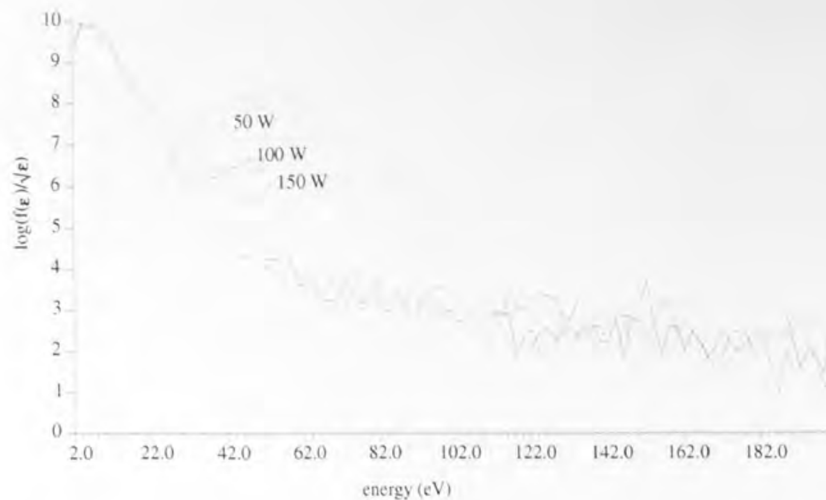

Figure 5.23. Simulated EEDF for powers of 50 W, 100 W and 150 W at a pressure of 10 mTorr, measured in the plasma bulk (midway between the electrodes), 12 % methane.

5.1.6 Change in secondary electron emission coefficient - γ

The effect on the plasma of changes in the secondary electron emission coefficient is of importance in practical applications where different cathode plate materials might be used. Such plates are often quartz as it is resistant to chemical etching, but can be other materials such as graphite. Theoretical investigations by Xu and Sides [269] found step changes in the secondary electron emission coefficient (γ) produced large changes in the plasma density. Changes in the value of γ for electron bombardment understandably caused no change in the EEDF. The effect is equivalent to electron reflection from the cathode which occurs almost entirely when the sheath potential is at a minimum. The resulting electron therefore reenters the plasma with only a small change in energy from when it first entered the sheath (the sheath is almost stationary with respect to the electron). Changes in the value of gamma from ion impact, did have a noticeable effect on the EEDF, however. This is likely to occur throughout the rf cycle and the resulting, often high energy, electrons can be an important source of energy to the plasma. Figure 5.24 shows the EEDFs measured in the plasma bulk for three simulations, where the value of γ was 0.1, 0.3 and 0.6 respectively. Figure 5.25 shows the effect is more noticeable at 10 mTorr and at the plasma/sheath boundary where most of the ionisations occur. The effect on the sustainability of the plasma is great, the high energy secondary electrons causing many of the ionisations. For the γ values of 0.1, 0.3 and 0.6, this leads to ionisation ratios (the total number of ionisations resulting from each initial arbitrary electron) of 7.7, 163 and 203 respectively for all other parameters being equal. In reality this would lead to a lowering of the average plasma potential.

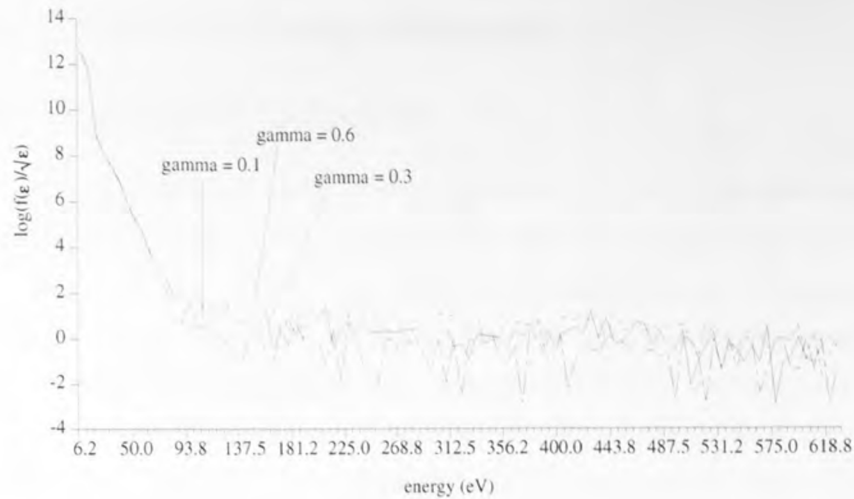

Figure 5.24 The effect on simulated EEDFs of changes in the ion impact secondary electron emission function at a pressure of 50 mTorr in the plasma bulk, 12 % methane.

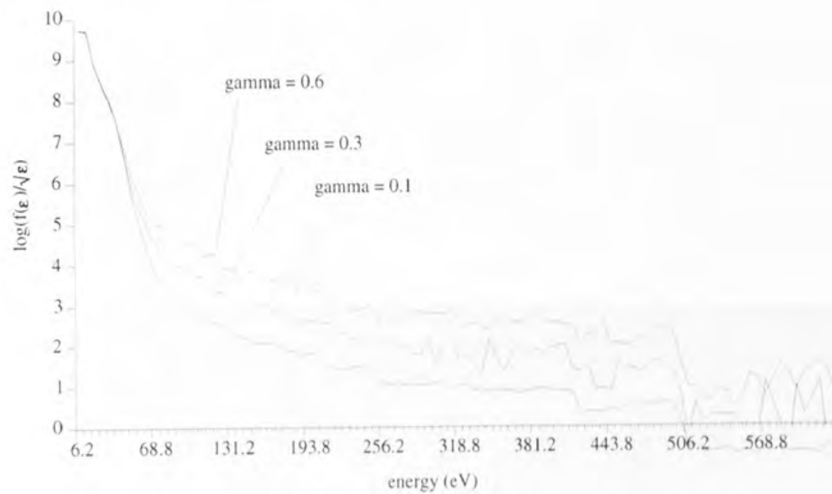

Figure 5.25 The effect on simulated EEDFs of changes in the ion impact secondary electron emission function at a pressure of 10 mTorr at the plasma/sheath boundary, 12 % methane.

It is also worth noting that over the range of pressures, powers and methane concentrations investigated, the form of the spatial distribution of the ionisations is almost identical (except in magnitude) for all the ion species created, though the form of the ionisation cross sections for each ion are quite different. If the form, therefore, is robust to changes in the EEDF, then the model for ion creation relies mainly on accurate knowledge of the ionisation cross sections.

5.2 Model for ions and neutrals

The changes to the fluxes and energies of the ions and neutrals created in the plasma can be investigated similarly.

5.2.1 Effect of change in pressure (hydrogen)

5.2.1.1 Ion energy and angle distributions

As the pressure is increased in a pure hydrogen plasma, there is an increase most noticeably in the mechanism of the creation of H_3^+ from H_2^+. This occurs throughout the plasma and increases the flux of H_3^+ ions at the expense of H_2^+ ions. This creation of H_3^+ can occur within the sheath, mostly when slow H_2^+ ions are created there by charge transfer and in conjunction with increased scattering, this lowers the average energy of H_3^+ ions. The average energy of the H_2^+ ions is reduced by symmetric charge transfer and scattering and the energy of the H^+ is reduced mainly by scattering. This is illustrated in figures 5.26 to 5.31 which show the energy distribution of the particles H^+, H_2^+ and H_3^+ at 10 mTorr and 90 mTorr respectively. The average particle energy for the three species is shown in figure 5.32.

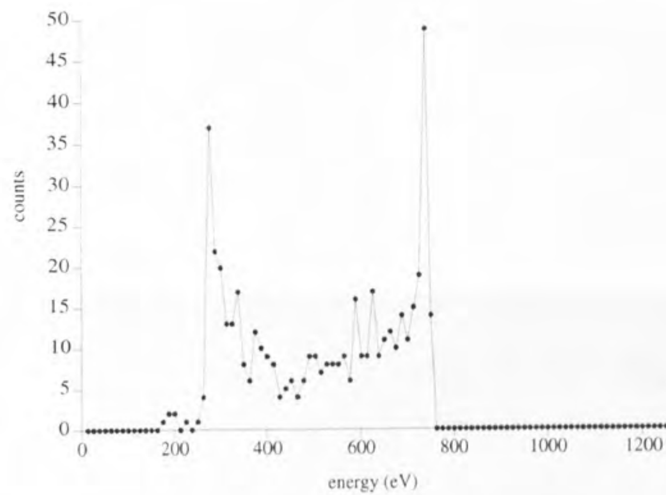

Figure 5.26 Predicted H^+ IEDs at the cathode for a pressure of 10 mTorr.

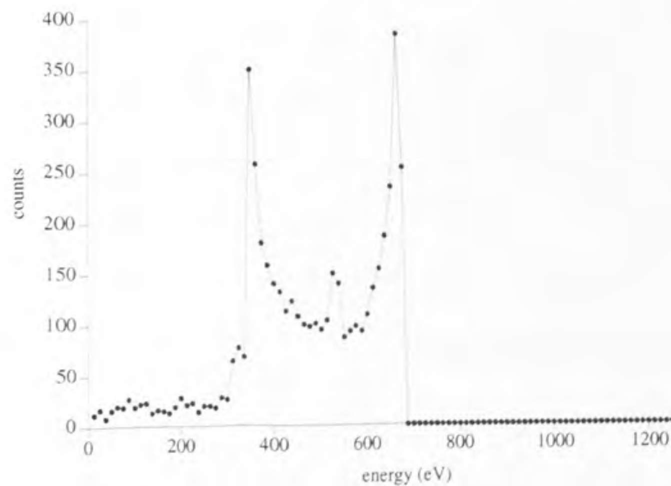

Figure 5.27 Predicted H_2^+ IEDs at the cathode for a pressure of 10 mTorr.

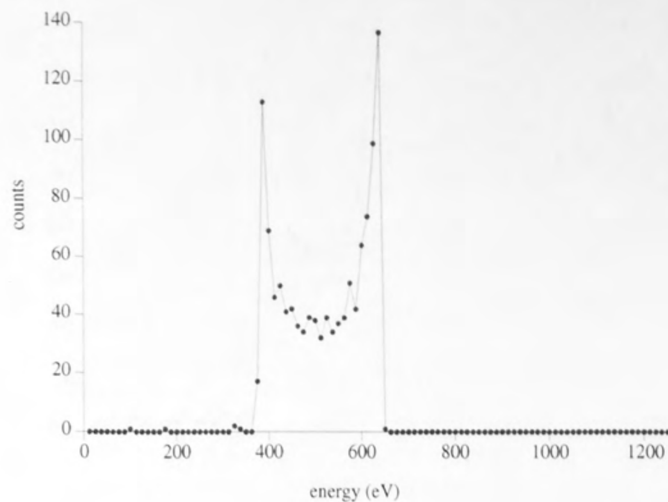

Figure 5.28 Predicted H_3^+ IEDs at the cathode for a pressure of 10 mTorr.

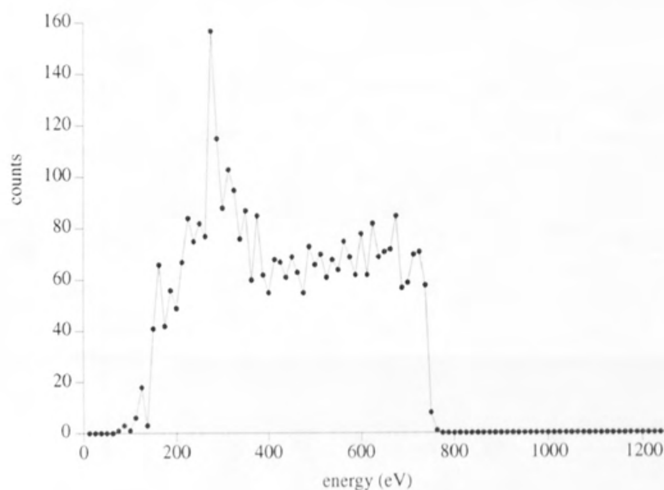

Figure 5.29 Predicted H^+ IEDs at the cathode for a pressure of 90 mTorr.

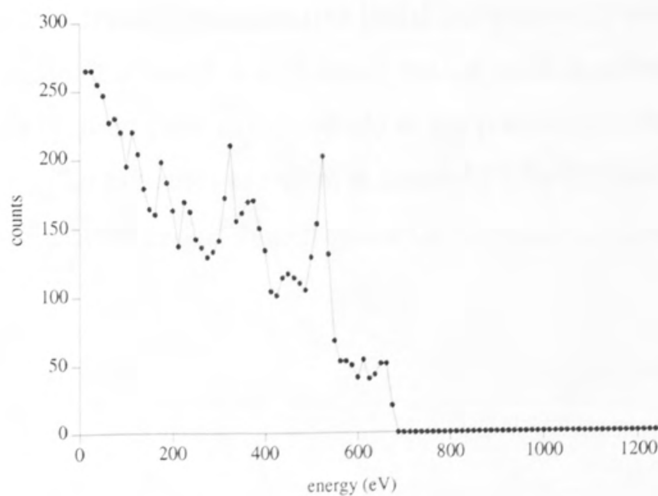

Figure 5.30 Predicted H_2^+ IEDs at the cathode for a pressure of 90 mTorr.

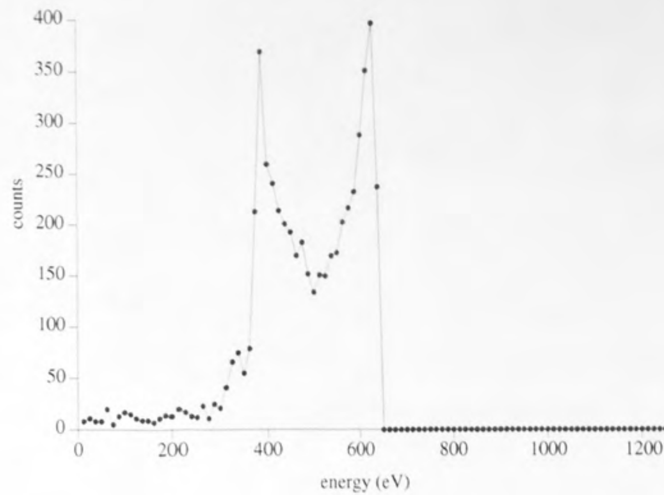

Figure 5.31 Predicted H_3^+ IEDs at the cathode for a pressure of 90 mTorr.

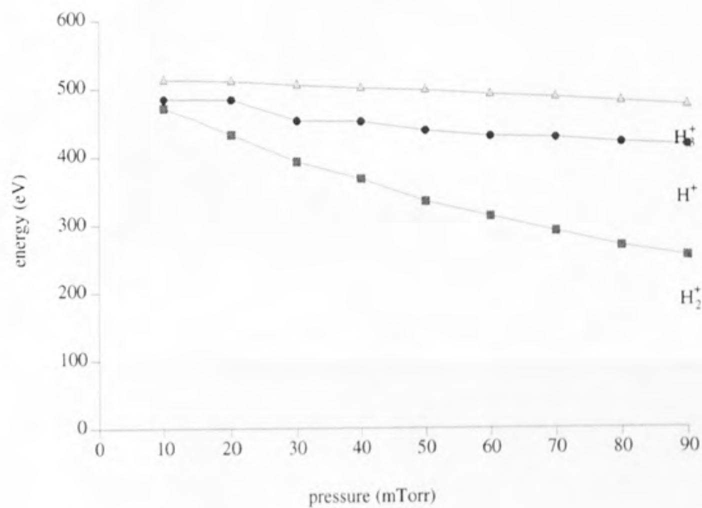

Figure 5.32 Average energy of the three ion species as a function of pressure.

Due almost entirely to scattering processes (the initial component of velocity parallel to the electrode of ions crossing the sheath is very small) the ion angle distributions change from being almost entirely perpendicular to the cathode at low pressures, to being spread to higher angles at the higher pressures as shown in figure 5.33 for H_3^+ ions at the cathode. The situation is similar at the anode, though with a smaller sheath, scattering is less evident.

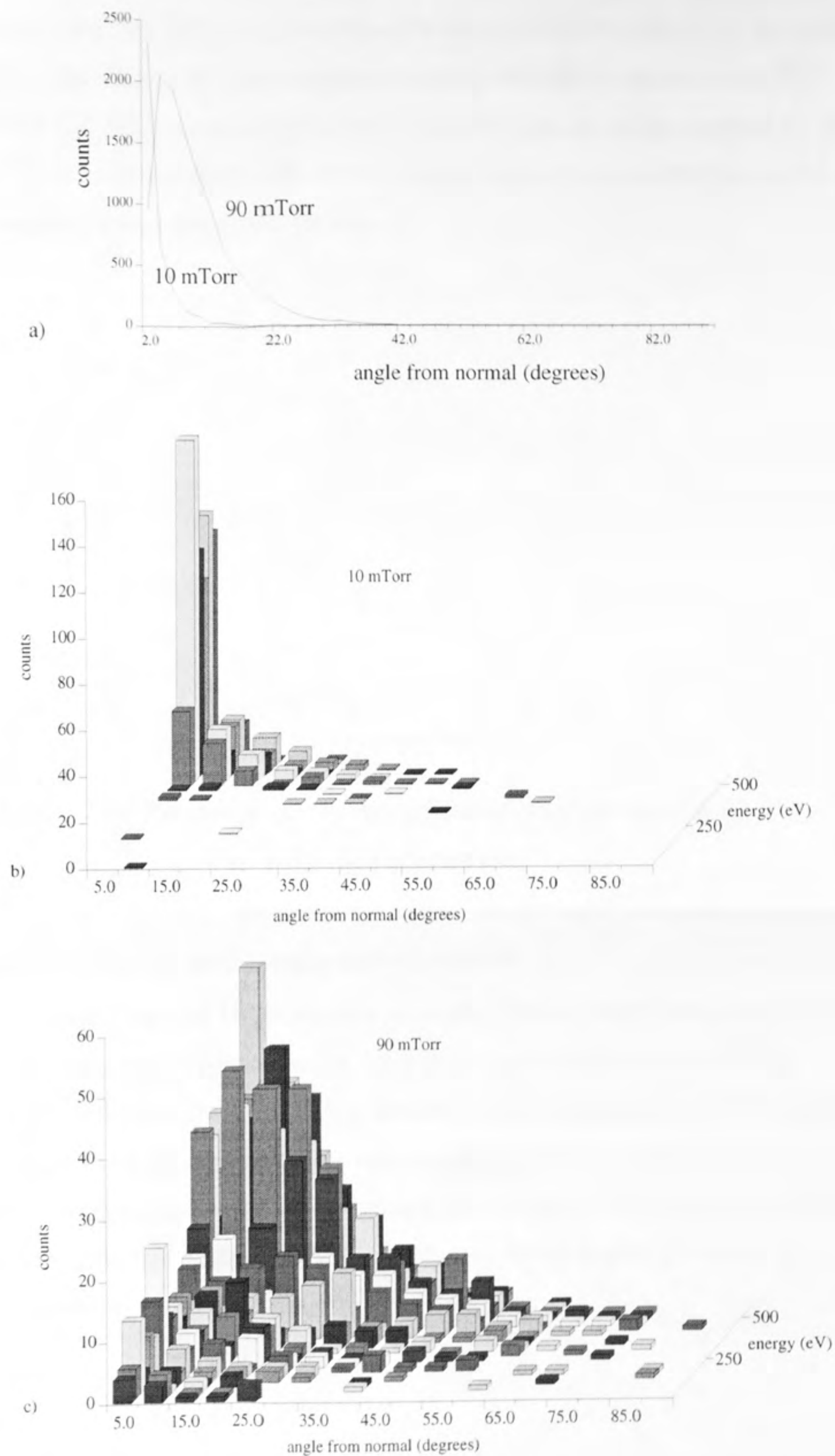

Figure 5.33 H_3^+ IAD at a) 10 mTorr and 90 mTorr b) 10 mTorr resolved into angle and energy and c) 90 mTorr resolved into angle and energy.

5.2.1.2 Ion fluxes

The relative flux of ions which arrives at the cathode is shown in figure 5.34. As the

pressure changes, the flux of H_2^+ is considerably reduced at the expense of an increased flux of H_3^+ ions. The flux of H^+ ions increases steadily with the pressure due to the increased flux of H_3^+ and its consequent destruction which results in the creation of H^+. The flux of H^+ ions is only slightly affected by charge transfer with neutral H_2 as this is an asymmetric reaction with a low cross section.

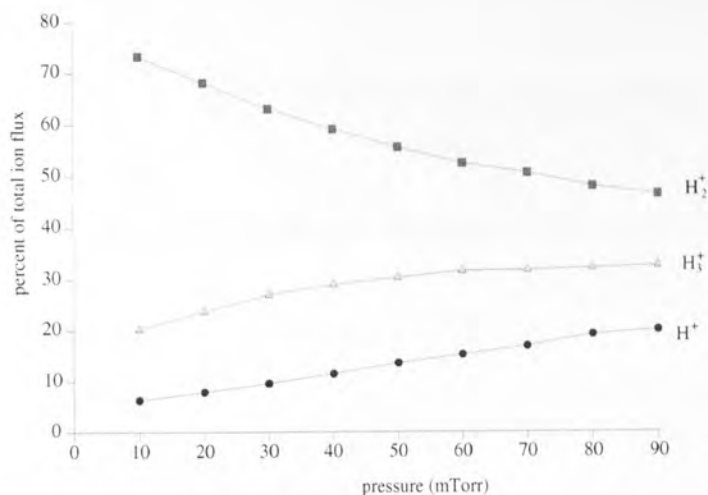

Figure 5.34 Relative fluxes to the cathode of the three ion species as a function of pressure.

5.2.1.3 Neutral energy and angle distributions

The energies of the fast neutral H_2 molecules are made of two components, those created by scattering are dominated by low energy, large impact parameter scatter recoils, whereas those created by asymmetric charge exchange have energies up to the maximum ion energy, though most are created at low relative energy where the cross section is highest. The resultant neutral energy distributions for the pressures of 10 mTorr and 90 mTorr are shown in figures 5.35 and 5.36 respectively. At the higher pressure, the neutrals are scattered to lower energies.

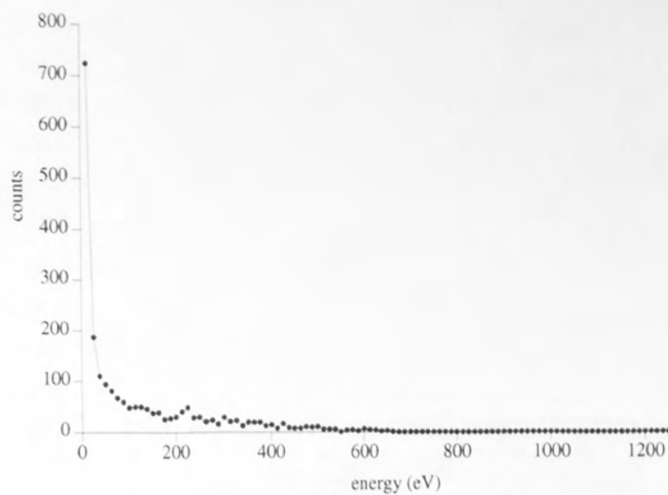

Figure 5.35 H_2 NED at the cathode at a pressure of 10 mTorr.

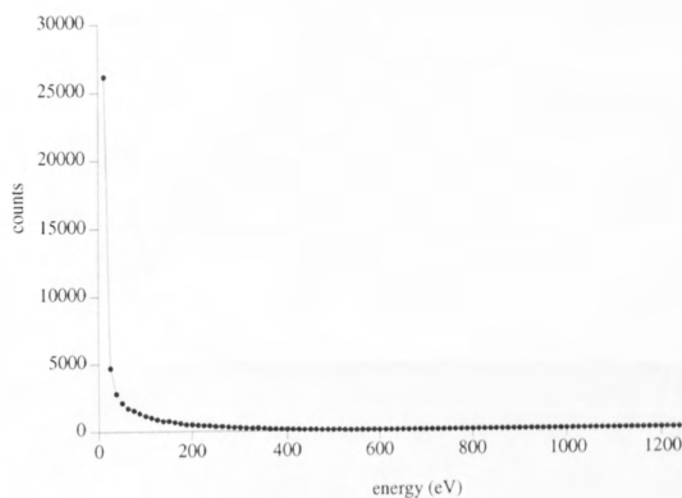

Figure 5.36 H_2 NED at the cathode at a pressure of 90 mTorr.

The angle distribution of the neutrals is close to isotropic except for the forward peak due to charge transfer especially at high pressure as shown in figures 5.37 and 5.38 for 10 mTorr and 90 mTorr respectively.

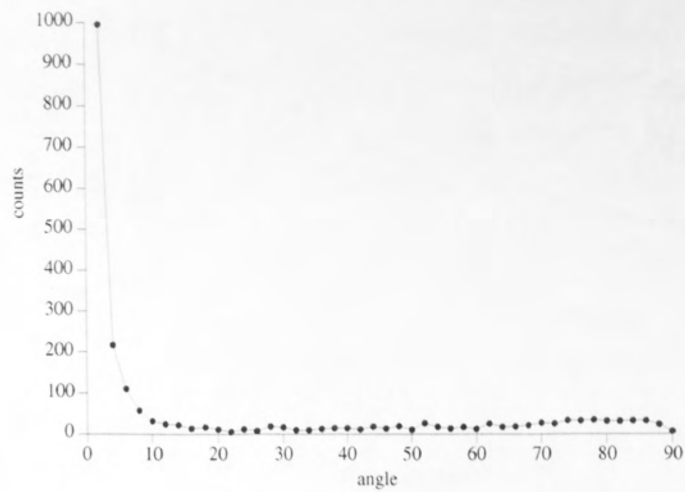

Figure 5.37 H_2 NAD at a pressure of 10 mTorr.

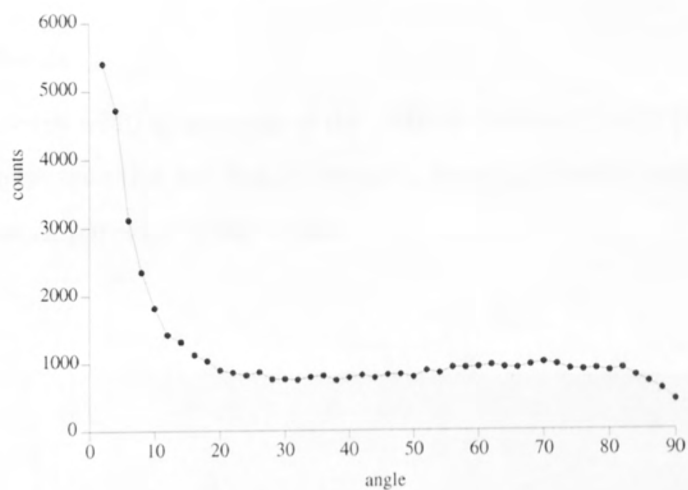

Figure 5.38 H_2 NAD at a pressure of 90 mTorr.

The average energy of a neutral arriving at the surface is shown in figure 5.39 as a function of pressure and can be seen to fall due to both a decrease in energy of the ions which create them and increased scattering in the sheath.

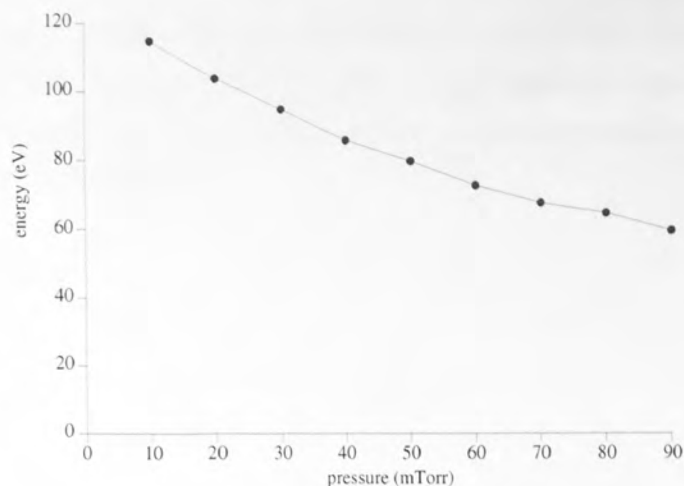

Figure 5.39 Average energy of neutral H_2 molecules arriving at the cathode as a function of pressure.

5.2.1.4 Neutral fluxes

The average number of neutrals arriving at the cathode (above 0.1 eV) per ion is shown in figure 5.40. It can be seen that the flux of neutrals, though of lower energy than the ions is an important flux of particles to the surface.

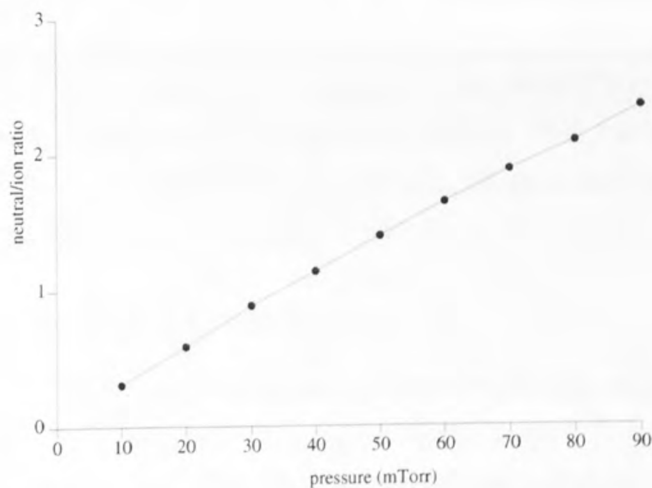

Figure 5.40 Ratio of neutrals to ions arriving at the cathode as a function of pressure.

5.2.2 Addition of methane

5.2.2.1 Ion energy and angle distributions

As the proportion of methane is increased, the effect on the ion energies is small.

5.2.2.2 Ion fluxes

The major effect of the increase in the partial pressure of methane is the change in the

ratio of the ions which arrive at the cathode as shown in figure 5.41. As the partial pressure of the methane increases, the proportion of hydrogen ions which arrive at the cathode drops drastically, due to the low ionisation potential of methane and the creation of the fragments CH_3^+ and CH_4^+.

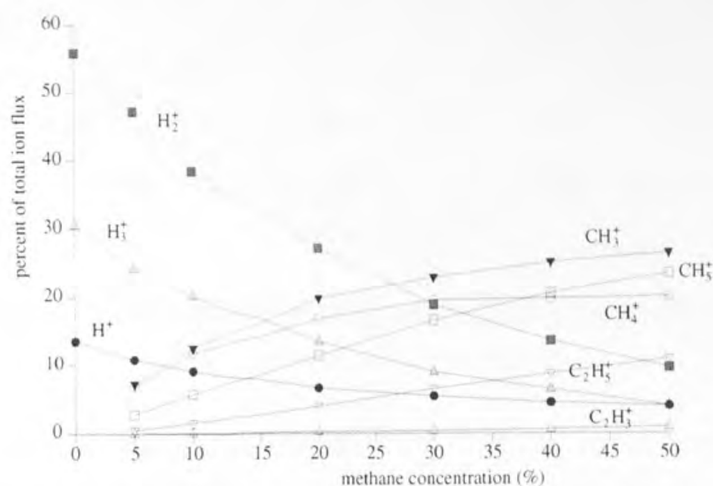

Figure 5.41 Relative fluxes to the cathode of the ion species as a function of methane concentration.

For example, at a methane partial pressure of only 5%, the methane fragments make up 18% of the flux and at a partial pressure of 50% of the total pressure, methane fragments make up 82% of the flux. As the pressure increases, creation of CH_5^+ from CH_4^+ and CH_4 becomes increasingly evident due to its large cross section. This reaction is analogous to the creation of H_3^+ discussed earlier. The flux of $C_2H_3^+$ is generally negligible, though the flux of $C_2H_5^+$ ions is substantial and generally mimics the CH_5^+ fluxes, though is lower.

5.2.2.3 Neutral energy and angle distributions

The average energy of the hydrogen neutrals is reduced by scattering with the heavier methane neutrals, but the average energy of the methane neutrals is less affected, possibly due to an increased production of fast CH_4 neutrals by charge transfer. Figure 5.42 shows the average energy of the neutral fragments as a function of the methane concentration.

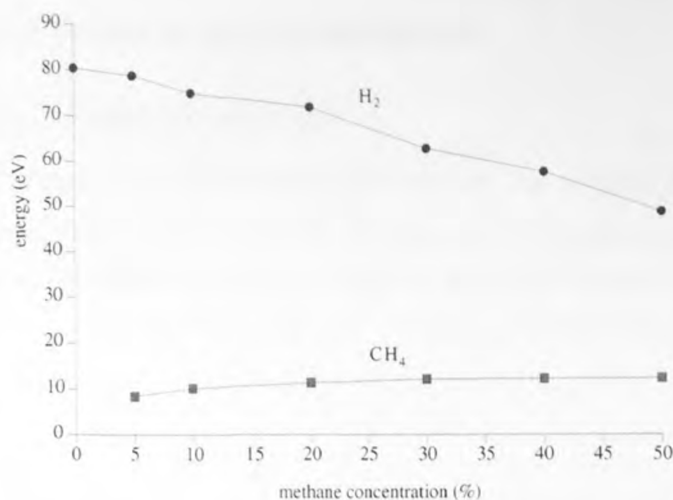

Figure 5.42 Average energies of H_2 and CH_4 neutrals at the cathode as a function of pressure.

The angle distributions of the neutrals are relatively isotropic and become more so for increases in methane concentration.

5.2.2.4 Neutral fluxes

As the methane ratio is increased, the neutral flux becomes increasingly dominated by CH_4 as shown in figure 5.43. At high methane ratios, the background gas available to be scattered is increasingly the neutral CH_4, but the reason the CH_4 neutral flux increases far beyond the 50 % partial pressure is that the majority of the ionic flux is methane fragments and these efficiently scatter from the methane background neutrals, increasing the recoil flux. Hydrogen neutrals on the other hand are more likely to be backscattered by methane neutrals and lost from the simulation.

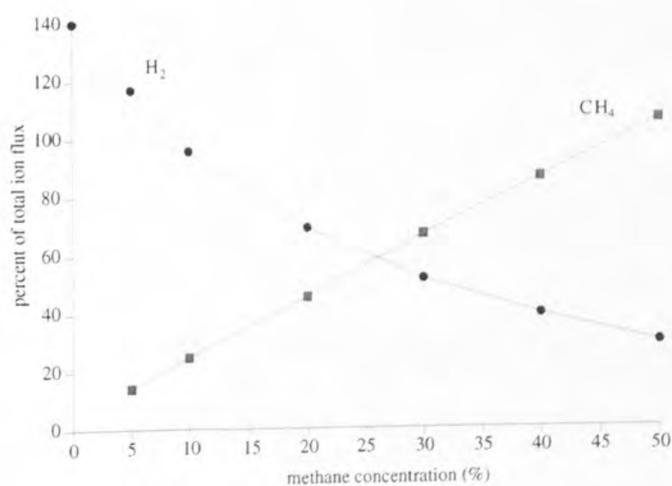

Figure 5.43 Flux of H_2 neutrals and CH_4 neutrals at the cathode as a percentage of total ion flux as a function of methane concentration, 40 mTorr

5.2.3 Change in pressure of methane/hydrogen

5.2.3.1 Ion energy and angle distributions

As the pressure increases in a methane/hydrogen mixture, the average energies of all the ion species is reduced due to both scattering and the various charge exchange and chemical reactions in the sheath. Figure 5.44 shows how this is most evident for H_2^+.

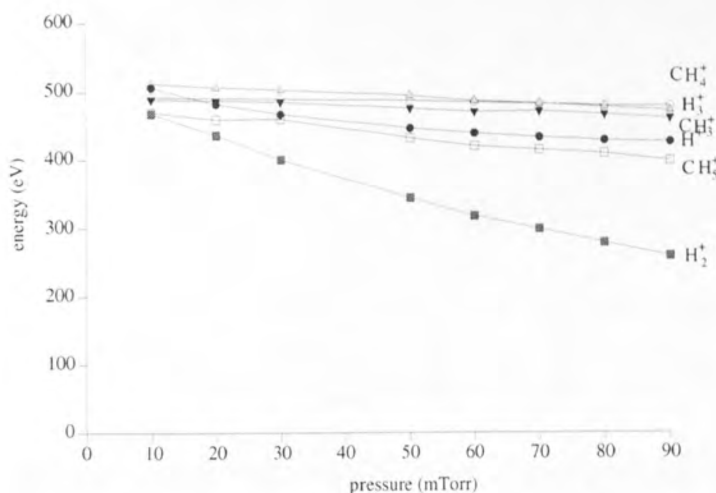

Figure 5.44 Average energy of the ion species at the cathode as a function of pressure.

5.2.3.2 Ion fluxes

The fluxes to the cathode change as the pressure is increased, with H_2^+ and H_3^+ shadowing the pure hydrogen case and the CH_4^+ ions decreasing due to the various destruction mechanisms. The result is displayed in figure 5.45.

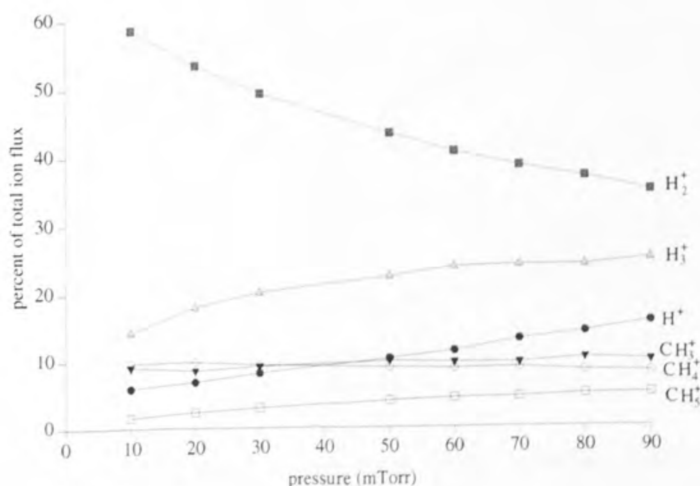

Figure 5.45 Relative fluxes to the cathode of the ion species as a function of pressure

5.2.3.3 Neutral energy and angle distributions

Similarly to the pure hydrogen case, the energy distributions of the neutral particles are peaked at low energies and their higher energy tails diminish as the pressure increases. The average energy of the neutrals as a function of pressure is shown in figure 5.46.

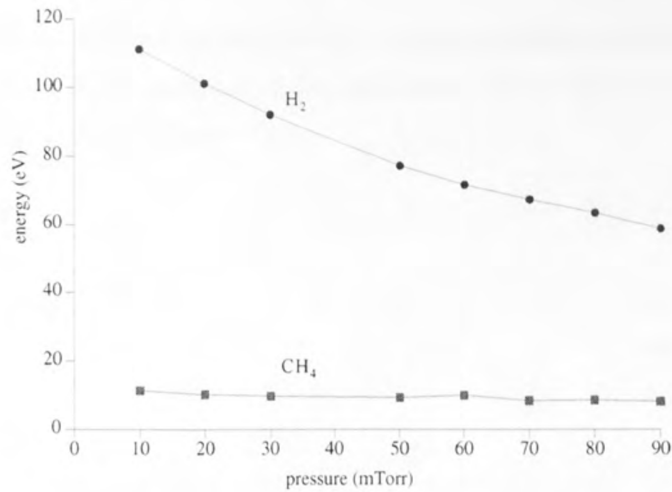

Figure 5.46 Average energy of H_2 and CH_4 neutrals at the cathode as a function of pressure.

5.2.3.4 Neutral fluxes

The neutral fluxes of both H_2 and CH_4 increase as the pressure increases as shown in figure 5.47.

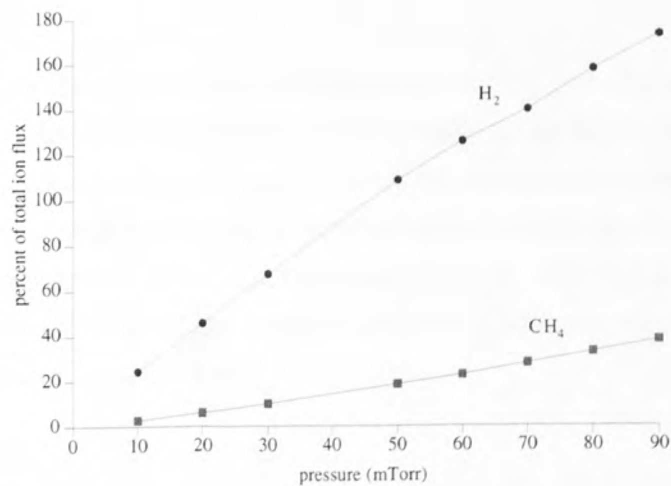

Figure 5.47 Relative flux of H_2 and CH_4 neutrals at the cathode as a function of pressure.

5.2.4 Change in driving potential (hydrogen)

Changing the driving potential, equivalent to changing the power input to the plasma elicits results which are summarised below.

5.2.4.1 Ion energy and angle distributions

The average energies of the ions at the cathode increase linearly with the driving potential as a consequence of the linear increase in the maximum sheath potential with the driving potential. This is illustrated in figure 5.48.

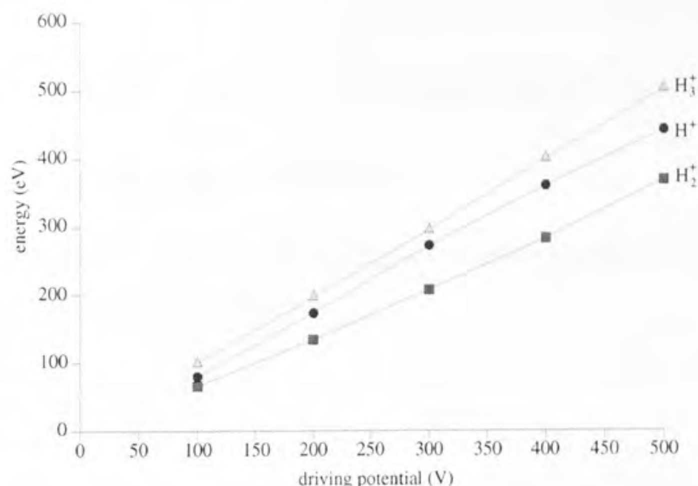

Figure 5.48 Average energy of the ion species at the cathode as a function of driving potential.

5.2.4.2 Ion fluxes

The relative fluxes of the ion species change with the driving potential as shown in figure 5.49. The change is due to either the change in the form of the EEDF which when convoluted with the ionisation cross sections gives the mass distribution of ionised particles, or due to a change in the spatial distribution of ionisations. *ie.* an ion creation profile which is more peaked at the plasma sheath boundary will lead to a greater proportion of H_2^+ ions arriving at the cathode than for the situation where the spatial ion creation profile is more homogeneous.

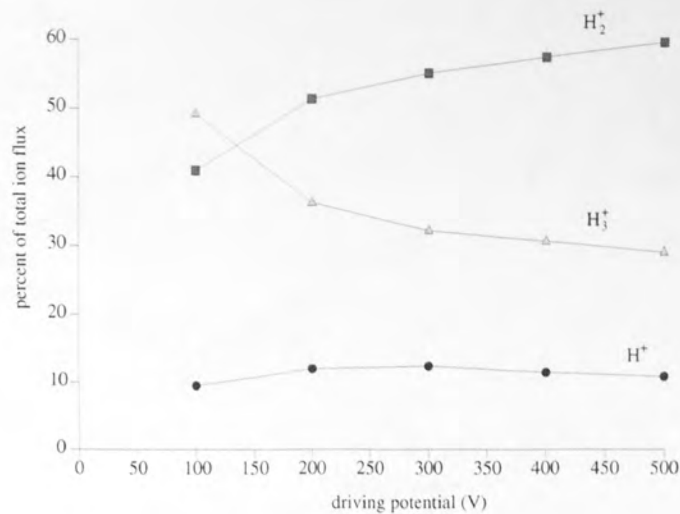

Figure 5.49 Relative flux of ions at the cathode as a function of driving potential.

5.2.4.3 Neutral energy and angle distributions

As a consequence of the ion energies increasing with increasing power, so do the average neutral energies as shown in figure 5.50.

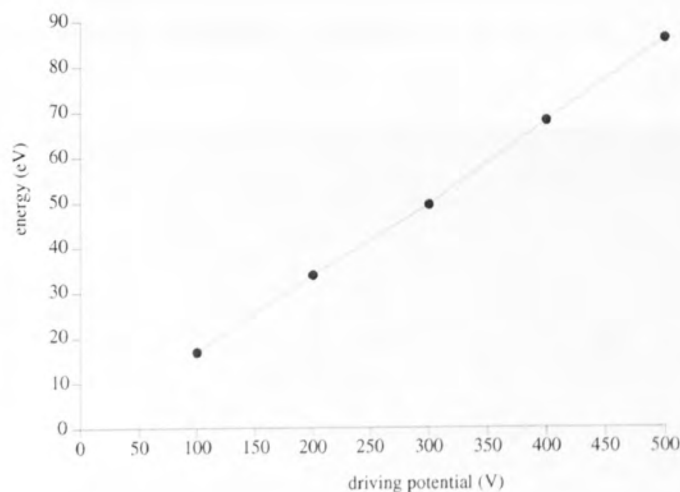

Figure 5.50 Average energy of H_2 neutrals at the cathode as a function of driving potential.

The neutral fluxes are, however, independent of the driving potential.

5.2.5 Change in driving potential (methane/hydrogen)

5.2.5.1 Ion energy and angle distributions

An increase in the driving potential for a mixture of methane and hydrogen gives a similar increase in ion energies as for the pure hydrogen case.

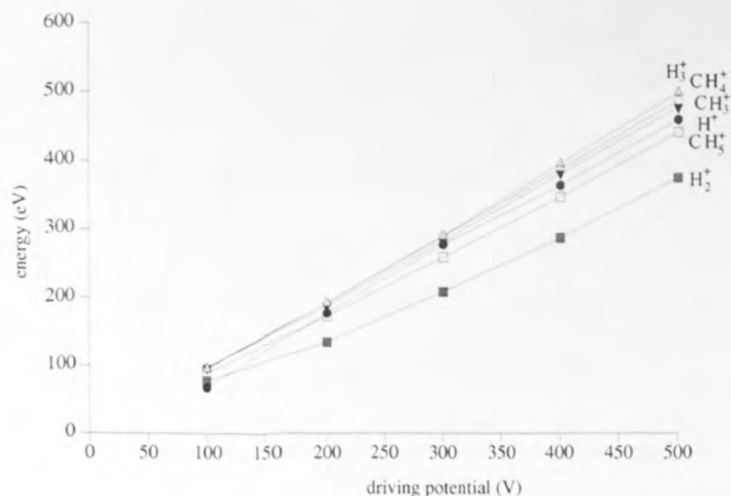

Figure 5.51 Average energy of ions at the cathode as a function of driving potential.

5.2.5.2 Ion fluxes

There is an interesting result for the ion fluxes, in that below 200 V driving potential, the fluxes change considerably. The H_2^+ ion becomes more dominant as the driving potential increases as a consequence of the spatial ionisation distribution becoming more asymmetric and an increasing proportion of ions are created close to the cathode. This has the opposite effect on the flux distribution at the anode as shown in figure 5.53.

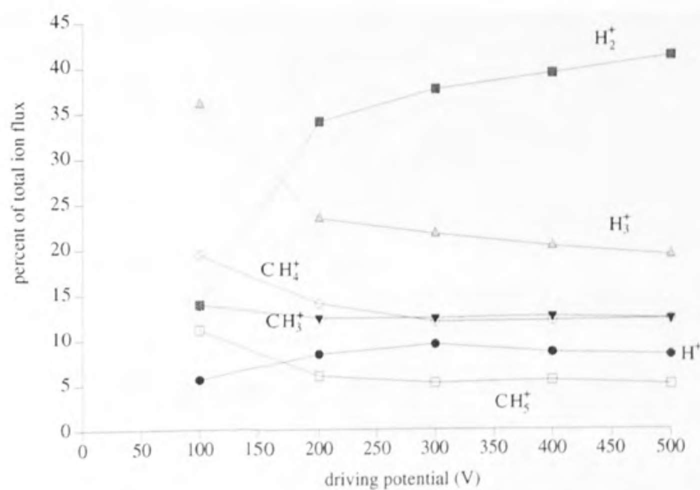

Figure 5.52 Relative flux of ions at the cathode as a function of driving potential.

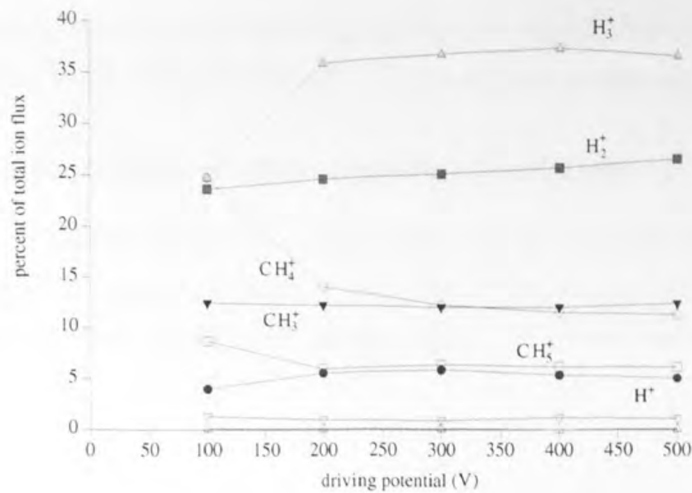

Figure 5.53 Relative flux of ions at the anode as a function of driving potential.

5.2.5.3 Neutral energy and angle distributions

The average energy of the CH_4 and H_2 neutrals increases linearly with the driving potential as in the pure hydrogen case. The average energies of the neutrals are shown in figure 5.54. The neutral fluxes to the surface of the cathode are almost unchanged as the driving potential increases.

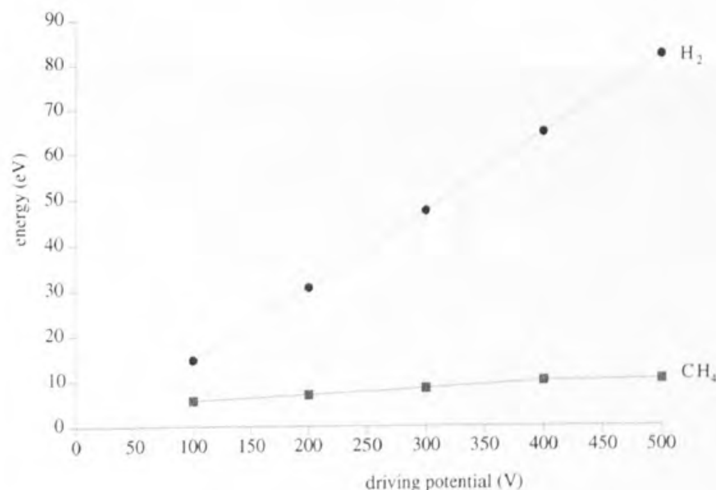

Figure 5.54 Average energy of neutrals at the cathode as a function of driving potential.

5.2.6 Change in the cathode sheath width

The sheath width is one of the most important parameters which determines the ion energies. A doubling of the sheath width for example changes the width of the saddle structure in the IED, making it narrower and causing ions to have energies closer to the sheath average potential. The energies of ions at the cathode are also generally reduced due to increased scattering. Ions with large cross sections for inelastic collisions will correspondingly have their average energies reduced further. The creation of neutrals is greater with an increase in the sheath width. Doubling the sheath leads to a doubling in

the neutral to ion ratio with the neutrals being scattered to slightly lower energies. There is, however, no significant change in the ratio of ions arriving at either cathode or anode.

5.2.7 Change in secondary electron emission coefficient - γ

Though the value of γ has been shown to be important for the form of the EEDF, it causes negligible changes in the predicted fluxes or energies of ions and neutrals at the surface (though it is likely that the total flux will change with the degree of ionisation of the plasma).

Chapter 6. Experimental Results

6.1 Plasma diagnostics

6.1.1 Langmuir probe

6.1.1.1 Argon

Argon plasmas tend to give the most consistent results from the Langmuir probe, probably due to it being inert, while the heavy ion bombardment of the probe tip when the probe voltage is negative keeps the tip clean. Figure 6.1 shows the plasma potential as a function of the pressure. The plasma potential measured is some average of the plasma potential over one rf cycle. As the pressure is increased, the mean free path of the electrons in the plasma decreases and the average plasma potential falls in order that the electrons can more easily escape to the walls.

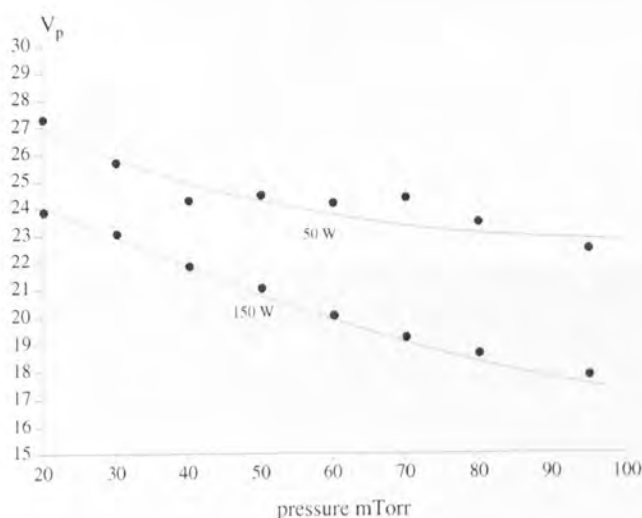

Figure 6.1 Plasma potential as a function of pressure for a 50 W and 150 W argon plasma

At pressures below 20 mTorr, the results become very noisy. This is a result of the cathode sheath width increasing at low pressure and the probe tip sampling the sheath rather than the plasma. The positive space charge in the sheath leads to the probe current being severely reduced. This change in the position of the plasma/sheath boundary with respect to the position of the probe tip is a severe problem for the analysis of the Langmuir probe results. The assumption made of the spatial invariance of the plasma parameters in the plasma bulk is possibly more true of argon which has a very abrupt plasma/sheath boundary than of hydrogen where the boundary is both tenuous and extended. It is perhaps this which also leads to the better Langmuir probe results from the argon plasma than from hydrogen. For simulations of helium type plasmas for instance [270] the average electron energy is predicted to change by 100 % from the plasma bulk to a peak at the

plasma/sheath boundary. The electron and the ion density for the same plasmas are shown in figures 6.2 and 6.3 respectively.

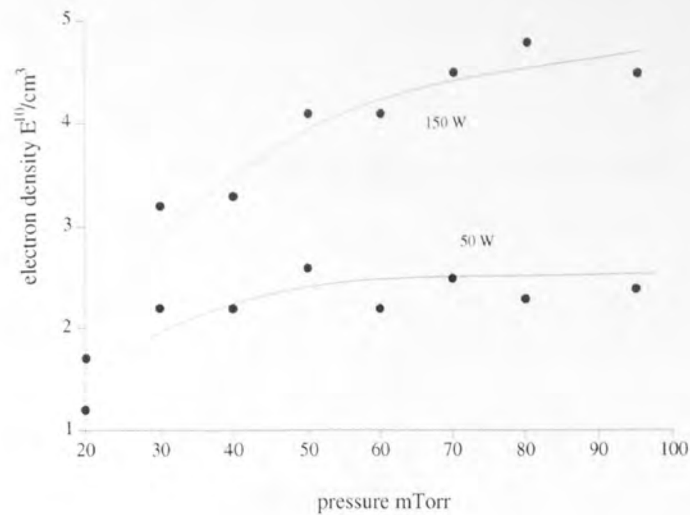

Figure 6.2 The electron density as a function of pressure for a 50 W and 150 W argon plasma.

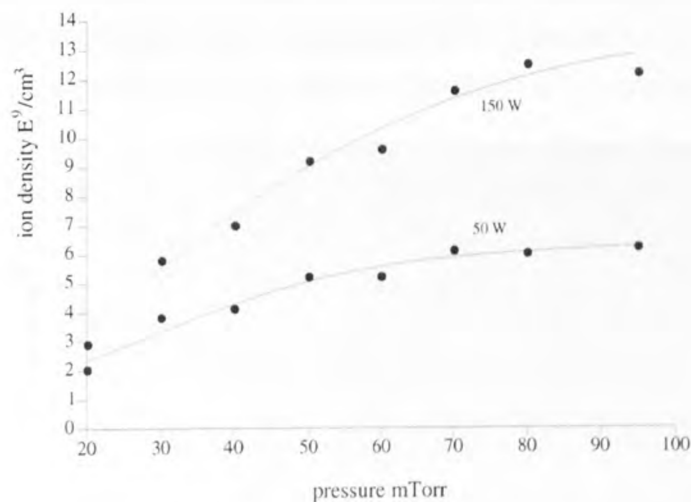

Figure 6.3 The ion density as a function of pressure for a 50 W and 150 W argon plasma

6.1.1.2 Hydrogen

Figure 6.4 shows the plasma potential of 50 W and 150 W hydrogen plasmas calculated using either the point at which the 2nd differential of the electron current is zero or by the crossing of the two tangents to the logarithm of the electron current as discussed in section 2.2.1. The potential again reduces as the pressure increases but the results contain larger errors probably due to contamination on the probe tip. This contamination is not so easily sputter cleaned by the light hydrogen ions, though doing this by holding the tip at a large negative potential does improve the results. Figure 6.4 shows the results from one set of experiments. Measurements taken at other times show the same trend but with systematic

error in the results, possibly due to the extent and nature of contamination in the chamber.

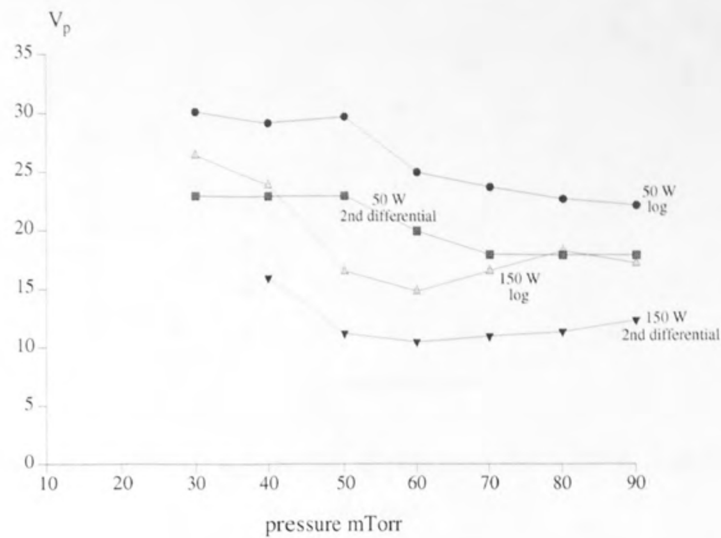

Figure 6.4 Plasma potential as a function of pressure for a 50 W and 150 W hydrogen plasma.

Figures 6.5 and 6.6 show the ion and electron density for the same plasmas as in figure 6.4. The ion and electron density both rise with increasing pressure, but again the results are complicated by the movement in the tenuous plasma/sheath boundary.

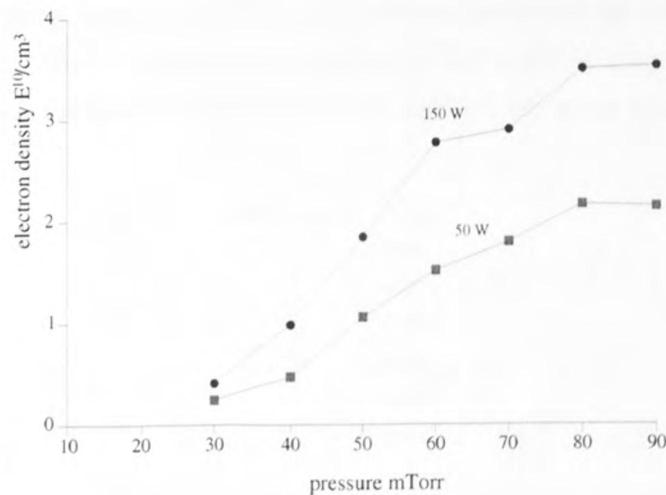

Figure 6.5 The electron density as a function of pressure for a 50 W and 150 W hydrogen plasma

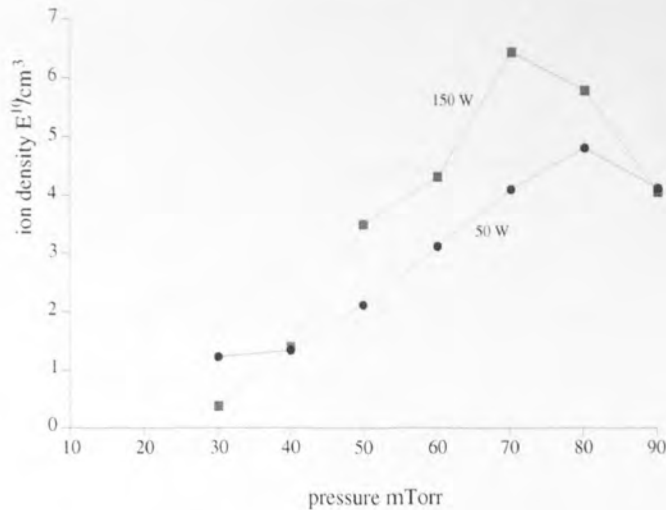

Figure 6.6 The ion density as a function of pressure for a 50 W and 150 W hydrogen plasma

Figure 6.7 is the original *I-V* characteristic for a 50 mTorr pure hydrogen plasma at a power of 100 W. It can be seen that the plasma potential is between about 10 and 20 V. After having the small ion current removed, the logarithm of the resulting pure electron current is found and displayed in figure 6.8. For a Maxwellian electron energy distribution, the portion of the graph between around 6 V and 15 V should be a straight line, the gradient of which gives the electron temperature. The saturation electron current also yields a straight line, the intersection of the two giving the plasma potential. As can be seen, however, the portion which gives the information about the electron temperature is not a straight line. The resulting plasma potential and electron temperature have an error associated with them which depends on the form of this portion of the characteristic.

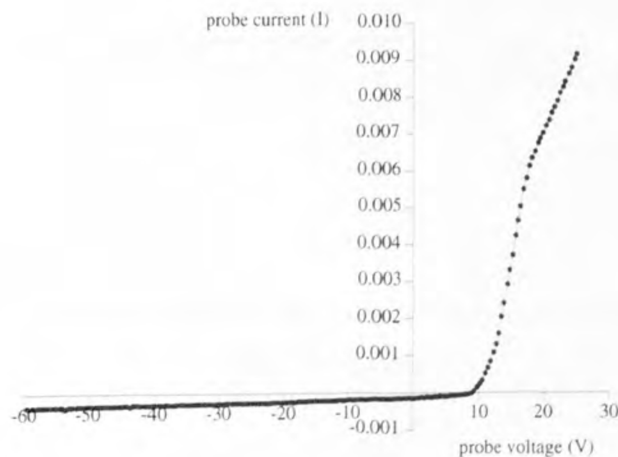

Figure 6.7 The probe I-V characteristic for a 100 W 50 mT hydrogen plasma (sum of 10).

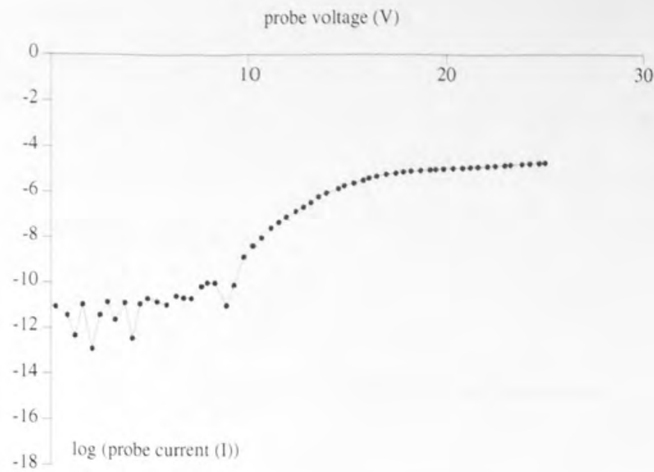

Figure 6.8 The logarithm of the pure electron current for a 100 W 90 mT hydrogen plasma.

Due to the non-Maxwellian appearance of the electron energy distribution function, it is perhaps more sensible to talk about the electron energies than an electron temperature [271]. The electron energy distribution function (EEDF) is found from the second differential of the probe characteristic. Figure 6.9 shows the second differential of the electron current for the same plasma conditions as figure 6.7. Assuming the plasma potential is equal to the crossing point of the second derivative (16 V) then the EEDF is given by the function in figure 6.10.

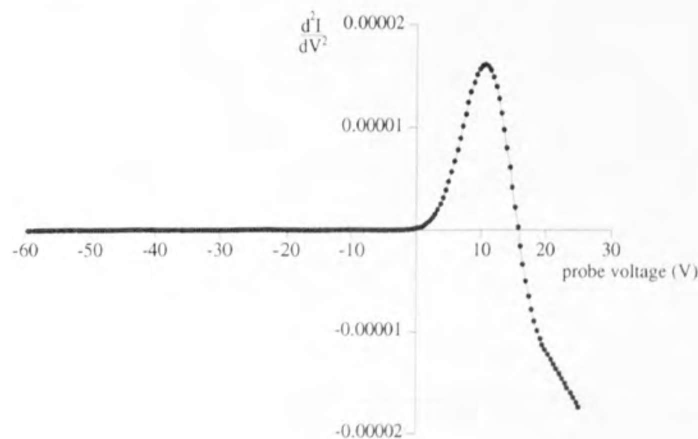

Figure 6.9 The second differential of the pure electron current for a 100 W 90 mT hydrogen plasma.

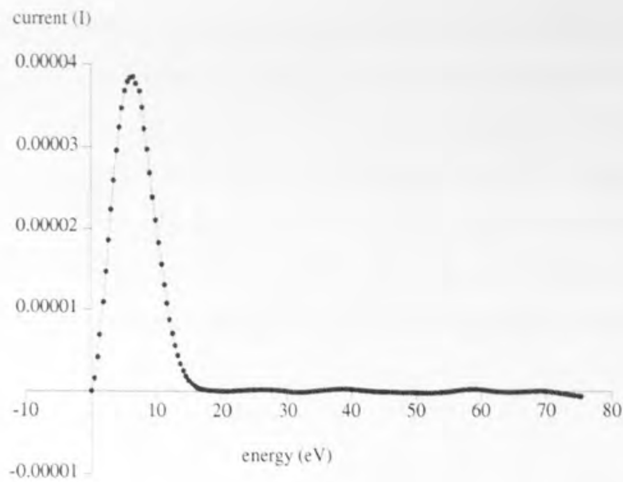

Figure 6.10 The electron energy distribution function assuming Vp is 16 V.

Due to the uncertainty in the plasma potential, however, and that some now use the maximum of the second differential of the electron current [272], the EEDF could be that shown in figure 6.11 for a plasma potential of 10.5 V.

In conclusion, the uncertainty in the measurements from the Langmuir probe due to difficult reproducibility, the non-Maxwellian nature of the EEDF and the spatial non-stationarity of the plasma over the region of sampling of the probe make the results comparable only in a qualitative way.

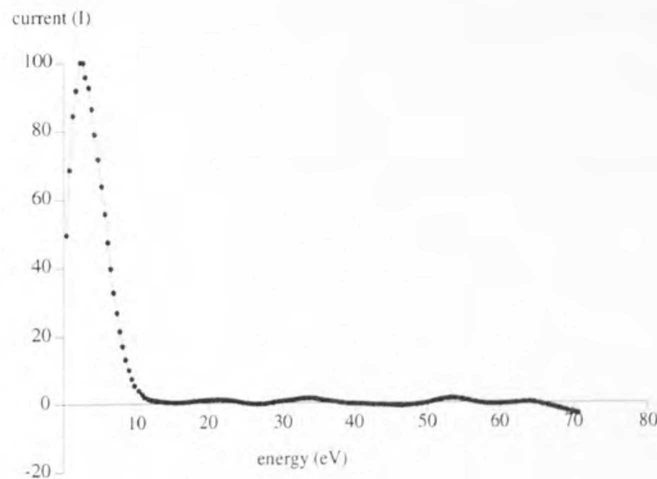

Figure 6.11 The The electron energy distribution function assuming Vp is 10.5 V.

6.1.1.3 Methane/hydrogen

For methane/hydrogen mixtures, the problem of fouling of the probe tip is extreme. Different ratios of methane to hydrogen in the plasma lead to either deposition or non-deposition on the cathode or quartz plate. All ratios, however, lead to deposition on surfaces exposed to the bulk of the plasma, where the small potential between plasma and tip does not lead to its easy sputter cleaning. As more characteristics are taken, the layer

of deposition on the probe increases and this decreases the current drawn from the plasma. Only prolonged exposure to a pure hydrogen or preferably oxygen plasma at high tip/ plasma potential fully restores the current. This makes it impossible to sum characteristics together to minimise statistical error. This point is illustrated in figures 6.12 to 6.14. Figure 6.12 shows the superposition of 5 characteristics from a hydrogen plasma. These are very similar and 10 are generally summed to give the final characteristic. In figure 6.13, with the introduction of some methane, each subsequent characteristic taken 20 or so seconds later has a lower current. Figure 6.14 shows the case for a higher addition of methane with the effect being greater again.

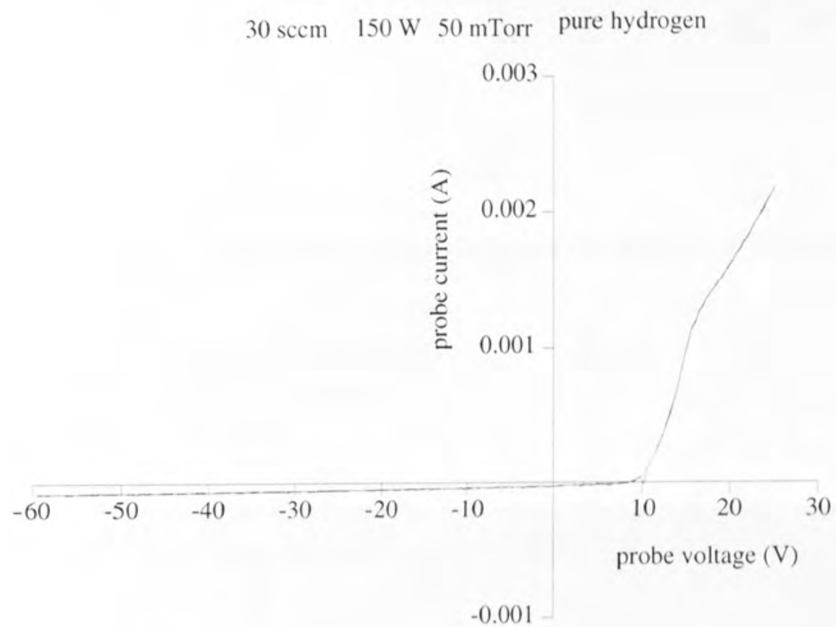

Figure 6.12 Five I-V characteristics superimposed for pure hydrogen.

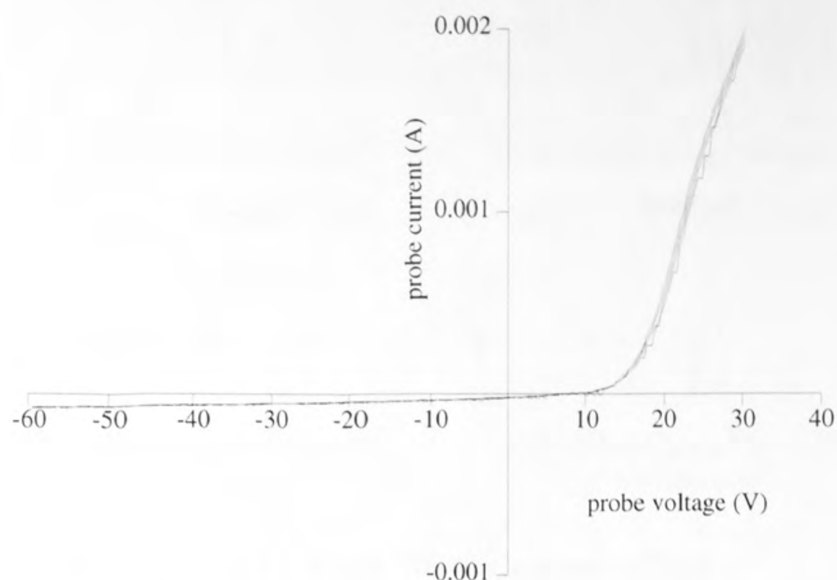

Figure 6.13 Five I-V characteristics superimposed for methane/hydrogen = 1/7.

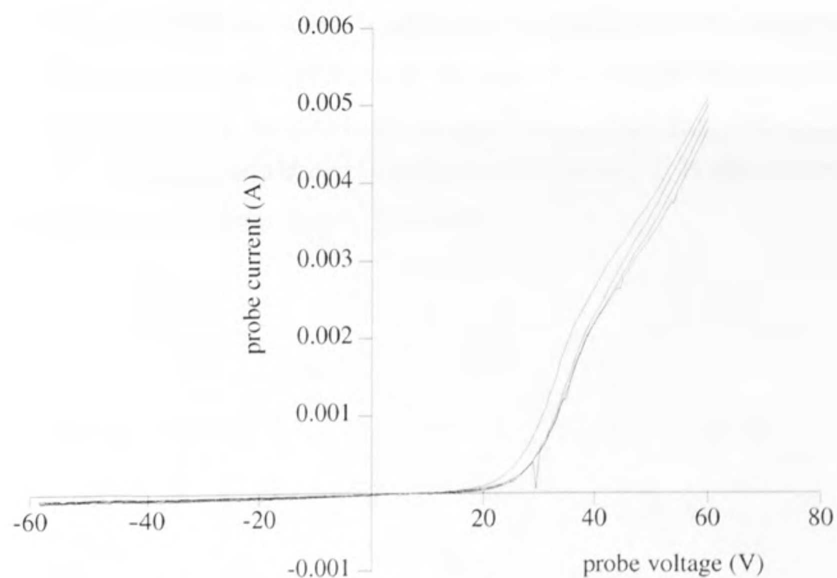

Figure 6.14 Five I-V characteristics superimposed for methane/hydrogen = 1/1.

6.1.2 Mass probe

6.1.2.1 Results

The sheath formed over the anode is small and this leads to peak splitting in the IED as shown in figure 6.15 for argon. The peak splitting is most pronounced at high pressures where the sheath is smallest.

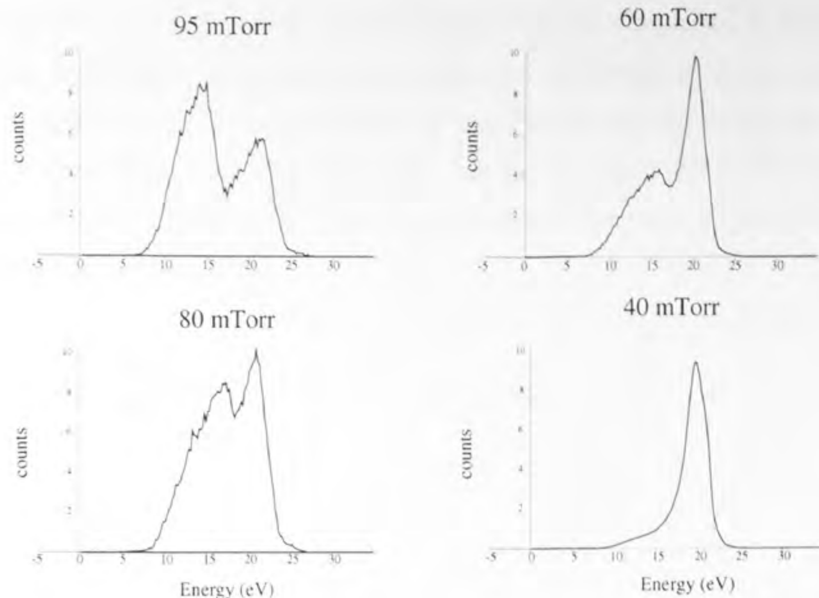

Figure 6.15 Argon IEDs for a power of 50 W.

As can be seen, even at the highest pressure the effect of collisions in the sheath is small and the mass probe is not effective for verifying the effect of collisions in the cathode sheath which is many times larger. Figure 6.16 shows the highest pressure IED for H_3^+ and again the effect of collisions is small whereas it is predicted to be important in the cathode sheath. There is no peak splitting in the case of hydrogen because the ions' low mass leads to the sheath being several times larger than in the argon case. The smearing of the peak to lower energies could be attributed to collisions. It is also a convolution of the detection function of the instrument, however.

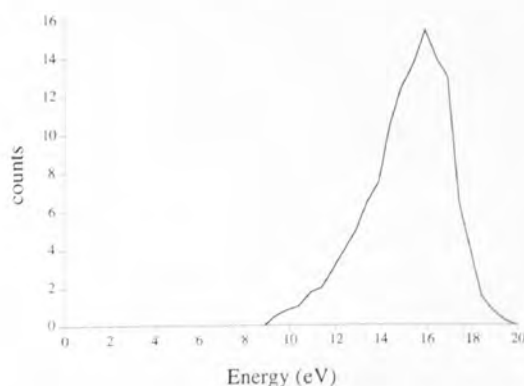

Figure 6.16 H_3^+ IED for a power of 50 W and pressure of 90 mTorr.

The advantage of the small sheath over the anode is that it can be assumed that the mass distribution of the ion species detected at the probe is equivalent to (or at least similar to) that crossing the plasma/anode sheath boundary. Figure 6.17 shows this mass distribution for a hydrogen plasma. As the pressure is increased, the conversion of H_2^+ to H_3^+ increases. At low pressures, the mass probe suffers from the same problem as the

Langmuir probe in that it samples the sheath rather than the plasma bulk, leading to a drop of the ion count into noise. The drop in the count rate of all species at high pressures could be attributed to either a change in the number density of ions in the region of the plasma being sampled or to the increased spread in ion angles at the probe due to collisions convoluted with the probes angular acceptance function, or possibly due to collisions in the flight tube itself.

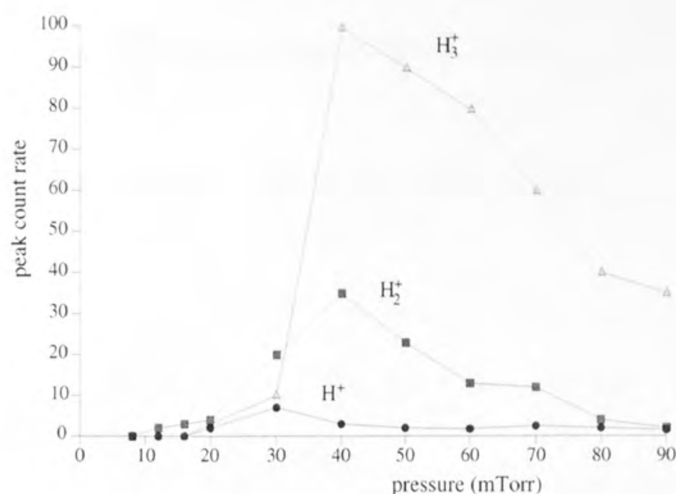

Figure 6.17 Peak values for the hydrogen species as a function of pressure at a power of 150 W.

Figures 6.18, 6.19 and 6.20 show the peak values of all species in a methane plasma as a function of power, pressure and methane fraction respectively.

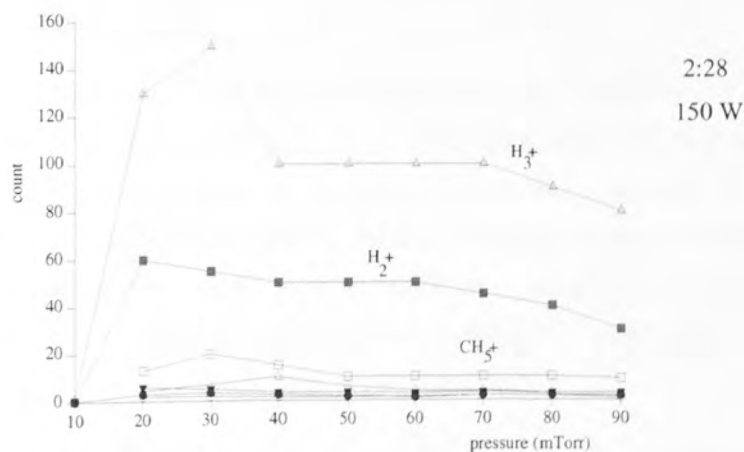

Figure 6.18 Peak values for methane species as a function of pressure.

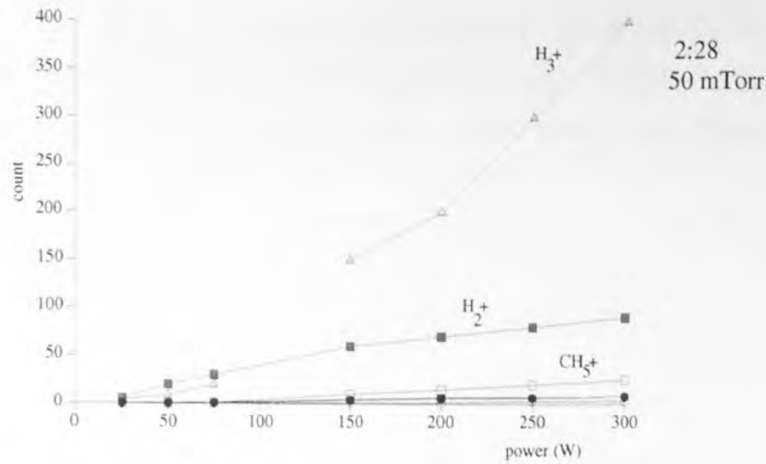

Figure 6.19 Peak values for methane species as a function of power.

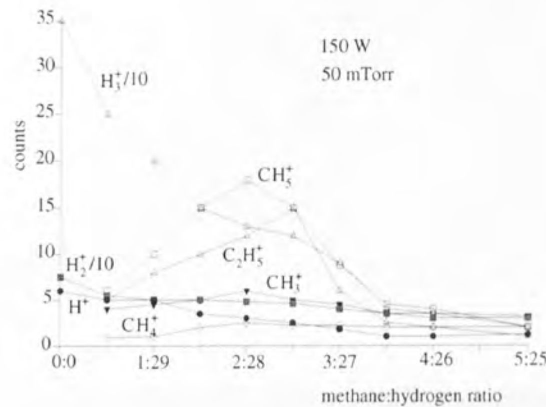

Figure 6.20 Peak values for methane species as a function of methane/hydrogen ratio.

6.1.2.2 Mass probe calibration

There are two potential sources of error associated with the results of the mass probe when used in comparisons with predictions from the modelling. The first is the sensitivity of the device as a function of the mass of the ions. The second is that the ratios of the partial pressures of hydrogen and methane in the chamber may not be equal to the ratios of their flow rates due to the relative pumping efficiency of the two gases. It is possible to calibrate the mass probe for the sensitivities and therefore to investigate the true partial pressures. This was done and the results are outlined below.

The pressures in the chamber are measured with a capacitance manometer (CM) gauge and are therefore independent of the gas type. Figure 6.21 shows the neutral count as a function of pressure when a) only hydrogen and b) only methane is flowing into the chamber and the plasma is not struck. The neutrals are ionised by the electron source in the head of the mass probe and the resulting ions are accelerated down the flight tube and detected. The only neutrals in the background gas should be H_2, but H^+ is seen due to its creation from H_2 by electron impact and it is seen in a greater proportion than the normal

cracking ratio would imply, indicating the probe is more sensitive to H^+ than to H_2^+. Water vapour is present as evidenced by the masses 17 and 18, though the lack of a clear increase with pressure indicates the source of the water vapour is the mass probe rather than the chamber.

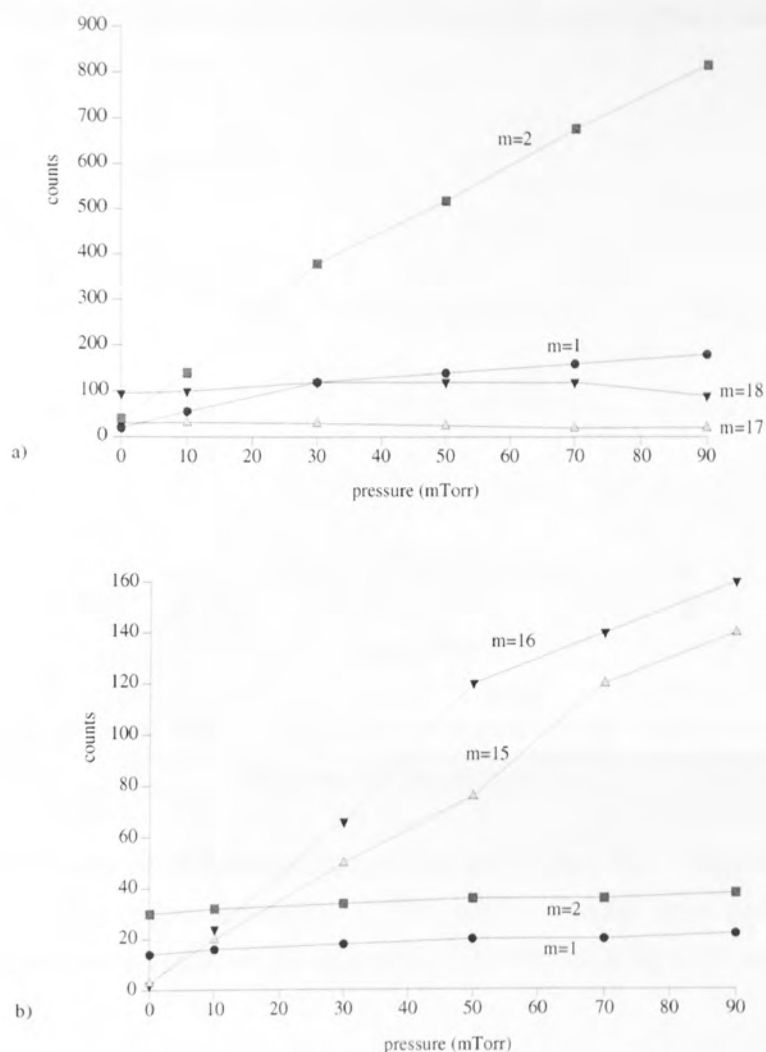

Figure 6.21 Flux of neutrals detected in the mass probe as a function of pressure for a) pure hydrogen and b) pure methane background gas.

The electron energy was 150 eV and the corresponding ionisation cross sections were

H_2^+ from H_2	= 0.71 Å^2
H^+ from H_2	= 0.016 Å^2
CH_4^+ from CH_4	= 1.36 Å^2
CH_3^+ from CH_4	= 1.13 Å^2
H_2^+ from CH_4	= 0.016 Å^2
H^+ from CH_4	= 0.099 Å^2

After shifting the graphs to pass through zero and correcting for the ionisation cross sections, comparison of the counts for the species yields the sensitivity factor for the instrument. Figure 6.22 shows the ratio of each ion species to H_2^+ after correction. It can be seen that the instrument is most sensitive to H^+ and least sensitive to the methane species. CH_4^+ and CH_3^+ having similar masses can be expected to have the same sensitivity to the mass probe and they do in fact have count rates which scale with their ionisation cross sections.

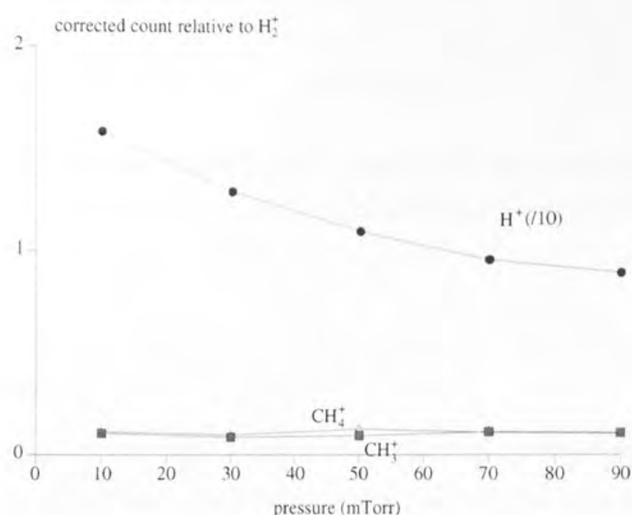

Figure 6.22 Ratio of the counts of the different species to H_2^+ after correction for the ionisation cross section.

The instrument appears 10-15 times more sensitive to H^+ than H_2^+. The ratio of the CH_4^+ and CH_3^+ ions to H_2^+ is approximately 0.11. The results from the mass probe, therefore, in SIMS mode need to be corrected by multiplying the H^+ count by 0.08 and the methane count by 9.1.

When using a 50 % methane and 50 % hydrogen mixture, recording the neutral count and correcting for the instrument response and ionisation cross sections, the graph in figure 6.23 is obtained. This implies that the proportion of methane in the plasma is approximately 100 % higher than is implied by its flow rate when mixed with hydrogen.

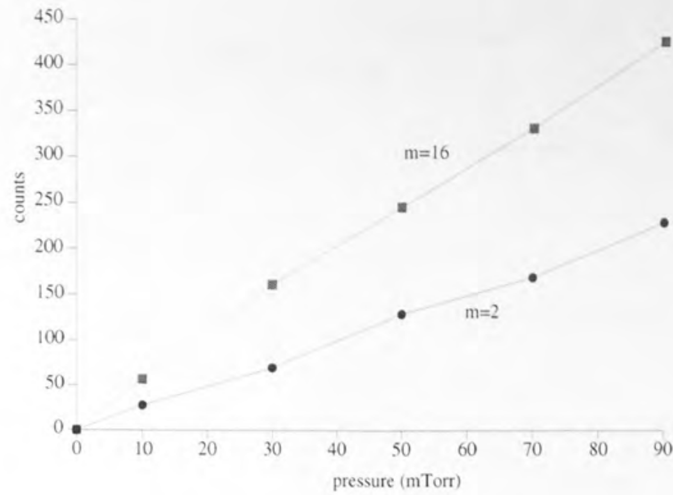

Figure 6.23 Flux of neutrals detected in the mass probe as a function of pressure for a 50 % methane and 50 % hydrogen background gas.

6.1.3 Voltages

6.1.3.1 The D.C. bias

In the absence of the quartz plate, the capacitively coupled cathode attains a D.C. bias which is dependent on the relative mobilities of the ions and electrons and their relative abundances. The D.C. bias was seen to be independent of the flow rate. The D.C. bias was found to be proportional to the square root of the applied power (figure 6.24) which is consistent with the D.C. bias being proportional to the current as observed by Morgan [273].

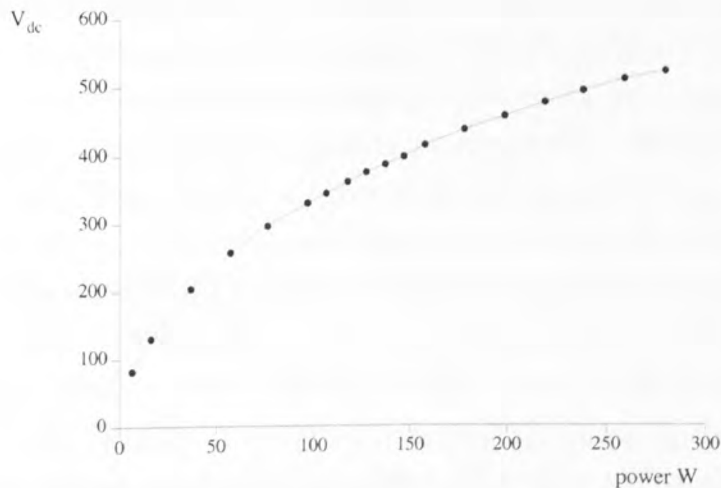

Figure 6.24 DC bias as a function of the applied power (pure hydrogen).

The bias increased in magnitude (became more negative) as the pressure increased until reaching a peak at 20 mT when it decreased as the pressure increased to 90 mT (figure 6.25).

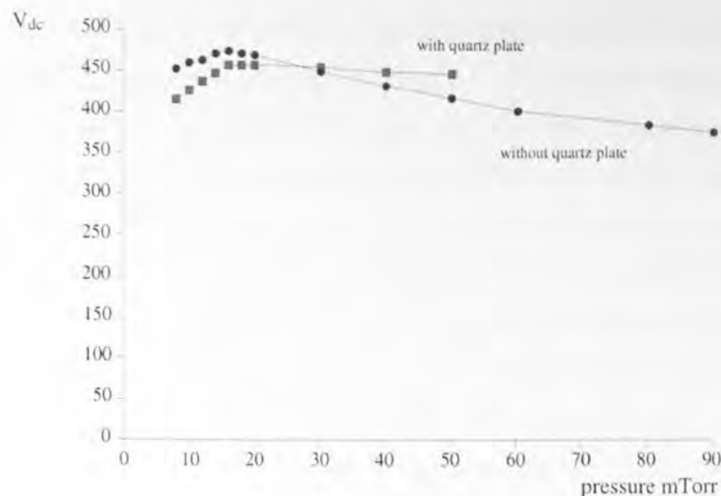

Figure 6.25 DC bias as a function of the pressure (pure hydrogen).

Measurement of the driving potential at the cathode gave values of V_{dc}/V_0 which were in the range 0.7 to 0.9 (implying the ratio A_c/A_a is not constant and should only be taken as an effective area ratio quite different from the geometrical ratio [274]).

The potentials in a methane/hydrogen discharge were not significantly different from those of a hydrogen discharge.

6.1.3.2 Potential at the quartz plate

The samples are transferred from the glove box to the cathode on a slab of quartz 12 mm thick. In industry quartz is used because it does not introduce contaminants to the chamber as other surfaces would. The quartz platen is circular and of radius slightly smaller than the cathode such that it covers almost all but leaves an annular ring of several millimetres cathode exposed directly to the plasma. The introduction of this slab of dielectric can be expected to have a non-negligible effect on the potentials in the system due to its conductivity, secondary electron emission function *etc.* If the quartz acted as a perfect insulator and shielded the cathode completely, the large D.C. bias which is a result of charge build up at the surface would not result in a D.C. bias at the backing plate (because it is not possible to draw a net D.C. current through the insulating target plate)[275]. Figure 6.25, however, shows this is not the case and either the annular ring provides sufficient current or there is a surface leakage current between the target face of the quartz and the backing plate. The difference in the D.C. bias at the cathode with and without the quartz is small and a value for the potential at the top of the quartz is not easily arrived at theoretically. The true potential through which the ions travel to the quartz and which forms the sheath above the substrate will be the difference between the time variant plasma potential which is a function of the cathode potential and this time variant potential at the quartz surface.

The measured D.C. biases at the surface of the quartz shown in figure 6.26 are

considerably lower than those at the cathode beneath and potentially are subject to error due to the wire from the quartz surface which travels through the sheath to the vacuum feedthrough. More recent discussions [276] have indicated these measurements should be treated cautiously and the D.C. bias measured at the cathode for all its faults is still one of the most popular plasma measurements used industrially. Additionally the results disagree with similar measurements made by Bunting [277] on the same experimental apparatus in 1986 with a wire attached to the quartz with silver paste. The most obvious disagreement is in the tendency followed as the pressure is increased, again implying an interaction with the sheath, the width of which also substantially changes. This could be due to improper shielding of the wire through the plasma to the vacuum feedthrough.

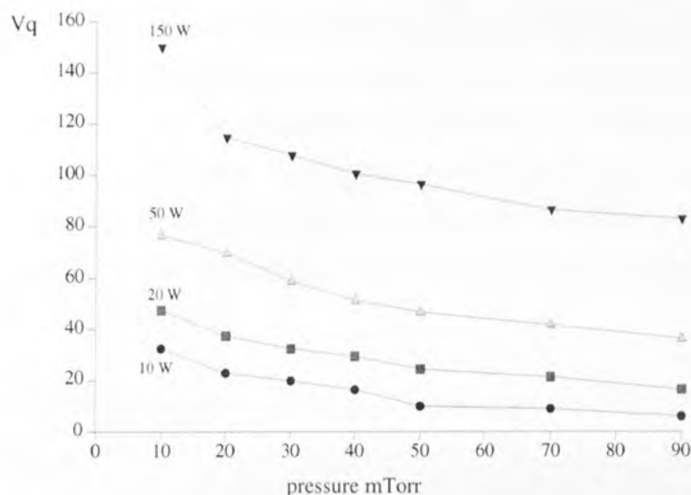

Figure 6.26 DC bias at the surface of the quartz as a function of the pressure (pure hydrogen).

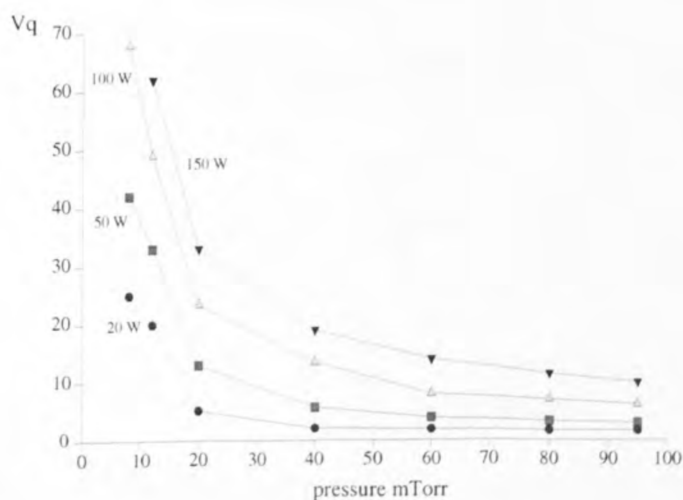

Figure 6.27 DC bias at the surface of the quartz as a function of the pressure (pure hydrogen). - measured by A. S. Bunting.

6.1.4 Sheath width

A travelling microscope was placed close to one of the viewing ports to measure the sheath width. Assuming that the electrical sheath width is approximated by the visual sheath width, it was possible to measure the distance from the substrate to the plasma/ sheath boundary by measuring the distance from the quartz plate to the position where the visible emissions increase substantially. Care was taken during these measurements due to the high level of UV emitted and a glass plate was inserted between the microscope and the quartz window. The accuracy of this measurement decreases as the pressure falls and the plasma/sheath boundary becomes more tenuous.

With the hydrogen plasmas, there is another interesting region termed here the cathode glow which has only been observed with hydrogen plasmas It consists of a glow region above the substrate between the quartz and the plasma sheath boundary. It has been suggested [278][279] that this is due to the potential at the substrate being higher than the plasma potential for the region of the rf cycle that the electrode is positive and the normal sheath would have collapsed. This leads to electron acceleration towards the substrate (rather than arrival by electrons due to their thermal motion alone) and therefore excitation of the neutrals near to the substrate.

Figure 6.28 shows the cathode glow and the plasma sheath boundary as measured from the top of the quartz. Figure 6.29 shows the distance to the plasma/sheath boundary as a function of pressure in a methane/hydrogen discharge, whilst figure 6.30 shows the distance as a function of methane/hydrogen ratio.

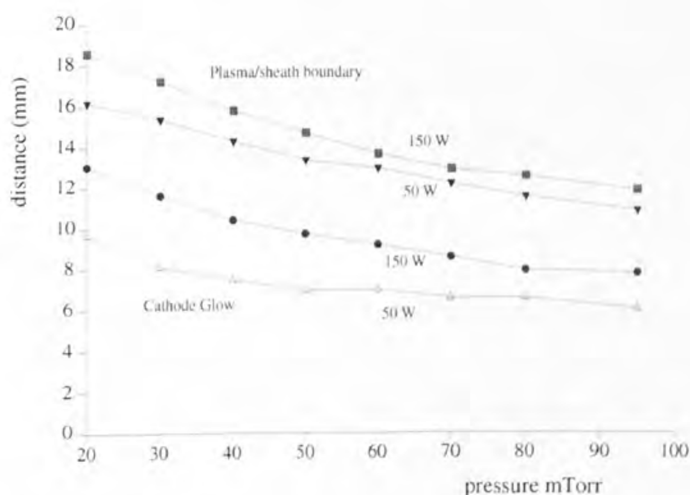

Figure 6.28 Distance from the quartz surface to the cathode glow and plasma/sheath boundary (pure hydrogen).

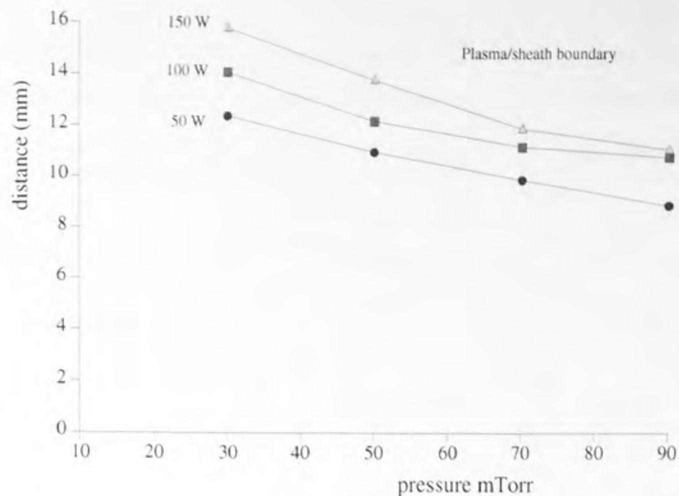

Figure 6.29 Distance from the quartz surface to the plasma/sheath boundary (methane/hydrogen 2/28) as a function of pressure.

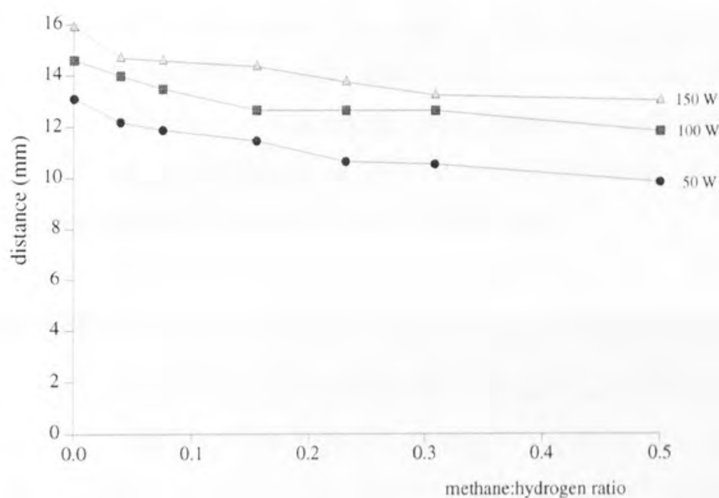

Figure 6.30 Distance from the quartz surface to the plasma/sheath boundary (methane/hydrogen 2/28) as a function of methane/hydrogen ratio.

6.2 Etch rates

PMMA masked GaAs samples were washed in acetone and isopropyl alcohol after etching to remove the mask before being blown dry in nitrogen (to prevent airborne dust sticking to any solvent residue and staying on the surface as it evaporates) prior to being analysed with the AFM.

Initial experiments defined the matrix of external plasma parameters and the regime of etching or deposition for a constant total flow of 30 sccm and powers of 50 to 150 W as shown in figure 6.31.

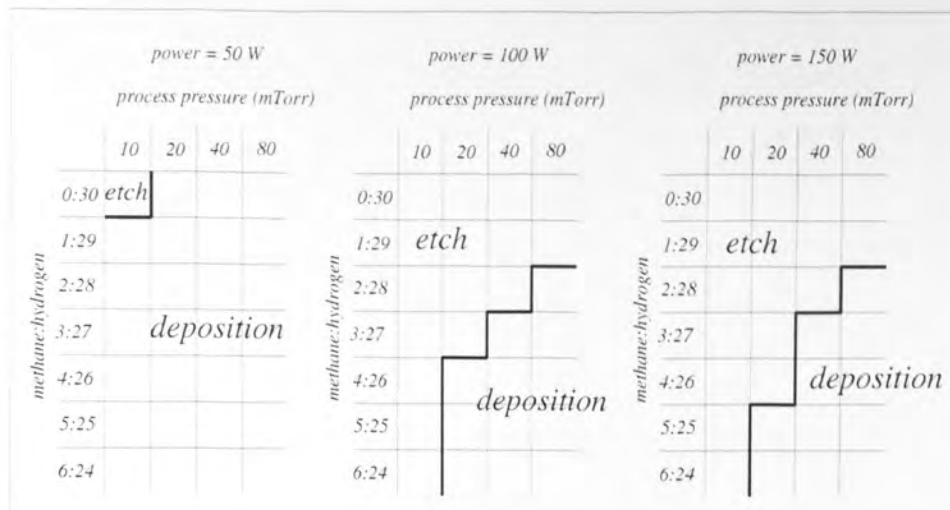

Figure 6.31. The regimes of etching and deposition

It has been suggested [280] that in the case of InP, it is necessary to 'season' the chamber walls before getting consistent etch rates. The effect of this was investigated by etching with a 2:28 CH_4:H_2 plasma at 150 W for 30 minutes after seasoning the chamber in the same plasma for 1 hour beforehand. The results were, however, indistinguishable. Subsequently the procedure was changed to allow seasoned chambers and clean only when necessary as this reduced the experimental repeat time.

6.2.1 Fixed flow rate

The results of the etch rates as a function of CH_4:H_2 ratio are shown in figure 6.32 for a pressure of 10 mTorr. At 50 W any greater percentage of methane than 14 % leads to polymer deposition. Samples etched in the same conditions for 240 minutes had the same etch rate as those etched for 30 minutes. The etch rates are quite reproducible at 10 mTorr and the data has a standard deviation of only several nm. At higher pressures, the standard deviation in the data increases, both between samples etched in the same run and to a greater extent between samples etched in different runs though with the same conditions.

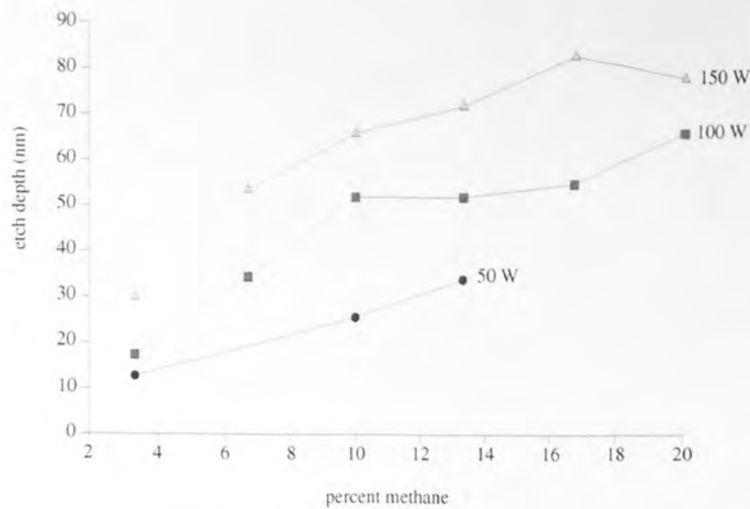

Figure 6.32 Etch depths after 30 minutes as a function of methane/hydrogen ratio at a pressure of 10 mTorr.

Figure 6.33 shows the results for 100 W and 150 W at 20 mTorr. At pressures higher than 10 mTorr, the accuracy of the etch depth measurement becomes poorer. The standard deviation between measurements at different positions on the same substrate remains quite low but the deviation between experimental runs increases. Due to time restrictions it was not possible to repeat many of the conditions more than twice to get a good statistical average, however.

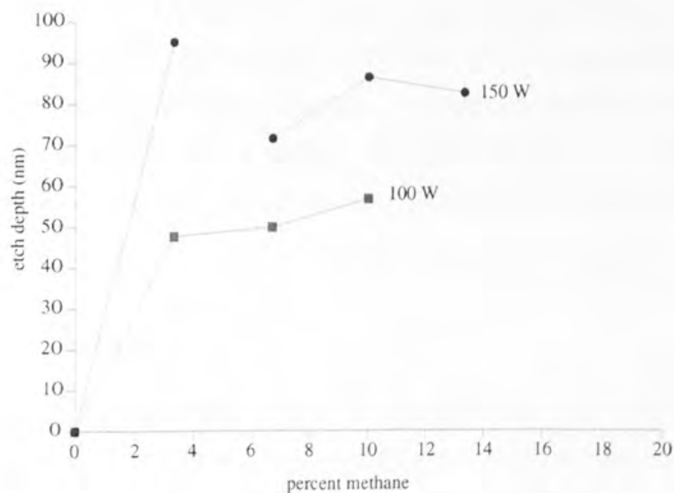

Figure 6.33 Etch depths after 30 minutes as a function of methane/hydrogen ratio at a pressure of 10 mTorr.

Figure 6.34 shows the etch rate as a function of pressure for a CH_4:H_2 ratio of up to 3:27. Where data is not shown, a polymer has been deposited.

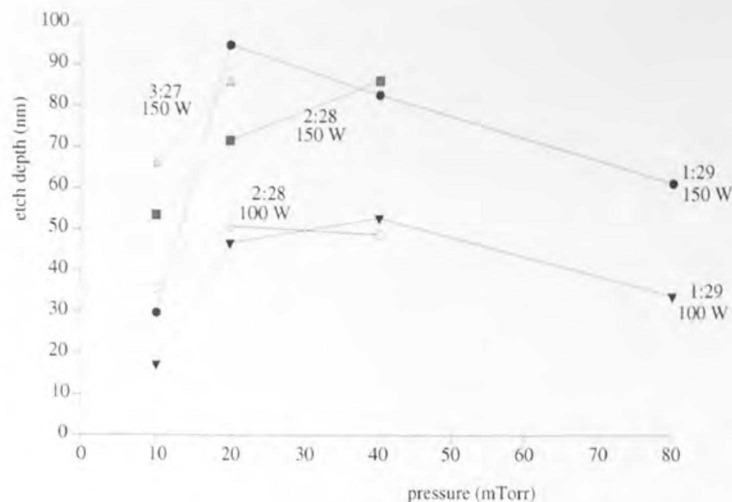

Figure 6.34 Etch depths after 30 minutes as a function of pressure.

The results indicate an etch rate which increases with increasing power, as expected, as the energies of the ions on the substrate are higher and so is the degree of ionisation in the plasma, with more reactive species available to promote the chemistry at the surface. The results also show an etch rate which scales with the number of methane molecules in the plasma, though this approaches a limit. The competition between etching and deposition leads to less reproducible etch rates near the polymer point. The change in the etch rate with pressure for the ratio of 1:29 is less easy to explain except by consideration of the competing processes of etching and deposition. At higher pressures, there are more methane molecules available potentially increasing the etch rate, but also potentially increasing the polymer process. Sheath processes will also create a significant flux of low energy neutrals to the surface, whose effect will be governed by their energies and the activation energies for reactions at the surface. It is possible that the saturation level of the surface with carbon compounds which will contribute to etching or polymer deposition is also an important factor.

6.2.2 Variable flow rate

The results for etching as a function of flow rate are shown in figure 6.35. The etch rate is low at low flows because of the lower rate of removal of etch products and lower replacement with fresh methane ions and radicals. The highest flow rate is at the limit of the experimental equipment.

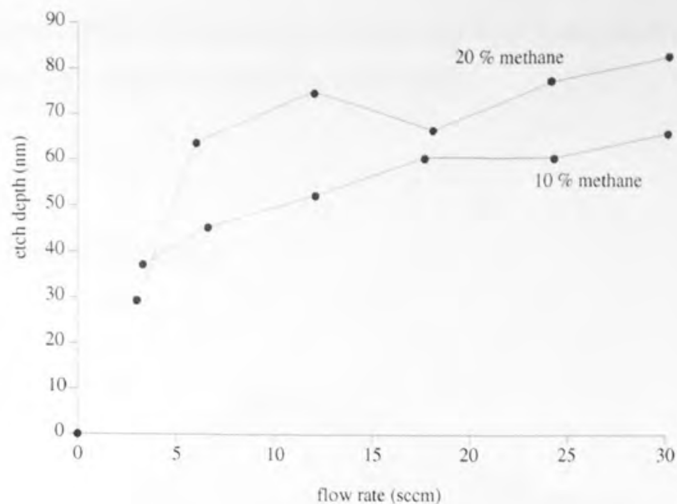

Figure 6.35 Etch rate as a function of flow rate in CH_4/H_2 for methane percentages of 10 % and 20 %

6.2.3 Neon/hydrogen

The etch depth for a pure neon plasma where only physical etching occurs was 26 nm and 46 nm respectively for powers of 100 W and 150 W respectively. Etch depth readings with pure hydrogen are almost unresolvable and etching for greater periods of time inevitably destroys the PMMA mask. Etching in neon/hydrogen mixtures also has the problem of degradation of the mask which does not occur in methane/hydrogen mixtures. The heavy ion bombardment also potentially changes the chemical structure of the organic photoresist the initial structure of which is shown in figure 6.36.

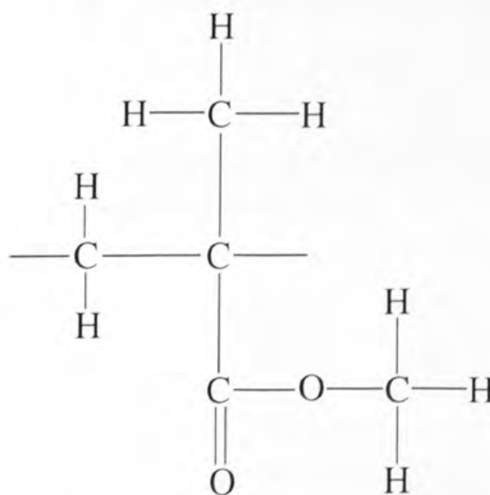

Figure 6.36. Polymethyl methacrylate (PMMA) mask

This change can lead to more difficulty in removing the remaining mask in acetone and consequently extremely rough surface areas. This makes the etch pit depth measurement subject to large error. Furthermore, mixtures of neon and hydrogen remove the PMMA mask more effectively than pure neon plasmas and this mask removal is more efficient

still at the higher pressures. Consequently no etch depth measurements could be confidently found when using neon/hydrogen mixtures.

6.3 AFM

6.3.1 Surface prior to etching

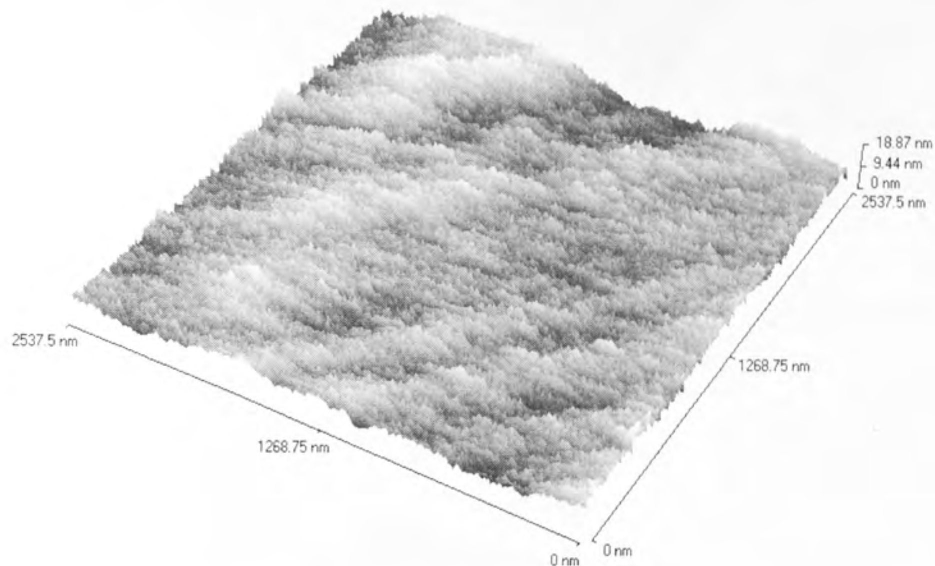

Figure 6.37 AFM topographic image of unetched GaAs: 2.5 μm scale.

Figure 6.37 shows an AFM image of a GaAs (100) surface prior to being etched. The surface is smooth with an average surface of height deviation from the mean (R_a) of 2 nm.

6.3.2 Surface after etching

The surfaces post etching are all very smooth, an example being shown in figure 6.38. Figure 6.39 is the same surface magnified by ten times.

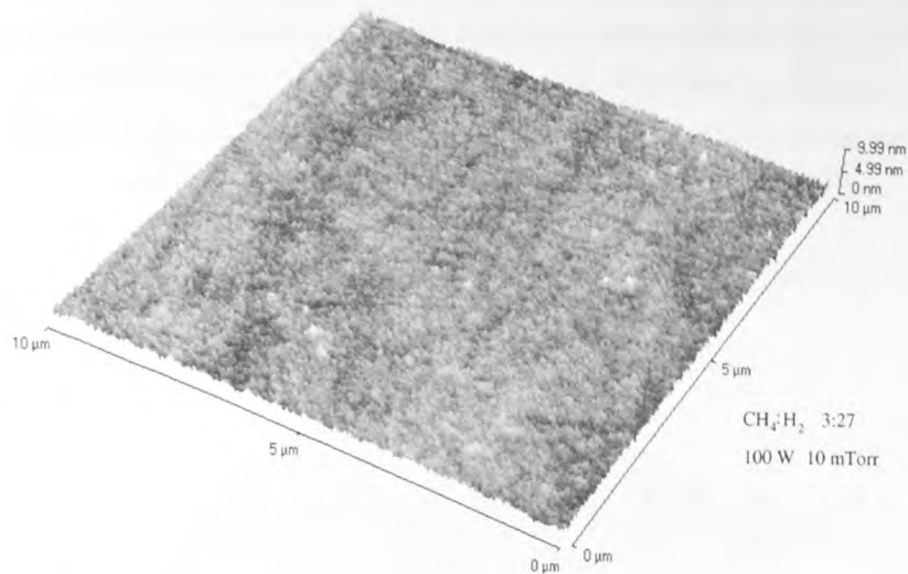

Figure 6.38 AFM topographic image of etched GaAs: 3:27, 100 W, 10 mTorr. 10 µm scale.

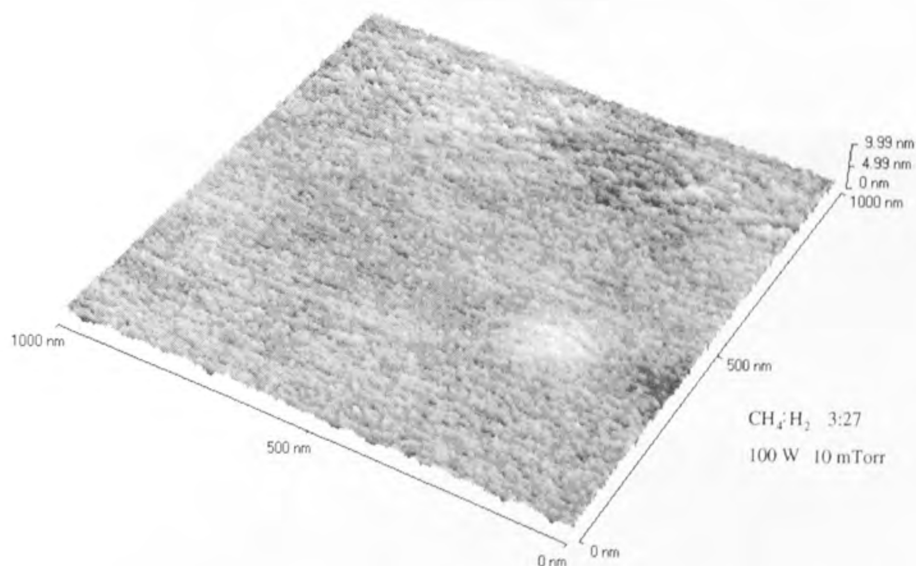

figure 6.39 AFM topographic image of etched GaAs: 3:27, 100 W, 10 mTorr. 1000 nm scale.

The smoothness of the surfaces measured means that much of the roughness seen is in fact instrument noise converted into topographic height by the tip feedback mechanism which attempts to keep a constant tip deflection as the instrument scans across the surface. The tip deflection is measured by reflecting a laser off the end of the tip and measuring the reflected light at two photodiodes. As the angle of the tip changes, there is a resultant current difference between the two. The feedback mechanism adjusts the tip height in order to keep this difference the same. If the feedback mechanism is switched off and

only the current difference between the two photodiodes measured as the tip scans across the surface then the resulting plot of surface features is much more accurate and less sensitive to instrument noise. The results are, however, difficult to convert into real heights. Figure 6.40 and 6.41 show these plots for samples from the plasma conditions shown at the two different scales. The plots seem to show no coherent surface topography.

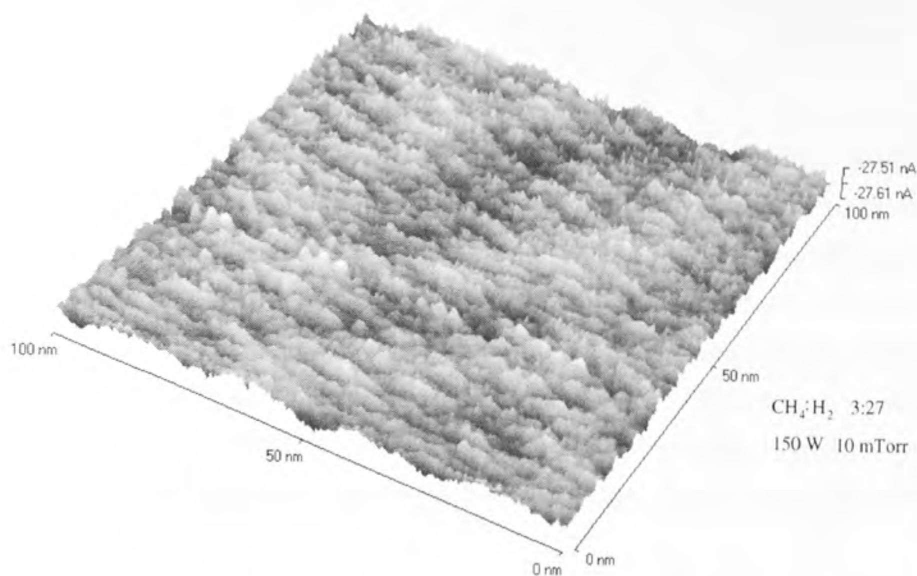

Figure 6.40 AFM tip deflection image of etched GaAs: 3:27, 100 W, 10 mTorr. 100 nm scale.

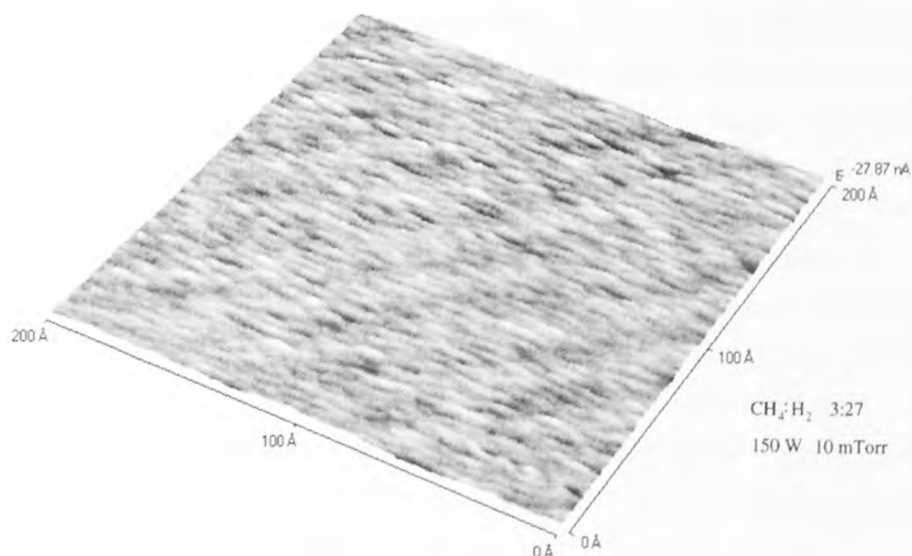

Figure 6.41 AFM tip deflection image of etched GaAs: 3:27, 100 W, 10 mTorr. 200 Å scale

For each set of experiments, surface images at 1 μm and 1000 Å were taken after

measurement of the etch depth. The resulting values of R_a were almost always very low (less than 1.5 nm) and consisted mainly of instrument noise. For this reason, there appeared no positive correlation between the values of the surface roughness and the parameters which defined the etch conditions. At high methane concentrations and/or high pressures (*ie.* close to the etching/deposition boundary) the etch pits have a build up of contamination which begins at the extreme edge of the pit adjacent to the sidewalls. The conditions for deposition appear to be reached firstly at the GaAs/mask boundary, the deposit being not removed in acetone.

6.4 XPS

After etching, the samples were transferred to the ESCALAB where angle resolved X-ray photoelectron spectroscopy (ARXPS) was performed using unmonochromated Al Kα (1486.6 eV) at take off angles (ToAs) of 0°, 45° and 60°. The As 3d core level consists of two widely separated components, As(GaAs) at a binding energy of 41.1 eV and As(As_2O_3) at 44.8 eV. The Ga peak consists of the two components Ga(GaAs) at a binding energy of 19.1 eV and Ga(Ga_2O_3) at 20.3 eV. The results are expressed as either the total ratio of gallium to arsenic - $(Ga/As)_T$ or the ratio of gallium (GaAs) to arsenic (GaAs) - $(Ga/As)_S$, the latter requires deconvolution of the gallium peak and is therefore subject to more error.

The unetched samples show a mixed oxide with a fairly stoichiometric substrate. The As(As_2O_3) peak is generally absent in the etched samples, indicating either the total removal of arsenic from the upper 1 nm or so of the surface which is subsequently oxidised or a change in the chemical reactivity of the surface which stops any surface arsenic oxidising (for instance by termination of free arsenic bonds with hydrogen). Evidence of substantial amounts of As_2O_3 in the etched samples is indicative of a problem with the plasma system such as the presence of oxygen or water vapour due to leaks or insufficient pump down times.

A large number of samples were etched at one plasma condition (CH_4:H_2 = 2:28, 10 mTorr, 150 W) on different occasions in order to attempt to quantify the errors in the system. The results implied a standard deviation in the Ga/As ratios of 6 % at 0° ToA increasing to 15 % at 60° ToA, though the distribution is not normal and up to one in four samples lay more than two standard deviations away from the mean (usually samples from different experiments at the same conditions). The rest of the XPS results presented are the average of results of at least two samples.

6.4.1 Methane/hydrogen

Considering the gallium and arsenic 3d peaks for post etch samples, the XPS signals consisted of gallium from gallium oxides, gallium from GaAs and arsenic from GaAs.

Oxygen and carbon 1s peaks were also present, but arsenic oxide was not seen in any of the samples in significant amounts. Pre-etch samples showed the presence of As and Ga oxides with a slight predominance of the Ga component. Thus the large increase in $(Ga/As)_T$ observed under all conditions and angles was due mainly to the formation of a wholly gallium oxide surface covering. A smaller yet significant increase in $(Ga/As)_S$ was also apparent in many of the samples. Though there was significant arsenic depletion, metallic gallium was not seen in any of the samples.

6.4.1.1 10 mTorr

Figure 6.42 shows $(Ga/As)_T$ for a power of 50 W at 10 mTorr. The trend is for a lower $(Ga/As)_T$ for higher methane concentration and is most obvious for the 0° ToA. At these low etch rates it is expected that the errors will be higher, due to the increased dependence of the etch on contaminants in the plasma and with the smaller distance past the oxide layer the etch will have progressed. Figure 6.43 shows the results from the same conditions though run for an etch time of 240 minutes and it appears to have lower errors possibly due to the greater etch depth or the 'seasoning' effect. At the higher methane concentrations, deposition occurred.

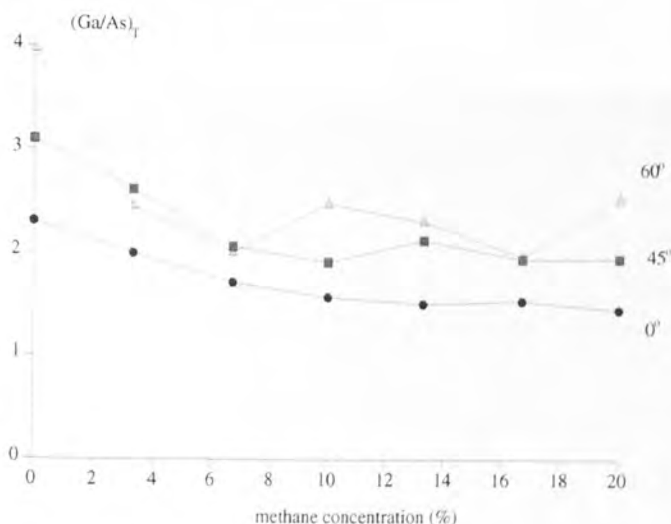

Figure 6.42 $(Ga/As)_T$ as a function of methane concentration for 50 W and 10 mTorr 30 minutes.

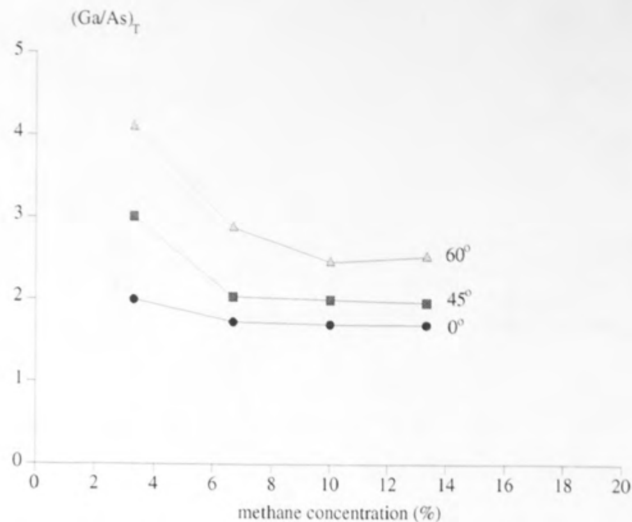

Figure 6.43 $(Ga/As)_T$ as a function of methane concentration for 50 W and 10 mTorr 240 minutes.

Figures 6.44 and 6.45 show the similar results for powers of 100 W and 150 W. The same trend of a lower value of $(Ga/As)_T$ at higher methane concentrations is seen, with most of the effect occurring at the lowest methane concentrations.

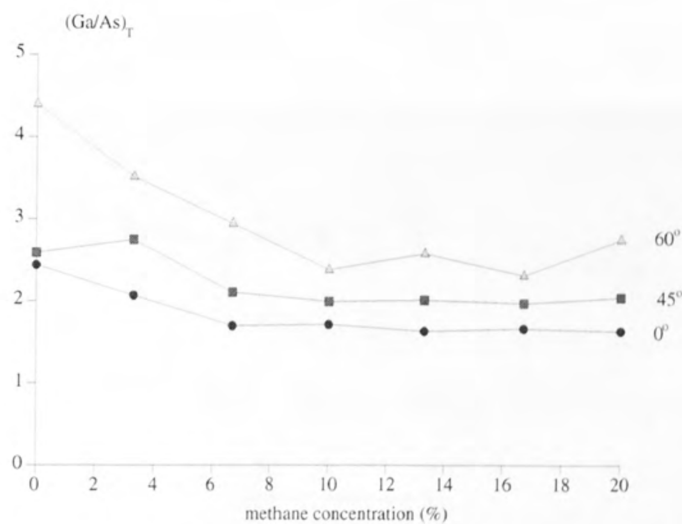

Figure 6.44 $(Ga/As)_T$ as a function of methane concentration for 100 W and 10 mTorr 30 minutes.

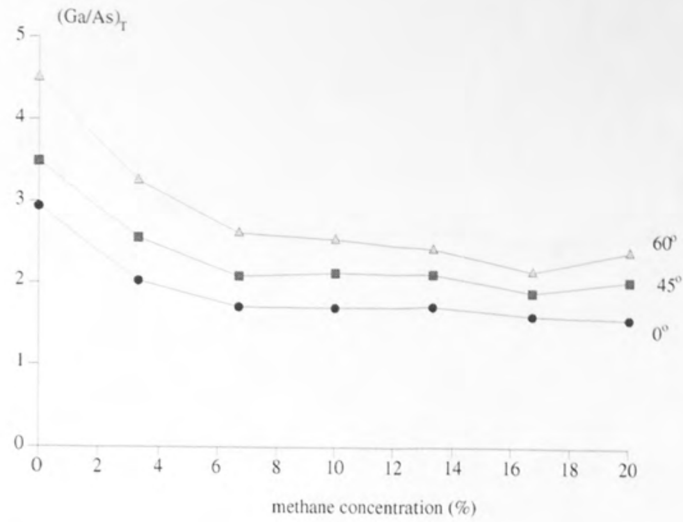

Figure 6.45 $(Ga/As)_T$ as a function of methane concentration for 150 W and 10 mTorr 30 minutes.

Figure 6.46 to 6.48 show the ratio $(Ga/As)_S$ for the powers of 50, 100 and 150 W respectively. The trend is less obvious than for $(Ga/As)_T$ but appears to be similar in showing a lesser change from stoichiometry at the higher methane concentrations.

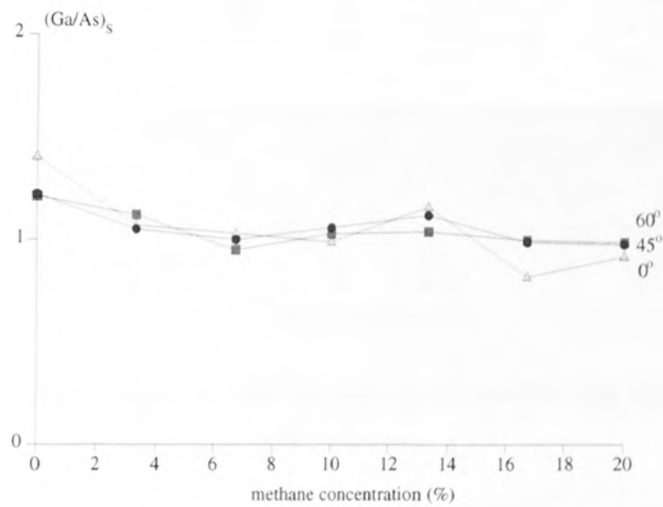

Figure 6.46 $(Ga/As)_S$ as a function of methane concentration for 50 W and 10 mTorr 30 minutes.

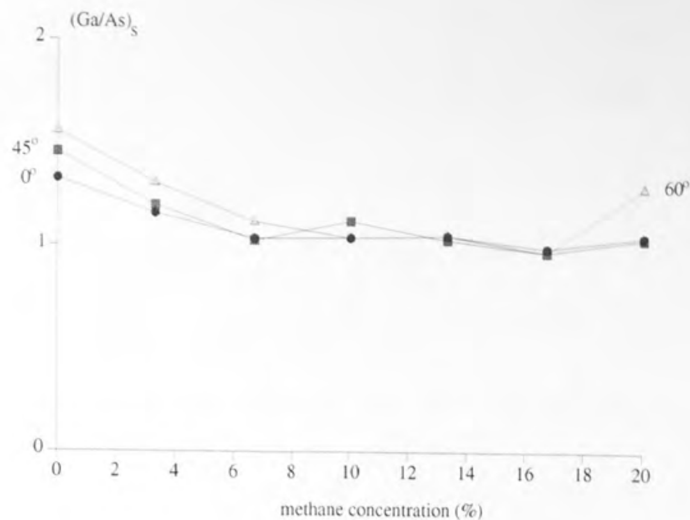

Figure 6.47 $(Ga/As)_S$ as a function of methane concentration for 100 W and 10 mTorr 30 minutes.

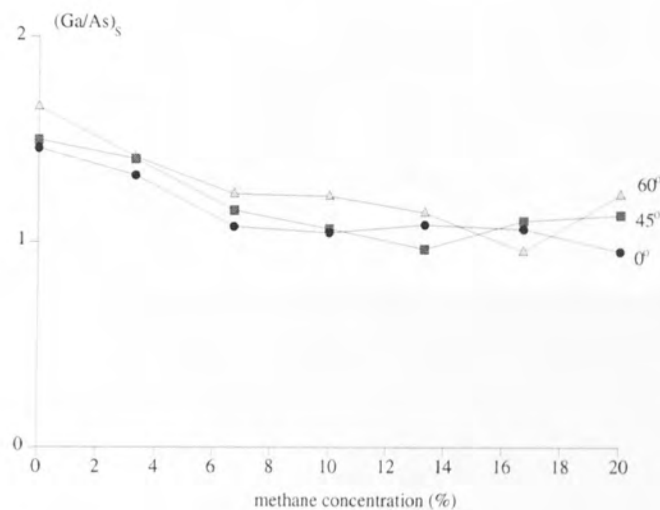

Figure 6.48 $(Ga/As)_S$ as a function of methane concentration for 150 W and 10 mTorr 30 minutes.

In order to find the effect of different penetration depths of the bombarding species on the gallium to arsenic ratio, the following figures 6.49 to 6.55 show the ratio $(Ga/As)_T$ as a function of power at 10 mTorr for pure hydrogen and 6 different ratios of methane to hydrogen. Unfortunately, the range 50 W to 150 W only represents a 70 % change in energy of bombarding species and a similar change in penetration depth of bombarding species. At lower energies than 50 W, the etch rates become very small and the plasma unstable, the data is therefore unreliable.

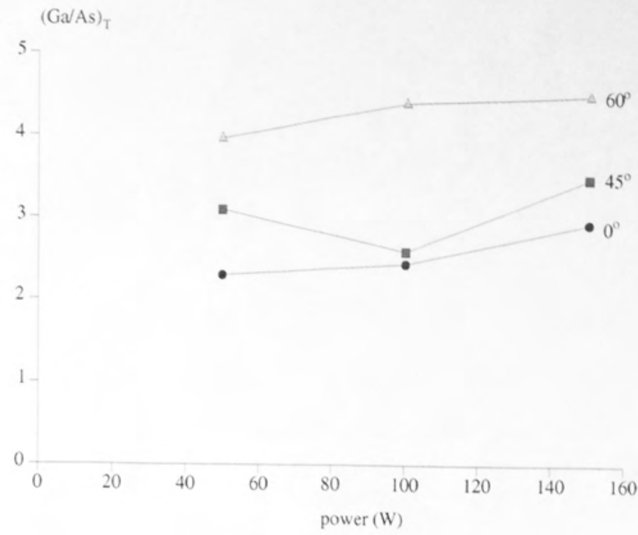

Figure 6.49 $(Ga/As)_T$ as a function of power for pure hydrogen, 10 mTorr for 30 minutes.

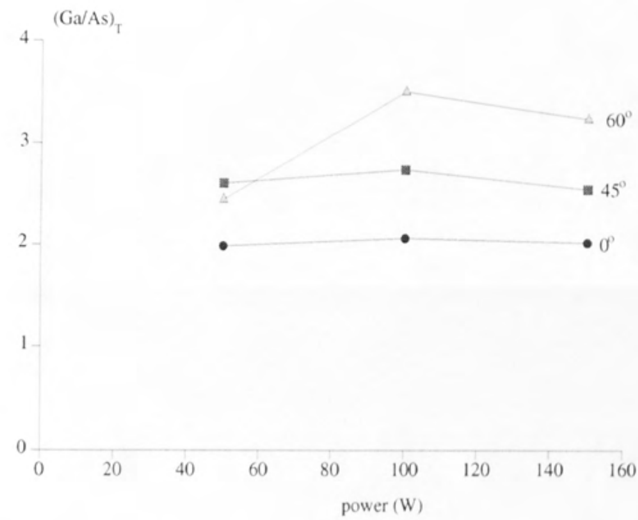

Figure 6.50 (Ga/As)T as a function of power for a ratio of 1:29, 10 mTorr for 30 minutes.

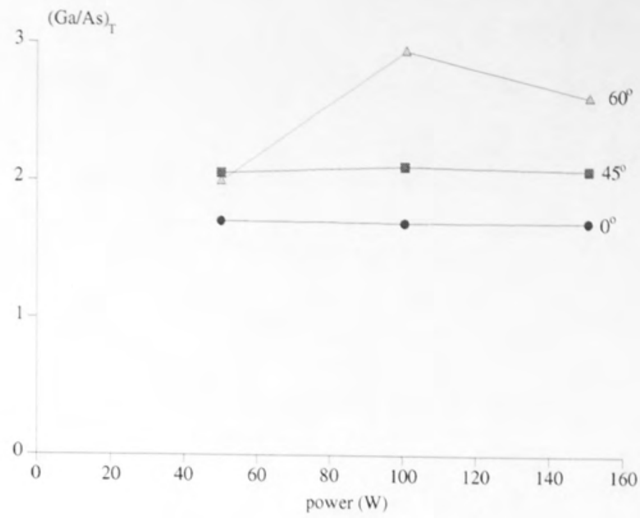

Figure 6.51 (Ga/As)$_T$ as a function of power for a ratio of 2:28, 10 mTorr for 30 minutes.

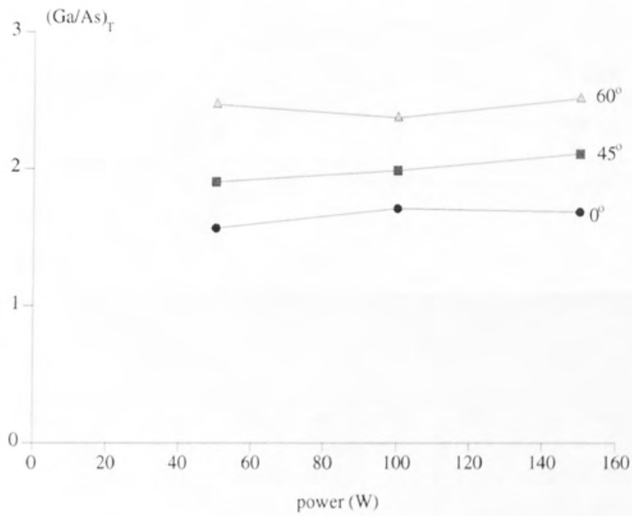

Figure 6.52 (Ga/As)$_T$ as a function of power for a ratio of 3:27, 10 mTorr for 30 minutes.

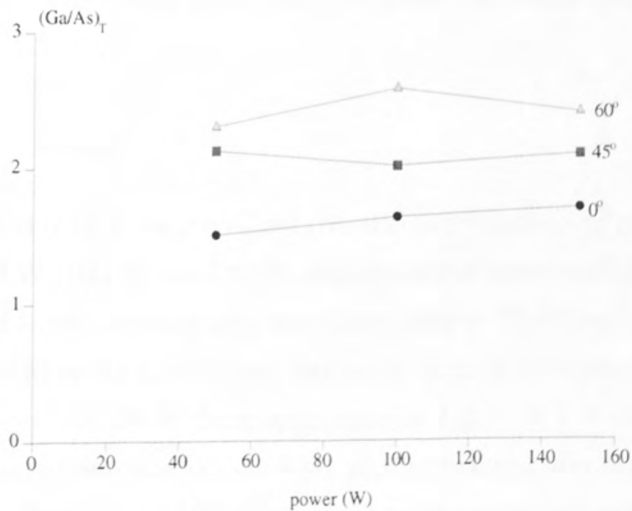

Figure 6.53 (Ga/As)$_T$ as a function of power for a ratio of 4:26, 10 mTorr for 30 minutes.

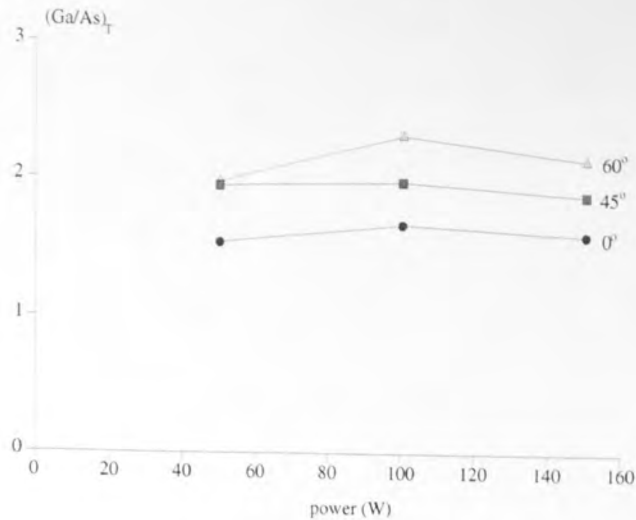

Figure 6.54 $(Ga/As)_T$ as a function of power for a ratio of 5:25, 10 mTorr for 30 minutes.

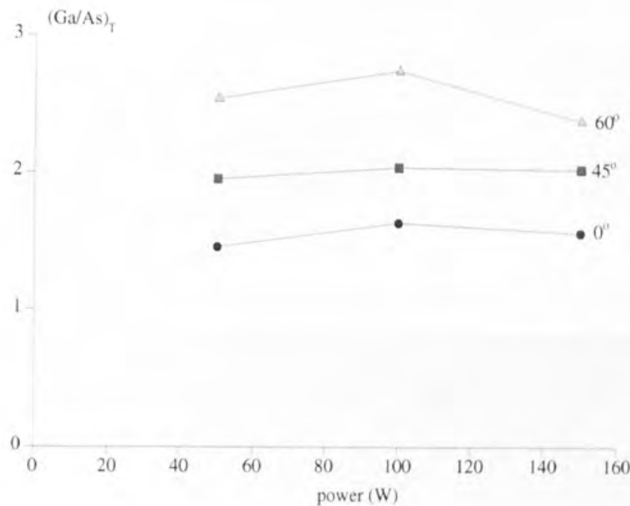

Figure 6.55 $(Ga/As)_T$ as a function of power for a ratio of 6:24, 10 mTorr for 30 minutes.

The values of $(Ga/As)_S$ show a slight increase over the power range from around unity for all methane concentrations except pure hydrogen which increases by a larger amount and with a value around 1.5.

6.4.1.2 20 mTorr

Figures 6.56, 6.57 and 6.58 show the $(Ga/As)_T$ ratio as a function of methane concentration for 50 W, 100 W and 150 W respectively at a pressure of 20 mTorr. Deposition occurs at lower methane concentrations than at 10 mTorr. At 50 W and 100 W the tendency appears to be for a decreased deviation from stoichiometry with increasing methane concentration. At 150 W there appears to be a peak at 7 % methane. The seemingly anomalously low value of $(Ga/As)_T$ at 3 % methane was reproduced in a second experiment. The values of $(Ga/As)_S$ show no systematic change with the experimental conditions and for all results have a magnitude slightly above 1.

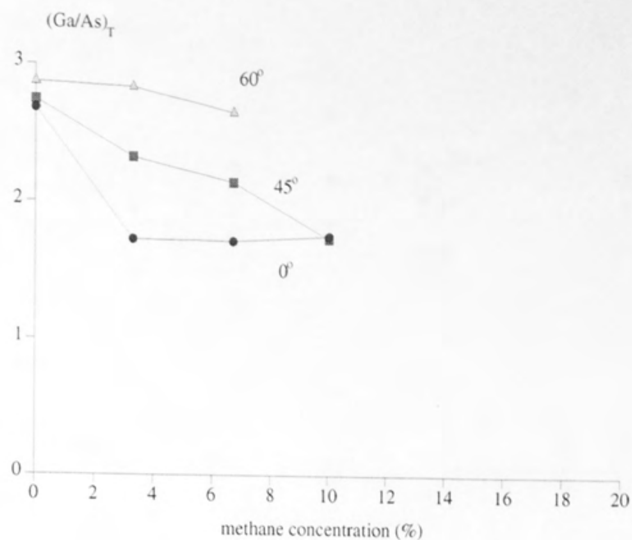

Figure 6.56 (Ga/As)$_T$ as a function of methane concentration, power 50 W, 10 mTorr for 30 minutes.

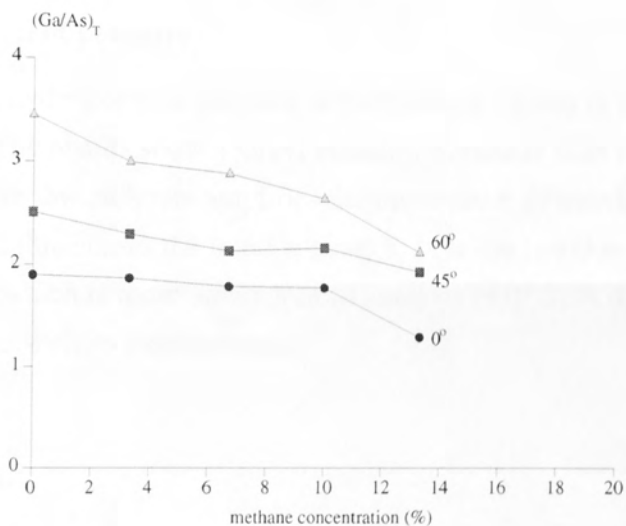

Figure 6.57 (Ga/As)$_T$ as a function of methane concentration, power 100 W, 10 mTorr for 30 minutes.

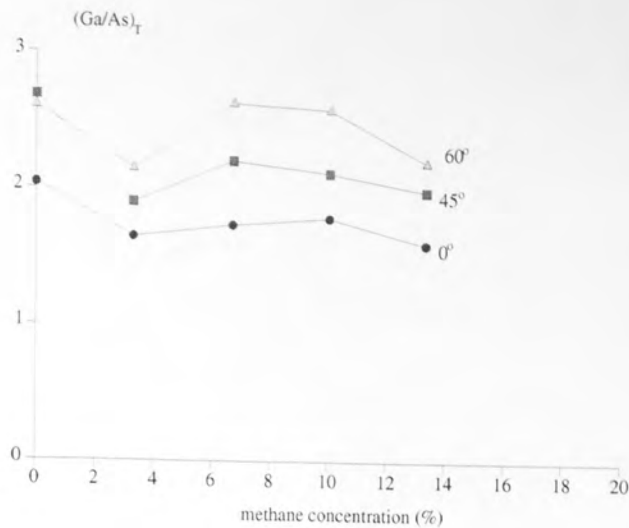

Figure 6.58 $(Ga/As)_T$ as a function of methane concentration, power 150 W, 10 mTorr for 30 minutes.

6.4.1.3 As a function of pressure

The results for pure hydrogen as a function of pressure are shown in figures 6.59, 6.60 and 6.61 respectively. The results show a larger standard deviation than for methane/ hydrogen because the low etch rate amplifies the importance of heavier chamber contaminants. In all three cases the trend appears to be a lower value of $(Ga/As)_T$ with increasing pressure which is more obvious from analysis of 0° ToA due to there being the least error associated with its measurement.

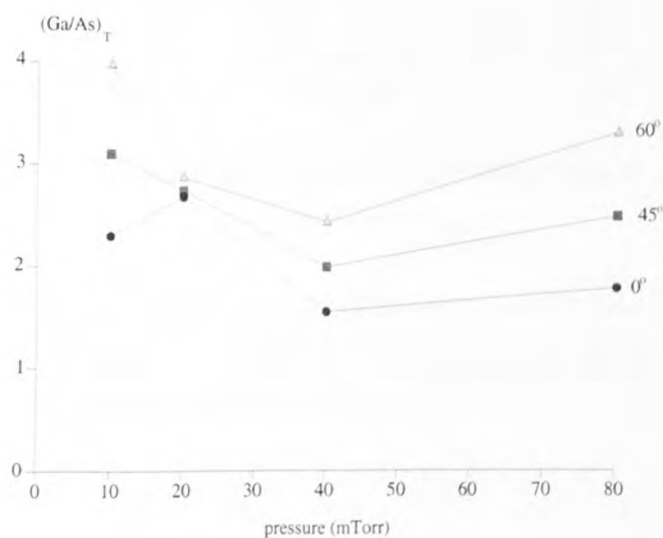

Figure 6.59 $(Ga/As)_T$ as a function of pressure, power 50 W for 30 minutes.

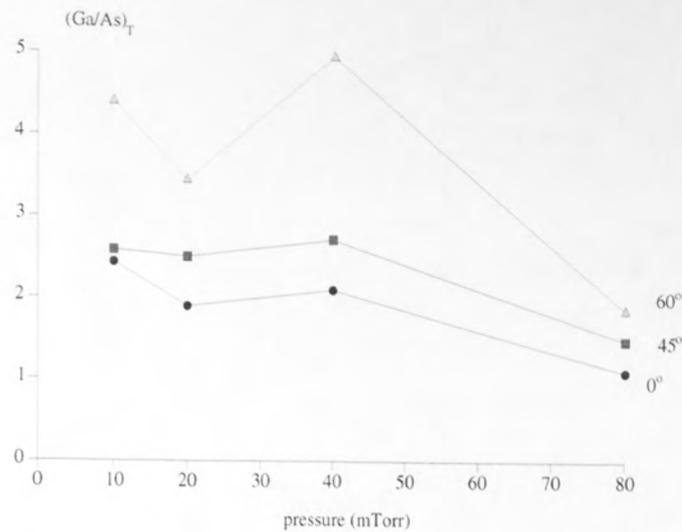

Figure 6.60 $(Ga/As)_T$ as a function of pressure, power 100 W for 30 minutes.

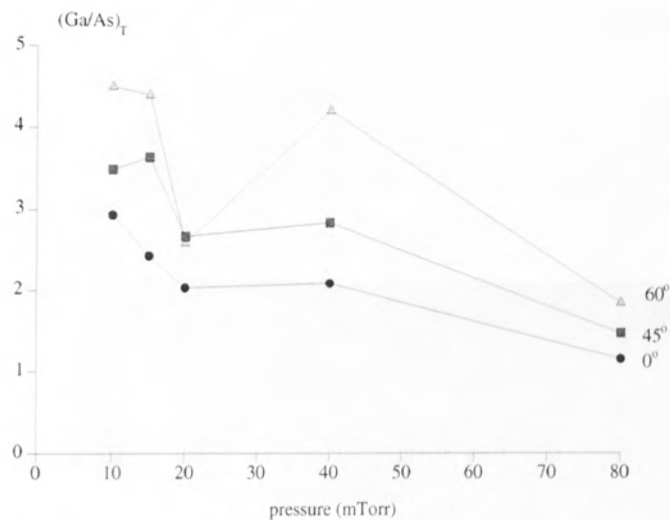

Figure 6.61 $(Ga/As)_T$ as a function of pressure, power 150 W for 30 minutes.

Figures 6.62, 6.63 and 6.64 show the results of $(Ga/As)_S$ for the same set of experimental conditions. Apart from the result at 50 W 80 mTorr, the results show a very clear decrease in $(Ga/As)_S$ as the pressure is increased.

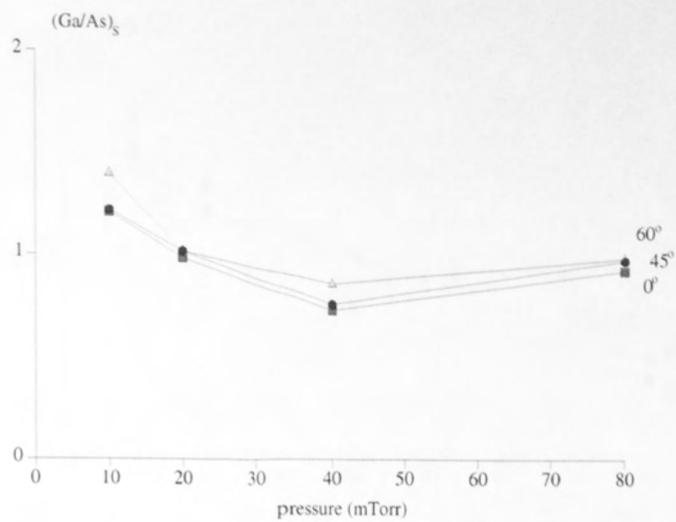

Figure 6.62 (Ga/As)$_S$ as a function of pressure, power 50 W for 30 minutes

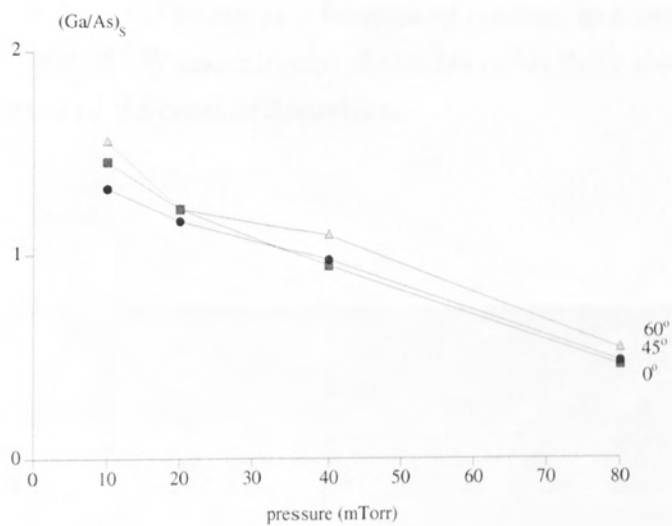

Figure 6.63 (Ga/As)$_S$ as a function of pressure, power 100 W for 30 minutes

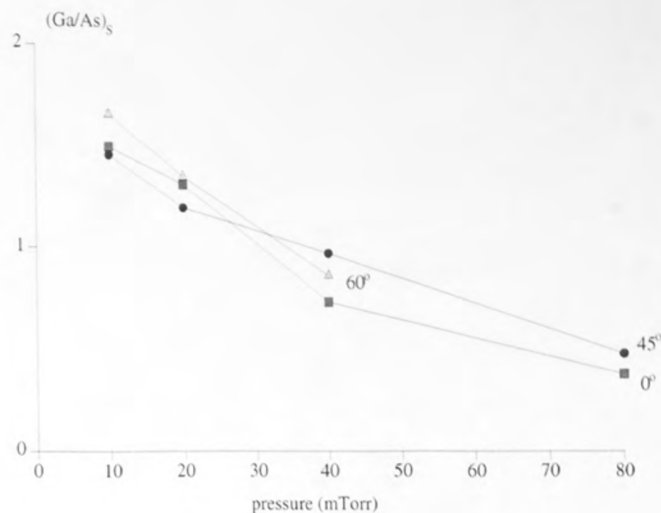

Figure 6.64 $(Ga/As)_S$ as a function of pressure, power 150 W for 30 minutes

Figures 6.65 and 6.66 show the results as a function of pressure at a ratio of 1:29 (3.4 % methane) for 100 W and 150 W respectively. At higher ratios there are not enough results to show a trend because of the onset of deposition.

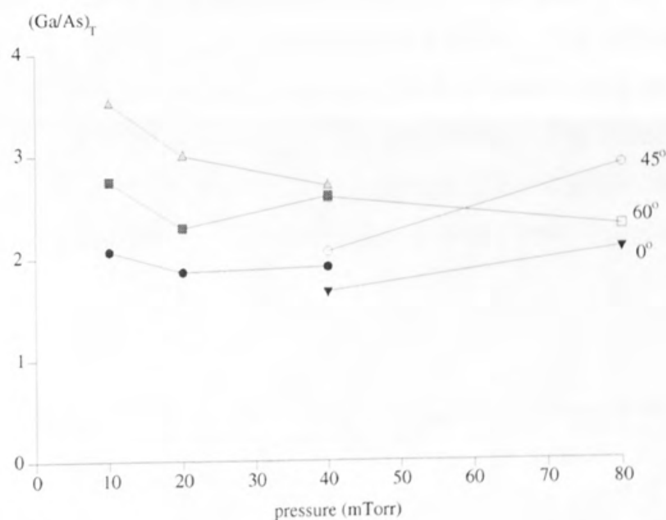

Figure 6.65 $(Ga/As)_T$ as a function of pressure, ratio 1:29, power 100 W, 30 minutes.

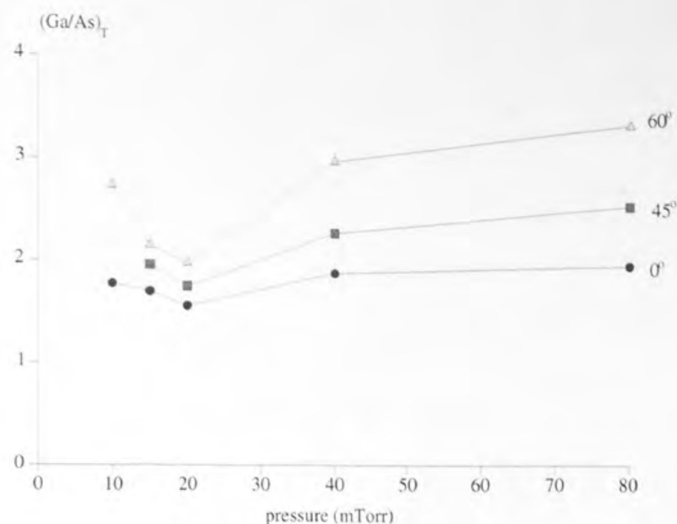

Figure 6.66 $(Ga/As)_T$ as a function of pressure, ratio 1:29, power 150 W, 30 minutes.

Again, the $(Ga/As)_S$ results show little trend (though what trend there is appears to follow the $(Ga/As)_T$ result) with a value slightly above 1.

6.4.1.4 As a function of power

Because of deposition, results of $(Ga/As)_T$ as a function of power are only possible for methane/hydrogen at 10 mTorr and were presented above. The following shows the results for $(Ga/As)_T$ for pure hydrogen as a function of power over the pressure range from 10 mTorr to 80 mTorr in figures 6.67 to 6.70 respectively. The results appear to indicate a rise in change from stoichiometry with power except at the highest pressure (assuming the results at 20 mTorr could rise with power within a larger error margin).

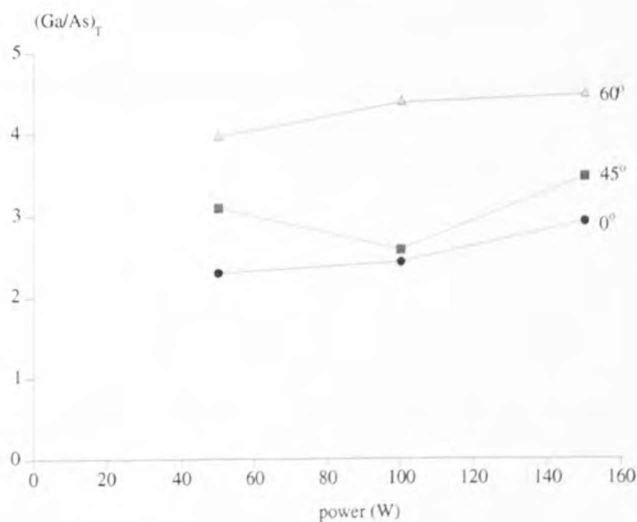

Figure 6.67 $(Ga/As)_T$ as a function of power for pure hydrogen, 10 mTorr for 30 minutes.

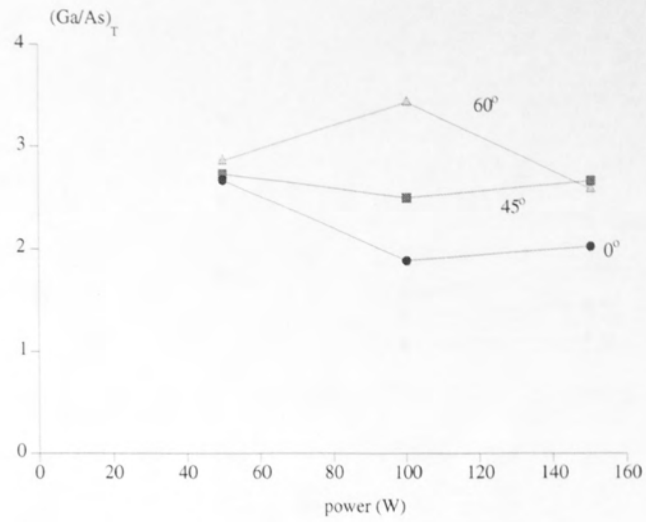

Figure 6.68 $(Ga/As)_T$ as a function of power for pure hydrogen, 20 mTorr for 30 minutes.

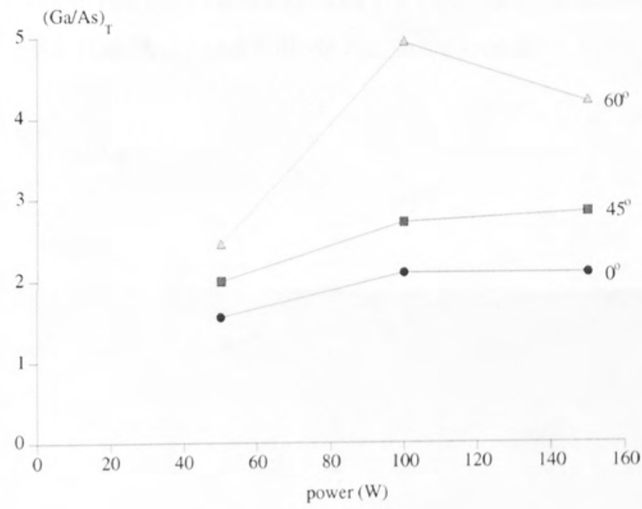

Figure 6.69 $(Ga/As)_T$ as a function of power for pure hydrogen, 40 mTorr for 30 minutes.

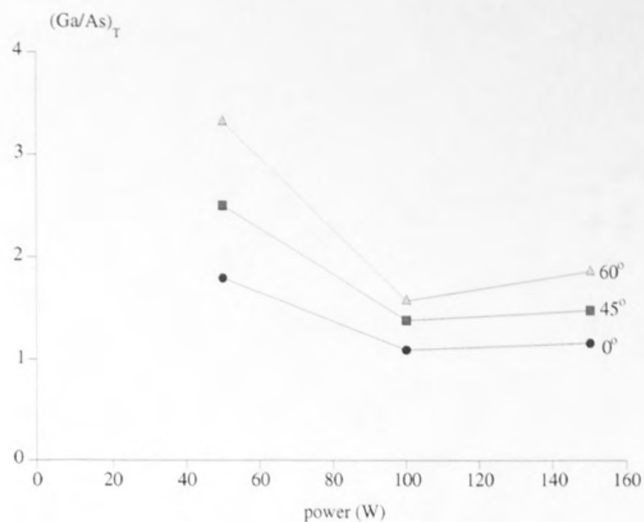

Figure 6.70 $(Ga/As)_T$ as a function of power for pure hydrogen, 80 mTorr for 30 minutes.

Figures 6.71 to 6.74 show the equivalent results for $(Ga/As)_S$. The results appear more consistent than those for $(Ga/As)_T$ and follow the same trend.

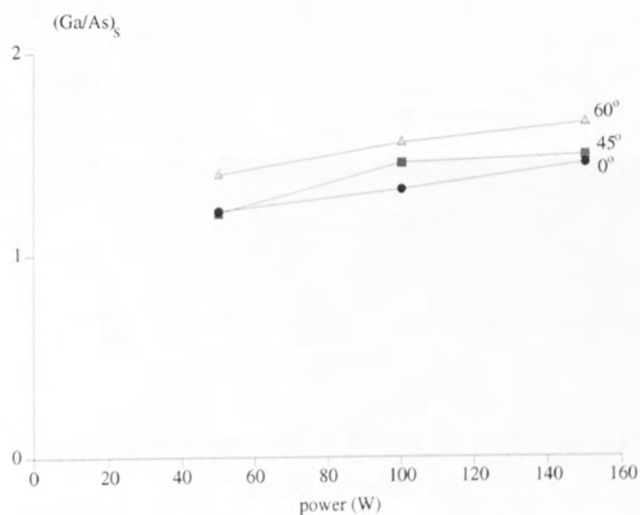

Figure 6.71 $(Ga/As)_S$ as a function of power for pure hydrogen, 10 mTorr for 30 minutes.

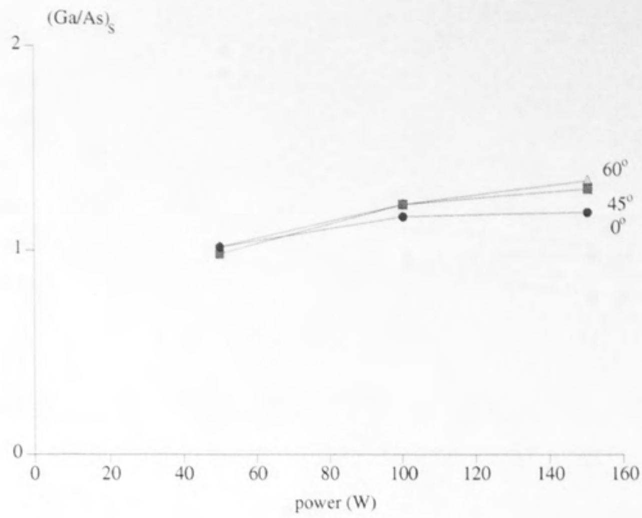

Figure 6.72 (Ga/As)$_S$ as a function of power for pure hydrogen, 20 mTorr for 30 minutes.

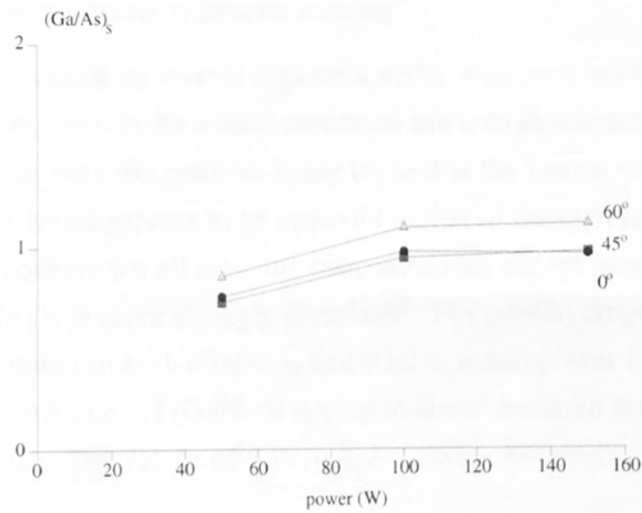

Figure 6.73 (Ga/As)$_S$ as a function of power for pure hydrogen, 40 mTorr for 30 minutes.

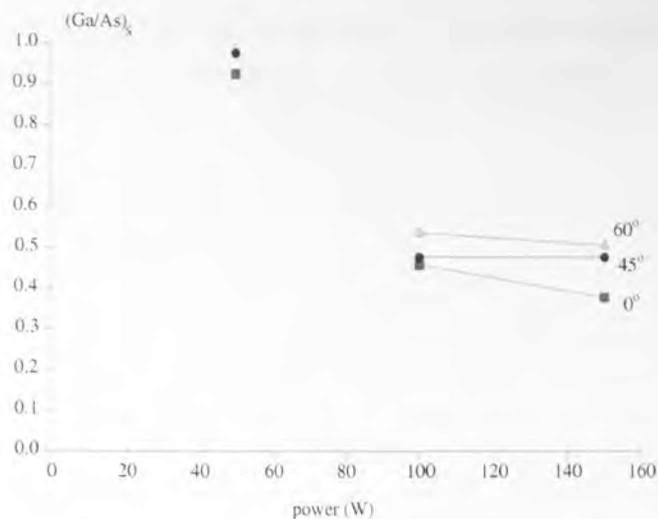

Figure 6.74 $(Ga/As)_S$ as a function of power for pure hydrogen, 80 mTorr for 30 minutes.

6.4.1.5 Summary of methane/hydrogen etching

In general, all samples showed arsenic depletion which was most severe in the near surface. At 10 mTorr, the $(Ga/As)_T$ ratio decreases towards stoichiometry with increasing methane concentration with the gradient being highest at the lowest methane concentrations. This trend appears to be opposite to that of the etch rate. The trend with power is small and positive for all methane concentrations except pure hydrogen where the increase in $(Ga/As)_T$ is more strongly correlated. For pure hydrogen there appears a positive correlation between both $(Ga/As)_T$ and $(Ga/As)_S$ and power for all pressures except 80 mTorr. The values of $(Ga/As)_S$ appear to show the same but smaller trend as the values of $(Ga/As)_T$. The values of $(Ga/As)_S$ are always between 1 and 1.6.

At 20 mTorr the trend is also for a decrease in $(Ga/As)_T$ with an increase in methane concentration for 100 W, at 150 W, however, there is a peak in $(Ga/As)_T$ at 7 % methane. These results also appear to have the opposite trend to the etch rate. The values of $(Ga/As)_S$ at 20 mTorr show no correlation with the methane concentration and have values which remain slightly above 1.

As a function of increasing pressure, the pure hydrogen results for $(Ga/As)_T$ at 100 W and 150 W show a steady decline which is shadowed in the results of $(Ga/As)_S$, the values of which fall significantly below 1. At 50 W the decline reaches a minimum at 40 mTorr, a result which is also followed by $(Ga/As)_S$. As a function of pressure, the $(Ga/As)_T$ ratio for methane/hydrogen at 1:29 (3.4%) also reflects the etch rate, with a minimum value at 40 mTorr for 100 W and 20 mTorr for 150 W, reflecting the maximum etch rates under these conditions.

Hypothesizing that the $(Ga/As)_T$ ratio is a function of the etch rate, then the plotting of one

against the other should give a recognisable trend. Figure 6.75 a) shows this for the results at 10 mTorr 0° ToA. Hydrogen etch rates have been plotted as zero.

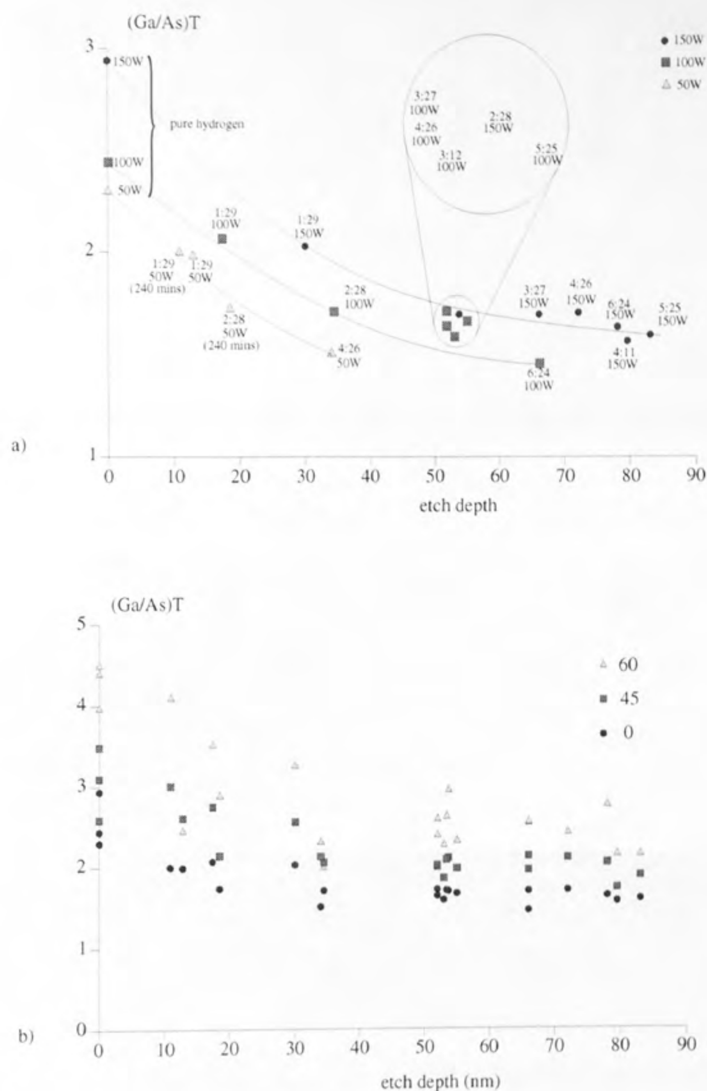

Figure 6.75 $(Ga/As)_T$ as a function of etch depth at 10 mTorr displaying a) 0° ToA and b) 0°, 45° and 60° ToA.

There is a definite trend down and to the right at each power (the lines are guides to the eye for 50, 100 and 150 W). A shift in etch depth appears to be the difference between the curves (excepting the pure hydrogen results).

Figure 6.75 b) shows the same conditions with the angles 45° and 60° also shown.

Figures 6.76 to 6.78 show the results for 20 mTorr, 40 mTorr and 80 mTorr respectively.

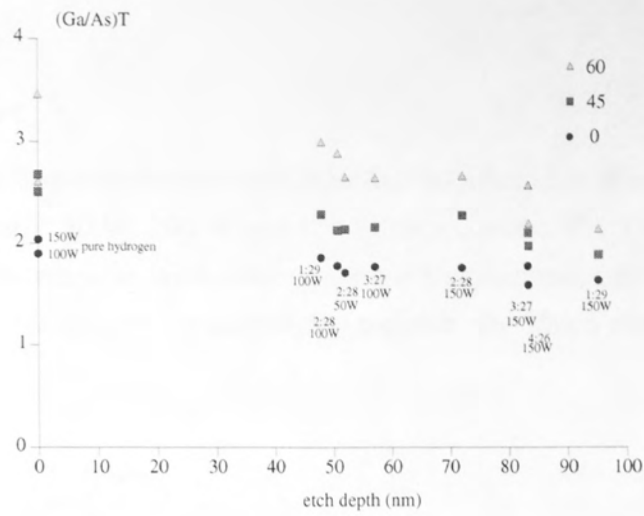

Figure 6.76 (Ga/As)$_T$ as a function of etch depth at 20 mTorr

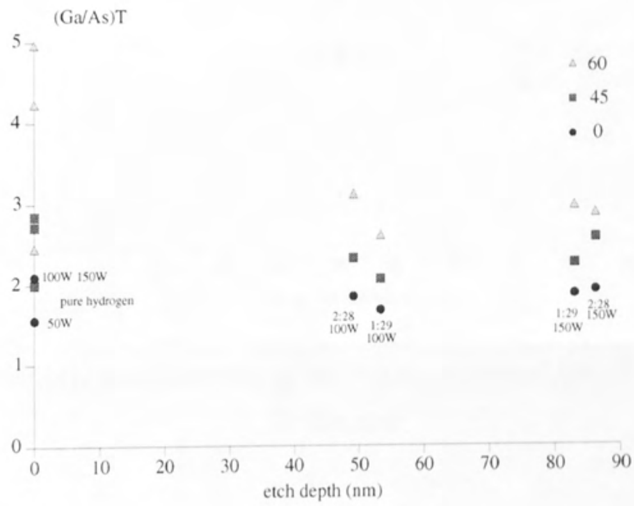

Figure 6.77 (Ga/As)$_T$ as a function of etch depth at 40 mTorr

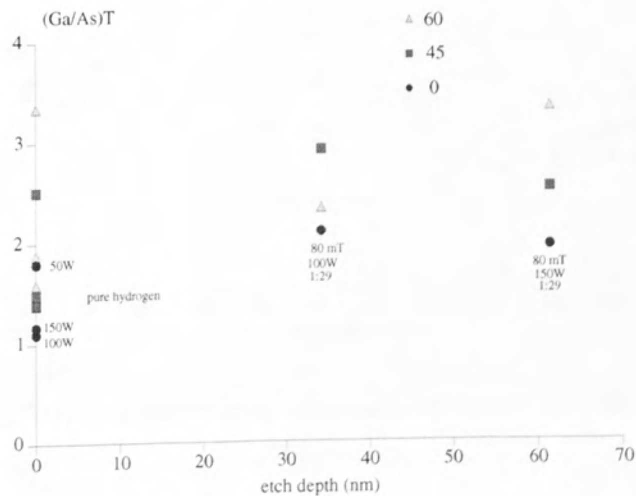

Figure 6.78 (Ga/As)$_T$ as a function of etch depth at 80 mTorr

6.4.2 Neon

6.4.2.1 10 mTorr

Figures 6.79 to 6.81 show the results of $(Ga/As)_T$ as a function of neon concentration for 10 mTorr plasmas at 50 W, 100 W and 150 W respectively. The trend is for a decrease in $(Ga/As)_T$ for an increase in neon concentration with a minimum at 14:3 (82 %). Again, the ratio $(Ga/As)_T$ is opposite to the trend in the etch rate which peaks at this neon concentration.

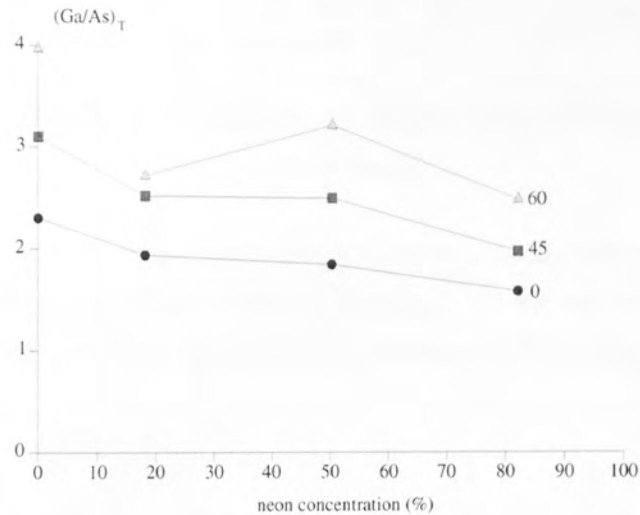

Figure 6.79 $(Ga/As)_T$ as a function of neon concentration for 50 W and 10 mTorr 30 minutes.

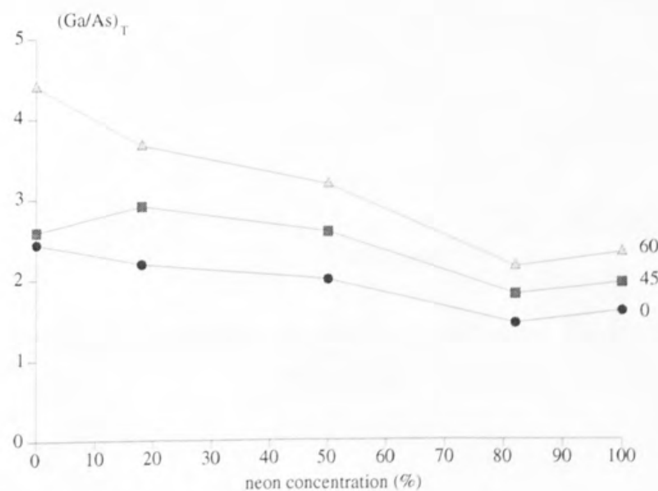

Figure 6.80 $(Ga/As)_T$ as a function of neon concentration for 100 W and 10 mTorr 30 minutes.

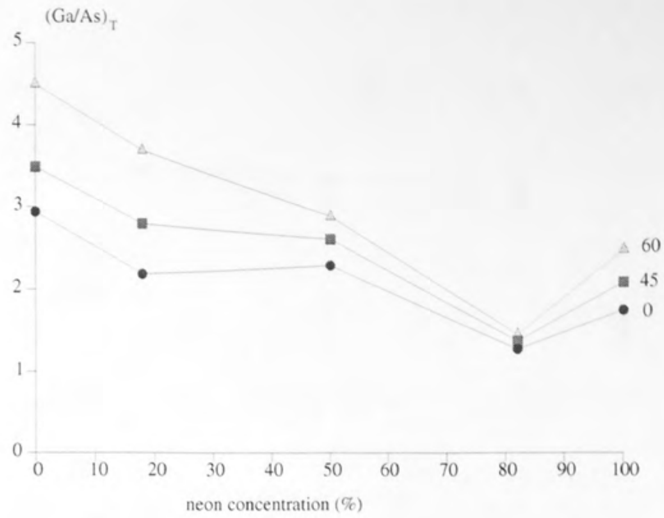

Figure 6.81 $(Ga/As)_T$ as a function of neon concentration for 150 W and 10 mTorr 30 minutes.

Figures 6.82, 6.83 and 6.84 show the results of $(Ga/As)_S$ for the three powers. Here the difference with methane/hydrogen etching is profound. As the neon concentration is increased to pure neon, the $(Ga/As)_S$ ratio drops far below 1 indicating arsenic enrichment in the GaAs.

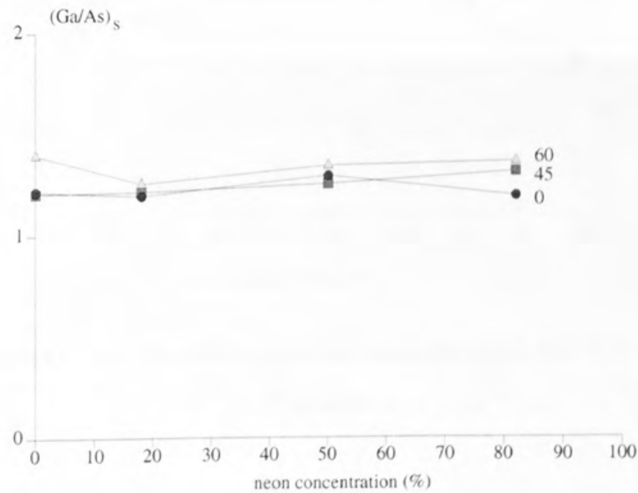

Figure 6.82 $(Ga/As)_S$ as a function of neon concentration for 50 W and 10 mTorr 30 minutes.

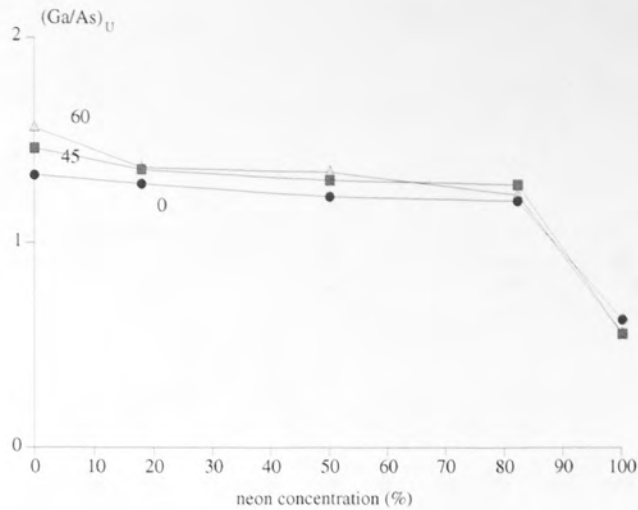

Figure 6.83 $(Ga/As)_S$ as a function of neon concentration for 100 W and 10 mTorr 30 minutes.

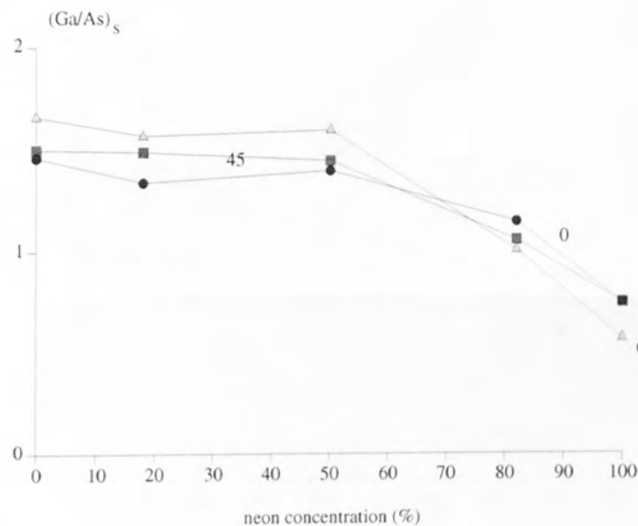

Figure 6.84 $(Ga/As)_S$ as a function of neon concentration for 150 W and 10 mTorr 30 minutes.

6.4.2.2 20-80 mTorr

The pressures 10-80 mTorr were performed only at 150 W due to processing time considerations. The $(Ga/As)_T$ results are shown in figures 6.85, 6.86 and 6.87 for pressures of 20 mTorr, 40 mTorr and 80 mTorr respectively with the $(Ga/As)_S$ results shown in figures 6.88, 6.89 and 6.90.

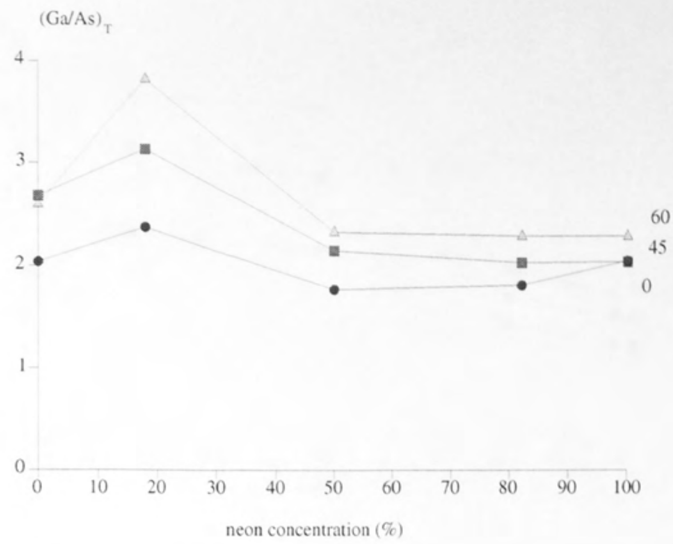

Figure 6.85 $(Ga/As)_T$ as a function of neon concentration for 150 W and 20 mTorr 30 minutes.

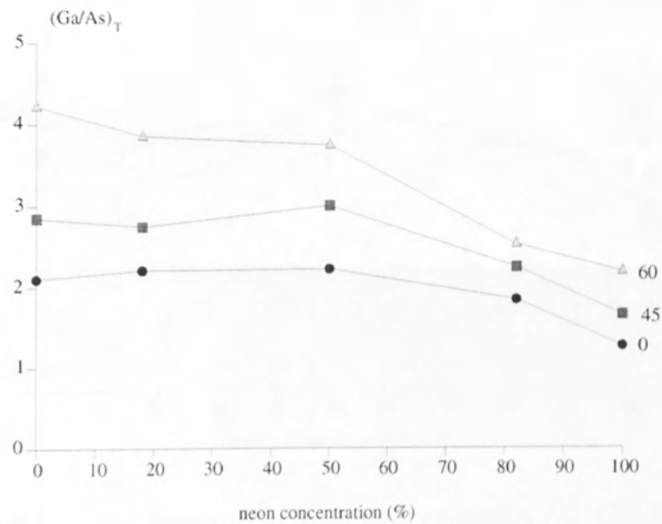

Figure 6.86 $(Ga/As)_T$ as a function of neon concentration for 150 W and 40 mTorr 30 minutes.

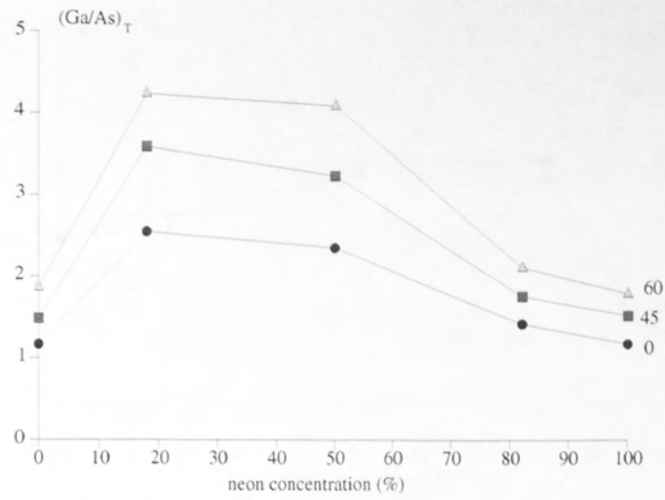

Figure 6.87 $(Ga/As)_T$ as a function of neon concentration for 150 W and 80 mTorr 30 minutes.

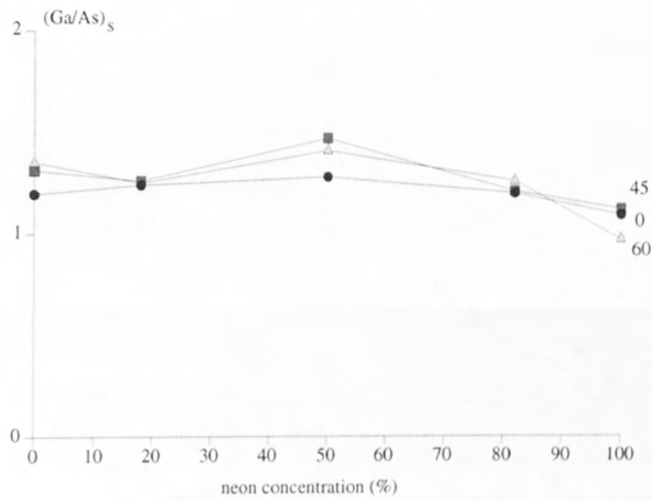

Figure 6.88 $(Ga/As)_S$ as a function of neon concentration for 150 W and 20 mTorr 30 minutes.

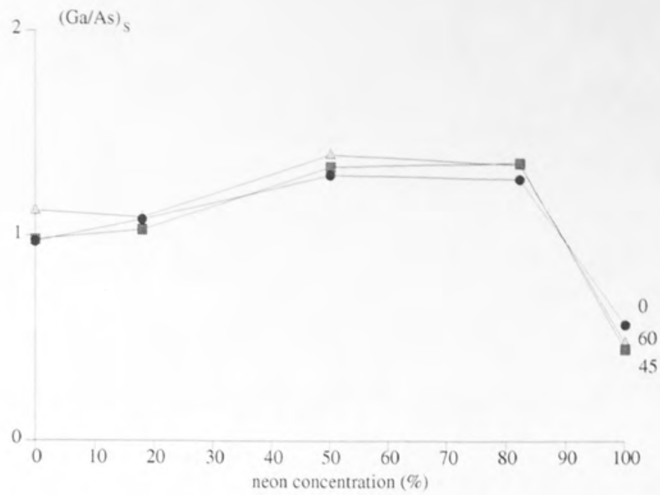

Figure 6.89 $(Ga/As)_S$ as a function of neon concentration for 150 W and 40 mTorr 30 minutes.

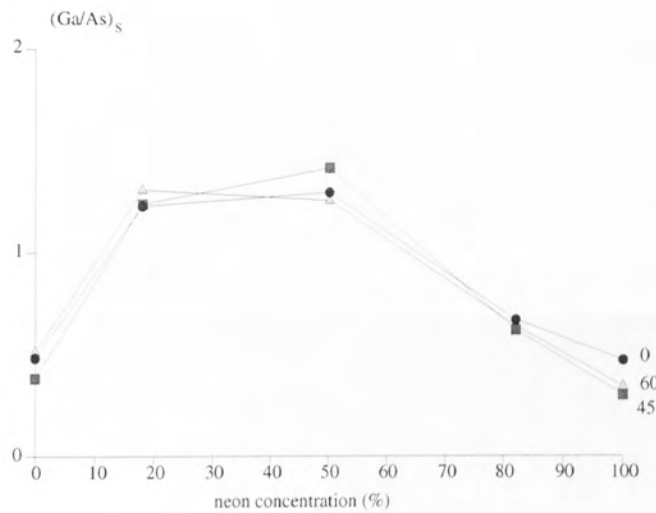

Figure 6.90 $(Ga/As)_S$ as a function of neon concentration for 150 W and 80 mTorr 30 minutes.

6.4.2.3 As a function of pressure

The following graphs show the ratios of $(Ga/As)_T$ and $(Ga/As)_S$ as a function of pressure for all the concentrations of neon except pure hydrogen, the results of which have already been given. The power in all cases is 150 W.

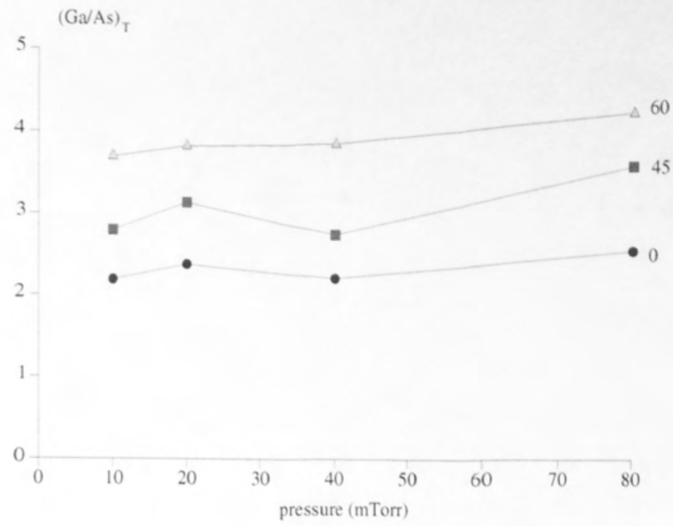

Figure 6.91 $(Ga/As)_T$ as a function of pressure for 150 W and 18 % neon 30 minutes.

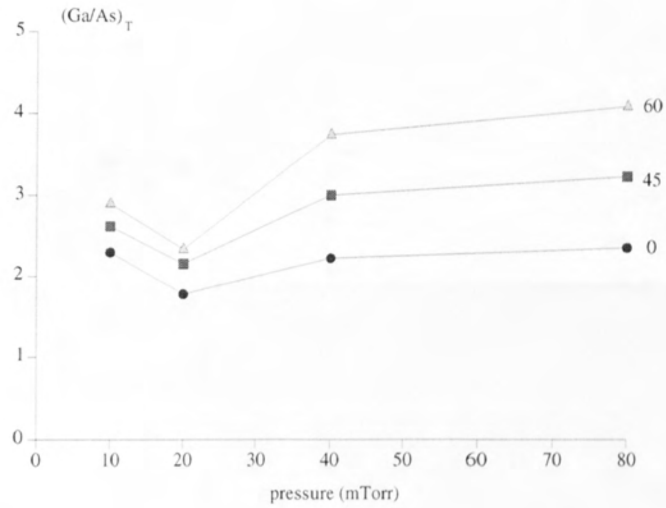

Figure 6.92 $(Ga/As)_T$ as a function of pressure for 150 W and 50 % neon 30 minutes.

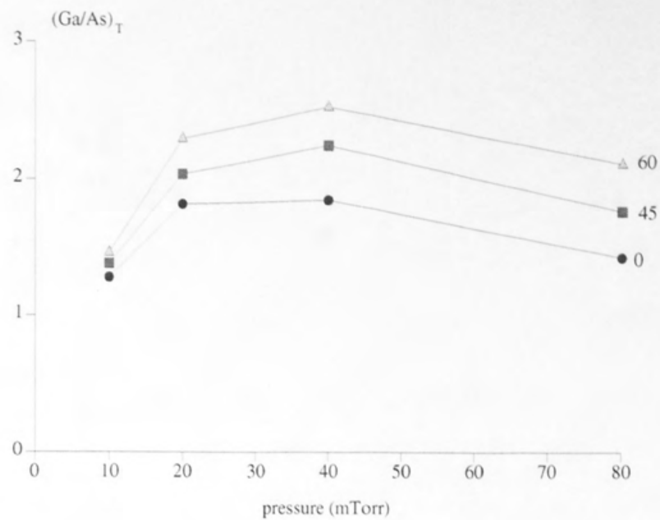

Figure 6.93 $(Ga/As)_T$ as a function of pressure for 150 W and 72 % neon 30 minutes.

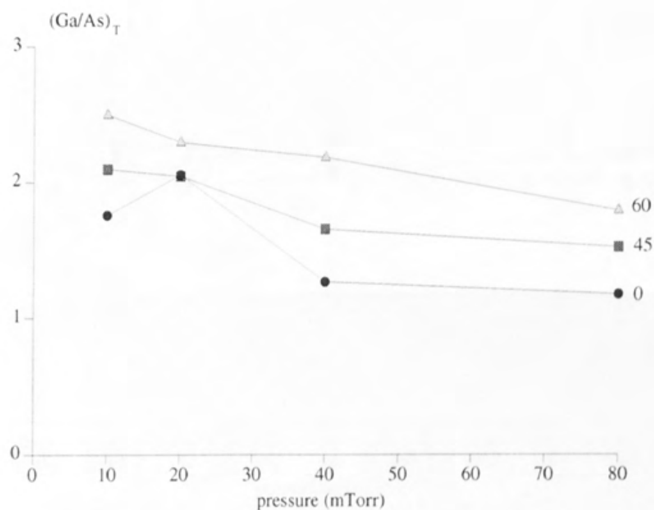

Figure 6.94 $(Ga/As)_T$ as a function of pressure for 150 W and 100 % neon 30 minutes.

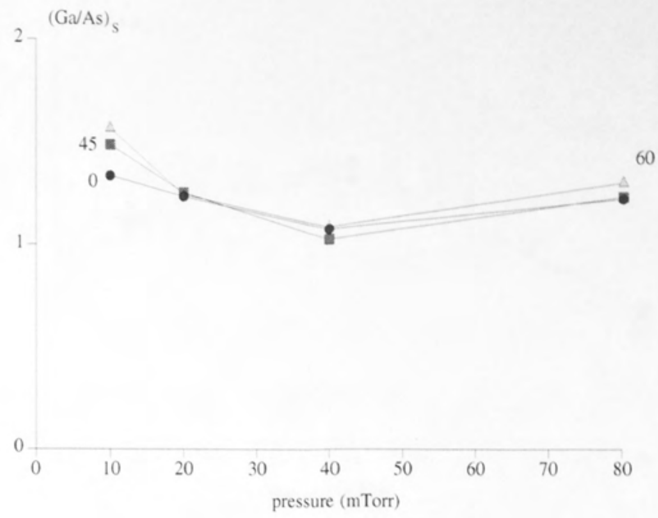

Figure 6.95 (Ga/As)$_S$ as a function of pressure for 150 W and 18 % neon 30 minutes.

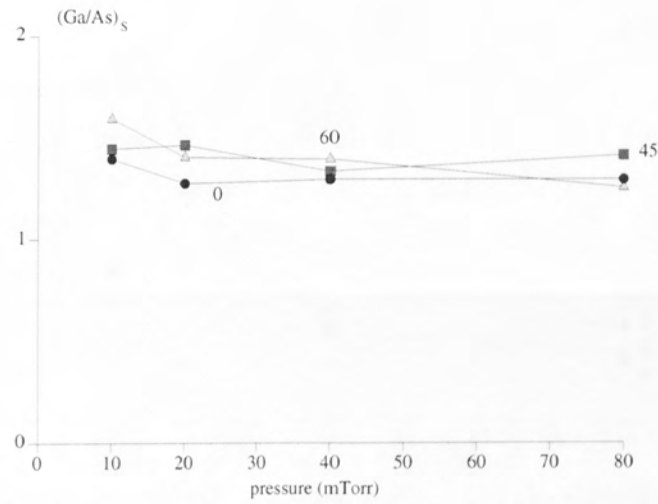

Figure 6.96 (Ga/As)$_S$ as a function of pressure for 150 W and 50 % neon 30 minutes.

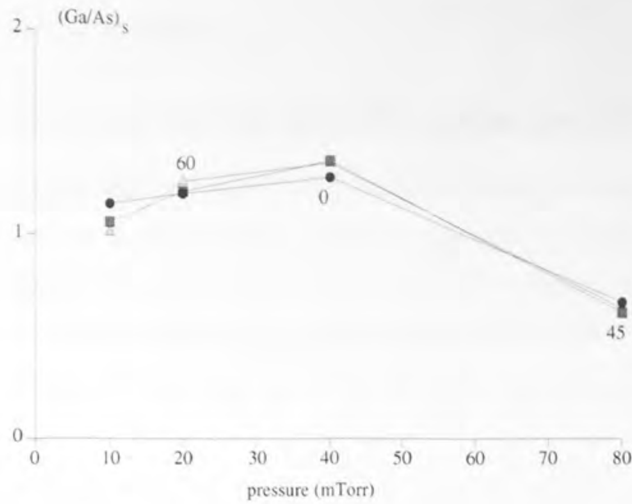

Figure 6.97 $(Ga/As)_S$ as a function of pressure for 150 W and 72 % neon 30 minutes.

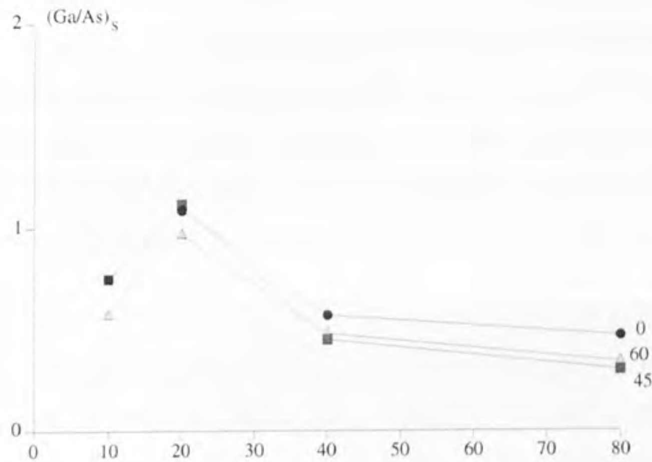

Figure 6.98 $(Ga/As)_S$ as a function of pressure for 150 W and 100 % neon 30 minutes.

6.4.2.4 Summary of neon/hydrogen etching

At 10 mTorr, the results from neon/hydrogen etching are similar to that from methane/ hydrogen etching except where pure neon is used. As the neon concentration is increased, the change from stoichiometry falls as it is expected the etch rate increases. Over the same neon concentration increase, the values of $(Ga/As)_S$ decrease slightly from levels above 1 and then drop rapidly with pure neon to values well below 1. At higher pressures, the increase in neon concentration appears to be correlated with a fall in the change from stoichiometry except for the pure hydrogen result which seems anomalously small, especially at 80 mTorr. The results for $(Ga/As)_S$ appear to follow the results for $(Ga/As)_T$. As a function of pressure, the $(Ga/As)_S$ results appear to vaguely follow the $(Ga/As)_T$ results. The correlation between increasing $(Ga/As)_T$ and pressure is not conclusive, being negative for 0 % and 100 % neon, positive for 18 % neon and containing opposite

inflexions for 50 % and 72 % neon.

6.5 Comparison of model and experimental results

The following sections are devoted to the comparison of experimental data and the results of the model to examine its applicability and explain any discrepancies between them. It will be concluded whether the 1-D model is good enough to allow it to accurately represent the energies and relative fluxes of ions and neutrals at the substrate of the etching experiments.

6.5.1 Electron energies

As the pressure input to the simulation is increased, from 10 to 90 mTorr, the resultant EEDF as given by $f(\varepsilon)$ (sampled at the sheath edge) has its peak value reduced from 8 V to 6V. In the plasma bulk mid-way between the electrodes (4 cm from the plasma/sheath boundary) the peak energy is further reduced to 2 eV. As discussed in section 5.1.2.4, the results from the Langmuir probe which at high pressures is 2 cm above the plasma/sheath boundary and at lower pressures begins to enter the sheath are also a function of the spatial change in electron characteristics. Hence, experimental and predicted values cannot be directly compared, although the general form of the measured EEDFs are in reasonable agreement. A typical characteristic peaks at ~6.5 V which is in agreement with the predicted values.

For a Maxwellian distribution we expect $\ln(f(\varepsilon)/\sqrt{\varepsilon})$ versus energy should yield a straight line. The predicted distributions are shown in section 5.1.2.4 and are similar to those predicted by Surendra and Graves [281]. The distributions are clearly not linear, but an increase in pressure is seen to reduce the extent of the high energy tail. This reflects the higher number of collisions experienced by electrons at the higher pressures. The EEDF is distinctly non-Maxwellian and therefore it is better to discuss the EEDF than attempt to extract an electron temperature. The increased rate of ionisations at the higher pressures also leads to a greater tendency for the electron cascades to 'run away'. This is inhibited by reducing the floating potential and thereby allowing the electrons a greater probability of escape to the walls. The floating potential, therefore, is an important parameter determining the probability of an electron causing an ionisation before undergoing recombination at the walls. For a plasma in equilibrium this value should be equal to one and the floating potential is adjusted to approximately bring this about. The resulting reduction in the floating potential with pressure of 5 V is reflected in the reduction in the average potential at the Langmuir probe with increasing pressure from 27 to 21 V at 50 W and 23 to 16 V at 150 W. Further comparison with methane/hydrogen is not possible because of the problems of deposition and the change in the sampling position of the probe relative to the sheath.

6.5.2 Plasma potential and IEDs at the anode

The ion energies at the cathode are determined mainly by the D.C. bias, whereas the ion energies at the anode are determined mainly by the extent and form of the plasma potential. Comparison of predicted and experimental energies at the anode will therefore test the validity of the plasma potential approximation used. This was initially performed for argon and then for hydrogen.

6.5.2.1 Argon

Ion energy distributions were taken for Ar^+ from 40 to 95 mTorr at 10 W, 30 W and 50 W. The results from the 10 W are noisy and the results from the 30 W and 50 W are very similar, those for 30 W being shown in figures 6.99 to 6.102 for pressures of 40 mTorr, 60 mTorr, 80 mTorr and 95 mTorr respectively. The ion energy distributions have been corrected by the addition of 3.7 eV to the measured energies due to the various lenses in the mass analyser, which lead to an overall loss in kinetic energy of the traversing ions of 3.7 eV. The predicted IEDs are superimposed for the same conditions with the values of the sheath widths used in the simulations given.

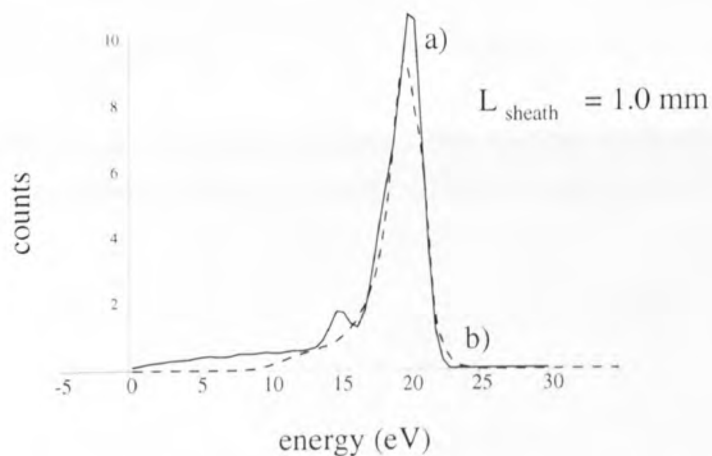

Figure 6.99 Comparison of (a) predicted and (b) experimental results for the IEDs at the anode of an argon RF plasma. Pressure 40 mTorr.

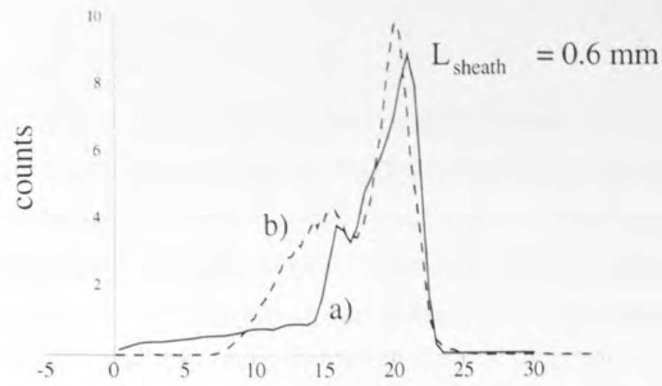

Figure 6.100 Comparison of a) predicted and b) experimental results for the IEDs at the anode of an argon rf plasma. Pressure = 60 mTorr.

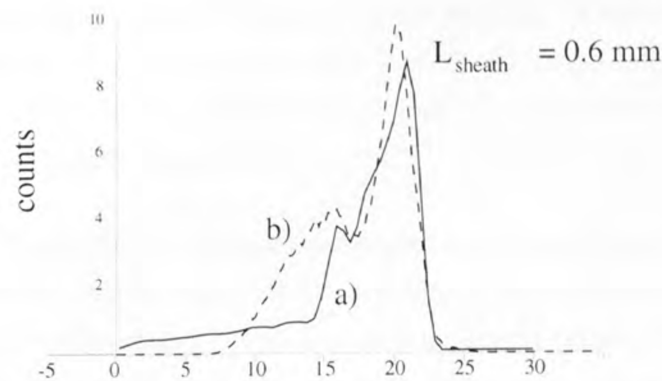

Figure 6.101 Comparison of a) predicted and b) experimental results for the IEDs at the anode of an argon rf plasma. Pressure = 80 mTorr.

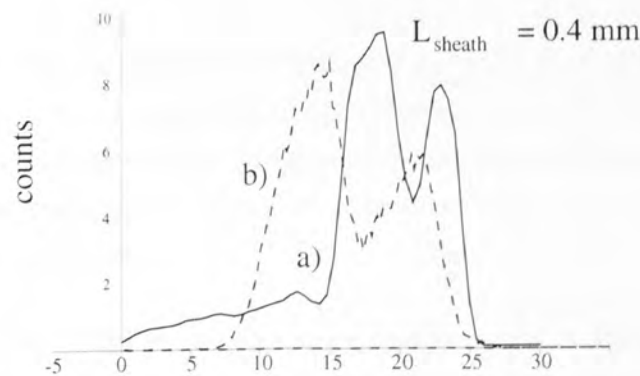

Figure 6.102 Comparison of a) predicted and b) experimental results for the IEDs at the anode of an argon rf plasma. Pressure = 95 mTorr.

It can be seen that the model reproduces the saddle-like structure of the experimental IED well. The sheath, over the anode, is much smaller than the sheath over the cathode and due to the geometry of the cell, cannot be measured directly. The sheath, however, is of the order of 0.5 mm, in agreement with theoretical studies carried out by May [282]. In addition, the sheath width decreases as the pressure increases and the ionic mean free path

falls.

The variable which most influences the ion energy distributions over this change in pressure is the sheath width, the increase in which as the pressure decreases causes the loss of the low energy peak. At 95 mTorr one of the effects of the collisions in the IED is to make the low energy peak increase relative to the high energy peak as neglecting collisions always leads to a more intense higher energy peak. The seeming inability of the energy analyser to detect ions with energies below 5 eV is a phenomenon seen before in a similar off-axis geometry investigated by Olthoff et al [283].

The geometric ratio of the cathode to anode areas, A_c/A_a of 0.1 or less gives rise to an effective ratio used in the calculations of 0.3 and this remains fixed for all the calculations. If the D.C. bias and driving potential are directly measured at the cathode and applied to equation 1.19, then an A_c/A_a ratio of between 0.37 at 10 mTorr and 0.27 at 95 mTorr is found. Dickenson [284] however, shows that this value, as in our study does not give the best fitting parameter for the simulation.

The effect of different potential variations across the sheath made little difference to the ion energy distributions and the exact form of the time dependent plasma potential was considerably less important than it's maximum and minimum values. When predicting ion energy distributions at the negatively biased substrate, the plasma potential becomes an even less important parameter. Similarly, modification of ion energies to take account of the Bohm criterion had no effect on the shape of the ion energy distribution.

6.5.2.2 Hydrogen

Figure 6.103 shows the experimental and predicted H_3^+ IEDs at 90 mTorr for a sheath width of 3.5 mm. A problem with the hydrogen plasmas (which is less of a problem for plasmas of higher molecular masses) is that at pressures below 40 mTorr, the mass probe is no longer adjacent to the plasma but to the plasma/sheath boundary and the readings of the mass probe fall into noise.

The sheath width is larger in the case of hydrogen as indicated by the lack of peak splitting, however the sheath is still thin and the collision processes within it do not contribute greatly to a change in the IED. Consequently, the mass probe tends to show species which are in the plasma bulk rather than giving an insight into processes in the sheath. This is also true of the methane/hydrogen plasmas and ion species IEDs tend to peak at the average anode sheath potential with a width given by collision processes and the rf modulation in convolution with the instrument response function.

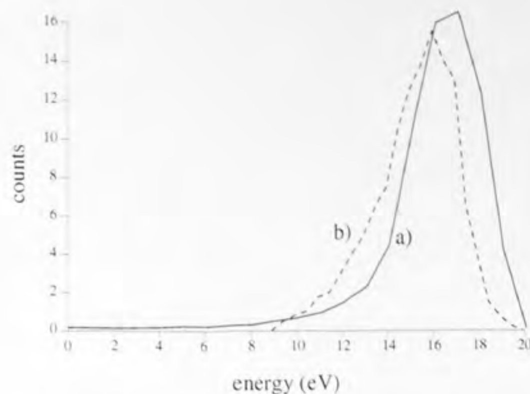

Figure 6.103 Comparison of a) predicted and b) experimental results for the IEDs at the anode of a hydrogen rf plasma. Pressure = 90 mTorr.

6.5.3 Ion fluxes

The following gives a comparison between the fluxes (deemed proportional to peak heights in the IED) of species which are entering the mass probe orifice. Experimental results are scaled for the sensitivity of the mass probe as described in section 6.1.2.2, except for H_3^+ which has no correction factor and is assumed to have the same instrument response as H_2^+.

6.5.3.1 Hydrogen

The trends in the fluxes of the three ionic species H^+, H_2^+ and H_3^+ as a function of pressure are well predicted by the code as shown by a comparison of figures 6.104 and 6.105. For pure hydrogen, the main external parameter affecting the ratio is the pressure. This is due mainly to the conversion of H_2^+ to H_3^+. Both agree on the two ion species being equal around 30 mTorr and the H^+ ion being relatively unaffected by the pressure. The agreement in the results implies that the instrument response is the same for H_3^+ as for H_2^+. It can be seen that the breakdown of the flux to the cathode shown in figure 6.106 is significantly different to that at the anode.

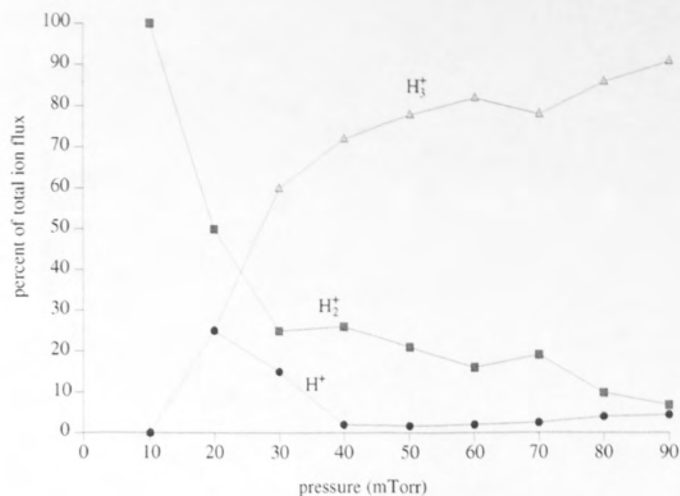

Figure 6.104 Experimental results of the fluxes of hydrogen ions to the anode as a function of pressure for a power of 150 W.

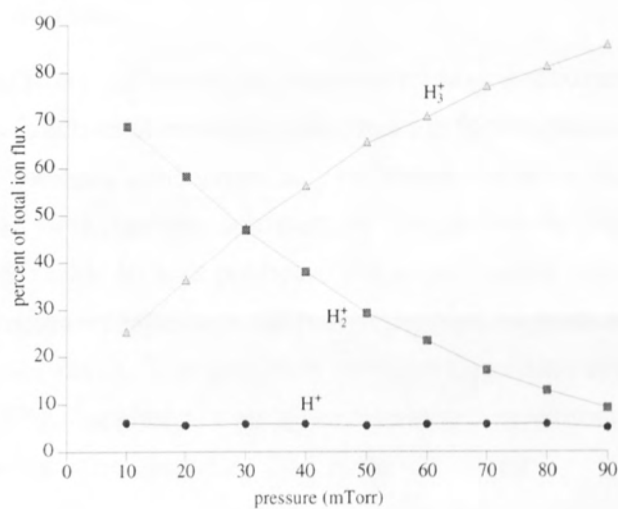

Figure 6.105 Predicted fluxes of hydrogen ions to the anode as a function of pressure for a power of 150 W.

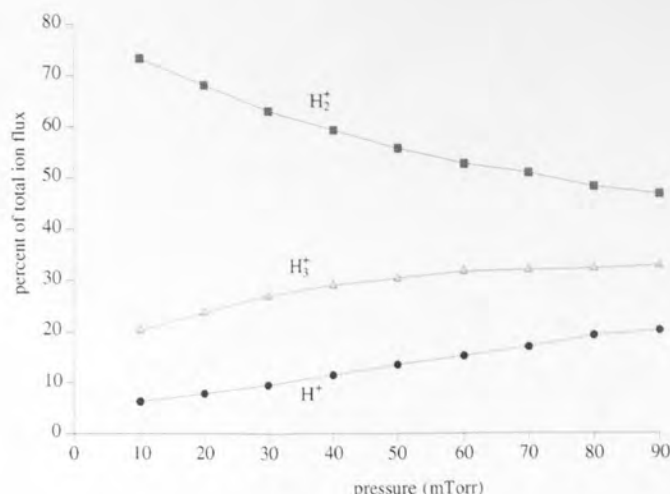

Figure 6.106 Predicted fluxes of hydrogen ions to the cathode as a function of pressure for a power of 150 W.

6.5.3.2 Addition of methane

The trends within the fluxes of ions in the methane/hydrogen mixture are shown in figure 6.107 and 6.108 as a function of methane concentration for experiment and simulation respectively. As the methane concentration is increased, the H^+ is relatively unaffected, whilst the H_2^+ and H_3^+ both decrease substantially. Again the H_3^+:H_2^+ ratio is in general agreement with experiment. In both predicted and experimental fluxes, the proportion of methane fragments increases rapidly as the partial pressure of methane is increased and then levels off at higher ratios. The dominant methane fragments appear to be CH_5^+ followed by CH_3^+, CH_4^+ and $C_2H_5^+$ in both simulation and experiment. In the experiment, however, $C_2H_5^+$ appears more important than in the simulation.

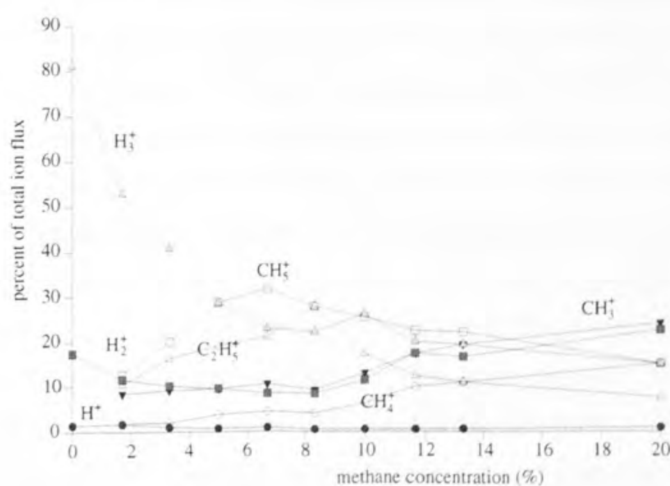

Figure 6.107 Experimental results of the fluxes of ions to the anode as a function of methane concentration for a power of 150 W and pressure of 50 mTorr.

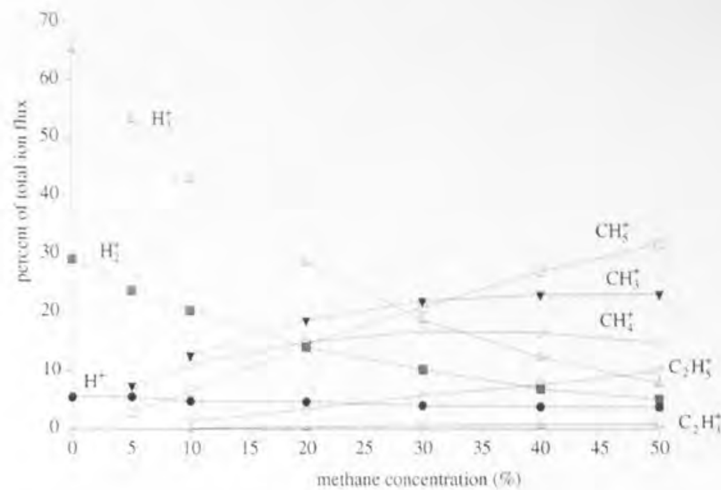

Figure 6.108 Predicted fluxes of ions to the anode as a function of methane concentration for a power of 150 W and pressure of 50 mTorr.

Figure 6.109 shows the predicted ion flux to the cathode for the same conditions as figure 6.108. It can be seen that the relative importance of H_2^+ and H_3^+ has been reversed and the mass distribution of the ion flux to the mass probe cannot be used as an approximation to that to the substrate in etching experiments. The experimental results are only shown up to 20 % methane concentration because deposition at the mass probe orifice makes the results more subject to error and less reproducible. The simulation appears to show the total methane and hydrogen fragments to be equal at a methane concentration of 20 %, whereas the experiment shows them equal at around 4 % concentration. Most of the discrepancy is to be found in the fact that there is a higher ratio of methane to hydrogen in the plasma than the ratio of the flow rates of the gases due to differential pumping efficiency as found in section 6.1.2.2. Taking this into account (and for all further simulations in this chapter) figure 6.110 shows the corrected ion flux breakdown predicted at the anode. The methane and hydrogen fragments appear equal at a methane concentration of 8-10 %. Further, the ratio of hydrogen ions to the total flux tends to 38% at 20 % methane concentration in the experiment whereas this value is reached at a methane concentration of 14 % in the simulation. There is, however, one other potential source of error when comparing experimental and simulated results. This is that in the 1-D model, the anode cathode distance is 10 cm whereas in the experiment, though this is true for most of the anode, the mass probe is located in an off-axis position with its orifice adjacent to the cathode plasma/sheath boundary. This boundary as previously explained for the Langmuir probe, changes position with the plasma conditions. Ions which arrive at the mass probe are more likely therefore to have been created here than at the anode plasma/sheath boundary. As most ions are created at the cathode plasma/sheath boundary, on average, ions in the experiment have not travelled as far to the mass probe as in the simulation. Direct comparison with results for the cathode would, as has been shown yield very different answers. This notwithstanding, the major trends in the fluxes are reproduced.

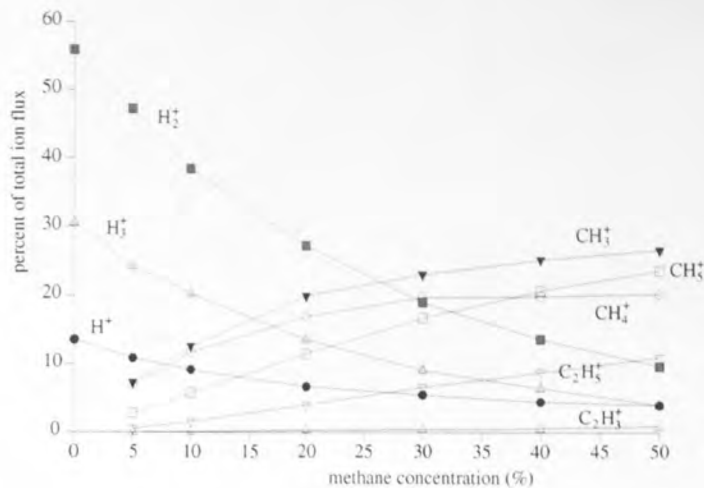

Figure 6.109 Predicted fluxes of ions to the cathode as a function of methane concentration for a power of 150 W and pressure of 50 mTorr.

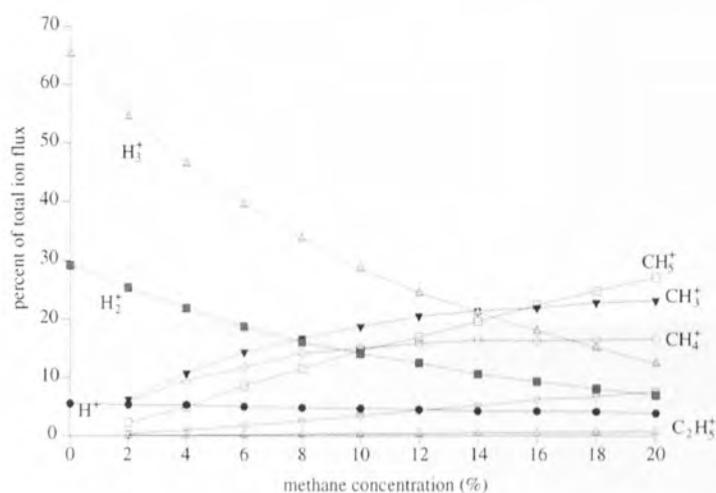

Figure 6.110 Predicted corrected fluxes of ions to the anode as a function of methane concentration for a power of 150 W and pressure of 50 mTorr.

6.5.3.3 Increase in pressure of methane/hydrogen

Figures 6.111 and 6.112 show the how the flux to the anode varies as a function of pressure for a fixed concentration of methane, in the experiment and simulation respectively. The total methane flux as a percentage of the total ion flux remains constant with pressure, at a level of 60 % in the experiment and 40 % in the simulation. As in the pure hydrogen case, there is predicted to be a gradual takeover of H_2^+ by H_3^+ as the pressure increases. This is not seen in the experimental results and yet one would expect it to (the difference between pure hydrogen and 7 % methane in hydrogen is not great) unless the results are unreliable due to a degradation in the mass probe response due to constant fouling with polymer. The results below are, in fact, some of the last taken with the probe before the chaneltron required cleaning or replacing.

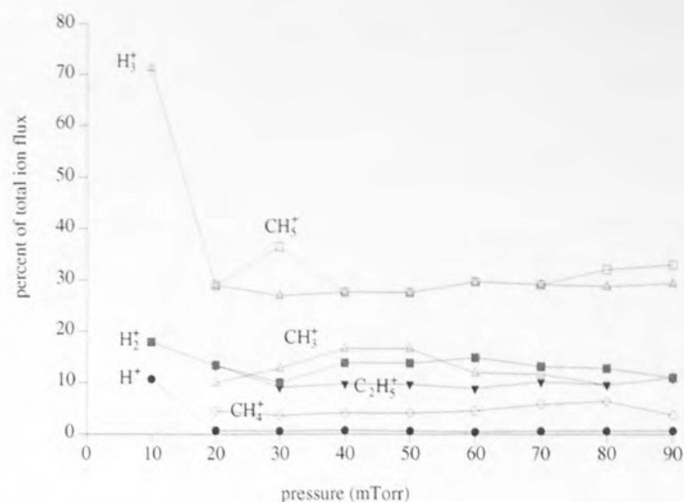

Figure 6.111 Experimental results of fluxes of ions to the anode as a function of pressure for a methane concentration of 7 % and a power of 150 W.

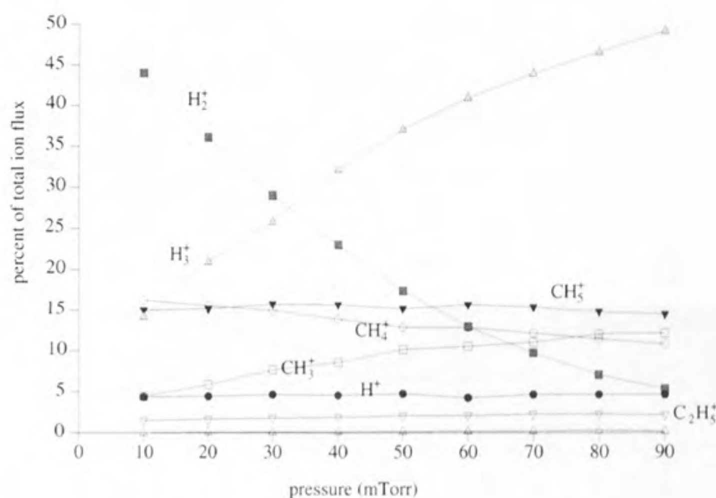

Figure 6.112 Predicted fluxes of ions to the anode as a function of pressure for a methane concentration of 7 % and a power of 150 W.

6.5.3.4 Increase in power of methane/hydrogen

The experimental result in figure 6.113 was taken from the raw data shown in figure 6.19 and it can be seen that below 150 W the results tend to descend into noise. With the change in power, the ratio of ions does not change drastically within the error of the mass probe and this is shown in the simulated results in figure 6.114.

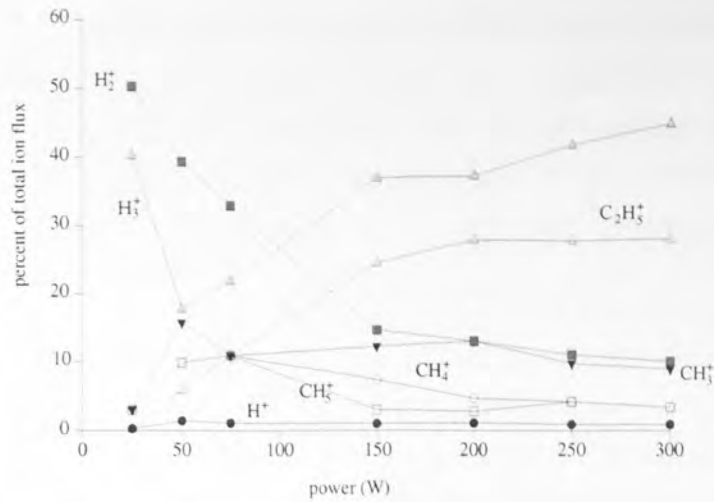

Figure 6.113 Experimental results of fluxes of ions to the anode as a function of power for a methane concentration of 7 % and a pressure of 50 mTorr.

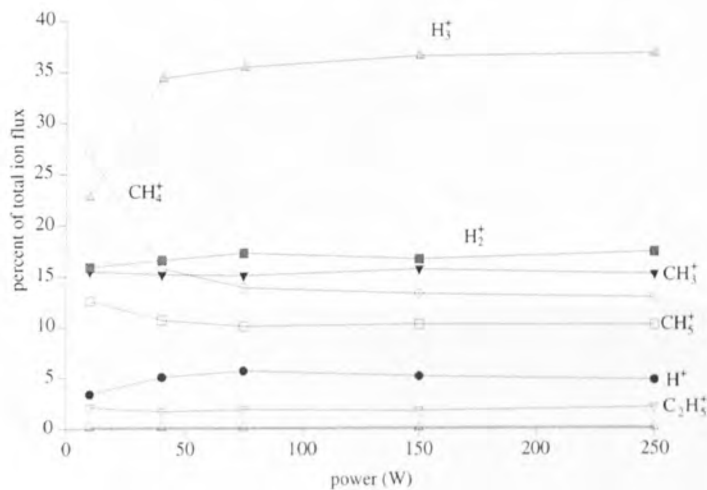

Figure 6.114 Predicted fluxes of ions to the anode as a function of power for a methane concentration of 7 % and a pressure of 50 mTorr.

The problems involved in the use of the mass probe can also be seen . The results given appear to be internally consistent (*ie.* show scatter that is considerably less than the resulting trend) as shown in figures 6.107, 6.111 and 6.113. However, a cursory look at the data presented reveals errors in consistency between the three data sets. This again implies problems with the mass probe and its change in response over time.

6.5.4 The predicted optical sheath width

One of the major parameters which affect much of the results of the simulations is the sheath width. This parameter is deduced from optical measurements, however, it is not obvious whether the electrical sheath width is similar to the optical sheath width. This is a problem discussed extensively by May [285] and Liu [286] who conclude the sheaths widths are similar at low pressures (10 mTorr and 50 mTorr) but at higher pressures (500 mTorr)

the visual sheath width overestimates the electrical sheath width. In this study, the optical sheath width is measured as the distance from the sample surface until the position where the plasma begins to get significantly brighter *ie.* the width of the dark space rather than to the point of maximum brightness. It was measured in this way because the estimation of the dark space is visually easier than the position of maximum brightness which appears more tenuous.

Figure 6.115 shows the simulated excitation profile for 10 mTorr, 40 mTorr and 80 mTorr at 150 W with the sheath width used in the simulation superimposed. The peak of the excitation profile appears at a distance somewhat greater than the position of the electric sheath edge in each of the simulations. It appears that the sheath width estimate at this range of pressures is a good estimate of the true sheath width if the excitation profile is similar to the optical emission profile.

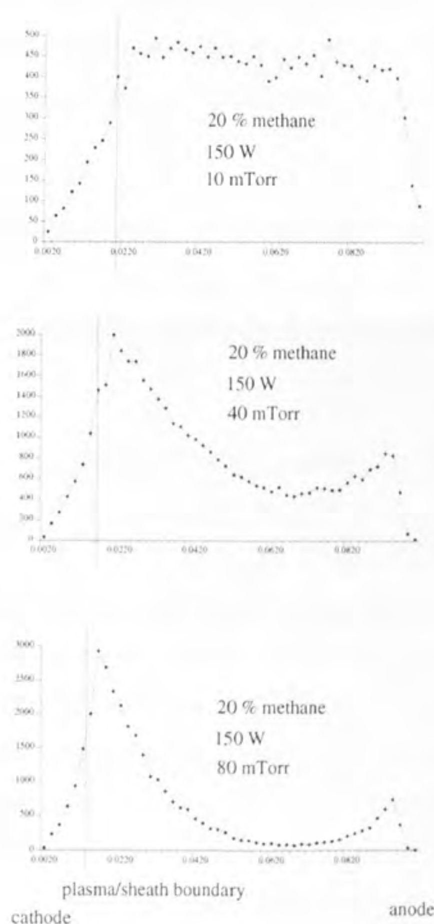

Figure 6.115 Spatial excitation profile for a range of conditions with the simulated electrical sheath width superimposed

6.5.5 Regimes of etching and deposition

There exists within the parameter space of the ion etcher regions where the gallium arsenide is either etched or deposited on and this is dependent on the fluxes and energies of particles at the surface. GaAs is etched by methane in an excess of hydrogen where it is thought the major purpose of the hydrogen is to competitively remove the polymer. Deposition generally occurs over all of the parameter space for objects at floating potential in the plasma (leading to problems when using a Langmuir probe), at the anode and on the quartz plate upon which the GaAs samples are placed. Over much of this parameter space, however, the GaAs is being etched. The likelihood of deposition occurring on the GaAs surface tends to increase with decreasing power (*ie.* the ion energy at the surface) and increasing pressure and/or methane concentration. The implication is that at higher energy, ions at the surface are removing polymer build up (the change in power has a relatively small effect on the mass distribution of the flux) as are hydrogen ions and that neutrals (the dominant result of raising the pressure) have an important rôle to play. The idea that the etching/deposition are competitive effects is emphasised by the etch rate which increases as the methane concentration is increased until deposition suddenly occurs.

The code which predicts ratios and energies of ions and neutrals at the surface was used to compare the fluxes and energies of the different species in the different etching experiments in order to find some parameter which would indicate the likelihood of etching or deposition.

With the idea that the hydrogen is removing the methane which is attempting to create a deposit on the surface, the most obvious ratio to look at would be the total hydrogen ion flux to the total methane flux. This ratio does not increase substantially with increasing pressure, mainly with the methane concentration, whereas the likelihood of deposition is a strong function of pressure. Likewise the ratio of the total (ion + neutral) flux of methane to hydrogen is not a strong function of pressure. Figure 6.116 shows the ratio of methane neutrals to hydrogen ions predicted as a function of pressure and methane concentration. Each point represents an experiment and is marked if deposition occurs. This ratio fits the criterion and implies that when the ratio of methane neutrals (low energy but considerably higher than thermal and sufficient to cause reactions at the surface) to hydrogen ions (with 100's of eV) is greater than about 1.2, then deposition will occur (the function neutral methanes/total hydrogen does not work, agreeing with the hypothesis that the hydrogens must be of high energy). Finally an even better plot is given in figure 6.117 of the ratio of methane neutrals to the ratio of all ions. The implication here is that not only do fast methanes not contribute to polymer build up but may actually act against it (*ie.* by sputtering).

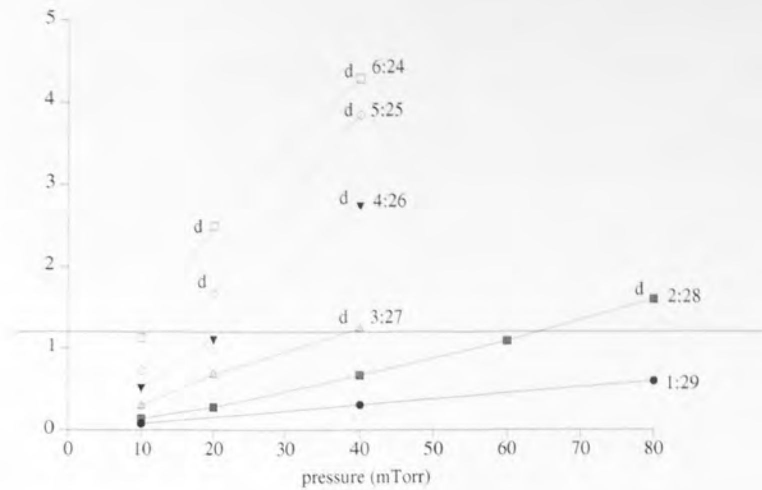

Figure 6.116 Ratio of (methane neutrals)/(hydrogen ions)

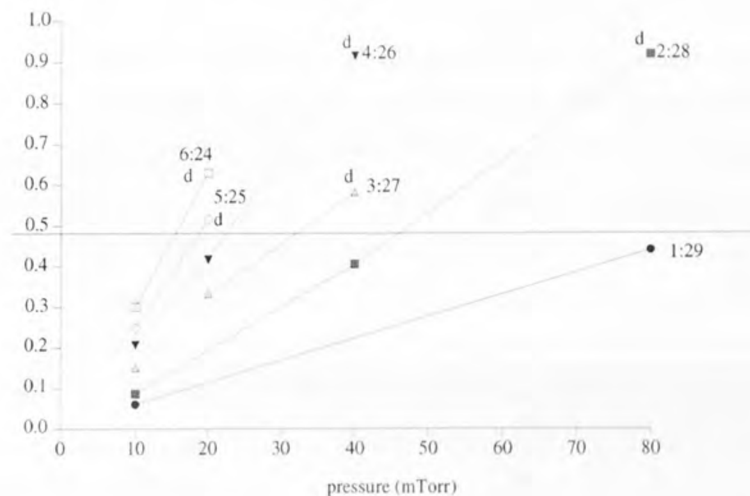

Figure 6.117 Ratio of (methane neutrals/total ion flux)

6.6 Predictions for the etching experiments

The good agreement between model and experiment allows confidence in the predicted fluxes to the substrate, a summary of which is given below.

6.6.1 Ion fluxes

Figure 6.118 shows the breakdown of the predicted fluxes of methane and hydrogen to the sample surface during the etching experiments as a function of methane concentration. As the concentration of methane increases, the relative flux of hydrogen to the surface falls, rapidly at first, with the methane to the surface increasing but increasingly slowly. The methane and hydrogen fragments are of equal flux at only 10 % methane. The relative neutral fluxes to the surface follows a similar dependency as therefore does the total flux of methane or hydrogen fragments at the surface. The energies of the fragments at the surface is not greatly affected by the methane concentration.

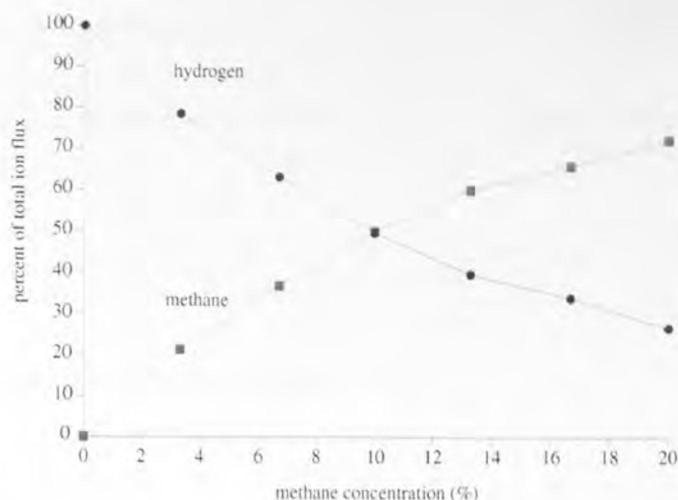

Figure 6.118 Predicted fluxes of methane and hydrogen ions to the cathode as a function of methane concentration at 10 mTorr and 150 W.

As the pressure increases at the lowest methane concentration the change in ion fluxes to the cathode is small except for the conversion of H_2^+ to H_3^+. The average ion energies over the pressure range is moderately reduced (<10 % except for H_2^+ which reduces by 50 %) and their angular distribution increases. The major change over the pressure range is the large increase in the flux of neutrals arriving at the surface. For example at a methane percentage of 3.7 % (a ratio of 1:29) at 10 mTorr the H_2 and CH_4 neutral fluxes make up 48 % and 6 % of the total ionic flux respectively, whereas at 80 mTorr the H_2 and CH_4 neutral fluxes make up 194 % and 44 % of the total ionic flux respectively. Over the same increase in pressure the average energy of a H_2 neutral falls by 50 % but the energy of a CH_4 neutral falls only slightly.

The effect of a change in power over the experimental range is primarily to change the energies of ions at the substrate.

6.6.2 Relevance of neutral fluxes

The neutral flux to the cathode has been shown to be considerable and exceeds the ion flux for some conditions. The neutral flux is, however, predominantly low energy and the question arises as to its importance relative to the large flux of thermal neutrals which arrive equally at all surfaces exposed to the gas. The following calculations give estimates of the background flux in comparison to the fast neutrals predicted by the code.

The neutral flux to a surface in a gas is given by

$$\phi = \frac{n < c >}{4} \qquad \text{eqn 6.1}$$

where n is the number of particles per cm^3 and $< c >$ is the average velocity of a gas particle. This equals 6×10^{19} methane or 1.8×10^{20} for hydrogen particles per second per

square centimetre at 100 mTorr.

For a Boltzmann distribution of velocities, the number of particles with energy between v and $v + dv$ is given by

$$\frac{dN}{dv} = \frac{4n}{\pi^{1/2}}\left(\frac{m}{2kT_i}\right)^{3/2} v^2 \exp\left(\frac{-mv^2}{2kT_i}\right) \qquad \text{eqn 6.2}$$

and the number of particles striking a surface

$$\frac{dN_{surface}}{dv} \propto v\frac{dN}{dv} \qquad \text{eqn 6.3}$$

is then given by

$$\frac{dN_{surface}}{dv} \propto v^3 \exp\left(\frac{-mv^2}{2kT_i}\right) \qquad \text{eqn 6.4}$$

The fraction of the total number of particles impingent on a surface which arrive with energies up to E is then given by

$$f(E) = \frac{\int_0^E v^3 \exp\left(\frac{-mv^2}{2k_i}\right)}{\int_0^\infty v^3 \exp\left(\frac{-mv^2}{2kT_i}\right)} \qquad \text{eqn 6.5}$$

Given that the ion temperature is 0.05 eV, this gives the fraction of the total number of particles which arrive above energy E as

E	$1 - f(E)$
0.23	10^{-1}
0.37	10^{-2}
0.5	10^{-3}
0.65	10^{-4}
0.77	10^{-5}
0.9	10^{-6}

Given that the ion current is approximately 10^{15} per second per square centimetre (see section 3.2.1), then the neutral flux to the electrode is substantially less than the ion flux to the electrode at energies above 1 eV. The neutral flux predicted in the model is therefore significantly above the background for energies above 1 eV. The neutral energy distributions are presented in 2 eV energy bins and as ignoring the first energy bin of 0.1 eV (the minimum neutral energy allowed) to 2 eV does not largely change the results, the neutral fluxes presented are considered to be significant and above that from the background gas.

The question of whether the neutral flux will cause chemical changes to the surface of the substrate largely depends on the activation energies of those chemical reactions. Thermal neutrals are likely to be adsorbed onto the surface where they may undergo chemical reactions if external energy is supplied *ie.* by a bombarding ion or high energy neutral. Higher energy neutrals will undergo chemical reactions if they are able to break surface bonds. These neutrals are likely to contribute to surface chemistry if they possess more than several eVs of energy, though the chemical reactions involved (polymer formation, attachment of hydrogens to arsenic *etc.*) are beyond the scope of this work.

6.6.3 Neutral fluxes

Figures 6.119 and 6.120 show the extent of the neutral flux in comparison to the ion flux for pressures of 10 mTorr and 90 mTorr. It can be seen that the neutral flux is extremely important and should not be ignored.

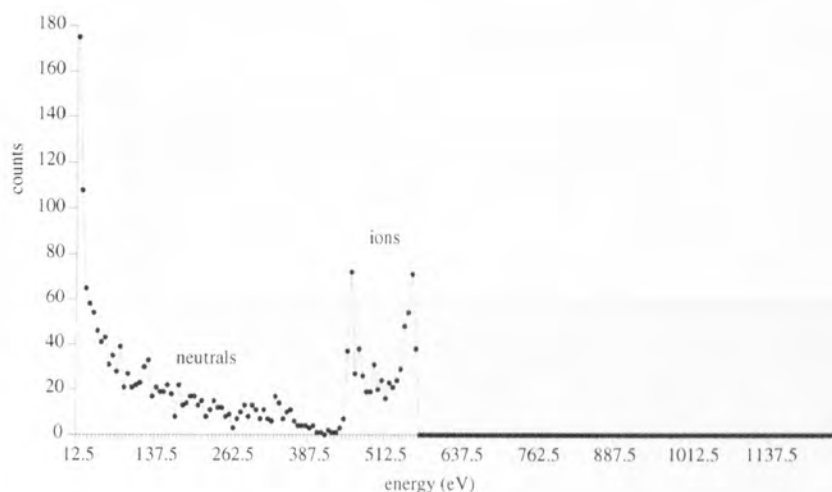

Figure 6.119 H_3^+ ions and H_2 neutrals superimposed for a pressure of 10 mTorr, 150 W, 3% methane concentration; only neutrals above 12.5 eV are shown).

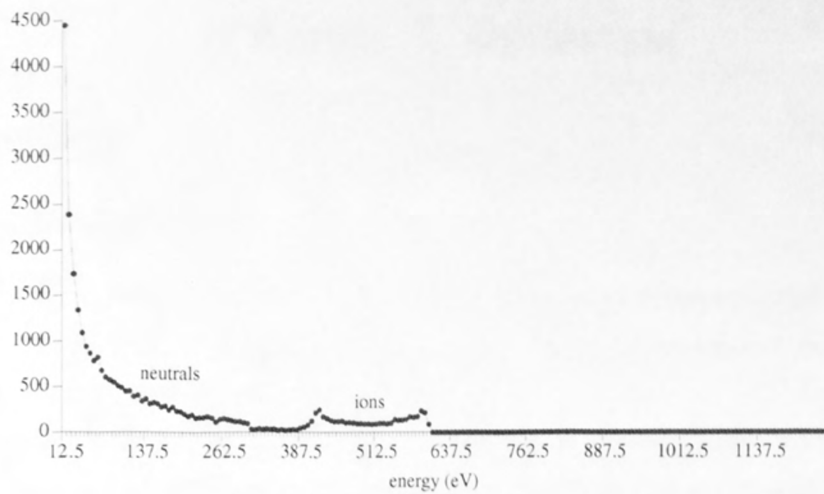

Figure 6.120 H_3^+ ions and H_2 neutrals superimposed for a pressure of 90 mTorr, 150 W, 3% methane concentration only neutrals above 12.5 eV are shown).

Chapter 7. Discussion

7.1 Modelling

7.1.1 Plasma modelling

A model has been proposed which, by following electrons and ions through assumed potentials in a radio frequency capacitively couple discharge can predict such plasma parameters as the spatial ionisation and excitation distribution functions, the electron energy distribution function, and the flux, energy and angles of all ion and neutral species at either electrode. These important parameters affect the etching of semiconductor surfaces and have therefore been investigated in terms of the external controllable plasma parameters such as pressure, power, relative gas concentration and electrode secondary electron emission function.

The code takes electrons, initially with random positions between cathode and anode and follows them through the well known potentials derived for the sheaths and bulk in rf plasmas. The electrons undergo elastic scattering with background molecules; the cross sections and angular distribution functions of scattered electrons being taken from experimental data. Also included are rotational, vibrational and electronic excitation and ionisation. The electrons continue back and forth between the electrodes, gaining energy via the interaction with the expanding and contracting sheath until eventually they overcome the potential at either the cathode or the anode and they leave the simulation. The electrons created by ionisations are stored in arrays and followed in turn through their trajectories until they are each lost. This part of the simulation then provides information on the electron energies and the creation profile of the methane and hydrogen ions from the background gas. The ion creation profile is a necessary input to the ion trajectory module which cannot be found in any other way. The extent to which electrons create further electrons is dependent on external variables such as the pressure and power but also on the ability with which electrons can overcome the sheath potentials or recombine with ions. The ease with which electrons reach either electrode is given by the floating potential (the minimum sheath potential) and to a lesser extent the time-variant plasma potential. Various values of the floating potential can therefore be used in each simulation and the values which lead to stable self-perpetuating plasmas generally agree with experimental results from the Langmuir probe. It was also found that electron recombination in the bulk plasma is a relatively unimportant electron loss mechanism (as expected) and that the majority of electron-ion recombination occurs at the chamber walls.

In addition to the above interactions, secondary emission due to both electron impact (*ie.* reflection) and ion impact were included in the model in order that the effect of different substrates (on which the sample was mounted) could be investigated.

Investigations of the effect of external plasma parameters on the recorded electron and ion properties gave interesting insights both into the nature of the plasmas and the code used to represent them. Although many workers ignore rotational and vibrational excitations due to the relatively low energies involved, it was found that the inclusion of vibrational excitations had a significant effect on the low energy portion of the electron energy distribution function. It could be argued that this portion of the energy distribution is not involved in ionisations and is therefore not important. It must be stressed, however, that it is electrons of these energies which are sampled with the Langmuir probe when attempting to justify the model. More importantly, perhaps, much of the energy input to the plasma is by way of low energy electrons interacting with the moving sheath. The phase and velocity at which electrons enter the sheath region defines the final energy gained by the electron when it reenters the plasma bulk. It is the energy distribution of these low energy electrons which defines the energy distribution of the high energy electrons. Additionally, as data is available, the inclusion of rotational and vibrational excitations is justified on the grounds of physical correctness alone.

The electron energy distribution function itself (EEDF) is shown to be distinctly non-Maxwellian, with a significant high energy tail, a result which has been found by others. This makes discussion of an electron temperature difficult and all discussion has been limited to the form of the EEDF. It has also been shown that the EEDF is extremely sensitive to the position at which the electrons are sampled. For example, electrons sampled at the plasma/sheath interface have a greater extended high energy tail than those electrons sampled in the plasma bulk. This effect is extreme at the higher pressures. The EEDF has been shown to peak at lower values of the electron energy as the pressure in the simulation is increased and energy loss mechanisms become increasingly important. The non-uniformity of the EEDF leads to highly asymmetrical spatial ionisation functions which at the high pressures become exceedingly bunched at the plasma/sheath boundary. Plots of the excitation profile across the plasma are similar to the ionisation profiles obtained. The peak of the profile is at the cathode plasma/sheath boundary and approximates to the visually brightest part of the plasma. The contrast between the plasma/sheath boundary and the plasma bulk increases with increasing pressure, a result which is reflected well visually. It is also interesting to note that the peak in the excitation profile generally occurs at a distance 20 % further from the cathode than the maximum extent of the electrical sheath width. Equating the maximum optical brightness to the sheath width would therefore be an overestimation. In this work, the measurement of the sheath width has been performed by measuring the apparent width of the dark space above the cathode, a distance visually easier to estimate and somewhat less than the distance to optical maximum. This method is, therefore, more accurate at finding the electrical sheath width.

An increase in pressure, as for the ionisation profile, increases the relative peak heights

and the asymmetry in the distribution. This result leads to the large changes in species which arrive at the electrodes as a function of pressure, due to the large changes in path length for the ion species. Increases in the proportion of methane in the plasma can be seen to have the effect of increasing the probability of ionisation due to the lower ionisation potential of methane than hydrogen and this leads to a lowering of the floating potential in the simulation. Power changes also lead to differences in the EEDF, though the differences are small and not expected to be resolvable with the Langmuir probe.

When compared with results from the diagnostic tools, the validity of the model can be examined, though these comparisons are problematical. Firstly, the electron energies predicted are similar to the energies expected for a low temperature, low pressure plasma. The results from the Langmuir probe on hydrogen and from theoretical work agree with the predicted electron energies. The predicted change in electron energy with a change in the position of sampling, with high energy electrons more likely to be found close to the plasma/sheath boundary than in the plasma bulk, also agrees with theoretical work. It is this change in energy which leads to some of the problems inherent in the use of the Langmuir probe. *ie.* the EEDFs cannot be rigorously compared with EEDFs from the Langmuir probe because the position of the plasma/sheath boundary changes as the conditions of the plasma change. This means that the stationary Langmuir probe is sampling a different part of the plasma with different plasma conditions. Experimental results of electron energy versus pressure, therefore, give results that are a convolution of the change in electron energy due to pressure and the change in electron energy due to the relative position at which the plasma is sampled.

The effect on the plasma of changes in the secondary electron emission coefficient is of importance in practical applications where different cathode plate materials might be used. Quartz is favoured as it resistant to chemical etching, but other materials such as graphite can be used. Changes in the value of γ from ion impact had a noticeable effect on the EEDF.

In terms of the plasma processing of semiconductors, the important parameters are the fluxes and energies of heavy particles at the sample surface (the cathode) as it is these particles that perform either physical or chemical etching of the surface. The electron analysis discussed is unimportant in terms of the surface, except in the effect it has on the heavy particle mass, energy and angle distribution and the total flux to the surface. The electron analysis has been performed merely to find the ion creation profile across the plasma (and to a lesser extent to use the results to compare with experimental results and hence justify the model).

The ions which result from the electron module are tracked through the electric fields in the plasma bulk and sheaths until they strike either electrode, when their energy, angle and

type are recorded. The ions interact in many ways with molecules of the background gas. As many chemical reactions as there was available data for were included, as were charge exchange and elastic scattering.

The problem of the angular distribution of polyatomic particles scattering from polyatomic particles was also addressed. Various codes were written and compared to results from quantum mechanical code and it was found that even for complicated molecules, simple spherical interactions based on screened coulomb potentials gave reasonable scattering functions. This was a considerable improvement on the unrealistic hard sphere interactions used by many others.

Experiment has shown that the proportion of methane in the ion flux arriving at the anode is much greater than the proportion of methane in the background gas. This has been predicted by the model, where the effect of the lower ionisation potential of methane is to cause the production of methane ion fragments in abundance. This has shown why, at a concentration of only 10 % methane, the methane flux to the surface contributes over 50% of the total flux.

Results of the simulations predict that as the pressure is increased, the average energies of ions at the cathode are reduced due to scattering and charge transfer in the sheath. The extent of the reduction in energy is smaller than would be the case in an argon plasma. This is because of the large charge exchange cross section for argon and because in a hydrogen plasma the stable H_3^+ is often created, preventing further charge exchange. In argon plasmas, repeated charge exchange collisions across the sheath have a drastic effect on the ion energy distribution, whereas in hydrogen plasmas, the cross-section for conversion of H_2^+ is dominant. Similarly for the conversion of CH_4^+ to CH_5^+. The reduction in energies at the surface as the pressure is increased is also mitigated by the reduction in the sheath width over the pressure range. The reduction in ion energies is nevertheless significant. The effect of chemical reactions in the plasma bulk and sheath is to change the mass distribution of ions at the cathode and anode. As has been previously mentioned, the asymmetric nature of the ion creation function (which becomes increasingly asymmetric as the pressure increases) leads to large path differences between ions which arrive at the cathode and the anode. This gives ions at the anode a greater chance of undergoing a chemical reaction with a background neutral and this causes the dominant ionic species to be quite different at each electrode. This has repercussions in that the mass distribution of ions measured at the anode cannot be used uncritically as an estimate of the mass breakdown of ions either crossing the cathode plasma/sheath boundary or arriving at the cathode. Thus, the use of the model is necessary to find the parameters of interest that are neither measurable nor can be inferred from the experimental measurements. The change in the mass distribution of ions at the anode with pressure also allows direct comparisons between simulation and measurement.

The simulation also predicts the changes in ion angle distributions. The ion angle distribution is an important parameter when considering the implantation of ions into a semiconductor surface. The extent to which ions travel further than predicted by simple non-crystallographic codes is given by the extent to which ions are channelled through the crystal planes. This can cause deep damage and the extent to which it occurs is a function partly of the flux of ions entering these specific channels. This flux is given by the convolution of the incident angular flux distribution and the randomizing effect of the amorphous bombarded layer over the crystal substrate.

The other important parameter which cannot be measured but is predicted to be important for etching applications is the flux of fast neutrals to the surface. Again, the flux of high energy neutrals is predicted to be lower than in the argon case due to the diminished importance of charge exchange collisions. The neutral creation by recoil from ion scattering events, however, is predicted to be high with a flux considerably greater than the ion flux for the higher pressures. This flux cannot be ignored when considering the particle fluxes to the surface and in this work the comparison of ion and neutral fluxes to the surface has given considerable insight into the etching/deposition process. Here, ions are attempting to etch the surface whilst slower neutral species are competitively attempting to polymerize it. The ratio of the fast ions (which additionally remove the polymer) to the slower neutrals (with energies considerably higher than thermal) gives a threshold between etching and deposition regimes.

The ion energy distributions at the anode have also been investigated for the simple gas argon in order to confirm the model assumptions. The advantage of this is twofold. Firstly, the lack of chemistry makes for a very simple case where the ion energies are defined by the electric fields, charge exchange and elastic scattering collisions. The second advantage is that the relatively high molecular mass of argon leads to ion energy distributions which are of the form of the saddle structure variously mentioned in the literature. The resulting agreement between the predicted and experimental argon ion energy distributions at the anode gives great confidence in the electric potentials used in the sheaths. Additional experimentation with the input parameters to the simulation reveals that the sheath width is given by the peak separation in the ion energy distribution and that the form of the ion energy distribution is given mainly by the sheath width and the sheath potential variation. It has been found that the maxima and minima in the sheath potential rather than the exact form of the potential variation is important for the ion energies, and the pre-sheath region given by the Bohm criterion is negligible. These second order effects become even less important over the cathode where by far the greatest contribution to the sheath potential is given by the cathode potential.

There is, inherent in the model a specific drawback, and this is the lack of self-consistency. The potentials used in the simulation have been assumed potentials which

have been shown to be realistic enough to model the ion motion. The introduction of self-consistency to the current model would be a major step and with the high number of interactions used may make the computation time inconveniently long. The introduction of self-consistency would, arguably, also add error to the most important plasma parameter, the ion energies at the substrate. Presently the DC bias which is the most important factor in determining the ion energies at the substrate is measured and used as an input to the simulation. Any attempt at self-consistency in the program would be likely to make this diverge from its measured value. In the case, therefore, where the ion energies at the substrate are needed for comparison with experimental data and the potentials are known with some degree of confidence, self-consistency is a time consuming detraction which introduces error in the predicted plasma parameters. The use of self-consistency is common and extremely important in the theoretical investigation of plasmas, generally of inert gases and is a necessary tool for confirmation of the assumptions used in the simpler models. It is not claimed, therefore, that the ion and electron concentrations which are determined by weak electric fields across the bulk of the plasma and especially near the sheath edges should be accurate. It is expected, however, that the simulation is good enough to determine the mass breakdown and the ionisation profile of ions and their subsequent drift and acceleration to the electrodes. This has been shown to be quite invariant to the details of the EEDF over the range of external parameters. The main source of error here lies in the cross sections, both for electron impact ionisation and heavy ion/neutral collisions, as emphasized by a recent US National Academy of Sciences report [287] which has identified the lack of fundamental data for the most important chemical species as the single largest factor limiting the successful application of models to problems of industrial interest.

The code, therefore, has been a significant advance over the work by May [288] and Dickenson [289] who modelled the behaviour of hydrogen ions in the sheath of an rf hydrogen plasma. In extending the model to methane fragments they used simplified hard-sphere scattering and made assumptions about the ions crossing the plasma/sheath boundary from experimental mass probe data which have been shown to be invalid. In this exercise, the mass distribution of ions across the plasma from the cathode to the anode has been shown to change radically with position, a result found by following electron trajectories. There is considerable confidence in the predictions of these codes which agree with both published and our own experimental results and the theoretical results of others. The output can therefore confidently be used as the input to models of particle/surface interactions.

7.1.2 Particle/surface interaction modelling

Ion/surface bombardment has been discussed in terms of codes such as TRIM and SUSPRE. These simple codes do not represent the true behaviour of the surface under

bombardment. For example preferential sputtering is affected by the relative binding energies of gallium and arsenic atoms to the surface, a value taken as unity in the codes. It has been shown that there are many and contradictory results for the relative binding energies ranging from estimates taken from the bulk sublimation energy of the pure element to estimates taken from the quantum mechanically derived energy of Ga_nAs_m clusters. Though there is little agreement, the general consensus is that arsenic is more tightly bound to the lattice and the relative binding energy cannot be used as an explanation of arsenic depletion in the surface.

It is thought, therefore, that the arsenic depletion due to physical bombardment is a result of the Gibbsian segregation of arsenic and its resultant preferential sputtering. This causes an arsenic gradient and diffusion of arsenic from bulk to surface. It has also been described how at high impact energies this is expected to lead to an arsenic enriched surface and arsenic depleted subsurface and at lower energies (such as those in this work) this is expected to lead to a generally depleted surface and subsurface. The Gibbsian segregation effect has often been described in terms of the surface energy of the arsenic and gallium atoms, with the surface energy of arsenic being lower. This, again, is taken from the elemental data and as in the previous case it is expected that the elemental data should not necessarily agree with the GaAs compound data. Both experiment and theory imply, as discussed in section 3.4.3, that for each GaAs surface (*ie.* (100) or (110)) the arsenic preferentially moves out of the surface to occupy positions higher than the plane of the surface. Quantum mechanical models show how this happens to minimise the total surface energy with a full consideration of the lattice structure. Though the surface of a bombarded GaAs sample is not a simple crystal plane, it will to an extent be polycrystalline and it can be expected that the segregation explanation can be used for the bombarded surface. A simple model was further proposed which explored the extent to which this segregating arsenic would be preferentially sputtered, by considering the trajectories of arsenic atoms attempting to leave the surface and found that the preferential sputtering of arsenic is considerable.

The results, though explaining satisfactorily the arsenic depletion due to inert ion bombardment, do not help in explaining the largely chemical interaction of methane and hydrogen with GaAs. More sophisticated quantum codes are becoming available to model some small specific aspects of these interactions but presently explanations of the surface changes in GaAs must rely on a more general knowledge of the possible chemistry involved.

7.2 Plasma/surface interaction

7.2.1 Discussion of etch rates

From the results given in section 6.2 it can be seen that in the case of 10 mTorr methane/

hydrogen etching of GaAs, the etch rate increases with the concentration of methane in the gas. This increase is not linear but rises most swiftly at the lowest methane concentrations and appears to approach a limit at high methane concentrations. This relationship is predicted by the plasma modelling where the methane flux to the surface follows the same trend. This relationship, due to the low ionisation threshold for methane, rises quickly at low methane concentrations. It appears, therefore, that the etching of GaAs is due to fast ions and/or neutrals bombarding the surface and removing gallium and arsenic either chemically or physically. If the background neutrals were extensively involved then one would expect the etch rate to rise linearly with the concentration of methane in the background gas.

Using the etch rates predicted in section 3.2.1 in conjunction with the predicted partial methane flux to the surface, it is possible to make predictions for the final etch depth for 150 W, 10 mTorr plasmas. This is shown in figure 7.1 a) as a function of methane concentration (with the experimental results superimposed). The results of etching with neon, however, suggest this etch rate is an overestimation. The etch rate predicted for a neon plasma of 0.18 nms^{-1} leads to an etch depth after 30 minutes of 324 nm. The experimental etch depth was found to be considerably lower (46 nm), indicating the value of 0.6 molecules per ion at 500 eV is too high an estimate for the sputter yield. Using the real etch depth and the same flux estimate gives a real sputter yield of .085 molecules per incident ion, a value very close to that of 0.1 molecules per ion found by Foad et al [290]. This implies the etch depth for carbon is also overestimated by several times and scaling the sputter rate for carbon with the results for neon gives a further etch depth prediction which is considerably lower and is shown in figure 7.1 b).

It can be seen that the first estimate (a) is quite close to the experimental results and is of a similar form. The second prediction (b) is considerably lower and implies a predominantly chemical process. Due to the obvious discrepancies between the sputter yields given in the literature for argon, and the fact that the only sputter yield in the literature at this energy for neon gives Y=0.1, it is likely that the latter is a more probable value for the sputter yield than the 0.6 originally used. Considering the potential error in extrapolating from inert neon bombardment to methane bombardment, the results must be taken with caution. It must also be stressed that the predictions rely heavily on the value of the current density to the surface.

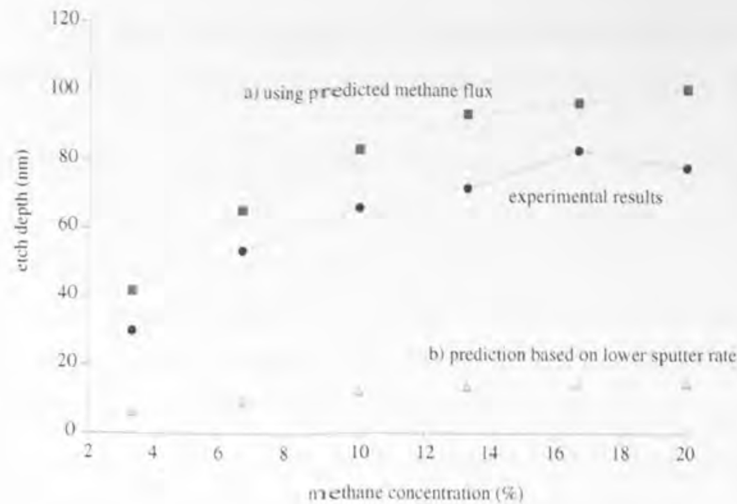

Figure 7.1 Predictions for the etch depths with the experimental results superimposed

7.2.2 Methane/hydrogen etching of GaAs

7.2.2.1 10 mTorr, 150 W

Initially the results will be discussed for the simplest conditions of 10 mTorr and 150 W. It can be seen from the results for neon, neon/hydrogen and methane/hydrogen etching that in all cases arsenic is preferentially removed due either to physical or chemical means. Both from the etch depth analysis and from the great extent of removal of arsenic (especially in the pure hydrogen case) this appears to be a chemical process for methane/ hydrogen.

The results from all methane/hydrogen etching experiments show arsenic depletion in the surface and the formation of a wholly gallium oxide surface covering. Angle resolved XPS shows the arsenic depletion to be more extreme close to the surface. The lack of metallic gallium implies the excess gallium is due either wholly to the existence of the gallium oxide or partially due to a non stoichiometric GaAs substrate, the latter being implied by the $(Ga/As)_S$ data. The change from stoichiometry appears inversely related to the etch rate and the obvious explanation is that the hydrogen removal of arsenic is more efficient than the methane removal of gallium. Because the removal rate of both atom types is equal, this implies a surface depleted in arsenic. The simulations show that the methane flux to the surface is far greater as a fraction of the total flux than is implied by the methane proportion of the background gas and this is due to its lower ionisation potential. The greater efficiency of the vacuum pump in removing hydrogen compounds the situation and this results in the methane and hydrogen fluxes to the surface being equal when the methane concentration in the gas entering the chamber is only 5-10 %. The removal of gallium by methane is less efficient due either to the lower penetration depth of methane into the surface thereby limiting the depth from which gallium can be removed or by chemical considerations or due to Gibbsian segregation and diffusion transporting arsenic to the surface more efficiently to where it is most easily removed. As the methane

concentration in the gas increases, so does the removal efficiency of gallium and as the etch rate increases the depth to which there is substantial arsenic depletion decreases.

Assuming, therefore, that during the etch there exists a layer of some depth determined by the etch rate which is arsenic depleted, then on exposure to atmosphere the top layer of this will oxidise. This will leave a structure consisting of three layers, the outer gallium oxide layer on top of an arsenic depleted layer below which is the stoichiometric GaAs substrate below. Assuming the gallium oxide is pure, the values $(Ga/As)_T$ and $(Ga/As)_S$ will be determined by the oxide thickness, thickness of depleted layer and the excess of Ga over As in this depletion layer. With these assumptions, the code described in 3.7.1 can be used to predict XPS results for the different take off angles.

Initially assuming the depletion layer thickness is zero, figure 7.2 shows how the predicted ratio $(Ga/As)_T$ increases with the thickness of the oxide layer. Figure 7.3 shows how the predicted ratio Ga(GaAs)/Ga(total) decreases as the oxide layer thickness increases. The value Ga(GaAs)/Ga(total), however, does not change substantially with the plasma conditions, whilst as shown in the results section, the value of $(Ga/As)_T$ does. This implies there is an oxide layer formed, the thickness of which does not change with conditions and also an arsenic depleted layer whose thickness is affected by process conditions.

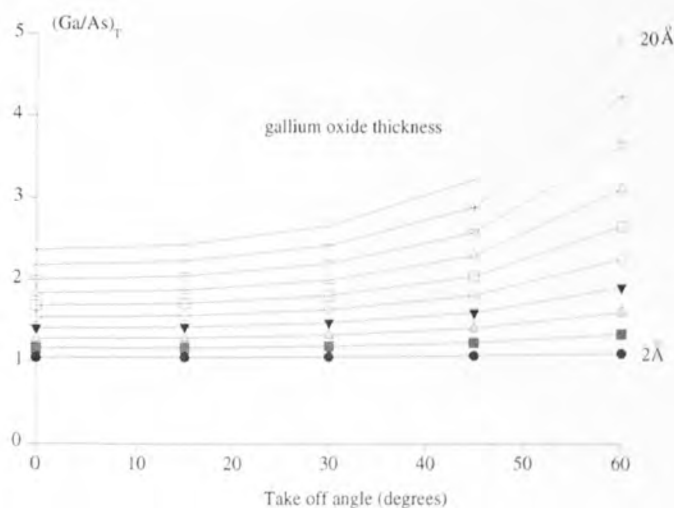

Figure 7.2 Predicted $(Ga/As)_T$ as a function of ToA.

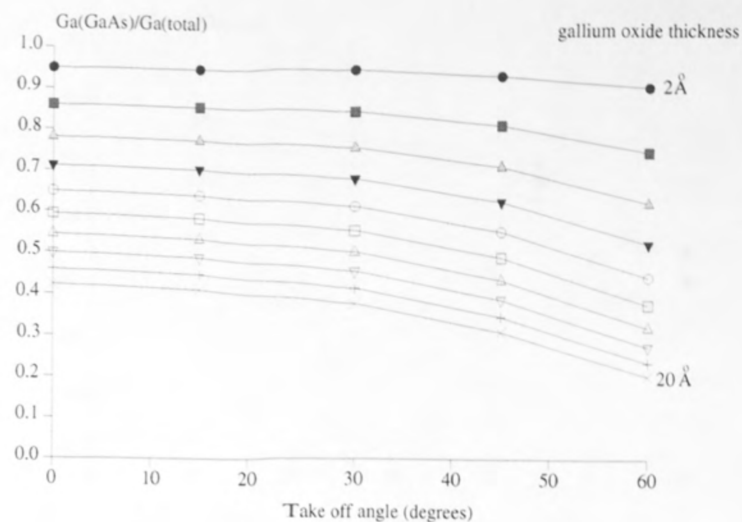

Figure 7.3 Predicted Ga(GaAs)/Ga(total) as a function of ToA.

For example at 1:29 methane:hydrogen ratio, 10 mTorr, 150 W, the following shows three XPS results for $(Ga/As)_T$ in figure 7.4 and Ga(GaAs)/Ga(total) in figure 7.5.

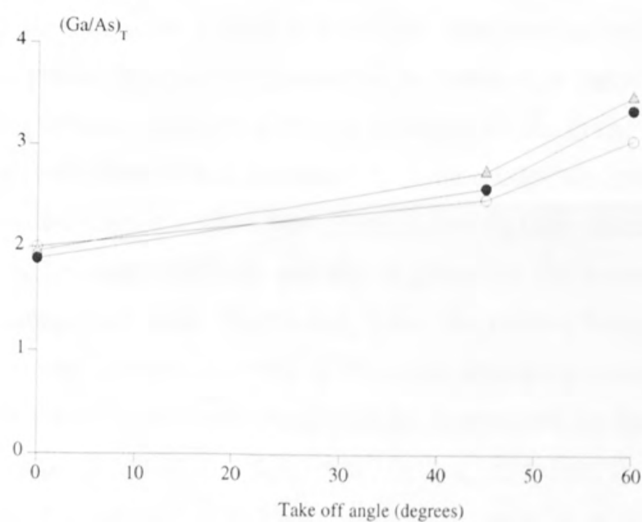

Figure 7.4 $(Ga/As)_T$ for 1:29 10 mTorr 150 W.

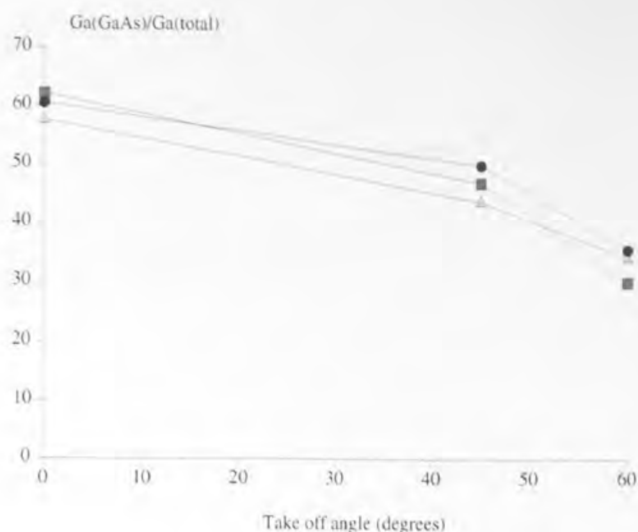

Figure 7.5 Ga(GaAs)/Ga(total) for 1:29 10 mTorr 150 W.

The implication by comparison of figure 7.2 and 7.4 is that the oxide layer is about 16 Å thick, whereas from figures 7.3 and 7.5 that it is only 10 or 12 Å. This again suggests there is a region of arsenic depletion below the surface dependent on the plasma conditions, the top 10 Å or so of which is oxidised. The portion below the oxide layer will consist of amorphous or semicrystalline GaAs rather than metallic gallium because the XPS signal from metallic gallium (clearly distinguishable in the spectra) is not seen. The extent of the arsenic depletion is unclear. For the model predictions, the same results are obtainable for an extensive layer where there is only a little arsenic depletion and for a thin layer of extreme arsenic depletion and this is generally the nature of inversion problems with no unique solution. There are, however, certain limits within which the Ga:As ratio must remain in order that the XPS signal appears to come from the Ga-As bond rather than the Ga-Ga bond and these will be determined by the precise behaviour of the surface to an excess of one atom type over another. In reality there probably exists a concentration gradient of arsenic in gallium, though for ease of calculation a ratio of Ga:As of 2:1 in this layer was taken. It is important to realise, therefore, that the depths obtained from the modelling program are not absolute depths (not least from the uncertainty in the inelastic mean free path) but are depths which depend on the assumptions made and are good for comparison between the experimental results when viewed qualitatively. For the assumption of a 12Å gallium oxide layer covering a Ga_2As_1 layer above a stoichiometric substrate, figures 7.6, 7.7 and 7.8 show the predictions for the $(Ga/As)_T$ ratio, the Ga(GaAs)/Ga(total) ratio and the $(Ga/As)_S$ as a function of the depleted layer thickness from 0 Å to 14 Å. It can be seen that there is little predicted variation in the $(Ga/As)_S$ over the range of ToA's but the value is consistently greater than unity.

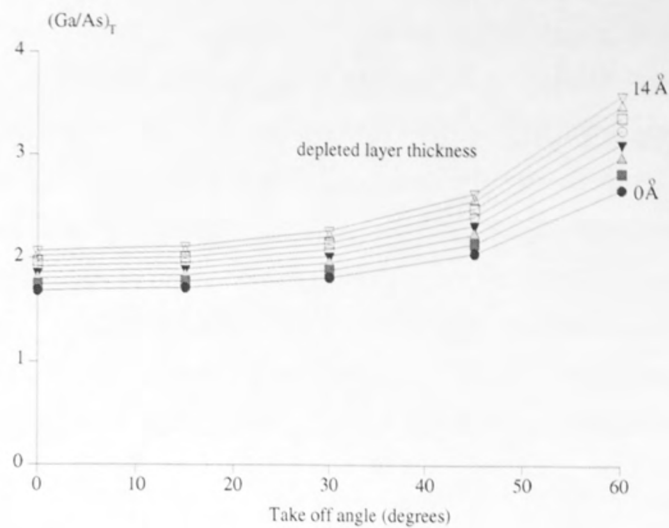

Figure 7.6 Predicted $(Ga/As)_T$ as a function of ToA.

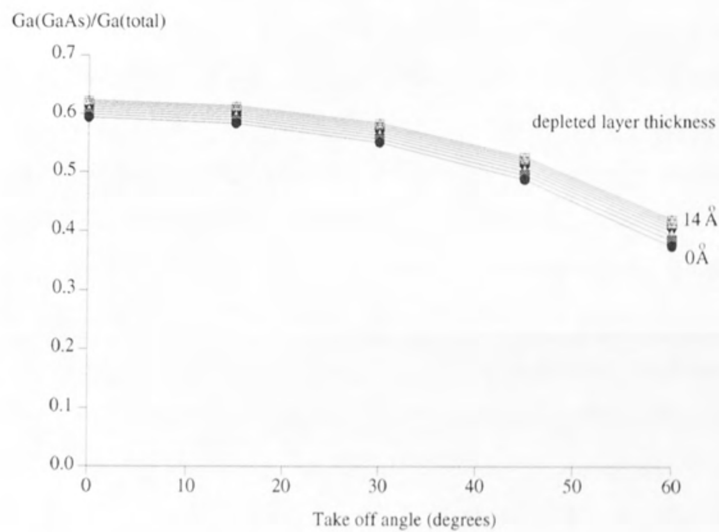

Figure 7.7 Predicted Ga(GaAs)/Ga(total) as a function of ToA.

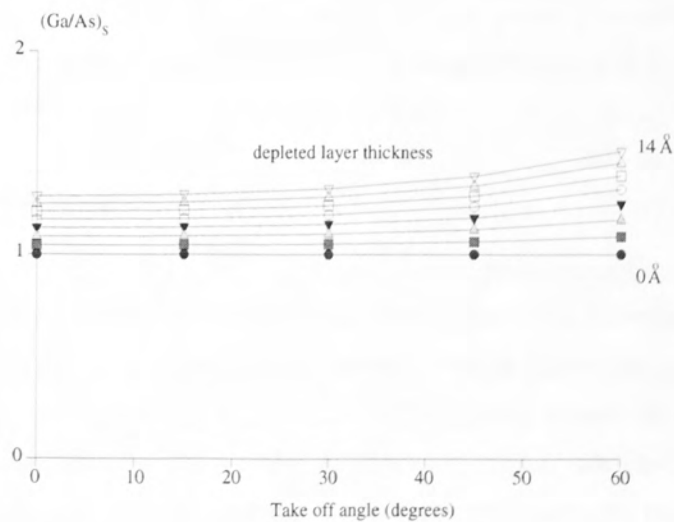

Figure 7.8 Predicted $(Ga/As)_S$ as a function of ToA.

These predictions do in fact fit in very well with the experimental results. It appears that for 150 W, 10 mTorr, the etched surface consists of 12 Å gallium oxide below which is a layer of arsenic depleted GaAs with a thickness ranging from zero for the higher methane concentrations to 10 Å at a ratio of 1:29. The pure hydrogen results have greater values of both $(Ga/As)_T$ and $(Ga/As)_S$ which cannot be explained by an increased depletion layer. The results suggest an oxide thickness of at least 20 Å below which is an arsenic depleted layer of similar thickness, though at these greater depths the results become necessarily more approximate. The greater depth of damage in the hydrogen case could be due to bombardment by contaminant oxygen which increases the extent of the oxide without being etched away.

The results for 150 W and 10 mTorr indicate, therefore, that for methane/hydrogen mixtures ranging 0 % to 20 % concentration, there is an arsenic depleted layer depth which ranges from >20 Å to 12 Å as the methane concentration is increased. The top 12Å subsequently oxidizes. This top 12 Å is certainly almost entirely free of arsenic or it would show as either metallic arsenic, arsenic oxide or as an excess of arsenic over gallium in the form GaAs. This is predicted by the premise that the damaged layer in equilibrium is a function of the characteristic bombardment damage depth profile and the etch rate. As the methane concentration increases, so only does the etch rate, therefore the damage depth and consequently the depth from which arsenic can be preferentially removed decreases. In the case of pure hydrogen the damage depth is high due to the low etch rate and the oxide layer formed is the result of bombardment over some time with contaminant oxygen and is therefore extensive, whereas in methane/hydrogen mixtures the oxide is formed either on extinguishing of the plasma or competitively with a relatively high etch rate during the process and is consequently not extensive.

The change in the gas flow rate can also be expected to change the depth of the damaged layer due to its effect on the etch rate. As the flow changes, the characteristic depth of damage remains the same, but if the gas chemistry leads to a higher etch rate then the actual damaged and arsenic depleted layer will be smaller leading to lower values of $(Ga/As)_T$.

7.2.2.2 Changes in power

It has been shown that there is a small positive correlation between the value of $(Ga/As)_T$ and the power across the range of methane concentrations. The correlation between the power and the etch rate is, however, much greater. This is shown on the plots of $(Ga/As)_T$ against etch rate in section 6.4.1.5 where the results for each power lie on separate curves, the transformation between which appears to be a shift in etch rate (and small positive shift in $(Ga/As)_T$), except for pure hydrogen where the etch rates are not measurable. According to the hypothesis, an increased etch rate should lead to a thinner damaged layer all other things remaining equal. In this case, however, as the power increases so too does

the characteristic depth of damage which is a function of the ion energies at the surface and these two effects oppose each other.

7.2.2.3 Changes in pressure, methane/hydrogen

Deposition occurs for most methane concentrations but for the trends which can be followed, the above hypothesis holds true. At 20 mTorr, as the concentration is increased, at 100 W the etch rate increases whilst the ratio $(Ga/As)_T$ decreases. At 150 W, the same is true except for a peak in the etch rate at a methane:hydrogen ratio of 1:29 (3.4 %) which coincides with a dip in the $(Ga/As)_T$ value. Reference to the original data shows these results are the average of two separate experiments and that in each case both etch rates seem anomalously high as do both $(Ga/As)_T$ values seem anomalously low. It appears, therefore, that there is a strong correlation between the etch rate and the values of $(Ga/As)_T$ and that individual experiments which due to some error yield different etch rates, also reflect this in the values of $(Ga/As)_T$. The plots of $(Ga/As)_T$ against pressure also show the same correlation. This appears also to confirm the hypothesis. As the pressure is increased, the predicted energies of the particles at the surface do not change as much as they do as a function of power. The etch rate change over the pressure range will be given by subtle changes in gas chemistry or by the competition between etching and deposition at the surface. Whatever the cause, however, the characteristic depth of damage will remain unaltered whilst the etch rate changes the equilibrium depth of the damaged arsenic depleted layer.

7.2.2.4 Changes in pressure, pure hydrogen

The changes in the surface composition as a result of changes in pressure of a pure hydrogen plasma are more difficult to explain. As the pressure increases, the ratio $(Ga/As)_T$ decreases in both the 100 W and 150 W cases. The ratio $(Ga/As)_S$ also decreases such that at 80 mTorr it is substantially below 1, indicating a substrate GaAs lattice rich in arsenic, contrary to all the other experiments. At 50 W the decrease also occurs up to 40 mTorr but both ratios increase slightly at 80 mTorr. The difficulty in explaining this arises because it has been shown by the plasma modelling that over this pressure range the change in ion energies, though substantial, is considerably lower than the change in ion energies that results from a change in power. As has been seen, over the range in power at the lowest pressure there is a small positive correlation between power and $(Ga/As)_T$ whilst the value of $(Ga/As)_S$ always remains above 1. The change in mass distribution of ions hitting the surface is shown by the model to be considerable but consists of a decrease in H_2^+ and increase in H_3^+ and H^+ and it is difficult to see how this would invoke the changes seen. The other changes to the particles arriving at the surface are the substantial increase in the flux of fast neutrals and the increase in the flux of contaminants. The increased flux of contaminants arrives both during the etch and after the plasma has been extinguished (as part of the background gas).

The change in the surface as the pressure is increased appears to involve the gallium oxide layer of 20 Å or so containing progressively higher amounts of arsenic in the form GaAs. It therefore seems likely that due to the very low etch rate in hydrogen plasmas, the etching of the surface with contaminant oxygen is causing significant changes to the stoichiometry by the preferential removal of gallium in opposition to the preferential removal of arsenic caused by hydrogen. The affinity of oxygen for gallium is considerably higher than for arsenic (ΔH=1080 kJ/mol and -647 kJ/mol respectively [291]).

7.2.3 Neon/hydrogen etching of GaAs

7.2.3.1 As a function of neon concentration, 10 mTorr

It is expected that the surfaces subject to pure neon etching will be depleted in arsenic due to Gibbsian segregation and preferential sputtering and this is in fact the case, with the change from stoichiometry being greater for the higher power. The results of $(Ga/As)_T$ are therefore similar to those from methane hydrogen, though the values of $(Ga/As)_S$ are all below 1.

At 10 mTorr, the results from pure hydrogen etching have been explained as a damaged layer depleted in arsenic due its removal by hydrogen and low etch rate. The top of this layer oxidises, leading to both $(Ga/As)_T$ and $(Ga/As)_S$ being greater than 1, with $(Ga/As)_T$ being considerably greater.

In order to fit the results from the pure neon etching, the same approach is followed as with the methane/hydrogen, which has both a similar Ga(GaAs)/Ga(total) and $(Ga/As)_T$. This, however predicts a value of $(Ga/As)_S$ which is greater than 1 and increases with ToA. In fact, the ratio decreases with ToA and is less than 1. This implies that the surface is arsenic depleted but there exists more arsenic than gallium in the form GaAs. It appears that the gallium has oxidised post etch, but unlike in the methane/hydrogen and hydrogen cases, there exists enough arsenic in the near surface to be significant after the gallium has oxidised. Figures 7.9 shows the predicted results for a gallium oxide thickness of 23 Å which contains arsenic in the proportion As:Ga:O = 0.6:2:3.

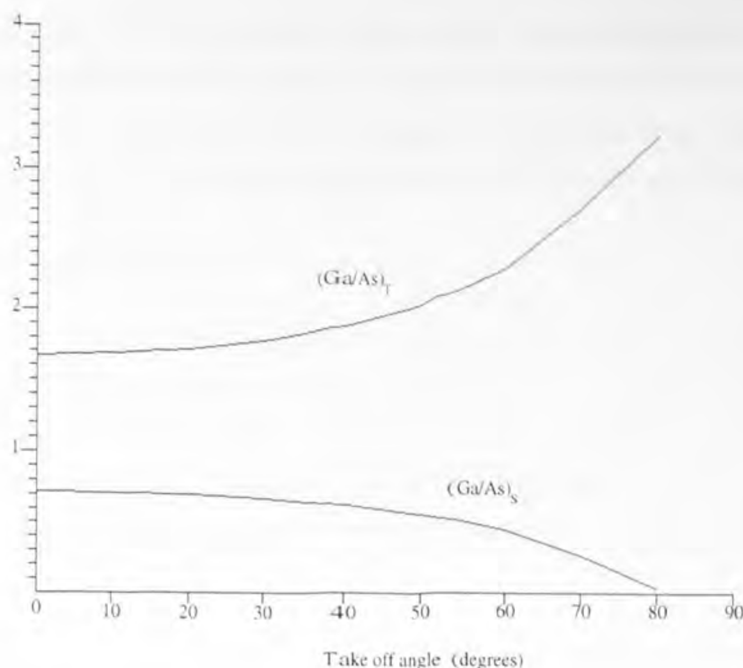

Figure 7.9 Predicted $(Ga/As)_T$ and $(Ga/As)_S$ results for an oxide thickness of 23 Å containing a trace of arsenic.

It seems, therefore, that when surfaces are bombarded with neon, Gibbsian segregation and preferential sputtering of arsenic leads to an arsenic depleted layer similar to that seen by Yu [292]. This layer will, however, contain significant amounts of arsenic as the process does not completely remove it. The surface oxidises with the oxygen being taken preferentially by the gallium which leads to the excess of arsenic over gallium in the form GaAs. It is likely that the inability of the remaining arsenic in the surface to oxidise is due to one of two reasons. Firstly, the low partial pressure of oxygen present preferentially oxidises gallium and secondly the bombardment of the surface with oxygen causes preferential oxidation of gallium due to the higher effective temperature of the collision complexes formed. Gallium is known to scavenge oxygen from arsenic at elevated temperatures [293]. This analysis suggests that arsenic is removed more completely from the surface by hydrogen and methane/hydrogen than by inert gas bombardment.

As the total neon concentration in the gas mixture is reduced and replaced by hydrogen, the value of $(Ga/As)_S$ increases rapidly above 1 as the hydrogen present removes any arsenic in the subsurface. As the concentration of neon decreases, the value of $(Ga/As)_T$ reaches a minimum at 82 % neon and increases thereafter to the high values for pure hydrogen. It appears, therefore, that like the methane/hydrogen case, the ratio $(Ga/As)_T$ in neon/hydrogen etching is related to the etch rate. The etch rate is not measurable for pure hydrogen but can be expected to increase as more neon is added. It is also likely that the highest etch rate coincides not with pure neon but with a high level of neon with some finite level of hydrogen. This would agree with the experimental results which suggest an inflexion in $(Ga/As)_T$ against concentration with a minimum value at 82 % neon. It

therefore appears that a similar process is occurring as in the methane/hydrogen case. The hydrogen is able to remove arsenic from the damaged layer but the extent of depletion is limited by the etch rate which removes the damage. In this case neon is sputtering both gallium and arsenic but the hydrogen is preferentially chemically removing the arsenic.

7.2.3.2 As a function of pressure

As in the hydrogen case, major changes in ion flux or energy to the surface as the pressure increases will not be expected, except for the increase in the flux of fast neutrals. The partial pressure of contaminant oxygen and water vapour will also be higher. The results for neon/hydrogen etching as a function of pressure are similarly hard to explain without a more careful analysis of the precise surface chemistry which is beyond the scope of this work.

Chapter 8. Conclusion and further work

8.1 Plasma modelling

A 1-D Monte-Carlo model has been devised in order to predict the ion and neutral relative flux and energy distributions at the surface of a cathode in an rf methane/hydrogen plasma. The code uses assumed potentials and is, therefore, quite inexpensive in computing time and this has allowed a large number of chemical interactions to be included. Comparisons with ion energies at the anode has confirmed the assumptions about the electrical potential. The model gives confidence in the energies at the substrate surface and the predictions of the relative fluxes are generally in agreement with measurements taken at the anode with a mass/energy analyser. It has also been shown how there is a large methane flux at the electrodes for very small methane concentrations in the gas and this is why generally the etch mixture involves a large excess of hydrogen. The form of the increase in etch rate with methane concentration has also been shown to follow the model prediction for the methane flux to the surface. The code has also predicted the etching and deposition regimes in terms of the flux of both neutrals and ions to the surface and this reinforces the view that the neutrals are an important particle flux to the surface and should not be ignored even at relatively low pressures of 10 mTorr.

8.2 Plasma/surface modification

An investigation has been performed into the effects of the plasma processing of GaAs. The gas of interest is methane/hydrogen, but it was necessary to also use neon/hydrogen in order that the fundamental processes of the etch could be understood and the chemical effects separated from the physical effects of bombardment.

The investigation has resulted in a comprehensive data set for the ratio of gallium and arsenic and their chemical states over a large matrix of pressure, power and concentration. Simultaneously etch rates were taken and the surface roughness investigated using atomic force microscopy. It was found that pure neon etching causes depletion of arsenic in the semiconductor surface due to segregation and preferential sputtering. The arsenic removal in the first few layers is not complete, however, and a concentration gradient is established. After surface oxidation, the gallium preferentially combines with the oxygen leaving an excess of arsenic in the form GaAs. The introduction of hydrogen into the gas mixture causes the arsenic to be more completely removed and the resultant surfaces have large values of both $(Ga/As)_T$ and $(Ga/As)_S$ and these values increase as the relative concentration of neon falls.

Etching with methane/hydrogen has a similar effect on the stoichiometry as etching with neon/hydrogen in that the surface is depleted in arsenic and the depth to which the depletion occurs is greater than the subsequent depth of surface oxidation and this leads to

values of $(Ga/As)_T$ and $(Ga/As)_S$ both greater than unity. Comparison of the etch rates with the changes in surface stoichiometry show the two to be intimately related, with low etch rates leading to high deviations from stoichiometry. This has been explained in terms of the removal rates of gallium by methane and arsenic by hydrogen, with the methane removal of gallium limiting the etch rate. It has been concluded that the etching of GaAs by methane/hydrogen is a predominantly chemical process.

8.3 Further work

8.3.1 Plasma modelling

The main improvement in the model would be the use of self-consistent electrical potentials throughout the plasma. The large increases in computation time and the significant effort involved in re-writing the code would have to be weighed against the specific advantages it would confer. The main advantage would be in the lack of reliance on the assumed plasma potentials, which in the 1-D case seems unnecessary; but if the code was to be extended to 2-D would be very important (the electrical potentials for 2-D geometry are non-trivial). The 2-D potentials could be found in the following way. Firstly, the ions and electrons could be followed in a fluid model where Poissons equation is solved over the coordinate matrix representing the chamber geometry simultaneously with the continuity equations for the charged species. The resulting electrical potentials would be used directly in a 2-D version of the code written for this project (a trivial extension) and would follow the electron and ion trajectories to find the energy distribution functions. The assumptions underlying fluid models are not valid at these low pressures (the electric field changes substantially over the path length of the charged species) and there is evidence that PIC models and fluid models diverge below 100 mTorr [294]. This does not, however, invalidate their use. Kushner [295,296,297,298,299,300,301] uses kinetic electron and fluid ion for modelling of 5-20 mTorr regime and justifies this by reference to work which shows fluid models are applicable below the normal limit if ionisation is well represented [302]. Many other workers choose this kinetic electron fluid ion approach *ie.* Belengeur and Beouf [303], Sato and Tagashira [304], Surendra *et al* [305]. In fact most 2D ICP models are presently based either fully or partly on the fluid approximation and Surendra [306] has recently compared fluid and PIC models and shows them to be quite robust at low pressures even when the assumptions upon which they rest are highly suspect. Turner reaches very similar conclusions for both ICP and CCPs [307,308].

In addition to the extension of the code to 2-D and the calculation of electrical potentials, to parallel the experimental work on GaAs etching, the inclusion of inductive coupling would form the next stage in the modelling work. From the 2-D, kinetic electron, fluid ion model it would be necessary to add the forces due to the inductive coupling, solve Maxwells equations and use these fields in the electron model.

For all these simulations, for gases which include significant chemistry it will be necessary to model the gas flow and the mass distribution of the background gas, in a fluid model similar to that for the ions. The resultant distribution is used as the input to the electron model which finds the spatial ionisation distribution.

8.3.2 Particle/surface interaction modelling

Due to the complexity of particle/surface interactions, only a simple study of it has been made in this thesis. Codes such as TRIM and other binary collision approximation codes are generally of use above 1 keV. At energies below this and especially the energies of the neutrals (tens of eV) the approximation appears increasingly tenuous when the effective radius of the incident and surface particle is considerable. In these cases the incident particle interacts not with a surface particle but with the local lattice and this can only be modelled as a many body problem. Codes such as HYPERCHEM will model many body collisions using classical interaction potentials and it is likely that this will be necessary to investigate the low energy penetration and dechannelling of ions in semiconductor surfaces (especially the implantation of chlorine).

In order to investigate the chemistry at the surface it will be necessary to use fully quantum mechanical codes such as CASTEP [309] which are extremely computer intensive and inadequate for high energy interactions The code can, however, be used to investigate the evolution of a GaAs surface containing methane and hydrogen fragments with sufficient energy that the resulting chemistry will give realistic insights into the true surface processes and the creation of the volatile etch products.

8.3.3 Etching experiments

The basic matrix of external plasma parameters has been investigated for its effects on methane/hydrogen etching of GaAs. InP is another important III-V semiconductor which suffers from problems of phosphorus depletion but to a greater extent such that islands of indium are formed on the surface. Other III-V's such as GaInAs *etc.* could also be used with the initial stoichiometry as an additional variable. In order to reduce the stoichiometry change further it would be necessary to perform experiments at lower energies than are possible with the present experimental arrangement. At lower energies than were used in this project, however, the plasmas become unstable. The next step would therefore be to have an rf discharge with low DC bias which is sustained in part by additional electron creation mechanisms such as inductive coupling. This allows the power to sustain the plasma to be decoupled from the bias at the substrate and high fluxes and etch rates to result from very low damage ion bombardment.

References

[1] J. M. Carroll, "Microelectronic circuits and applications", McGraw Hill (1965).
[2] D. J. Elliott, "Integrated Circuit Fabrication Techniques", McGraw Hill (1982).
[3] S. J. Pearton, F. Ren, "Science of dry-etching of III-V materials", Journal of Material Science: Materials in Electronics, Vol 5, No 1, pp1-12 (1994).
[4] T. Sugano, Applications of plasma processing to VSLI technology. John Wiley and Sons. New York (1985).
[5] A von Engel, "Electric Plasmas and their uses", Taylor and Francis, London (1983).
[6] J. A. Bittencourt, "Fundamentals of Plasma Physics", Pergammon Press, Oxford (1986).
[7] E. Nasser, "Fundamentals of Gaseous Ionization & Plasma Electronics", (Wiley, 1971).
[8] B. Chapman, "Glow Discharge Processes", (Wiley, New York, 1980).
[9] H. V. Boenig, "Fundamentals of Plasma Chemistry and Technology", (Technomic,1988).
[10] O. A. Popov and V. A. Godyak, "Power dissipated in low-pressure radio-frequency discharge plasmas", J. Appl. Phys. Vol 57, No 1, pp53-58 (1985).
[11] C. Lai, R. A. Breun, P. W. Sandstrom, A. E. Wendt, N. Hershkowitz and R. C. Woods, "Langmuir probe measurements of electron-temperature and density scaling in multidipole radio-frequency plasmas", J. Vac. Sci. Tech. A, Vol.11, No.4, Pt1, pp.1199-1205 (1993).
[12] P. W. May, D. F. Klemperer and D. Field, "Monte-carlo simulations of electron distributions in the sheath region of reactive-ion-etching plasmas", J. Appl. Phys, Vol 73, No 4, pp1634-1643 (1993).
[13] R. H. Huddlestone and S. L. Leonard, "Plasma Diagnostic Techniques", Academic Press, (1965).
[14] K. Kohler, J. W. Coburn, D. E. Horne, E. Kay and J. H. Keller, "Plasma potentials of 13.56-MHz argon glow discharges in a planar system", J. Appl. Phys. Vol 57, No 1, pp59-66 (1985).
[15] M. J. Kushner, "Distribution of ion energies incident on electrodes in capacitively coupled rf discharges", J. Appl. Phys. Vol 58, No 11, pp4024-4031 (1985).
[16] M. A. Sobolewski, "Electrical characteristics of argon radio frequency glow discharges in an asymmetric cell", IEEE Transactions on Plasma Science, Vol 23, No 6, pp1006-1022 (1995).
[17] B. Chapman, "Glow Discharge Processes", Wiley, New York, (1980).
[18] O. A. Popov and V. A. Godyak, "Power dissipated in low-pressure radio-frequency discharge plasmas", J. Appl. Phys. Vol 57, No 1, pp53-58 (1985).
[19] P. W. May, D. F. Klemperer and D. Field, "Monte-carlo simulations of electron distributions in the sheath region of reactive-ion-etching plasmas", J. Appl. Phys, Vol 73, No 4, pp1634-1643 (1993).
[20] M. J. Druvetsyn and F. M. Penning, Rev. Mod Phys. 20 820 (1987).
[21] W. L. Morgan and L. Vriens, "Two-electron-group model and boltzmann calculations for low-pressure gas discharges", J. Appl. Phys. Vol 51, No 10, pp5300-5306 (1980).
[22] J. Vlcek and V. Pelikán, "Electron-energy distribution function in the collisional radiative model of an argon plasma", J. Phys. D: Appl. Phys. Vol 18, No 3, pp347-358 (1985).
[23] M. Surendra and D. B. Graves, "Particle simulations of radiofrequency glow-discharges", IEEE Transactions on Plasma Science, Vol 19, No 2, p144-157 (1991).
[24] D. Maundrill, J. Slatter, A. I. Spiers and C. C. Welch, "Electrical measurements of rf-generated plasmas using a driven electrostatic probe technique", J. Phys. D: Appl. Phys. Vol 20, No 7, pp815-819, (1979).
[25] V. A. Godyak, R. B. Piejak and B. M. Alexandrovich, "Evolution of the electron-energy-distribution function during rf discharge transition to the high-voltage mode", Phys. Rev. Lett. Vol 68, No 1, pp40-43 (1992).
[26] E. W. McDaniel, "Collisional Phenomena in Ionized Gases", (Wiley, London, 1964).
[27] C. A. Ordonez, and R. E. Peterkin, ", Secondary electron emission at anode, cathode,

and floating plasma-facing surfaces", Vol 79, No 5, pp2270-2274 (1996).
[28] B. Chapman, "Glow Discharge Processes", Wiley, New York, (1980).
[29] M. D. Gill, "Sustaining mechanisms in rf plasmas", Vacuum, Vol 34, No 3-4, pp357-364 (1984).
[30] X. Z. Yao and D. Y. Jiang, "Effect of secondary electron emission on sheath potential in an electron cyclotron resonance plasma", J. Appl. Phys. Vol 81, No 5, pp2119-2123 (1997).
[31] W. Xu and P. J. Sides, "Spatial variations of radio-frequency plasma-density caused by a step-change of secondary-electron emission coefficient", J. Appl. Phys. Vol 77, No 9 pp4293-4301 (1995).
[32] A. Date, K. Kitamori, Y. Sakai and H. Tagashira, "Self-consistent monte-carlo modelling of rf plasma in a helium-like model gas", J. Phys. D: Appl. Phys. Vol 25, No 3, pp442-452 (1992).
[33] Electrostatic 1 dimensional code (ES1), Plasma theory and simulation group, University of California, Berkeley, 1987-1992.
[34] N. Mutsukura, K. Kobayashi and Y. Machi, "Monitoring of radio-frequency glow-discharge plasma", J. Appl. Phys. Vol 66, No 10, pp4688-4695 (1989).
[35] C. M. O. Mahony, R. Al. Wazzan and W. G. Graham, "Sheath dynamics observed in a 13.56 mhz-driven plasma", Appl. Phys. Lett, Vol 71, No 5, pp608-610 (1997).
[36] D. Field, D. F. Klemperer, P. W. May and Y. P. Song, "Ion energy distributions in radio-frequency discharges", J. Appl. Phys. Vol 70, No 1, pp82-92 (1991).
[37] A. D. Kuypers, PhD thesis. Utrecht, The Netherlands (1989).
[38] U. Flenderand K. Wiesemann, "Ion distribution functions behind an rf sheath", J. Phys. D: Appl. Phys, Vol 27, No 3, pp509-521 (1994).
[39] J. Liu, G. L. Huppert, H. H. Sawin, "Ion bombardment in rf-plasmas", J. Appl. Phys. Vol 68, No 8, pp3916-3934 (1990).
[40] M. Fivaz, S. Brunner, W. Schwarzenbach, A. A. Howling, Ch. Hollenstein, (1994).
[41] P. W. May, D. Field, D. F. Klemperer, "Modelling radiofrequency discharges - effects of collisions upon ion and neutral particle energy-distributions", J. Appl. Phys. Vol 71, No 8, pp3721-3730 (1992).
[42] G. G. Lister, "Low pressure gas discharge modelling", J. Phys. D: Appl. Phys. Vol 25, No 12, pp1649-1680 (1992).
[43] A. J. vanRoosmalen, "Plasma parameter estimation from impedance measurements in a dry etching system", Appl. Phys. Lett. Vol 42, No 5, pp416-418 (1983).
[44] M. S. Barnes, T. J. Colter and M. E. Elta, "Large-signal time-domain modelling of low-pressure rf glow discharges", J. Appl. Phys. Vol 61, No 1, pp81-89 (1987).
[45] J. P. Beouf, "Numerical model of rf glow discharge", Phys. Rev. A. Vol 36, No 6, pp2782-2792 (1987).
[46] P. Belengeur and J. P. Beouf, "Transition between different regimes of rf glow discharges", Phys. Rev. Vol 41, No 8, pp4447-4459 (1990).
[47] J. H. Tsai and C. Wu, "2-dimensional simulations of rf glow-discharge in N2 and SF6", Phys. Rev. A, Vol 41, No 10, pp5626-5644 (1990).
[48] A. D. Richards, B. E. Thompson and H. H. Sawin, "Continuum modelling of argon rf glow discharges", Appl. Phys. Lett. Vol 50, No 9, pp492-494 (1987).
[49] D. B. Graves, "Fluid model simulations of a 13.56-mhz rf discharge - time and space dependence of rates of electron-impact excitation", J. Appl. Phys. Vol 62, No 1, pp88-94 (1987).
[50] Y. H. Oh, N. H. Choi and D. I. Choi, "A numerical-simulation of rf glow-discharge containing an electronegative gas-composition", J. Appl. Phys. Vol 67, No 7, pp3264-3268 (1990).
[51] S. K. Park and D. J. Economou, "Analysis of low-pressure rf-glow discharges using a continuum model", J. Appl. Phys. Vol 68, No 8, pp3904-3915 (1990).
[52] M. Meyyappan and T. R. Govindan, "Modeling of electronegative radiofrequency discharges", IEEE Trans. Plasma. Sci. Vol 19, No 2, pp122-129 (1991).
[53] K. Okazaki, T. Makabe and Y. Yamaguchi, "Modeling of a rf glow-discharge

plasma", Appl. Phys. Lett. Vol 54, No 18, pp1742-1744 (1989).
[54] T. Makabe, F. Tochikubo and N. Nishimura, "Influence of negative-ions in rf-glow discharges in SiH4 at 13.56 MHz", Phys. Rev. A. Vol 42, No 6, pp3674-3677 (1990).
[55] T. Makabe, N. Nakano and Y. Yamaguchi, "Modeling and diagnostics of the structure of rf glow-discharges in Ar at 13.56 MHz", Phys. Rev. A. Vol 45, No 4, pp2520-2531 (1992).
[56] E. Gogolides and H. H. Sawin, "Continuum modeling of radiofrequency glow-discharges .1. theory and results for electropositive and electronegative gases", J. Appl. Phys, Vol 72, No 9, pp3971-3980 (1992).
[57] E. Gogolides, C. Buteau, A. Rhallabi and G. Turban, "Radiofrequency glow-discharges in methane gas - modeling of the gas-phase physics and chemistry", J. Phys. D: Appl. Phys, Vol 27, No 4, pp818-825 (1994).
[58] N. Sato and H. Tagashira, "A hybrid monte carlo/fluid model of rf plasmas in a SiH4/H2 mixture", IEEE transactions on plasma science, Vol 19, No 2, pp102-112 (1991).
[59] W. J. Goedheer, Two-Dimensional Modelling of RF Discharges, Conference Proceedings, ESCAMPIG, Slovakia (1996).
[60] A. Fiala, L. C. Pitchford and J. P. Beouf, "2-dimensional, hybrid model of low-pressure glow-discharges", Phys. Rev. E 49, No 6, pp5607-5622 (1994).
[61] W. J. Goedheer and P. M. Meijer, "Kinetic modeling of positive-ions in a low-pressure rf discharge", IEEE transactions on plasma science, Vol 19, No 2, pp245-249 (1991).
[62] T. E. Nitschke and D. B. Graves, "A comparison of particle-in-cell and fluid model simulations of low-pressure radio-frequency discharges", J. Appl. Phys. Vol 76, No 10, pp5646-5660 (1994).
[63] H. W. Trombley, F. Terry, M. Elta, "A self-consistent particle model for the simulation of rf glow-discharges", IEEE transactions on plasma science, Vol 19, No 2, pp158-162 (1991).
[64] A. Date, K. Kitamori, Y. Sakai and H. Tagashira, "Self-consistent monte-carlo modeling of rf plasma in a helium- like model gas", J. Phys. D: Appl. Phys. Vol 25, No 3, pp442-452 (1992).
[65] Electrostatic 1 dimensional code (ES1), Plasma theory and simulation group, University of California, Berkeley, 1987-1992.
[66] J. Umohoibhi, C. M. O. Mahoney, D. Riley and W. G. Graham, Conference Proceedings ESCAMPIG, Slovakia (1996).
[67] M. J. Kushner, "Distribution of ion energies incident on electrodes in capacitively coupled rf discharges", J. Appl. Phys. Vol 58, No 11, pp4024-4031 (1985).
[68] J. Lucas, Int J. Electron. 32, pp393 (1972).
[69] Y. P. Song, D. Field and D. F. Klemperer, "Electrical potentials in rf discharges J. Phys D: Appl. Phys. Vol 23, No 6, pp673-681 (1989).
[70] M. J. Kushner, "Distribution of ion energies incident on electrodes in capacitively coupled rf discharges", J. Appl. Phys. Vol 58, No 11, pp4024-4031 (1985).
[71] C. A. Moore, G. P. Davis and R. A. Gottscho, "Sensitive, nonintrusive, insitu measurement of temporally and spatially resolved plasma electric-fields", Phys. Rev. Lett. Vol 52, No 7, pp538-541 (1984).
[72] C. Wild and P. Koidl, "Ion and electron dynamics in the sheath of radiofrequency glow- discharges", J. Appl. Phys. Vol 69, No 5, pp2909-2922 (1991)
[73] B. E. Thompson, K. D. Allen, A. D. Richards and H. H. Sawin, "Ion-bombardment energy-distributions in radiofrequency glow- discharge systems", J. Appl. Phys. Vol 59, No 6, pp1891-1903 (1986).
[74] A. Maneschijn and W. J. Goedheer, "Angular ion and neutral energy-distribution in a collisional rf sheath", J. Appl. Phys. Vol 69, No 5, pp2923-2930 (1991).
[75] W. D. Davis and T. A. Vanderslice, "Ion energies at the cathode of a glow discharge", Phys. Rev. Vol 131, No 1, pp219 (1963).
[76] B. E. Thompson and H. H. Sawin, "Monte-carlo simulation of ion-transport through rf glow- discharge sheaths", J. Appl. Phys. Vol 63, No 7, pp2241-2251 (1988).

[77] D. Field, D. F. Klemperer, P. W. May and Y. P. Song, "Ion energy-distributions in radiofrequency discharges", J. Appl. Phys. Vol 70, No 1, (1991).
[78] A. D. Kuypers, University of Utrecht, Netherlands, (1989).
[79] W. D. Davis and T. A. Vanderslice, "Ion energies at the cathode of a glow discharge", Phys. Rev. Vol 131, No 1, pp219 (1963).
[80] M. J. Kushner, "Distribution of ion energies incident on electrodes in capacitively coupled rf discharges", J. Appl. Phys. Vol 58, No 11, pp4024-4031 (1985).
[81] J. M. Hammersley and D. C. Hanscomb, "Monte Carlo Methods", Chapman and Hall, London (1964).
[82] C. Wild and P. Koidl, "Ion and electron dynamics in the sheath of radio frequency glow discharges", J. Appl. Phys. Vol 69, No 5, pp2909-2922 (1991).
[83] B. E. Thompson and H. H. Sawin, "Monte-Carlo simulation of ion transport through rf glow discharge sheaths", J. Appl. Phys. Vol 63, No 7, pp2241-2251 (1988).
[84] J. O. Hirschfelder, C. F. Curtiss and R. B. Bird, "Molecular Theory of Gases and Liquids", Wiley, New York (1954).
[85] J. M. Hammersley and D. C. Hanscomb, "Monte Carlo Methods", Chapman and Hall, London (1964).
[86] K. P. Brand and H. Jungblut, "The interaction potentials of sf6 ions in sf6 parent gas determined from mobility data", J. Chem. Phys. Vol 78, No 4, pp1999-2007 (1983).
[87] J. O. Hirschfelder, C. F. Curtiss and R. B. Bird, "Molecular Theory of Gases and Liquids", Wiley, New York (1954).
[88] A. Maneschijn and W. J. Goedheer, "Angular ion and neutral energy distribution in a collisional rf sheath", J. Appl. Phys. Vol 69, No 5, pp2923-2930 (1990).
[89] P. W. May, D. Field, D. F. Klemperer, "Modeling radiofrequency discharges -effects of collisions upon ion and neutral particle energy-distributions", J. Appl. Phys. Vol 71, No 8, pp3721-3730 (1992).
[90] A. V. Phelps, "The application of scattering cross-sections to ion flux models in discharge sheaths", J. Appl. Phys. Vol 76, No 2, pp747-753 (1994).
[91] J. Liu, G. L. Huppert, H. H. Sawin, "Ion bombardment in rf-plasmas", J. Appl. Phys. Vol 68, No 8, pp3916-3934 (1990).
[92] W. H. Cramer, J. Chem. Phys. 30, 641 (1959).
[93] A. Maneschijn and W. J. Goedheer, "Angular ion and neutral energy distribtuion in a collisional rf sheath", J. Appl. Phys. Vol 69, No 5, pp2923-2930 (1990).
[94] P. W. May, D. Field, D. F. Klemperer, "Modelling radiofrequency discharges - effects of collisions upon ion and neutral particle energy distributions", J. Appl. Phys. Vol 71, No 8, p3721-3730 (1992).
[95] A. D. Kuypers, PhD thesis.Utrecht, The Netherlands (1989).
[96] A. C. Dickenson, 'Measurement and Simulation of Ion Energy Distributions in a Reactive Ion Etcher', Phd Thesis Bristol University (1994).
[97] A. V. Phelps, "Cross-sections and swarm coefficients for nitrogen-ions and neutrals in n2 and argon ions and neutrals in ar for energies from 0.1 ev to 10 kev", J. Phys. Chem. Ref. Data. Vol 20, No 3, pp567-573 (1991).
[98] D. Field, D. F. Klemperer, P. W. May and Y. P. Song, "Ion energy distributions in radio frequency discharges", J. Appl. Phys. Vol 70, No 1, pp82-92 (1991).
[99] P. Sigmund, "Mechanisms and theory of physical sputtering by particle impact", Nucl. Inst. and Meth. in Phys. Res. B27, No 1, pp1-20 (1987).
[100] P. Sigmund, "Theory of sputtering I. Sputtering yield of amorphous and polycrystalline targets", Phys. Rev. Vol 184, No 2, pp383-416 (1969).
[101] J. B. Malherbe, "Sputtering of compound semiconductorsurfaces .1. ion-solid interactions and sputtering yields", Critical Rev. in Solid State Mat. Sci. Vol 19, No 2, pp55-127 (1994).
[102] W. H. Gries and H. J. Strydom. Fres. Z. Anal. Chem. 319 727 (1984).
[103] H. J. Strydom and W. H. Gries, "A comparison of 3 versions of sigmund model of sputtering using experimental results", Rad. Eff. Lett. Vol 86, No 4, pp145-151 (1984).
[104] J. P. Bierszack and J. F. Ziegler, "Refined universal potentials in atomic-collisions",

Nucl. Instrum. Meth. Vol 194, No 1-3, pp93-100 (1982).
[105] J. B. Malherbe, "Sputtering of compound semiconductor surfaces .1. ion-solid interactions and sputtering yields", Critical Rev. in Solid State Mat. Sci. Vol 19, No 2, pp55-127 (1994).
[106] P. C. Zalm, "Energy-dependence of the sputtering yield of silicon bombarded with neon, argon, krypton, and xenon ions", J. Appl. Phys. Vol 54, No 5, pp2660-2666 (1983).
[107] P. C. Zalm, "Some useful yield estimates for ion-beam sputtering and ion plating at low bombarding energies ", J. Vac. Sci. Tech. B2, No 2, pp151-152 (1984).
[108] D. L. Smith, J. Nucl. Mat, 75 20 (1978).
[109] N. Matsunami, Y. Yamamura, Y. Itikawa, N. Itoh, Y. Kazumata, S. Miyagawa, K. Morita and R. Shimuzu, Rad. Eff. Lett, 57 15 (1980).
[110] P. Sigmund in Chapter 2 of "Sputtering by particle bombardment", ed R. Behrisch, Springer-Verlag, Heidelberg (1981).
[111] C. Jardin, D. Robert, B. Achard, B. Gruzza and C. Pariset, "An aes and els study of inp (100) surface subjected to argon ion-bombardment", Surface and Interface Analysis, Vol 10, No 6, pp301-305 (1987).
[112] J. S. Pan, A. T. S. Wee, C. H. A. Huan, H. S. Tan and K. L. Tan, "Arxps analysis of surface compositional change in ar ion bombarded gaas (100)", J. Phys. D: Appl. Phys. Vol 30, No 18, pp2514-25 19 (1997).
[113] J. B. A. Malherbe, W. O. Barnard, I. L. R. Strydom and C. W. Louw, "Preferential sputtering of gaas", Surface and Interface Analysis, Vol 18, No 7, pp491-495 (1992).
[114] J. Comas and C. B. Cooper, J. Appl. Phys. 38 2956 (1967).
[115] J. B. Malherbe, S. Hofmann and J. M. Sanz, "Preferential sputtering of oxides - A comparison of model predictions with experimental data", Appl. Surf. Sci. Vol 27, No 3, pp355-365 (1986).
[116] L. Pauling, "The Chemical Bond", Cornell University Press, New York (1967).
[117] Yu. W, "Ion bombardment induced compositional changes in compund semiconductor surfaces studied by XPS combined with LEISS", PhD Thesis, Aston University (1995).
[118] F. L. Williams and D. Nason, "Binary alloy surface compositions from bulk alloy thermodynamic data", Surface. Sci. Vol 45, pp377-408 (1974).
[119] A. Scandurra, "SNMS characterization of ion irradiated gaas surfaces", Applied Surface Science, Vol 103, No 1, pp19-25 (1996).
[120] J. B. Malherbe, "Sputtering of compound semiconductor surfaces .1. ion-solid interactions and sputtering yields", Critical Rev. in Solid State Mat. Sci. Vol 19, No 2, pp55-127 (1994).
[121] R. Kelly, "The surface binding-energy in slow collisional sputtering", Nucl. Inst. Meth. B18, No 4-6, pp388-398 (1987).
[122] J. Kirschner, "Surface segregation and its implications for sputtering", Nucl. Inst. and Meth. B7/8, No 7-8, pp742-749 (1985).
[123] R. Kelly and A. Oliva, NATO ASI Series E. 112 41-69 (1986).
[124] HYPERCHEM, Hypercube Inc, 1115 N.W. 4th Street, Gainesville, Florida 32601, USA (1994).
[125] SUSPRE, Surrey University Sputter Profile Resolution from Energy Deposition Program V.
[126] J. P. Bierszack, "Computer-simulations of sputtering", Nucl. Instr. and Meth. B27 pp21-36 (1987).
[127] MARLOWE: Oak Ridge National Laboratory, Oak Ridge, Tennessee.
[128] R. N. Thomas, et al. "Semiconductors and semimetals", Vol 20. Academic Press, Orlando (1984).
[129] S. Thomas and S. W. Pang, "Dependence of contact resistivity and schottky diode characteristics on dry-etching induced damage of GaInAs", J. Vac. Sci. Tech. B, Vol.12, No.5, pp.2941-2946 (1994).
[130] KK. Ko and S. W. Pang, "Surface damage on gaas etched using a multipolar electron-cyclotron-resonance source", J. Electro. Soc. Vol.141, No.1, pp.255-258 (1994).

[131] S. K. Murad, C. D. W. Wilkinson and S. P. Beaumont, "Selective and nonselective RIE of GaAs and Al(x)Ga(1-x)As in SiCl4 plasma", Microelectronic Engineering, Vol 23, No. 1-4 pp357-360 (1994).
[132] S. K. Murad, P. D. Wang, N. I. Cameron, S. P. Beaumont and C. D. W. Wilkinson, "Damage free and selective RIE of GaAs/AlGaAs in SiCl4/SiF4 plasma for MESFET and pseudomorphic HEMT's gate recess etching", Microelectronic engineering, Vol.27, No.1-4, pp.439-444 (1995).
[133] M. Rahman, S. K. Murad, M. C. Holland, A. R. Long and J. G. Williamson, "Method of dry-etching evaluation using quantum dots", Microelectronic engineering, Vol.35, No.1-4, pp.91-94 (1997).
[134] S. J. Pearton, W. S. Hobson, C. R. Abernathy, F. Ren, T. R. Fullowan and A. Katz, "Dry etching characteristics of III-V semiconductors in microwave BCl3 discharges", plasma Chemistry and Plasma Processing, Vol.13, No.2, pp.311-332 (1993).
[135] M. Vernon, T. R. Hayesand V. M. Donnelly, "Intrinsic mechanism of smooth and rough morphology in etching of InP by Cl2 determined by infrared-laser interferometry", J. Vac. Sci. Tech. A, Vol.10, No.6, pp.3499-3506 (1992).
[136] Y. Z. Juang, Y. K. Su, S. C. Shei and B. C. Fang, "Comparing reactive ion etching of III-V compounds in Cl2/BCl3/Ar and CCl2F2/BCl3/Ar discharges", J. Vac. Sci. Tech. A, Vol.12,
No.1, pp.75-82 (1994).
[137] J. W. Lee, S. J. Pearton, C. J. Santana, J. R. Mileham, E. S. Lambers, C. R. Abernathy, F. Ren and W. S. Hobson, "High ion density plasma etching of InGaP, AlInP, and AlGaP in CH4/H-2/Ar", J. Elec. Soc. Vol.143, No.3, pp.1093-1098 (1996).
[138] S. J. Pearton, F. Ren, T. R. Fullowan, A. Katz, W. S. Hobson, U. K. Chakrabarti and C. R. Abernathy, "Plasma etching of III-V semiconductor thin films", Materials Chemistry and Physics, 32 pp215-234 (1992).
[139] V. J. Law, S. G. Ingram, M. Tewordt and G. A. C. Jones. "Reactive ion etching of GaAs using CH4 - in He, Ne and Ar", Semicond. Sci. Technol. Vol 6, No 5, pp411-413 (1991).
[140] R. Cheung, S. Thoms, S. P. Beaumont, G. Doughty, V. Law and C. D. W. Wilkinson, "Reactive ion etching of GaAs using a mixture of methane and hydrogen", Electron. Lett. Vol 23, No 16, pp857-859 (1987).
[141] G. F. McLane, M. W. Cole, D. W. Eckart, P. Cooke, R. Moerkirk and M. Meyappan, "Magnetron-enhanced reactive ion etching of GaAs and AlGaAs using CH4/H2/Ar", J. Vac. Sci. Tech. A, Vol 11, No 4, Pt 2, 1753-1757 (1993).
[142] T. R. Hayes, M. Dreisbach, P. Thomas, W. Dautremont-Smith and L. A. Heimbrook, "Reactive ion etching of InP using CH4/H2 mixtures - mechanisms of etching and anisotropy", J. Vac. Sci. Tech. B, Vol 7, No 5, pp1130-1140 (1989).
[143] S. J. Pearton, U. Chakrabarti, A. Katz, A. Perley, W. S. Hobson and C. Constantine, "Comparison of CH4/H2/Ar reactive ion etching and electron-cyclotron resonance plasma-etching of In-based III-V alloys", J. Vac. Sci. Tech. B9 1421-1432 (1991).
[144] S. J. Pearton and F. Ren, "Science of dry-etching of III-V-materials", Journal of Mat. Sci: Materials in Electronics, Vol 5, No 1, pp1-12 (1994).
[145] J. Werking, J. Schramm, C. Nguyen, E. L. Hu and H. Kroemer, "Methane hydrogen-based reactive ion etching of InAs, InP, GaAs, and GaSb", J. Appl. Phys. Lett. Vol 58, No 18 pp2003-2005 (1991).
[146] V. J. Law, S. G. Ingram, M. Tedwort and G. A. C. Jones, "Reactive ion etching of gaas using CH4 - in He, Ne and Ar", Semi. Sci. Tech. Vol 6, No 5 pp411-413 (1991).
[147] S. J. Pearton, U. K. Chakrabarti, A. P. Perley, W. S. Hobson and M. Geva, "Dry etching of gaas, algaas, and gasb using electron-cyclotron resonance and radio-frequency ch4/h2/ar or c2h6/h2/ar discharges", J. Electrochemical Society, Vol 138, No 5 pp1432-1439 (1991).
[148] R. Cheung, S. Thoms, S. P. Beaumont, G. Doughty, V. Law and C. D. W. Wilkinson, "Reactive ion etching of gaas using a mixture of methane and hydrogen", Elec. letters. Vol 23, No 16, pp857-859 (1987).

[149] "Inelastic ion surface collisions", Edited by N.H. Tolk, J.C. Tully, W. Heiland and C. W. White, Academic, New York (1977).
[150] V. J. Law and G. A. C. Jones, "Obtaining high etch rates of GaAs AI0.3Ga0.7As using methane-hydrogen MORIE and organic photoresist masks", Semicond. Sci. Tech. Vol 4, No 9, pp833-835 (1989).
[151] R. Cheung, S. Thoms, S. P. Beamont, G. Doughty, V. Law and C. D. W. Wilkinson, "Reactive ion etching of GaAs using a mixture of methane and hydrogen", Elec. Letters. Vol 23, No 16, pp857-859 (1987).
[152] A. Semu and P. Silverberg, "Methane hydrogen III-V metal-organic reactive ion etching", Semicond. Sci. Tech. Vol 6, No 4 pp287-289 (1991).
[153] R. Cheung, S. Thoms, S. P. Beamont, G. Doughty, V. Law and C. D. W. Wilkinson, "Reactive ion etching of GaAs using a mixture of methane and hydrogen", Elec. Letters. Vol 23, No 16, pp857-859 (1987).
[154] V. J. Law and G. A. C. Jones, "Obtaining high etch rates of gaas ai0.3ga0.7as using methane - hydrogen morie and organic photoresist masks", Semicond. Sci. Tech. Vol 4, No 9, pp833-835 (1989).
[155] V. J. Law, S. G. Ingram, M. Tedwort and G. A. C. Jones, "Reactive ion etching of GaAs using CH4 in He, Ne and Ar", Semi. Sci. Tech. Vol 6, No 5, pp411-413 (1991).
[156] S. Thoms, I. McIntyre, S. P. Beaumont, M. Al-Mudares R. Cheung and C. D. W. Wilkinson, J. Vac. Sci. Tech B 6 (1) pp127 (1988).
[157] J. Werking, J. Schramm, C. Nguyen, E. L. Hu and H. Kroemer, "Methane hydrogen-based reactive ion etching of inas, inp, gaas, and gasb", J. Appl. Phys. Lett. Vol 58, No 18, pp2003-2005 (1991).
[158] S. J. Pearton, J. W. Lee, E. S. Lambers, J. R. Mileham, C. R. Aberbathy, W. S. Hobson, F. Ren and R. J. Shul, "High microwave power electron cyclotron resonance etching of iii-v semiconductors in ch4/h-2/ar", J. Vac. Sci Tech. B 14, No 1, pp118-125 (1996).
[159] V. J. Law, M. Tewordt, S. G. Ingram and G. A. C. Jones, "Alkane based plasma-etching of GaAs", J. Vac. Sci. Tech. B9, No 3, pp1449-1455 (1991).
[160] V. J. Law, S. G. Ingram, M. Tedwort and G. A. C. Jones, "Reactive ion etching of gaas using ch4 - in he, ne and ar", Semi. Sci. Tech. Vol 6, No 5, pp411-413 (1991).
[161] S. J. Pearton, J. W. Lee, E. S. Lambers, J. R. Mileham, C. R. Abernathy, W. S. Hobson, F. Ren and R. J. Shul, "High microwave power electron cyclotron resonance etching of iii-v semiconductors in ch4/h-2/ar", J. Vac Sci. Tech B 14, No 1, pp118-125 (1996).
[162] V. J. Law, M. Tewordt, S. G. Ingram and G. A. C. Jones, "Alkane based plasma etching of GaAs", J. Vac. Sci. Tech. B. Vol 9, No 3, pp1449-1455 (1991).
[163] S. J. Pearton, "Characterization of damage in electron cyclotron resonance plasma etched compound semiconductors", Applied Surface Science, Vol 117, pp597-604 (1997).
[164] A. Semu and P. Silverberg, "Methane hydrogen III-V metal organic reactive ion etching of GaAs", Semicond. Sci. Tech. Vol 6, No 4, pp287-289 (1991).
[165] S. J. Pearton, F. Ren, "Science of dry-etching of III-V materials", Journal of Material Science: Materials in Electronics, Vol 5, No 1, pp1-12 (1994).
[166] J. B. Malherbe, W. O. Barnard, I. L. R. Strydom and C. W. Louw, "Preferential sputtering of gaas", Surf. and Int. Anal. Vol 18, No7, pp491-495 (1992).
[167] I. L. Singer, J. S. Murday and J. Comas, "Preferential sputtering from disordered gaas
J. Vac. Sci. Tech. Vol 18, No 2, pp161-163 (1981).
[168] J. B. Malherbe, W. O. Barnard, I. L. R. Strydom and C. W. Louw, "Preferential sputtering of GaAs", Surf. and Int. Anal. Vol 18, No7 pp491-495 (1992).
[169] G. Padeletti and G. M. Ingo, "Small-area xps investigation on ion-induced chemical modifications during depth-profiling of an alxga1-xas/gaas structure", Surf. and Int. Anal. Vol 22, No 1-12, pp31-35 (1994).
[170] A. Scandurra, "SNMS characterization of ion irradiated gaas surfaces", Applied Surface Science, Vol 103, No 1, pp19-25 (1996).

[171] J. L. Sullivan, W. Yu and S. O. Saied, "A study of the compositional changes in chemically etched, ar ion-bombarded and reactive ion etched gaas(100) surfaces by means of arxps and leiss", Applied Surface Science, Vol 90, No 3, pp309-319 (1995).
[172] T. Aoyama, M. Tanemura and F. Okuyama, "Angular distribution of particles sputtered from gaas by ar+ and xe+ ion bombardment",Applied Surface Science, Vol 101, pp351-354 (1996).
[173] J. S. Pan, A. T. S. Wee, C. H. A. Huan, H. S. Tan, K. L. Tan, "arxps analysis of surface compositional change in ar+ ion bombarded gaas (100)", J. Phys. D: Appl. Phys. Vol 30, No 18, pp2514-2519 (1997).
[174] L. M. Weegels, T. Saitoh, H. Oohashi and K. Kanbe, "In-situ monitoring of electron-cyclotron-resonance plasma processing of gaas-surfaces by optical reflection spectroscopy", Appl. Phys. Lett, Vol 64, No 20, pp2661-2663 (1994).
[175] C. Debiemme-Chouvy, D. Ballutaud, J. C. Pesant and A. Etcheberry, "x-ray photoelectron-spectroscopy study of gaas surface-exposed to a rf hydrogen plasma", Appl. Phys. Lett. Vol 62, No 18 pp2254-2255 (1993).
[176] J. L. Sullivan, S. O. Saied , R. L. Layberry and M J Cardwell, "Surface modification of (100) n-gaas by radio frequency hydrogen plasmas", J. Vac. Sci. Tec. A. Vol 16, No 4, pp 2567-2571 (1998).
[177] G. F. McLane, W. R. Buchwald, L. Casas and M. W. Cole, "Magnetron enhanced reactive ion etching of gaas in ch4/h2/ar - surface damage study", J. Vac. Sci Tech. A 12, No 4, Pt 1, pp1356-1359 (1994).
[178] S. J. Pearton, J. W. Lee, E. S. Lambers, J. R. Mileham, C. R. Abernathy, W. S. Hobson, F. Ren and R. J. Shul, "High microwave power electron cyclotron resonance etching of iii-v semiconductors in ch4/h-2/ar", J. Vac Sci. Tech B 14, No 1, pp118-125 (1996).
[179] P. F. A. Meharg, E. A. Ogryzlo, I. Bello and W. M. Lau, "Surface damage and deposition on gallium-arsenide resulting from low-energy carbon ion-bombardment", Surface Science, Vol 271, No 3, pp468-476 (1992).
[180] P. F. A. Meharg, E. A. Ogryzlo, I. Bello and W. M. Lau, "Low-energy carbon ion bombardment on indium-phosphide and its implications for alkane-based reactive ion etching", J. Appl. Phys. Vol 71, No 11, pp5623-5628 (1992).
[181] S. Murad, M. Rahman, N. Johnson, S. Thoms, S. P. Beaumont and C. D. W. Wilkinson, "Dry etching damage in iii-v semiconductors", J. Vac. Sci. Tech. B 14, No 6, pp3658-3662 (1996).
[182] Zdislaw Wronski. Marie-Sklodowska University, Lublin, Poland.
[183] A. D. Kuypers, University of Utrecht, Netherlands (1989).
[184] D. Field, D. F. Klemperer, P. W. May and Y. P. Song, "Ion energy distributions in radiofrequency discharges", J. Appl. Phys. Vol 70, No 1, pp82-92 (1991).
[185] A. V. Phelps, "Cross-sections and swarm coefficients for h+, h-2+, h-3+, h, h- 2, and h- in h-2 for energies from 0.1 ev to 10 kev", J. Phys. Chem. Ref. Data, Vol 19, No 3, pp653-675 (1991).
[186] Knuth, "Semi-numerical algorithms", Addison, Wesley (1968).
[187] B. H. Bransden and M. R. C. Mcdowell, "Charge exchange and the theory of ion atom collisions", Clarendon (1992).
[188] E.W. McDaniel, J. B. A. Mitchell, M. E. Rudd, "Atomic Collisions-Heavy Particle Projectiles", Wiley, New York (1993).
[189] Z. Wronski, "Computer simulation of energy angle distributions of ions generated in the cathode fall of a glow discharge", Vacuum, Vol 42, No10, pp635-644 (1991).
[190] Z. Wronski, C. G. Pearce, "Computer-simulation of a fast atom ion-source", Vacuum, Vol 43, No 10, pp931-942 (1992).
[191] A. D. Kuypers, University of Utrecht, Netherlands (1989).
[192] P. W. May, D. Field, D. F. Klemperer, "Modeling radiofrequency discharges - effects of collisions upon ion and neutral particle energy-distributions", J. Appl. Phys. Vol 71, No 8, pp3721-3730 (1992).
[193] J. Liu, G. L. Huppert, H. H. Sawin, "Ion bombardment in rf plasmas", J. Appl. Phys.

Vol 68, No 8, pp3916-3934 (1990).
[194] A. V. Phelps, "Cross sections and swarm coefficients for nitrogen ions and neutrals in N2 and Ar ions and neutrals in Ar for energies from 0.1 eV to 10 keV", J. Phys. Chem. Ref. Data, Vol 20, No 3, pp557-573 (1991).
[195] HYPERCHEM, Hypercube Inc, 1115 N.W. 4th Street, Gainesville, Florida 32601, USA (1994).
[196] A.A. Radcig, B. M. Smirnow, Sprawocznik po atomnoj i molekularnoj fizikie, Atomizdat, Moskwa (1980).
[197] W. Kolos, "Extrapolated born-oppenheimer energy for the ground-state of the hydrogen molecule", J. Chem Phys, Vol 101, No 2, p1330-1332 (1994).
[198] A.A. Radcig, B. M. Smirnow, Sprawocznik po atomnoj i molekularnoj fizikie, Atomizdat, Moskwa (1980).
[199] A. V. Phelps, "Cross-sections and swarm coefficients for nitrogen-ions and neutrals in n2 and argon ions and neutrals in ar for energies from 0.1 ev to 10 kev", J. Phys. Chem. Ref. Data, Vol 20, No 3, pp567-573 (1991).
[200] A. C. Dickenson, 'Measurement and Simulation of Ion Energy Distributions in a Reactive Ion Etcher', Phd Thesis Bristol University (1994).
[201] P. W. May, Bristol University. Private communication.
[202] Tibor Simko, Comenius University, Bratislava, Slovakia. Private communication.
[203] A. C. Dickenson, 'Measurement and Simulation of Ion Energy Distributions in a Reactive Ion Etcher', Phd Thesis Bristol University (1994).
[204] J. Glosik, "Measurement of the reaction rate coefficients of reactions of H2+ with Ne, Ar, Kr, Xe, H2, D2, N2 and CH4 at thermal energy", Int. J. Mass. Spec. Ion. Pross. Vol 139 pp15-23 (1993).
[205] R. P. Clow and J. H. Futrell, Int. J. Mass. Spec. Ion. Phys. 4 pp165 (1970).
[206] R. T. McIver and R. Dunbar, Int. J. Mass. Spec. Ion. Phys. 7 pp471 (1971).
[207] A. Giardini-Guidoni and L. Friedman, "Energy transfer in ion molecule reactions in the methane system", J. Chem. Phys. 45 pp937 (1966).
[208] G. Csanak, D. C. Cartwright, S. K. Srivastava and S. Trajmar, "Electron-molecule interactions and their applications". Plenum, New York (1984).
[209] B. Lohmann and S. J. Buckmann, "Low energy electron scattering from methane", J. Phys. B: At. Mol. Phys. Vol 19, No 16 pp2565-2570 (1986).
[210] S. L. Lunt, J. Randell, J. P. Ziesel, G. Mrotzek and D. Field, "Low-energy-electron scattering from ch4, c2h4 and c2h6", J. Phys. B: At. Mol. Opt. Phys. Vol 27, No 7, pp1407-1422 (1994).
[211] B. Adamczyk, A. H. Boerboom, B. L. Shram and J. Kistermaker, "Partial ionisation cross sections of He, Ne, H2 and CH4 for electrons from 20 to 500 eV", J. Chem. Phys. Vol 44, pp4640 (1966).
[212] E.W. McDaniel, "Atomic Collisions-Electron and Photon Projectiles", Wiley, New York (1993).
[213] S. Trajmar and D. C. Cartwright, Excitation of molecules by electron impact, ICPEAC XIV, Stanford pp77 (1985).
[214] C. Winstead, Q. Sun and V. McKoy, "Electronic excitation of ch4 by low-energy electron-impact", J. Chem. Phys. Vol 98, No 3, pp2132-2137 (1992).
[215] L. Vuskovic and S. Trajmar, "Electron-impact excitation of methane", J. Chem. Phys. Vol 78, No 8, pp4947-4951 (1983).
[216] T. W. Shyn, "Vibrational-excitation cross-sections of methane by electron- impact", J. Phys. B: At. Mol. Opt. Phys. Vol 24, No 24, pp5169-5173 (1991).
[217] H. Tanaka, M. Kubo, N. Onodera and A. Suzuki, "Vibrational-excitation of ch4 by electron-impact - 3-20 ev", J. Phys B: At. Mol. Phys. Vol 16, No 15, pp2861-2869 (1983).
[218] B. Mapstone and W. R. Newell, "Vibrational-excitation of methane by electron-impact", J. Phys. B: At. Mol. Opt. Phys. Vol 27, No 23, pp5761-5772 (1994).
[219] S. Trajmar and D. C. Cartwright, Excitation of molecules by electron impact, ICPEAC XIV, Stanford pp77 (1985).
[220] D. J. Auerbach, R. Cacak, R. Caudano, T. D. Gaily, C. Kaiser, J. W. McGowan, J.

B. A. Mitchell and S. F. J. Wilk, "Merged ion-electron beam experiments I Method and measurements of dissociative recombination cross sections", J. Phys. B: At. Mol. Phys. Vol 10, pp3797 (1977).
[221] B. Peart and K. T. Dolder, "The production of de-excited H3+ ions and measurement of the energies of two electronically excited states", J. Phys. B: At. Mol. Phys. Vol 7, No 12, pp1567-1573 (1974).
[222] M. T. Leu, M. A. Biondi and R. Johnsen, "Measurements of recombination of electrons with H3+ and H5+ ions", Phys. Rev. A8, No 1, pp413-419 (1973).
[223] H. Hus, F. B. Yousif, C. Noren, A. Sen and J. B. A. Mitchell, "Dissociative recombination of electrons with h-2+ in low vibrational-states", Phys. Rev. Lett. Vol 60, No 11, pp1006-1009 (1988).
[224] F. B. Yousif, P. Van der Donk and J. B. A. Mitchell, "Ion-pair formation in the dissociative recombination of h-3(+)", J. Phys. B: At. Mol. Opt. Phys. Vol 26, No 22, pp4249-4255 (1993).
[225] M. Surendra and D. B. Graves, "Particle simulations of radiofrequency glow-discharges", IEEE Transactions on Plasma Science, Vol 19, No 2, p144-157 (1991).
[226] H. A. Fowler and H. E. Farnsworth. Phys. Rev. 111 1 pp103-112 (1958).
[227] C. A. Ordonez and R. E. Peterkin, "Secondary electron emission at anode, cathode, and floating plasma-facing surfaces", J. Appl. Phys. Vol 79, No 5, pp2270-2274 (1995).
[228] C. Böhm and J. Perrin, "Retarding-field analyzer for measurements of ion energy distributions and secondary electron emission coefficients in low-pressure radio frequency discharges", Rev. Sci. Instrum. 64 (1), pp31-44 (1992).
[229] J. P. Biersack, "Computer simulations of sputtering", Nucl. Instr. and Meth. B. Vol 27, No 1, pp21-36 (1987).
[230] J. B. Malherbe, "Sputtering of compound semiconductor surfaces 1 ion solid interactions and sputtering yields", Critical Rev. in Solid State Mat. Sci. Vol 19, No 2, pp55-127 (1994).
[231] M. A. Foad, S. Thoms and C. D. W. Wilkinson, "New technique for dry etch damage assessment of semiconductors", J. Vac. Sci. Tech. B. Vol 11, No 1, pp20-25 (1993).
[232] A. J. van Roosmalen, W. G. M. van den Hoek and H. Kalter, "Electrical properties of planar rf discharges for dry etching", J. Appl. Phys. Vol 58, No 2, pp653-658 (1985).
[233] V. A. Godyak, R. B. Piejak and N. Sternberg, "A comparison of rf electrode sheath models", IEEE Trans. Plasma Science, Vol 21, No 4 pp378-382 (1993).
[234] D. J. Heading, Aston University, UK. Private communication.
[235] M. Rahman, "Channelling and diffusion in dry-etch damage", J. Appl. Phys. Vol 82, No 5, pp2215-2224 (1997).
[236] J. L. Sullivan, W. Yu and S. O. Saied, "A study of the compositional changes in chemically etched, Ar ion bombarded and reactive ion etched GaAs(100) surfaces by means of ARXPS and LEISS", Applied Surface Science,Vol 90, No 3, pp309-319 (1995).
[237] J. S. Pan, A. T. S. Wee, C. H. A. Huan, H. S. Tan and K. L. Tan, "ARXPS analysis of surface compositional change in Ar+ ion bombarded GaAs (100)", J. Phys. D: Appl. Phys. Vol 30, No 18, pp2514-2519 (1997).
[238] J. B. Malherbe, S. Hofmann and J. M. Sanz, "Preferential sputtering of oxides - A comparison of model predictions with experimental data", Appl. Surf. Sci. Vol 27, No 3, pp355-365 (1986).
[239] W. Yu, Aston University. Private communication.
[240] Y. P. Feng, C. K. Ong, H. C. Poon and D. Tomanek, "Tight-binding molecular dynamics simulations of semiconductor alloys: clusters, surfaces, and defects", J. Phys. Condens. Matter. Vol 9, No 21, pp4345-4364 (1997).
[241] Y. P. Feng, C. K. Ong, H. C. Poon and D. Tomanek, "Tight-binding molecular dynamics simulations of semiconductor alloys: clusters, surfaces, and defects", J. Phys. Condens. Matter. Vol 9, No 21, pp4345-4364 (1997).
[242] G. Qian and R. M. Martin, "1st-principles study of the atomic reconstructions and energies of ga-stabilized and as-stabilized gaas(100) surfaces", Physical Review B, Vol

38, No 11, p7649-7663 (1988).
[243] G. Qian and R. M. Martin, "1st-principles study of the atomic reconstructions and energies of ga-stabilized and as-stabilized gaas(100) surfaces", Physical Review B, Vol 38, No 11, p7649-7663 (1988).
[244] P. Sigmund, "Mechanisms and theory of physical sputtering by particle impact", Nucl. Inst. and Meth. in Phys. Res. B. Vol 27, No 1, pp1-20 (1987).
[245] R. Kelly, Nucl. Instr. Meth. B18 388 (1987).
[246] © Clares Micro Supplies, 98 Middlewich Road, Northwich, Cheshire, CW9 7DA. 1997.
[247] C. S. Fradley, "Angle resolved x-ray photoelectron spectroscopy", Progress in Surface Science, Vol 16, pp275-388 (1984).
[248] S. Tanuma, C. J. Powell and D. R. Penn, "Calculations of electron inelastic mean free paths .3. data for 15 inorganic-compounds over the 50-2000-ev range", Surf. Int. Anal. Vol 17, No 13, pp927-939 (1991).
[249] S. Tanuma, C. J. Powell and D. R. Penn, "Calculations of electron inelastic mean free paths .2. data for 27 elements over the 50-2000-ev range", Surf. Interface Anal, Vol 17, No 13, pp911-926 (1991).
[250] M. P. Seah and W. A. Dench, "Quantitative electron spectroscopy of surfaces", Surf. Int. Anal. Vol 1, No 1, pp2-11 (1979).
[251] Dr Simon Hicks, Glasgow University. Private communication.
[252] S. J. Pearton, J. W. Lee, E. S. Lambers, J. R. Mileham, C. R. Abernathy, W. S. Hobson, F. Ren and R. J. Shul, "High microwave power electron cyclotron resonance etchingof iii-v semiconductors in ch4/h-2/ar", J. Vac Sci. Tech B 14, No 1, pp118-125 (1996).
[253] Keith Vanner, Caswell, GEC-Marconi, Tadcaster, Northamptonshire. Private communication.
[254] J. D. Swift & M. J. R. Schwar, "Electrical Probes for Plasma Diagnostics", Iliffe (1970).
[255] J. V. Scanlan and M. B. Hopkins, "Langmuir probe measurements of the electron-energy distribution function in radiofrequency plasmas", J. Vac. Technol. A, Vol. 10, No 4, Pt 1, p1207-1211 (1992).
[256] D. Maundrill, J. Slatter, A. I. Spiers and C. C. Walsh, "Electrical measurements of rf-generated plasmas using a driven electrostatic-probe technique", J. Phys. D: Appl. Phys. Vol 20, No 7, pp815–819 (1987) .
[257] T. I. Cox, V. G. I. Deshmukh, D. A. O. Hope, A. J. Hydes, N. St. J. Braithwaite and N. M. P. Benjamin, "The use of langmuir probes and optical-emission spectroscopy to measure electron-energy distribution-functions in rf-generated argon plasmas", J. Phys. D: Appl. Phys. Vol 20, No 7, p820-831 (1987).
[258] P. A. Chatterton, J. A. Rees, W. L. Wu and K. Al-Assadi, "A self-compensating langmuir probe for use in rf (13.56 mhz) plasma systems", Vacuum. Vol 42, No 7, p489-493 (1991).
[259] A. Howling. Centre de Recherches en Physiques des Plasmas, Ecole Polytech Fed Lausanne, Switzerland.
[260] E. Hamers, W van Sark, J. Bezemer, W van der Weg. Plasma and surface characterisation symposium. Hiden Analytical, Warrington.
[261] W. D. Davis and T. A. Vanderslice, "Ion energies at the cathode of a glow discharge", Phys. Rev. Vol 131, No 1, pp219 (1963).
[262] S. B. Radovanov, J. K. Olthoff and R. J. Van Brunt, NIST, Gaithersburg USA.
[263] C. A. M. de Vries and W. G. M. van den Hoek, "Validity of self-bias voltage measurements on insulating electrodes in radio-frequency dry etching systems", J. Appl. Phys. Vol 58, No 5, pp2074-2076 (1985).
[264] A. C. Dickenson, 'Measurement and Simulation of Ion Energy Distributions in a Reactive Ion Etcher', Phd Thesis Bristol University (1994).
[265] P.W. May, 'The Energies of Ions, Electrons and Neutrals in Reactive Ion Etching Plasmas', PhD Thesis Bristol University (1991).

[266] C. M. O. Mahoney, R. Al Wazzan and W. G. Graham, Conference Proceedings, ESCAMPIG, Slovakia (1996).
[267] C. M. O. Mahoney, R. Al Wazzan and W. G. Graham, "Sheath dynamics observed in a 13.56 mhz-driven plasma", Appl. Phys. Lett. Vol 71, No 5, pp608-610 (1997).
[268] M. Surendra and D. B. Graves, "Particle simulations of radiofrequency glow-discharges", IEEE Transactions on Plasma Science, Vol 19, No 2, p144-157 (1991).
[269] W. Xu and P. J. Sides, "Spatial variations of radio-frequency plasma-density caused by a step-change of secondary-electron emission coefficient", J. Appl. Phys. Vol 77, No 9 pp4293-4301 (1995).
[270] M. Surendra and D. B. Graves, "Particle simulations of radiofrequency glow-discharges", IEEE Transactions on Plasma Science, Vol 19, No 2, p144-157 (1991).
[271] M. Surendra and D. B. Graves, "Particle simulations of radiofrequency glow-discharges", IEEE Transactions on Plasma Science, Vol 19, No 2, p144-157 (1991).
[272] Z. Wronski, Marie-Sklodowska University, Lublin, Poland. Private communication.
[273] R. A. Morgan, "Plasma Etching in Semiconductor Fabrication", Phd, University of Sussex (Elsevier, 1985).
[274] P. W. May, Bristol University, UK. Private communication.
[275] C. A. M. de Vries and W. G. M. van den Hoek, "Validity of self-bias voltage measurements on insulating electrodes in radio-frequency dry etching systems", J. Appl. Phys. Vol 58, No 5, pp2074-2076 (1985).
[276] Keith Vanner, Caswell, GEC-Marconi, Tadcaster, Northamptonshire. Private communication.
[277] A. S. Bunting, Aston University, UK. Private communication.
[278] C. M. O. Mahoney, R. Al Wazzan and W. G. Graham, Conference Proceedings, ESCAMPIG, Slovakia (1996).
[279] C. M. O. Mahoney, R. Al Wazzan and W. G. Graham, "Sheath dynamics observed in a 13.56 mhz-driven plasma", Appl. Phys. Lett. Vol 71, No 5, pp608-610 (1997).
[280] S. J. Pearton, J. W. Lee, E. S. Lambers, J. R. Mileham, C. R. Abernathy, W. S. Hobson, F. Ren and R. J. Shul, "High microwave power electron cyclotron resonance etchingof iii-v semiconductors in ch4/h-2/ar", J. Vac Sci. Tech B 14, No 1, pp118-125 (1996).
[281] M. Surendra and D. B. Graves, "Particle simulations of radiofrequency glow-discharges", IEEE Transactions on Plasma Science, Vol 19, No 2, p144-157 (1991).
[282] P.W. May, 'The Energies of Ions, Electrons and Neutrals in Reactive Ion Etching Plasmas', PhD Thesis Bristol University (1991).
[283] J. K. Olthoff, R. J. Van Brunt, S. B. Radovanov, "Ion kinetic-energy distributions in argon rf glow discharges", J. Appl. Phys. Vol 72, No 10, pp4566-4574 (1992).
[284] A. C. Dickenson, 'Measurement and Simulation of Ion Energy Distributions in a Reactive Ion Etcher', Phd Thesis Bristol University (1994).
[285] P.W. May, 'The Energies of Ions, Electrons and Neutrals in Reactive Ion Etching Plasmas', PhD Thesis Bristol University (1991).
[286] J. Liu, G. L. Huppert, H. H. Sawin, "Ion bombardment in rf-plasmas", J. Appl. Phys. Vol 68, No 8, pp3916-3934 (1990).
[287] National Research Council, Board on Physics and Astronomy, Database Needs for Modelling and Simulation of Plasma Processing, National Academy Press, Washington, 1996.
[288] P.W. May, 'The Energies of Ions, Electrons and Neutrals in Reactive Ion Etching Plasmas', PhD Thesis Bristol University (1991).
[289] A. C. Dickenson, 'Measurement and Simulation of Ion Energy Distributions in a Reactive Ion Etcher', Phd Thesis Bristol University (1994).
[290] M. A. Foad, S. Thoms and C. D. W. Wilkinson, "New technique for dry etch damage assessment of semiconductors", J. Vac. Sci. Tech. B. Vol 11, No 1, pp20-25 (1993).
[291] Z. Lu, M.T. Schmidt, R.M. Osgood Jr., W.M. Holber, D. Podlesnik, J. Vac. Sci. Technol. A 9 (3) 1040, (1991)

[292] Yu. W, "Ion bombardment induced compositional changes in compund semiconductor surfaces studied by XPS combined with LEISS", PhD Thesis, Aston University (1995).
[293] M. T. Cuberes and J. L. Sacedon, Surface Science, 269/270 pp 929-933 (1992).
[294] T. E. Nitschke and D. B. Graves, "A comparison of particle-in-cell and fluid model simulations of low-pressure radio-frequency discharges", J. Appl. Phys. Vol 76, No 10, pp5646-5660 (1994).
[295] W. Z. Collison and M. J. Kushner, "Ion drag effects in inductively coupled plasmas for etching", J. Appl. Phys. Lett. 68 (7) pp903 (1996).
[296] P. L. G. Ventzek, T. J. Sommerer, R. J. Hoekstra and M. J. Kushner, "Two-dimensional hybrid model of inductively coupled plasma sources for etching", J. Appl. Phys. Lett. 63 (5) pp605 (1993).
[297] H. H. Hwang and M. J. Kushner, "Regimes of particle trapping in inductively coupled plasma processing reactors", J. Appl. Phys. Lett. 68 (26) pp3716 (1996).
[298] T. J. Sommerer and M. J. Kushner, "Numerical investigation of the kinetics and chemistry of rf glow discharge plasmas sustained in He, N2, O2, He/N2/O2, He/CF4/O2 and SiH4/NH3 using a Monte-Carlo-fluid hybrid model", J. Appl. Phys. 71 (4) pp1654 (1992).
[299] M. J. Grapperhaus and M. J. and Kushner, "A semianalytical radio frequency sheath model integrated into a two-dimensional hybrid model for plasma processing reactors", J. Appl. Phys. 81 (2) pp569 (1997).
[300] L. G. Ventzek, M. J. Grapperhaus and M. J. Kushner, "Investigation of electron source and ion flux uniformity in high plams density inductively coupled etching tools using two-dimensional modelling" J. Vac. Sci. Technol. B 12(6) pp3118 (1994)
[301] T. J. Sommerer, M. S. Barnes, J. H. Keller, M. J. McCaughey and M. J. Kushner, "Monte Carlo-fluid hybrid model of the accumulation of dust particles at sheath edges in radio frequency discharges", Appl. Phys. Lett. 59 (6) pp638 (1991).
[302] Graves et al Abstract DB6 44th Gaseous electonics conference, Albuquerque, NM Oct 1991.
[303] P. Belengeur and J. P. Beouf, "Transition between different regimes of rf glow discharges", Phys. Rev. Vol 41, No 8, pp4447-4459 (1990).
[304] N. Sato and H. Tagashira, "A hybrid monte carlo/fluid model of rf plasmas in a SiH4/H2 mixture", IEEE transactions on plasma science, Vol 19, No 2, pp102-112 (1991).
[305] M. Surendra, D. B. Graves and G. M. Jellum, "Self consistent model of a direct current glow discharge - treatment of fast electrons", Phys. Rev. A 41 pp1112-1125 (1990).
[306] M. Surendra, "Radio frequency discharge benchmark model comparison", Plasma Sources Sci. Technol. 4 pp56-73 (1995).
[307] M.M. Turner, "Simulation of kinetic effects in inductive discharges", Plasma Sources in Science and Technology, 5, 2, pp159-165 (1996)
[308] M.M. Turner, "Multidimensional kinetic-fluid simulation of inductive discharges", Jap. J. Appl. Phys. 36, 7B, pp4784-4788 (1997)
[309] CASTEP, quantum mechanical code for material scientists. Licensed through MSI, http://www.msi.com.

APPENDIX 4 - Published Papers

Conference proceedings, Iasis, Romania, 1998.

Content has been removed for copyright reasons

ontent has been removed for copyright reasons

Content has been removed for copyright reasons